Bistatic Synthetic Aperture Radar Data Processing and Analysis

Alvin Soonlien Goh

A thesis submitted for the degree of Doctor of Philosophy

School of Electrical & Electronic Engineering
Faculty of Engineering, Computer and Mathematical Sciences
The University of Adelaide

February 2012

Contents

List of Figures

List of Tables

Abstract

Synthetic Aperture Radar (SAR) operation in a bistatic configuration offers various advantages over its now well-established monostatic counterpart but also poses various challenges, among which are the inversion of the raw bistatic SAR data into imagery, the maintenance of time and phase synchronisation between the separated transmitter and receiver, the application of interferometric techniques to bistatic data, and the polarimetric calibration of field-based bistatic systems in constant motion (particularly those with airborne/spaceborne components).

As part of a research programme into the potential benefits and challenges of bistatic SAR, the *Ingara* fully polarimetric X-band airborne imaging radar system, developed and operated by the Australian Defence Science and Technology Organisation, was upgraded to conduct experimental SAR data collections in a bistatic geometry. Experimental trials of the new bistatic SAR system were conducted in 2007 and 2008 in which the existing airborne radar was operated in a fine-resolution (600 MHz bandwidth) circular spotlight-SAR mode, in conjunction with a newly developed fully polarimetric stationary ground-based bistatic receiver. These trials produced a set of fully polarimetric simultaneously collected monostatic and bistatic SAR data, collected over a wide range of bistatic angles, for research purposes.

The work reported in this thesis is motivated by the various processing challenges presented by these data sets. Herein, image formation from raw spotlight-mode bistatic SAR data using the Polar Format Algorithm (PFA), particularly as it pertains to a circling-transmitter-stationary-receiver bistatic geometry, is discussed. The limitations of the first-order (plane-wave) phase approximation employed in deriving the PFA are examined for the case of a stationary-receiver bistatic collection geometry with co-planar transmitter, receiver and scatterers: expressions for the size of the focussed region are derived by restricting the magnitude of the second order phase term, and the complicated behaviour of the shape of this region in this bistatic case (which is not encountered in the monostatic case) is discussed. Fine-resolution imagery results from the PFA-based processing of simultaneously collected monostatic and bistatic data sets are shown, and results from the interferometric processing of single-pass simultaneously collected monostatic and bistatic SAR data with a relatively large (approx. 5°) grazing-angle difference and of repeat-pass bistatic data with a temporal delay of hours, both demonstrating interferometric coherence in the fine-resolution interferograms, are presented. Finally, the polarimetric calibration of a field-based bistatic SAR with an airborne component is addressed: minor variants of three previously published distributed-target-based polarimetric calibration algorithms are derived; the results of Monte Carlo numerical studies to compare their accuracies are discussed; a new calibration approach involving a hybrid of two of these algorithms which takes account of channel noise is proposed; the use of standard calibration targets (dihedrals, trihedrals etc.) potentially supplemented by the direct-path signal for polarimetric calibration is considered; and calibration results from the *Ingara* data are presented.

Declaration

I, Alvin Soonlien Goh, certify that this work contains no material which has been accepted for the award of any other degree or diploma in any university or other tertiary institution and, to the best of my knowledge and belief, contains no material previously published or written by another person, except where due reference has been made in the text.

I give consent to this copy of my thesis, when deposited in the University Library, being made available for loan and photocopying, subject to the provisions of the Copyright Act 1968.

I also give permission for the digital version of my thesis to be made available on the web, via the University's digital research repository, the Library catalogue and also through web search engines, unless permission has been granted by the University to restrict access for a period of time.

Signature: _____

Date: _____

Acknowledgements

I wish to thank my supervisors Professor Doug Gray, Dr Mark Preiss and Dr Nick Stacy for their invaluable guidance, advice, support and encouragement through the course of my Ph.D. studies.

I also wish to thank the Defence Science and Technology Organisation (DSTO) for supporting my Ph.D. candidature and for providing me with the opportunity to carry out this interesting research.

I would also like to thank the various members of the *Ingara* team at DSTO, whose dedicated efforts in designing and building the bistatic system and in planning and conducting the trials were so instrumental to achieving the many successful results reported in this thesis.

Finally, thank you to my family and friends for all their support and encouragement through this long and arduous journey.

A. S. G.

List of publications

1. A. S. Goh, M. Preiss, D. A. Gray, and N. J. S. Stacy, "Comparison of parameter estimation accuracy of distributed-target polarimetric calibration techniques," *Proc. IEEE Int. Geosci. Remote Sens. Symp., IGARSS*, Barcelona, Spain, July 2007.

2. A. S. Goh, M. Preiss, N. J. S. Stacy and D. A. Gray, "The *Ingara* bistatic SAR upgrade: first results," *Int. Conf. Radar, RADAR 2008*, Adelaide, Australia, September 2008, pp. 329–334.

3. A. S. Goh, M. Preiss, N. J. S. Stacy and D. A. Gray, "Bistatic SAR experiment with the *Ingara* imaging radar: preliminary results," *Proc. 7th Eur. Conf. Synthetic Aperture Radar, EUSAR 2008*, Friedrichshafen, Germany, June 2008, pp. 49–52.

4. A. S. Goh, M. Preiss, N. J. S. Stacy and D. A. Gray, "Bistatic SAR experiment with the *Ingara* imaging radar," *IET Radar Sonar Navig.*, vol. 4, no. 3, pp. 426–437, 2010.

List of symbols and abbreviations

For ease of reference, a selection of important and/or recurring symbols and abbreviations in the text of this thesis are summarised below.

Mathematical symbols

Image formation

Term	Introduced	Description
α	Page 38	Angle between axes of parallelogram grid.
$\mathbf{B}_n$	Page 30	Vector along bisector of bistatic angle.
c	Page 28	Speed of wave propagation.
$\chi_n(\tau)$	Page 27	SAR (deskewed) signal from scene.
δk_u	Page 44	Sampling interval along k_u-axis of parallelogram grid.
δk_v	Page 45	Sampling interval along k_v-axis of parallelogram grid.
f_c	Page 20	Centre frequency.
$g(\mathbf{R})$	Page 21	Scene spatial complex reflectivity function.
Δk_u	Page 46	Size of parallelogram grid along k_u dimension.
Δk_v	Page 46	Size of parallelogram grid along k_v dimension.
$D_n(\mathbf{R})$	Page 21	Transmitter-to-scatterer-to-receiver propagation delay.
$E_{\mathrm{d},n}$	Page 25	Timing offset in dechirp delay.
$E_{\mathrm{s},n}$	Page 25	Timing offset in sampling delay.
η	Page 61	Slant plane slope relative to k_v-axis.
γ	Page 19	Chirp rate.
$\hat{\mathbf{V}}$	Page 29	Unit vector in the direction of $\mathbf{V}$.
$\mathbb{I}_n(\tau;\mathbf{R})$	Page 23	An indicator function.
$\mathbf{K}_n(\tau)$	Page 30	Spatial-frequency domain wave-vector.
$\bar{k}_u$	Page 46	k_u coordinate of centre of parallelogram grid.
$\bar{k}_v$	Page 46	k_v coordinate of centre of parallelogram grid.
$\tilde{k}_u$	Page 49	Local displacement from $\bar{k}_u$.
$\tilde{k}_v$	Page 49	Local displacement from $\bar{k}_v$.
λ_c	Page 64	Wavelength.
n	Page 19	Pulse index.

N_{k_u}	Page 45	Number of rows in parallelogram grid.
N_{k_v}	Page 45	Number of columns in parallelogram grid.
$\mathbf{P}_{1,n}$	Page 28	Transmitter position at n^{th} pulse.
$\mathbf{P}_{2,n}$	Page 28	Receiver position at n^{th} pulse.
ψ	Page 61	Slant plane slope relative to k_u-axis.
$\Psi_n(\tau;\mathbf{R})$	Page 27	SAR (deskewed) signal phase from scattering at $\mathbf{R}$.
$\mathbf{R}$	Page 21	Position of scatterer.
$\text{rect}(x)$	Page 19	Rectangle function.
ρ_u	Page 64	Resolution along u (range) direction.
ρ_v	Page 64	Resolution along v (cross-range) direction.
$\text{sinc}(x)$	Page 26	Sinc function.
$s_n(\tau;\mathbf{R})$	Page 27	SAR (deskewed) signal from scattering at $\mathbf{R}$.
τ	Page 22	Intra-pulse (fast) time after start of sampling.
$T_{\text{d},n}$	Page 21	Dechirping pulse generation time.
$T_{\text{dg},n}$	Page 23	Pulse generation to dechirping delay.
$T_{\text{g},n}$	Page 20	Transmitted pulse generation time.
$T_{\text{s},n}$	Page 22	Time of start of sampling.
$T_{\text{sg},n}$	Page 23	Pulse generation to sampling delay.
T_p	Page 19	Pulse length.
u_0	Page 62	u-axis (range) component of $\mathbf{R}$.
$U_n(\mathbf{R})$	Page 25	Differential delay of $\mathbf{R}$ relative to $\mathbf{0}$.
$\mathbf{U}_{\perp\mathbf{V}}$	Page 29	Component of $\mathbf{U}$ perpendicular to $\mathbf{V}$.
v_0	Page 62	v-axis (cross-range) component of $\mathbf{R}$.
w_0	Page 62	w-axis (height) component of $\mathbf{R}$.

Interferometry

Term	Introduced	Description
γ	Page 104	Complex correlation coefficient.

Polarimetric calibration

Term	Introduced	Description
A	Page 131	Co-/cross-polarised covariances.
$\mathbf{A}$	Page 129	α channel imbalance matrix.
α	Page 129	Transmit and receive channel imbalance parameter.
B	Page 131	Co-/cross-polarised covariances.
β, β'	Page 131	Cross-polarised powers and covariance.
$\mathbf{C}$	Page 130	Noise-compensated observed covariance matrix.
C_{ij}	Page 133	Entry in row i and column j of $\mathbf{C}$.

$\mathbf{C_n}$	Page 130	Covariance matrix of noise.
$\mathbf{C_o}$	Page 130	Observed covariance matrix of distributed-target.
$\mathbf{C_s}$	Page 130	True covariance matrix of distributed-target.
G	Page 131	Co-/cross-polarised covariances after cross-talk and α channel imbalance correction.
H	Page 131	Co-/cross-polarised covariances after cross-talk and α channel imbalance correction.
γ, γ'	Page 131	Cross-polarised powers and covariance after cross-talk and α channel imbalance correction.
$\Im(\cdot)$	Page 134	Imaginary part of argument.
k	Page 129	Channel imbalance ratio for receive.
$\mathbf{K}$	Page 129	k channel imbalance matrix.
m	Page 138	Ratio of receiver noise powers.
$\mathbf{M}$	Page 129	Cross-talk distortion matrix.
N_{ij}	Page 130	Entry in row i and column j of $\mathbf{C_n}$.
$n_{\mathrm{hh}}, n_{\mathrm{hv}}, n_{\mathrm{vh}}, n_{\mathrm{vv}}$	Page 127	Polarimetric channel noise.
$\mathbf{P}$	Page 129	Polarimetric distortion matrix.
$\mathbf{Q}$	Page 131	Cross-talk and α channel imbalance matrix.
$r_{\mathrm{hh}}, r_{\mathrm{hv}}, r_{\mathrm{vh}}, r_{\mathrm{vv}}$	Page 127	Receive polarimetric distortion.
$\Re(\cdot)$	Page 134	Real part of argument.
$s_{\mathrm{hh}}, s_{\mathrm{hv}}, s_{\mathrm{vh}}, s_{\mathrm{vv}}$	Page 127	Polarimetric scattering response.
$\sigma_{11}, \sigma_{41}, \sigma_{44}$	Page 131	Co-polarised powers and covariance.
$t_{\mathrm{hh}}, t_{\mathrm{hv}}, t_{\mathrm{vh}}, t_{\mathrm{vv}}$	Page 127	Transmit polarimetric distortion.
$\tau_{11}, \tau_{41}, \tau_{44}$	Page 131	Co-polarised powers and covariance after cross-talk and α channel imbalance correction.
u, v, w, z	Page 129	Cross-talk ratios.
Y	Page 129	vv-channel gain.

General acronyms/abbreviations

Term	Description
BPA	Back-Projection Algorithm
BPTRS	Bistatic Point Target Reference Spectrum
BSA	Back-Scattering Alignment
CARABAS	Coherent All RAdio BAnd Sensing (Swedish radar testbed)
CSA	Chirp-Scaling Algorithm
CSIRO	Commonwealth Scientific and Industrial Research Organisation
DEM	Digital Elevation Model
DFT	Discrete Fourier Transform
DLR	Deutsches Zentrum für Luft- und Raumfahrt (German Aerospace Centre)
DMO	Dip Move-Out

DRDC	Defence Research and Development Canada
DSP	Digital Signal Processing
DSR	Double Square-Root
DSTO	Defence Science and Technology Organisation
DTFT	Discrete Time Fourier Transform
ESA	European Space Agency
FFT	Fast Fourier Transform
FGAN	Forschungsgesellschaft für Angewandte Naturwissenschaften (German Research Establishment for Applied Sciences)
FSA	Forward-Scattering Alignment
GNSS	Global Navigation Satellite Systems
GPS	Global Positioning System
IRF	Impulse Response Function
ISLR	Integrated Side-Lobe Ratio
LBF	Loffeld's Bistatic Formula
MF	Matched-Filter
MMR	Multi-Mode Radar
MSR	Method of Series Reversion
ONERA	Office National d'Études et de Recherches Aérospatiales (French Aerospace Research Centre)
PAMIR	Phased Array Multifunctional Imaging Radar
PFA	Polar Format Algorithm
PGA	Phase Gradient Autofocus
PRF	Pulse Repetition Frequency
PSF	Point Spread Function
PSLR	Peak-to-Side-Lobe Ratio
RAMSES	Radar Aéroporté Multi-spectral d'Etude des Signatures (ONERA radar system)
RCS	Radar Cross Section
RMA	Range-Migration Algorithm
SAR	Synthetic Aperture Radar
SNR	Signal-to-Noise Ratio
TanDEM-X	TerraSAR-X add-on for Digital Elevation Measurement
TDC	Time-Domain Correlation
TWT	Travelling-Wave-Tube (amplifier)
UPC	Universitat Politècnica de Catalunya (Technical University of Catalonia)
WSS	Wide-Sense Stationary
XWEAR	X-band Wideband Experimental Airborne Radar

Chapter 1

Introduction

A radar is essentially an instrument for detecting and locating objects of interest using radio waves: indeed, the word 'radar' was originally coined as an acronym for '*ra*dio *d*etection *a*nd *r*anging'. Typically, a basic modern radar system consists of a transmitter for emitting radio-frequency electromagnetic (EM) energy, and a receiver for coherently collecting the scattered returns from any radar targets in the region under surveillance. The spatial location of any detected targets may then be inferred from the time delay between the received and transmitted signals and the directions in which the transmitting and receiving antennas were pointing: the former gives a measure of the transmitter-to-target and target-to-receiver range sum while the latter indicates the direction to the scatterer.

A high precision in locating targets is frequently advantageous in many radar applications. Generally, it is relatively easy to obtain fine resolution in range by simply transmitting a signal with a wide bandwidth. However, resolution in the direction to the scatterers (i.e. cross-range resolution), as determined by the orientation and beamwidths of the transmitting and receiving antennas, is often comparatively coarse. Finer directional resolution may be achieved by increasing the antenna sizes so as to reduce their beamwidths. However, a doubling of antenna size only produces a halving of the beamwidth, so, in many cases, the achievement of sufficiently fine resolution by this approach is infeasible.

Synthetic Aperture Radar (SAR) is essentially a technique for overcoming the antenna beamwidth limitations on directional resolution by exploiting relative motion between scatterers and a *moving* radar system. It relies on the sensitivity of the phase of the received signal from a scatterer to changes in the range sum caused by any relative motion between the scatterer and the radar. Generally, scatterers in different positions in the region under surveillance will have different relative motions, giving rise to distinct variations in the phase of their received signals: hence, the observed phase history in the received signal can be used to determine the position of the scatterer. As two closely separated scatterers can nevertheless produce distinct changes of phase in their received signals, quite fine resolution may be achieved. As the product of SAR systems are typically images showing the surface of the Earth (or other planets), SARs are also often referred to as imaging radars.

Since their inception in the 1950s [1], SARs have found wide application and numerous systems are currently in operation. Of these, practically all have co-located transmitting and receiving antennas: indeed, the common practice is to use the same antenna for both transmitting and receiving. Such systems are referred to as *monostatic* in contrast to *bistatic* systems, in which a significant separation exists between the transmitting and receiving elements. Although early experimental radar systems were bistatic [2], advances in technology, particularly the advent of the duplexer, eventually allowed the use of a single antenna, with

its concomitant advantages of simplicity, compactness and cost-effectiveness: to this may be attributed the current predominance of monostatic radar systems. In recent years, however, there has been a resurgence of interest in bistatic radar and bistatic SAR, with a growing number of papers being devoted to the subject in recent radar conferences.

The renewed enthusiasm for bistatic radar systems stems from various potential advantages offered by the bistatic over the monostatic configuration, among which are the following:

- A reduction in vulnerability of the receiver to both electronic countermeasures (particularly directional jamming) and physical attack, as the receiver may be operated covertly and at a distance from the overt and exposed transmitter.
- The potential to employ illuminators-of-opportunity rather than expend effort in deploying a dedicated transmitter platform. Potentially, with the use of a covert receiver, this allows surreptitious imaging to be performed. Furthermore, the use of VHF and UHF broadcast and communication signals from illuminators-of-opportunity allows the employment for radar applications of frequency bands which have been allocated for other purposes and would not otherwise be available.
- Freedom to deploy the transmitting platform independently of the receiver, such as at a long standoff distance from the target area, or even close to hazards if expendable transmitters are used.
- The ability to conduct imaging in unconventional geometries to exploit potentially useful features of the scattering phenomenology, e.g. placing the receiver at low grazing angles to enhance textural and shadowing effects, employing a large bistatic angle to increase scattered return from stealthy objects, etc.
- A reduction in retro-reflector effects when imaging urban areas, so that weaker scatterers are less prone to obscuration by the strongly monostatically reflecting corner reflector-like structures which are prevalent in built-up areas.
- The ability to achieve good resolution along the direction of motion of the receiver; in contrast, resolution in a forward-looking geometry is poor for a monostatic SAR system.
- The ability to collect two sets of data of a scene simultaneously if the transmitter platform also carries a second receiver, thus avoiding the temporal decorrelation effects which afflict repeat-pass interferometry.
- The potential to exploit bistatic radar polarimetric information about scatterers in the imaged scene which is not available in monostatic radar polarimetry.

SAR operation and data exploitation in the bistatic mode is, however, more complicated than in the monostatic mode and poses a varied set of challenges, including:

- Robust and efficient algorithms need to be developed to produce focussed SAR imagery from bistatic data.
- Precise time synchronisation must be established between the transmitter and receiver for accurate measurement of the bistatic range sum.
- High phase stability is needed between oscillators in the transmitter and receiver for at least the coherent integration time to allow the formation of focussed imagery.
- Precise position and motion measurement of two independently moving platforms (bistatic transmitter and receiver) is needed for processing the bistatic data (in contrast to only one platform in the monostatic case). In addition, this must allow accurate and precise determination of the baseline to apply interferometric techniques to the bistatic SAR data.

- Field-based procedures for accurate polarimetric calibration are required to permit polarimetric scattering properties to be inferred from collected bistatic SAR data.
- The development of techniques for exploiting the polarimetric and interferometric potential of bistatic SAR data sets is needed.

To gain experience in the engineering and operation of a bistatic SAR system and insight into the properties of bistatic SAR imagery, the Australian Defence Science and Technology Organisation (DSTO) has conducted a programme of upgrades to add a bistatic collection capability to the fully polarimetric *Ingara* Multi-Mode Radar (MMR) airborne imaging radar system [3–5]. This work was completed in December 2007, and experimental trials exercising the new bistatic operating modes were conducted shortly thereafter. This experimental work involved bistatic data collection in a continuous-imaging circular spotlight SAR mode, in which the existing airborne radar was operated as a transmitter as it flew in circles around a ground scene of interest, while a newly developed fully polarimetric stationary ground-based receiver was used to receive the bistatically scattered signals. In the majority of the SAR data collection runs, the airborne radar was also receiving the monostatically scattered signals, so a rich set of both monostatic and bistatic data sets, simultaneously collected from a variety of angles, was subsequently available for analysis.

This thesis presents a detailed description of the methods used for processing and analysing bistatic SAR data (with a particular emphasis on the collected *Ingara* data) and a discussion of the results which were obtained. The main achievements reported in this work are:

1. A detailed exposition of the Polar Format Algorithm (PFA) for monostatic and bistatic spotlight-mode SAR image formation (particularly as it pertains to the circular spotlight SAR mode of operation employed by the *Ingara* system).
2. The calculation of the theoretical size of the focussed region in PFA-processed SAR imagery for a fixed-receiver bistatic circular spotlight collection geometry in which transmitter, receiver and scatterers are effectively co-planar.
3. The formation of fine-resolution monostatic and bistatic SAR images from the *Ingara*-collected spotlight-mode SAR raw echo data.
4. The generation of fine-resolution spotlight-mode SAR interferograms using the *Ingara* single-pass simultaneously collected monostatic and bistatic data as well as repeat-pass bistatic data collected with a temporal delay.
5. A Monte Carlo method-based comparison of the accuracy achieved by various distributed target-based polarimetric calibration algorithms in calculating the system polarimetric distortion.
6. A combination of minor variants of two distributed target methods into a hybrid method for polarimetric calibration which also estimates and accounts for system noise.
7. The polarimetric calibration of the *Ingara* monostatic and bistatic polarimetric data sets.

In the remainder of this introductory chapter, we set the stage for the material to follow in the later chapters which comprise the body of this thesis. Thus, we begin in Section 1.1 by presenting a general review of the research literature on bistatic SAR. Following this, in Sections 1.2 and 1.3, we give a technical overview of the *Ingara* bistatic SAR system and describe the recent bistatic SAR experimental trials. Finally, in Section 1.4, we outline the overall structure of this thesis.

1.1 Review of literature

To provide some context for this work, we now present a brief review of the recent research literature. In the interests of brevity, some of the topics will only be introduced in the present discussion, with more extensive background given later in Chapters 2 to 4.

1.1.1 Experiments in bistatic SAR

Willis [6] has noted that, since the end of the Second World War, interest in bistatic radar has experienced periodic resurgences approximately every 15 to 20 years. Although radar imaging was not a particularly prominent application in the earlier (first and second) surges of interest,[1] the present (third) cycle has seen a considerable level of research interest specifically directed towards SAR. Hence, to date, various theoretical studies on potential bistatic SAR systems and experiments involving the collection and processing of bistatic SAR data have been conducted.

Much of the current interest in future operational bistatic SAR systems is concentrated on the potential of space-based bistatic SAR satellite constellations [7–9]. In fact, the benefits and challenges posed by the deployment of such space-based systems is a major factor spurring much of the current research activity in bistatic SAR. Some examples of these systems include the Interferometric Cartwheel, in which a formation of micro-satellites flies ahead of or behind an active SAR satellite illuminator [10, 11]; BISSAT, in which a receiver on board a small satellite observes the area illuminated by an existing SAR [12]; and TanDEM-X, in which an add-on satellite supplements the TerraSAR-X satellite for high-resolution interferometry [13]. In addition to the already-mentioned general advantages and disadvantages of bistatic systems, such space-based systems offer an attractive means for frequent monitoring of areas of interest and for acquiring interferograms on a global scale, but may suffer increased ambiguity levels from small receiver antennas and require strategies to manage the large volume of collected data [14].

In contrast to fully spaceborne systems, attention has also focussed on the use of spaceborne satellite-based illuminators with non-spaceborne receivers: such a configuration has been termed 'hybrid bistatic SAR' [15] and 'space-surface bistatic SAR' (SS-BSAR) [16]. In this configuration, the receiver is generally ground-based or airborne. Some examples of the former are found in: an experiment conducted in 2002 using RADARSAT-1 as the illuminator combined with a stationary ground-based receiver [17]; bistatic SAR work using ESA's ENVISAT and ERS-2 SAR satellites as illuminators for a ground-based receiver [18]; and experiments employing Global Navigation Satellite Systems (GNSS) as transmitters in conjunction with a moving roof-top receiving apparatus [19]. Experiments involving an airborne receiver include: a series of SAR experiments in 1994 using the ERS-1 satellite and the shuttle SIR-C as spaceborne illuminators combined with an airborne receiver on a NASA DC-8 aircraft [20]; and more recent work employing TerraSAR-X as transmitter and the F-SAR and PAMIR systems as receivers [21, 22].

In the above-mentioned systems which employ satellite-based illuminators, the satellite is essentially used as an illuminator-of-opportunity: this curtails operational freedom, as it does not allow much choice in the imaging schedule or geometry. Hence, the use of dedicated bistatic transmitters is of interest and various experiments employing such transmitters have recently been performed. Examples involving the use of an airborne transmitter with a ground-based receiver include an experiment in 2002 using the airborne Environment Canada CV 580 SAR as illuminator and a ground-based receiver [17], a bistatic flight campaign conducted in 2006 using the Defence Research and Development Canada's (DRDC) XWEAR radar as transmitter and a

[1] Willis does mention, however, interest in clutter-tuning and forward-looking SAR during the second resurgence.

tower-mounted ground-based receiver [23], a bistatic experiment with the Swedish Defence Research Agency's CARABAS-II as transmitter and a receiver mounted atop a Swiss mountain [24], and the DSTO *Ingara* bistatic experiments [25]. In addition to these, an experiment employing a stationary ground-based transmitter with the airborne PAMIR system as receiver has also been conducted [26]. Fully airborne bistatic configurations have also been the subject of experiments, examples of which include: a bistatic SAR experiment in 2002 using QinetiQ's Enhanced Surveillance Radar (ESR) on an aircraft as transmitter and the Thales/QinetiQ Airborne Data Acquisition System (ADAS) on a helicopter as the receiver [27]; an airborne bistatic experiment in February 2003, conducted by ONERA and DLR, using the RAMSES and E-SAR systems [28]; and an airborne bistatic experiment in November 2003 using the FGAN SAR sensors AER-II and PAMIR as transmitter and receiver respectively [29, 30]. In the ESR/ADAS SAR experiment, data was collected in a spotlight mode but, in the RAMSES/E-SAR and AER-II/PAMIR experiments, translationally invariant configurations, in which the aircraft flew linear trajectories with equal velocities, were used.

1.1.2 Issues in bistatic SAR operation

SAR system operation in the bistatic mode poses challenges not encountered in the monostatic. An obvious difficulty is that of synchronising the operation of the spatially separated transmitter and receiver so that they both act in unison to acquire SAR data, but somewhat less obvious issues include the effects on the coverage and resolution of the resultant imagery exerted by different choices of imaging geometry.

Maintaining time and phase synchronisation between the transmitter and receiver requires high stability in the oscillators employed. Indeed, oscillator stability requirements are more stringent for bistatic than monostatic SAR, as a monostatic system uses the same oscillator for modulation and demodulation whereas a bistatic system uses separate oscillators in the transmitter and receiver: hence, although the effects of low-frequency phase errors are largely cancelled out in the monostatic case, they are left unmitigated in the bistatic case. This need for precise synchronisation and phase stability between transmitter and receiver for bistatic radar imaging has been noted by various authors [31, 32], and detailed analyses of the effects on bistatic SAR performance of oscillator synchronisation and phase errors have been conducted by Gierull [17] and by Krieger and Younis [33]: in general, constant frequency offsets produce displacements in imagery but no defocussing, linear frequency drifts mainly produce defocussing in the Doppler direction (which may reach unacceptable levels for long coherent integration times), and random phase noise increases the overall side-lobe levels. Interestingly, although the ESR/ADAS [27] and *Ingara* bistatic SAR experiments employed high-accuracy Caesium and Rubidium oscillators, the RAMSES/E-SAR [28] and AER-II/PAMIR [29, 30] experiments reported success without such specialised efforts at synchronisation.

A further aspect of synchronising transmitter and receiver operation is ensuring that the transmit and receive antennas are pointing correctly so that their footprints (swaths) overlap. This issue is particularly relevant to satellite-based bistatic systems where a low-cost secondary receiving satellite is tacked onto a pre-existing primary SAR mission, as the beam steering agility of the satellites may be limited thus requiring carefully designed strategies to ensure swath overlap [34]. The effects of errors in antenna-direction synchronisation have been investigated by Wang and Cai [35] using an oscillatory sinusoidal model: they demonstrate a consequent deterioration of the bistatic SAR impulse response, but propose an approach for maintaining antenna synchronisation based on the use of a pair of receive-antennas.

The bistatic imaging geometry affects imaging performance by determining the area under surveillance (and hence observation time) of a scatterer and the imaging resolution. In the general bistatic case, where the transmitter and receiver are moving in independent, non-linear trajectories, the coverage and observation

time (and hence the achievable azimuthal resolution) may vary in a complicated manner depending on the collection geometry: this has been analysed by Gierull [17] for the general 3-D case. For the restricted case of parallel transmitter and receiver tracks, however, a method for determining azimuth coverage and integration time using space-time diagrams depicting the time evolution of the antenna footprints has been presented by Nico and Tesauro [36].

The resolution with which the time-delay and Doppler frequency can be measured by the radar determines the achievable SAR image resolution. Thus, the resolution is related to the spacing between the level sets of range sum and its derivative. Due to the shapes of these level sets, in the general bistatic case the range and Doppler resolutions are usually aligned along non-orthogonal directions: this is unlike the simple case of broadside imaging with a monostatic SAR. Simple approximate expressions for the theoretically achievable imaging resolution and its directional dependence have been derived by Walterscheid et al. [37] and Cardillo [38] using a gradient-based approach: these reduce to the familiar expressions for range and cross-range resolution in the monostatic case [39].[2] Bistatic SAR resolution can also be calculated by using generalised ambiguity functions in the spatial domain, as demonstrated by Zeng et al. [40].

1.1.3 Image formation

Generally, the nature of the phase histories in bistatic SAR is quite different from that in monostatic SAR (particularly in the general case of independently moving transmitter and receiver) and the task of processing bistatic SAR raw data to form imagery is more complicated than for monostatic SAR. The reason for this is that, unlike the monostatic case, where the range history of a point target is determined by the motion of a single radar platform, in the bistatic case, the individual motions of the transmitter and receiver both contribute to the range history: as the transmitter and receiver may move independently of each other, complicated range histories can easily arise. An analysis of a signal model for bistatic SAR shows that the range history in the bistatic case differs from the simple hyperbola encountered in the monostatic case in both shape and scaling [41]: thus, in general, bistatic SAR signals cannot be simply processed using the established monostatic algorithms. Hence, an area of current research interest is the development of efficient and robust algorithms for processing bistatic SAR data into imagery.

Fundamentally, image formation can be achieved by direct matched-filtering. This essentially amounts to performing time-domain correlation of the bistatic SAR signal with a reference signal. Although relatively simple to implement, this approach is computationally expensive and, usually, unacceptably slow for real-time processing. Hence, it is not often used except in non-time-critical applications. Consequently, there is considerable interest in fast-convolution processing approaches in the frequency-domain. Such methods rely on the availability of a point target reference spectrum but, whereas this is readily derived using the principle of stationary phase [42] in the monostatic case, it is much harder in the bistatic case due to the independent range history contributions of the transmitter and receiver. Numerical computation of the required transfer function is certainly one solution but analytic approaches are preferred: two examples which have recently seen high levels of research activity are Loffeld's bistatic formula [41] and Neo and colleagues' method of series reversion [43].

The above image formation approaches are concerned with SAR imaging of extended scenes: for spotlight-mode SAR imaging of small scenes, however, a simpler approach in the form of the Polar Format Algorithm (PFA) may be adequate for SAR data processing. The PFA is a computationally efficient Fast Fourier

[2] However, Gierull [17] has been pointed out that these expressions do not properly account for the motion of the transmitter and receiver during the coherent processing interval (although they may suffice for quick estimation of bistatic SAR resolution performance): a more rigorous treatment taking the transmitter and receiver motion into account is presented therein.

Transform-based method but is subject to geometric distortions and defocussing due to uncompensated range curvature [39, 44], Although originally developed for monostatic SAR, versions of the PFA capable of bistatic SAR processing have recently been discussed in the literature [45, 46].

The discussion of bistatic SAR image formation presented above has been brief: as Chapter 2 of this thesis is concerned with *Ingara* bistatic SAR image formation, a fuller discussion of the contextual background to bistatic SAR processing is presented in Section 2.2.

1.1.4 Interferometry

SAR interferometry is an established technique for exploiting the information contained in the phase difference between two SAR images acquired from different vantage points or times [47,48]: this is typically accomplished through the coherent combination of two complex-valued SAR images to generate an interferogram. The nature of the information which may be extracted is determined by the precise nature of the two images but, generally, images acquired in a cross-track mode (from different viewing geometries) allow the topography of the imaged scene to be inferred, and images acquired in an along-track mode (from similar geometries but with a slight time delay) allow the velocity of moving objects to be determined. In addition, images acquired at significantly different times but still from similar geometries allow the detection of changes in the imaged scene, such as geological surface deformation [49, 50] or human activity [51].

Interferometric data sets are often acquired in a repeat-pass mode, where a single radar platform collects two data sets as it retraces a trajectory as closely as possible. Such collections suffer from temporal decorrelation and atmospheric distortion arising from the difference in acquisition times of the two data sets. Bistatic systems offer the opportunity to collect both data sets simultaneously in a single-pass, hence avoiding such effects. In addition, with independently moving transmitting and receiving platforms, large interferometric baselines can be achieved, which will be helpful in topographic-mapping applications [14]. Not surprisingly, therefore, interferometry figures prominently as an application for various proposed bistatic systems [8, 10, 52, 53] and is an area of interest of some current experimental work [54, 55].

An interesting interferometry-related technique involves the enhancement of image resolution by the coherent combination of SAR data acquired from slightly different look angles. This technique relies on the wavenumber shift effect in SAR interferometry [56] in which the ground wavenumber spectra of a SAR image is dependent on the interferometric baseline and local terrain slope. This effect may be exploited by judiciously choosing appropriate off-nadir angles during SAR data collection so that the spectra of the received signals contain different but overlapping bands of the spectrum of the ground reflectivity function: by coherently combining the measured spectra, the total range bandwidth is increased and an image with finer resolution can be generated. Combination of the spectral bands may be performed by shifting one signal in frequency with respect to the other and adding the two or, equivalently, by adding a phase-shifted version of one signal to the other. To date, the technique has mostly been developed and applied to spaceborne monostatic SAR data [56–58] but the case of airborne monostatic SAR data, where nonlinear effects due to the strong variations in incidence angle need to be accounted for, has also been examined [59]. There is also current interest in applying this technique to bistatic data [60, 61].

In this thesis, Chapter 3 is devoted to the interferometric analysis of the *Ingara* bistatic data: accordingly, we defer a fuller discussion of the background to interferometry to Section 3.2.

1.1.5 Polarimetry

Electromagnetic radiation comprises wave-like oscillations of vectorial electric and magnetic fields. Being vectorial, different directions of oscillations are possible, so polarisation is an intrinsic property of radio waves. As scattering is sensitive to the polarisation of the incident wave, the polarisation response of scatterers contains information about their nature. Consequently, there is much ongoing interest in the use of polarimetric radar systems to measure and infer properties of targets and clutter from collected radar data. Indeed, polarimetric techniques have been employed in interferometric applications (see Section 1.1.4 below) to enhance the performance of conventional SAR interferometry, giving rise to the field of *polarimetric interferometry* [62]: this separates different scattering mechanisms by exploiting measurements of polarisation response, so as to select an optimum polarisation to improve the interferogram quality for an application of interest.

To date, the bulk of the established body of knowledge in polarimetry has concentrated on monostatic radar systems [63]. However, interest is increasing in bistatic polarimetry. One reason for this is the greater number of independent parameters in bistatic polarimetric measurements: in the monostatic case, the two cross-polarisation responses[3] of many scatterers of interest are equal (by the principle of reciprocity), but this is not the case for bistatic scattering. Hence, bistatic polarimetric measurements potentially contain a greater amount of information about the scattering process.

To date, a variety of theoretical and experimental work has been published on bistatic radar polarimetry. The focus of the theoretical efforts includes the extension of polarimetry theory to the bistatic case [64–69] and the elucidation (sometimes aided by simulation) of the likely value of bistatic over monostatic observations [70–74]. Experimental work has concentrated on building up a data base of bistatic clutter measurements of crops and natural terrain [75–77] (bistatic radar sea clutter has also received some attention [78]). Many of these experimental measurements have been conducted on a small scale, over distances of a few metres, under controlled laboratory or test-range conditions, and using small samples of the targets of interest; however, bistatic polarimetric measurements conducted under more field-like conditions, over distances of approximately 20 km using a hill-top-mounted transmitter and receiver, have also been reported [79]. Due to the complexity involved in deploying airborne platforms, however, there is a general dearth of bistatic measurements from such field-based systems. In general, whereas measurements of terrain backscatter are relatively numerous, the database of fully polarimetric bistatic radar measurements of natural surfaces is comparatively limited.

Ideally, a radar polarimeter should report the actual scattering matrix of the target being measured. However, in practice, polarimetric distortions are introduced by both the transmitter and receiver, and the measurements do not accurately reflect the true characteristics of the scattering process. Calibration of the radar polarimeter, in order to correct for these distortions, is thus an important part of radar polarimetry [80]. In contrast to the case of monostatic polarimetric calibration, where the reciprocity condition and the simpler geometry have been exploited with success, the calibration of bistatic radar polarimeters is a more challenging problem. To date, various papers have been published on this subject, but nearly all have concentrated on instrumented radars in laboratory or test-range settings rather than dynamic field-based applications involving air- or spaceborne radars. The primary reason for this seems to be the lack of suitable alignment-insensitive targets for bistatic calibration: the available targets require precise alignment which is feasible only under carefully controlled conditions. Chapter 4 of this thesis is concerned with the polarimetric calibration of the *Ingara* bistatic SAR data: further discussion of the background to the bistatic polarimetric calibration problem is thus deferred to Section 4.2.

[3]For example, in the linear polarisation basis, the two cross-polarisations are HV (transmit horizontal and receive vertical) and VH (transmit vertical and receive horizontal).

Figure 1.1: The airborne platform for the *Ingara* multi-mode radar.

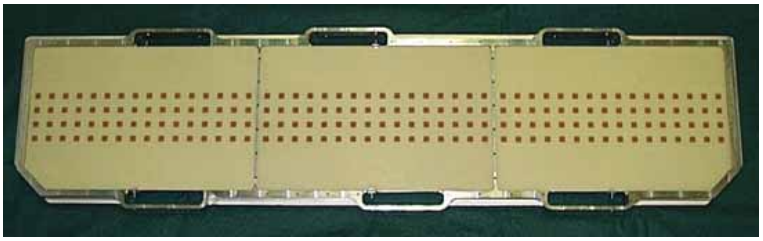

Figure 1.2: The multi-polarimetric antenna on the airborne system.

1.2 *Ingara* bistatic SAR system

The *Ingara* imaging radar is an airborne multi-mode X-band (centre frequency 10.1 GHz) SAR developed and operated by DSTO. When conducting experimental trials, *Ingara* is installed and operated in a Raytheon Beechcraft 1900C aircraft (see Figure 1.1). Primarily intended as a research instrument, the *Ingara* radar has undergone continual development and testing since its inception [3, 4]. In 2001–02, the system, at the time capable of transmitting and receiving HH-polarisation only, was upgraded to a full multi-polarimetric capability by integrating a new dual-linear-polarised microstrip patch array antenna developed by the Australian Commonwealth Scientific and Industrial Research Organisation (CSIRO) [5, 81] (see Figure 1.2): the -3 dB beamwidths of this antenna are approximately $1.5°$ in azimuth and $20°$ in elevation.

In around 2005, a programme of hardware and software upgrades to add a multi-polarimetric bistatic collection capability to the *Ingara* SAR system was commenced. To build on the polarimetric upgrade, this involved the construction of a stationary dual-polarimetric ground-based bistatic receiver to operate in conjunction with the existing fully polarimetric airborne monostatic SAR. To receive the scattered signals, the ground-based receiver employs an antenna comprising a receive-only dual-linear-polarised feedhorn mounted on a 1.8 m diameter parabolic dish (see Figure 1.3): the -3 dB beamwidth of this antenna is approximately $2°$.

To maintain synchronisation and coherence between the airborne and ground-based systems, the hardware of both systems was modified to use the 'one pulse per second' (1PPS) output signal from a Global Positioning System (GPS) receiver incorporated into each system as a common timing reference: a depiction of the functional blocks in the modified systems is shown in Figure 1.4. In each system, the 1PPS signal is used to

Figure 1.3: The multi-polarimetric antenna on the ground-based system.

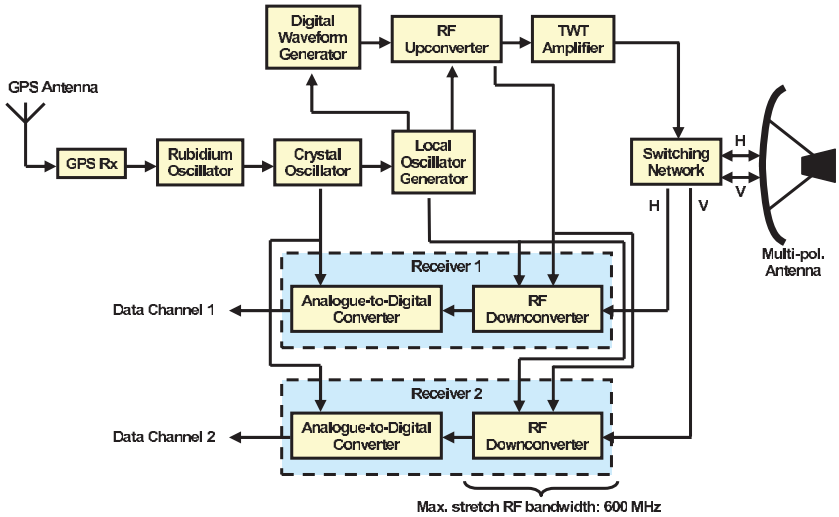

Figure 1.4: Simplified block diagram of airborne element of *Ingara* radar system: ground-based receiver is nearly identical but omits the TWT amplifier as it does not transmit.

discipline a low-phase-noise Rubidium oscillator, and the output signal from this in turn stabilises a crystal oscillator via a phase-locked loop. The crystal oscillators thus produce coherent reference signals in the two systems, and these are used as stable references for the local oscillator and clock-generator modules which produce the various timing and intermediate frequency (IF) signals used by the other modules in each system. As an additional measure to increase the timing stability, the oscillators in both systems were powered-up some 12–24 hours prior to SAR data collection and left running to allow time for them to settle before use.

For pulse generation, a basic linear FM chirp waveform is produced by a Digital Waveform Generator and this is modulated up to X-band by the RF upconverter. For transmission, this signal is amplified by the Travelling-Wave-Tube (TWT) amplifier and fed to a switching network which directs alternate pulses to the horizontally and vertically polarised (H and V) transmitting ports of the patch array multi-polarised antenna.

In both the airborne and ground-based systems, the scattered signal is received by their respective multi-polarimetric antennas, and the received H- and V-polarised signals are fed to separate receivers, where they are demodulated by RF downconverters to an IF of 300 MHz and sampled by analogue-to-digital converters

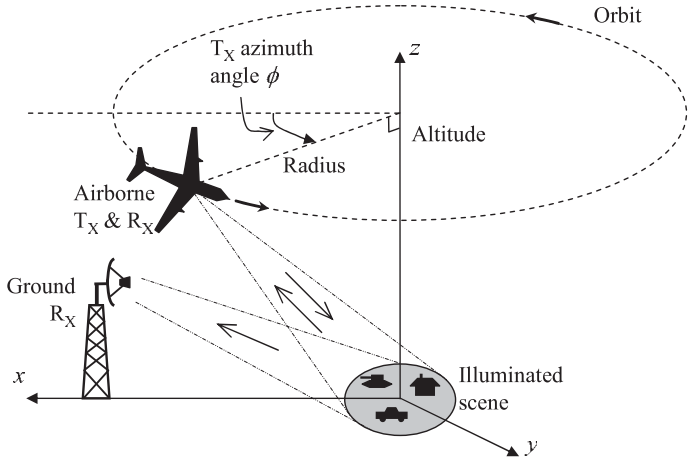

Figure 1.5: Bistatic collection geometry.

with a maximum sampling rate of 1 GS/s. When operating in circular spotlight SAR mode, stretch processing (also referred to as dechirp-on-receive or deramp-on-receive) is used in the demodulation process: the received signal is mixed with a delayed copy of the transmitted chirp, and the result is low-pass-filtered and sampled. The signal bandwidth supported by the RF hardware is approximately 600 MHz.

The resultant sampled data streams are simultaneously recorded on magnetic media and fed to digital computers for real-time processing. As data can only be recorded at maximum rates of approximately 25 MB/s in the airborne system and 11 MB/s in the ground-based system, care is needed in the selection of the pulse repetition frequency (PRF), pulse-length and sampling rates to keep the data collection rate within these limits. Real-time processing of the SAR data stream is mainly for monitoring the operation of the radar to allow any immediate adjustments which may be required to be made: in general, the full processing and analysis of the collected SAR data occurs off-line after landing. This is by necessity the case for the bistatic SAR data, as the generation of focussed imagery requires access to the aircraft position measurements for performing motion compensation, and these position data are not available until they are downloaded from the aircraft after it lands.

1.3 *Ingara* bistatic SAR trials

The first field trials of the new *Ingara* bistatic capability were conducted between December 2007 and April 2008, immediately following the completion of the upgrade programme. Subsequently, in December 2008, a second short trial was also conducted. In these trials, the nascent bistatic SAR system performed well, and produced a sizable set of simultaneously collected fully polarimetric monostatic and bistatic data for research purposes.

In these collections, data was acquired in a circular spotlight SAR mode, in which the airborne platform flew orbits around a designated scene of interest, with the airborne transmitter continually illuminating the scene while both airborne and ground-based receivers received the respective monostatically and bistatically scattered signals (see Figure 1.5). The transmitted bandwidth was 600 MHz and the PRF of the ground-based receiver was fixed at 650 Hz;[4] both receivers employed stretch processing (dechirp-on-receive) on the received

[4]The ground-based receiver opened its receiving windows at regular intervals of 1/650 s. Thus, for each pulse, the airborne radar adjusted its transmit (and receive times) according to its instantaneous distance from the scene, so as to ensure that the

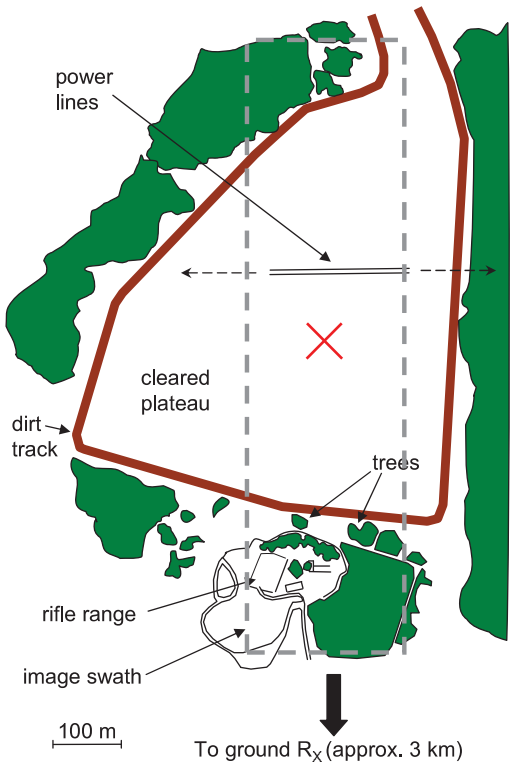

(a)

(b)

(c)

Figure 1.6: Hill-top plateau test site: (a) schematic elevation view; (b) view from antenna of ground-based receiver (red × marks approximate location at which radar reflectors were deployed); (c) local view showing ridged pattern of crop stubble and deployed quadruple-pack trihedral reflector.

(a) (b) (c)

Figure 1.7: Objects deployed at test site: (a) dihedral; (b) trihedral; (c) hemisphere.

Figure 1.8: Hay bales at test site c. March 2008.

signals. As the airborne platform orbited around the scene, data was continuously collected from the full 360° range of azimuthal directions ϕ. In addition, the heights and radii of the orbits were varied to also collect data over a range of incidence angles of illumination: typical heights ranged from 1000 m to 3600 m and radii from 3 km to 6 km, producing incidence angles from 53° to 82°. For this experiment, the ground-based receiving antenna was mounted atop a stationary tower structure: as the scene being imaged must lie in the receiver's line-of-sight, this constrained operation of the system to the imaging of test sites within only a few kilometres of the tower. Ultimately, for the majority of the imaging collections, the site used was a gently sloping plateau, covered by the remnants of a recently harvested wheat crop, on a hill approximately 3 km away from the ground-based receiver (see Figure 1.6). Various targets, such as vehicles and metallic radar reflectors of various types (e.g. dihedral, trihedral and hemisphere: see Figure 1.7) were deployed at the test site prior to imaging. Apart from these targets, the open field area at the test site was generally empty when SAR data was acquired, with the exception of numerous hay bales (Figure 1.8) which were present in March 2008 (these are also visible in Figure 1.6(b) which was taken around this time).

In addition to the general SAR imaging collections described above, a few specialised experimental data collections, intended for polarimetric calibration of the system, were also carried out. Polarimetric calibration is required to validly infer scattering characteristics from the collected data. However, calibration of bistatic imaging polarimeters in the field is non-trivial: the established point-target-based approaches require precise alignment to ensure the receiver is situated in the boresight of the reflected beam-pattern [82, 83] and this is difficult to achieve when the radar is carried on a manœuvring airborne platform. Hence, for the *Ingara* bistatic SAR system, it was planned to attempt calibration using two non-point-target based methods instead: one based on a direct-path approach [84] and another on distributed-targets [85–88]. The former involves measurement of the direct-path signal between the transmitting and receiving antennas and is specifically intended for bistatic radar systems. The latter involves the measurement of homogeneous areas with known statistical scattering properties and is based on an established class of methods designed for monostatic systems, but these were adapted to the bistatic case by employing monostatic-like imaging geometries where

bistatically scattered signal from the scene would arrive at the ground-based receiver when its receiving window was open.

the bistatic angle is minimised. Data collection for trialling these methods thus necessitated the use of special geometries: one to record the direct-path signal from the airborne transmitter to the ground-based receiver; and another to image the terrain in pseudo-monostatic geometries. Further discussion of these special data collections is deferred to Chapter 4.

1.4 Thesis structure

In this section, in the hope that it may aid the reader, we briefly outline the organisation of the material covered in this thesis.

- Chapter 1 (the present chapter) presents introductory material helpful for understanding this thesis as a whole. The contextual background to the topic of this thesis in given in the form of a review of the literature. A technical overview of the *Ingara* radar system is given, followed by a description of the field trials in which the bistatic data which is analysed in this thesis was collected. Finally, an outline of the structure of this thesis is presented.

- Chapter 2 discusses the signal processing employed to obtain focussed SAR images from the *Ingara* deramp-on-receive radar data. First, the stage is set by a review of the general literature on SAR image formation. A model for the raw deramped SAR signal is then derived and pre-processing steps (motion compensation and range-deskewing) to prepare the signal for subsequent Polar Format Algorithm (PFA) processing are discussed. A detailed discussion of the PFA, particularly as it pertains to the circling-transmitter-stationary-receiver bistatic geometry employed by the *Ingara* system, is then given. Next follows a discussion of the Phase Gradient Autofocus (PGA) algorithm employed for azimuthal phase error compensation. A signal model for the SAR image obtained from the PFA is then considered (this is subsequently used in a following chapter on interferometry). Limitations of the PFA processing approach (geometric distortion and defocussing) are discussed next. Finally, some results from applying the PFA to *Ingara* echo data are presented.

- Chapter 3 presents the results of an interferometric analysis of the data. First, some general contextual background to SAR interferometry is given with reference to the research literature. A description of two preparatory procedures important for interferometric processing then follows, namely the trimming of the SAR phase history data in the spatial frequency domain to improve correlation and the registration of the SAR images to ensure valid pixel-to-pixel correspondence. The interferometric coherence parameter is considered next, followed by a discussion of the extraction of height information from the interferogram phase. Some interferometric results from an analysis of the *Ingara* data are then presented: these include interferograms generated from single-pass monostatic-bistatic interferometric pairs as well as repeat-pass monostatic-monostatic and bistatic-bistatic pairs.

- Chapter 4 discusses the polarimetric calibration of the *Ingara* bistatic SAR system. Some background to this problem is first given in the form of a brief literature review. A mathematical model for the radar polarimetric distortion [86] is then presented, showing how the distortion can be related to inter-polarisation-channel cross-talk, channel-imbalance and overall receiver gain. Techniques for compensating for the cross-talk are next discussed: these are based on the expected statistics of the variously polarised returns from distributed-targets. The accuracy of three distributed-target-based polarimetric calibration algorithms are then compared and a hybrid calibration approach with account taken of

channel noise is proposed. Compensation of channel-imbalance using returns from standard calibration targets (trihedrals, dihedrals etc.) and/or the direct-path signal is then considered. The application of these techniques to the *Ingara* data is then discussed and results are presented.

- Finally, Chapter 5 concludes this thesis by summarising the main results and suggesting possible directions for further efforts.

Chapter 2

Image formation

2.1 Introduction

The production of focussed SAR imagery is an important and fundamental step in the analysis and exploitation of the raw echo data collected by a SAR system. Since the advent of digital SAR data processing, various computational algorithms have been developed to accomplish this important task. Until relatively recently, the focus of such algorithms has been on the processing of monostatic SAR data. With the current surge of interest in bistatic SAR, however, more recent efforts have been directed at the problem of image formation for bistatic systems. Such efforts have resulted in both modifications of existing algorithms as well as the development of new algorithms.

The algorithm used for image formation from the data collected in the *Ingara* bistatic SAR trials is the Polar Format Algorithm (PFA). This is a computationally efficient algorithm based on the Fast Fourier Transform (FFT) which is well suited to the dechirped circular spotlight-mode SAR data which was collected, but which produces an approximate inversion of the data resulting in images containing a certain degree of artefacts in the form of geometric distortion and defocussing [39,44]. Although an implementation of the PFA has previously been extensively used for processing monostatic *Ingara* circular spotlight-mode SAR data sets, for the work reported in this thesis, a more general version of the PFA [45], suitable for processing both the monostatic and bistatic *Ingara* data sets, was implemented and used instead.

This chapter gives an exposition of the method used to process the *Ingara* raw echo data into SAR imagery. To introduce the topic, a general overview is presented in the next section of different approaches to the processing of raw SAR data into focussed imagery. Then, to begin the discussion of the signal processing, a signal model is derived in Section 2.3 for the raw echo data collected by the *Ingara* system during radar operation. The preprocessing operations by which the raw echo data is prepared for processing by the PFA are discussed in Section 2.4. This is followed in Section 2.5 by a discussion of the concepts behind the PFA and the mechanics involved in its application to sampled data. Section 2.6 discusses an important adjunct to the PFA: the estimation of and compensation for azimuthal phase errors, in this case, via an approach based on the Phase Gradient Autofocus (PGA) algorithm. This is followed in Section 2.7 by a derivation of a signal model for the image produced by the PFA and in Section 2.8 by a discussion of the limitations on scene size imposed by higher-order phase terms which are ignored in PFA processing. Representative image results from these processing methods are presented in Section 2.9.

2.2 The image formation problem

Fundamentally, SAR image formation (also termed *focussing*) involves the process of correlating a set of collected SAR raw data with the expected point scatterer response of the SAR system for each point in the image: this procedure is known as *matched-filtering* (MF) or *time-domain correlation* (TDC), and represents a maximum likelihood estimator of scatterer reflectivity. However, as the point scatterer response varies with spatial position, the full correlation procedure must employ a different correlation kernel for each and every point in the image: hence, despite its conceptual simplicity, this has traditionally been a highly time-consuming and computationally intensive process. Nevertheless, image formation by this brute-force approach is feasible, albeit generally only in non time-critical, off-line (i.e. non real-time) applications where the considerable computational time and effort required is not a limiting consideration. An efficient implementation of TDC is the tomographic back-projection algorithm (BPA) [89, 90] but even this may not be sufficiently fast for some applications. Recently, however, the advent of fast backprojection techniques [91–93] and fast computing hardware (e.g. Graphics Processing Units) may have mitigated some of these speed-related limitations such that backprojection (also referred to as beamforming [94]) may now be acceptably fast for modest image sizes.

Hence, for many image formation applications, where the time and effort required by TDC and BPA remains prohibitive, various other algorithms are employed instead: these include the range-Doppler algorithm (RDA), the range-migration algorithm (RMA, a.k.a. the ω-k algorithm), the chirp-scaling algorithm (CSA) and the polar format algorithm (PFA) [39,44,95]. With the exception of the RDA (which, as its name suggests, operates on data in the range-time and azimuth-frequency domain), these algorithms operate on data in the two-dimensional spatial frequency-domain (a.k.a. the wavenumber domain) rather than the time-domain for higher processing efficiency. In general, the high computational efficiency of these algorithms are achieved through various approximations which greatly simplify the full MF processing procedure: however, this comes at the expense of introducing phase aberrations into the processing model with resultant image artefacts which are not present in the original optimal MF/TDC/BPA approach [96, 97].

Historically, since operational SARs have been predominantly (if not exclusively) monostatic, the well-established algorithms alluded to above were developed for processing monostatic SAR data. However, with the current surge of interest in bistatic SAR, techniques for processing bistatic SAR data into imagery have become the subject of active research. Bistatic SAR processing poses difficulties not found in the monostatic case arising from additional degrees of freedom in the problem which are introduced by allowing the transmitter and receiver to move independently. Unlike the monostatic case, where the range history may be expressed by a single square-root expression which describes a hyperbola, in the bistatic case the transmitter and receiver make independent contributions to the range history, producing a double square-root (DSR) form for the bistatic range sum which corresponds to a shape sometimes referred to as a *flat-top hyperbola* [98]: the form of this expression hinders the application of the stationary phase approximation in integrals and hence makes obtaining an analytic signal model difficult. Indeed, an analysis shows the range history in the bistatic case differs from the simple hyperbola encountered in the monostatic case in both shape and scaling [41]: thus, in general, bistatic SAR signals cannot be simply processed using the established monostatic algorithms. The major exceptions are special cases where the baseline vector between the transmitter and receiver is constant: such cases have been termed *azimuthally* or *translationally invariant*, or *stationary bistatic*, and the particular case when the baseline vector is constant and oriented along the track of the radar has been termed *tandem* [29].

Approaches to image formation processing for bistatic SAR data have involved both the extension of existing monostatic algorithms to the bistatic case as well as the development of new approaches to the

problem. Various BPA-type approaches to bistatic SAR processing have been developed [99–101] but, as in the monostatic case, frequency-domain processing is generally the preferred approach over time-domain methods for reasons of efficiency. As the point target reference spectrum (or transfer function) is the key to frequency-domain processing, a great deal of research effort has been devoted to obtaining an accurate bistatic point target reference spectrum (BPTRS). One approach to this problem is to simply calculate the required transfer function using numerical methods: this has been applied to the RMA in the azimuthally invariant case [29, 102, 103]. Although this approach works, it tends to be computationally intensive: hence, other efforts have pursued analytic approaches to the problem.

One such analytic approach is to transform the bistatic data to a monostatic-equivalent form which can then be processed with existing monostatic SAR processing algorithms. This is the basis of the Dip Move-Out (DMO) approach which was inspired by geometric methods from the field of seismic reflection surveying: to achieve the bistatic-to-monostatic transformation of the data, it convolves the initial bistatic data set with a short arc-shaped time-domain operator, referred to as Rocca's Smile [98]. The method is applicable to the stationary bistatic case but may be extended to the non-stationary azimuth-variant case [104]. Ultimately, however, bistatic-to-monostatic transformations of the data are limited in their applicability since, as alluded to above, the DSR form of the bistatic range sum cannot be exactly transformed into the hyperbolic form which occurs in expressions for monostatic range, and the discrepancy between the two may be unacceptable for extreme bistatic geometries.

A major approach to the analytic calculation of the BPTRS is based on approximating the DSR form of the range history with a simpler expression which will allow the principle (or method) of stationary phase to be applied for calculating the azimuth Fourier transform integral: this approach is employed in the methods leading to Loffeld's Bistatic Formula (LBF) and the Method of Series Reversion (MSR). In the LBF method, the phase of the integral is separated into two terms, corresponding to the phase contributions from the one-way propagation paths from transmitter to target and from target to receiver, and each term is then expanded in a Taylor series about its point of stationary phase, with only terms up to second-order retained: the resulting spectrum contains a quasi-monostatic phase term and a bistatic deformation phase term, which suggests a two-step processing approach involving compensation for bistatic deformation followed by quasi-monostatic processing [41]. The original LBF only works well in cases where both transmit and receive platforms make comparable contributions to the the combined Doppler modulation: this condition is not met in some important cases of interest, e.g. the spaceborne/airborne bistatic configuration where one platform is a fast-moving satellite. Such cases can be accommodated by weighting the phase modulations of the two platforms according to their time-bandwidth products, which leads to the extended LBF (ELBF) [105]. However, neither LBF nor ELBF are able to focus well in high squint geometries: this shortcoming has been addressed by an optimisation approach [106] and by weighting the transmitter and receiver contributions [107].

In the MSR method, the phase is expanded around the time that the centre of the composite beam from the transmitter and receiver crosses the target: by expanding the bistatic range as a Taylor series in azimuth time and solving for the stationary phase point by using the series reversion formula, a power series representation of azimuth time in terms of azimuth frequency is obtained [43]. A virtue of this method is that more series terms can be retained as needed to achieve a specified accuracy in cases of higher resolution, wider aperture or larger bistatic angle. It has been shown that the MSR, LBF and Rocca's Smile operator produce equivalent representations of the BPTRS under certain restricted conditions, and that the MSR is, in fact, the most general formulation of the three [108]. In addition to the Taylor and series reversion-based approximations of the range history used in the LBF and MSR approaches, other approximation methods have also been suggested based on Legendre polynomials [109] and Fresnel approximation [110].

Various attempts have also been made to adapt the established monostatic SAR processing algorithms to process bistatic SAR data. As mentioned earlier, however, an analytic expression for the target spectrum is difficult to obtain in the bistatic case. Consequently, the bistatic versions of these algorithms tend to focus on the azimuth-invariant case. Numerically based versions of the RMA for azimuthally invariant bistatic data have already been alluded to above; bistatic versions of the RDA and CSA have also been developed for the azimuth-invariant case [111–114] and for the non-azimuth-invariant case [115, 116]. The theoretical basis for bistatic SAR focussing by the PFA has also been covered in the literature [45, 46]: the PFA approach relies on simplifying assumptions to obtain a simple linearised approximation of the BPTRS, which thus permits efficient SAR image formation by Fourier transforms. These benefits come, however, at the expense of uncompensated range curvature in the signal phase, resulting in geometric distortions and defocussing effects which limit the useful size of the image. Since the scene-size in spotlight-mode SAR tends not to be prohibitively large, the PFA is a reasonable choice for processing spotlight-mode SAR data, including that collected in the *Ingara* bistatic SAR experiments. By design, the PFA operates on dechirped SAR raw data which has been motion-compensated to a point: this is the case for data from the *Ingara* system, which demodulates the returning RF signal with a copy of the transmitted chirp which has been delayed to match the delay corresponding to a reference point in the scene. Thus, the PFA is well-suited to processing the *Ingara* raw SAR data, so a general version of the PFA, suitable for processing both the monostatic and bistatic SAR raw data sets, was implemented and used for the work reported in this thesis.

2.3 Raw echo signal model

The basis for any discussion of a processing chain for SAR raw data is a mathematical model of the signals: in this section, we derive such a model for the raw echo data recorded by the *Ingara* system. Since, in general, a faithful representation of the signals is neither feasible (due to the presence of unknown distortions introduced during signal propagation through the RF hardware and free-space) nor desirable (as the pursuit of fidelity might result in an unnecessarily complicated signal model), our aim will be merely to obtain a simplified signal model which will suffice for the purposes of illuminating the motivation behind the steps in the processing chain and specifying the processing operations which are to be performed. Hence, although the resultant model will only be approximate by design, it should nevertheless reflect reality to a sufficient degree as to be practically *useful*.

The starting point for the derivation is the basic waveform employed in the *Ingara* system: a linear FM chirp. This may be represented by

$$a(t) = \mathrm{rect}\left(\frac{t - T_p/2}{T_p}\right) e^{j\pi\gamma(t-T_p/2)^2}, \tag{2.1}$$

in which T_p is the pulse length, γ is the chirp rate and $\mathrm{rect}(x)$ is the familiar rectangular function:

$$\mathrm{rect}\,(x) = \begin{cases} 1 & |x| < 1/2, \\ 0 & \text{otherwise.} \end{cases} \tag{2.2}$$

Observe that the rectangular window restricts the support of the baseband chirp waveform $a(t)$ to the time interval $0 < t < T_p$ and its bandwidth to γT_p.

During operation, linear FM chirp pulses are repeatedly generated and transmitted by the *Ingara* radar hardware: this process may be modelled as follows. For the nth pulse, a copy of the basic chirp waveform

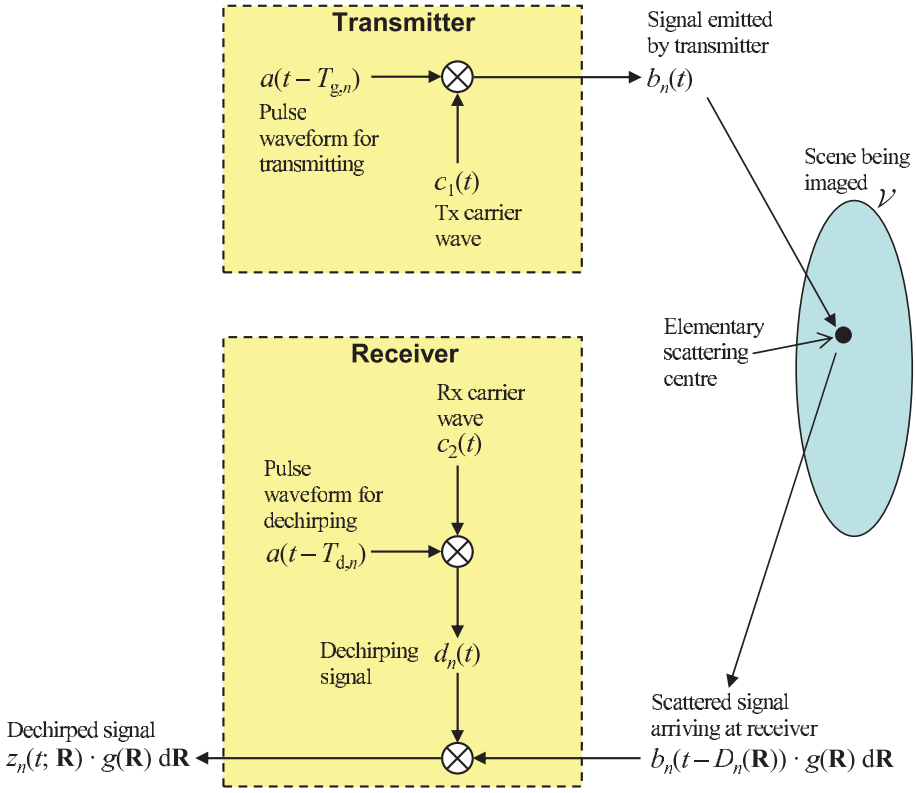

Figure 2.1: Simplified conceptual model of pulse transmission, scattering and reception processes.

$a(t)$ is generated at the time $T_{g,n}$, and modulated onto a carrier signal generated within the transmitter (see Figure 2.1). The chirp waveform which has been generated may be represented by $a(t-T_{g,n})$, and the carrier may be represented by

$$c_1(t) = e^{j2\pi f_c t} e^{j\phi_1(t)}, \tag{2.3}$$

where f_c is the centre frequency of the transmitted signal and $\phi_1(t)$ represents phase noise in the transmitter's oscillator. Hence, after the chirp is mixed with the carrier signal, the resultant transmitted signal may be represented by

$$\begin{aligned} b_n(t) &= a(t-T_{g,n})\,c_1(t) \\ &= \mathrm{rect}\left(\frac{t-T_p/2-T_{g,n}}{T_p}\right) e^{j\pi\gamma(t-T_p/2-T_{g,n})^2} e^{j2\pi f_c t} e^{j\phi_1(t)}. \end{aligned} \tag{2.4}$$

In the course of normal radar operation, the transmitted signal $b_n(t)$ leaves the transmitting antenna and is scattered by the various elementary scattering centres which comprise the scene being imaged. As multiple scattering events can occur (where the scattered signal from one scatterer is, in turn, scattered again by another, and so on), a complete treatment of the scattering process can be extremely complicated. Fortunately, for most practical situations, the multiply scattered signals are relatively weak: this allows us to ignore multiple scattering events for simplicity in this discussion, and only consider those signals which are scattered directly to the receiver (this is essentially the Born approximation in which the driving field for the scattering process is taken to comprise only the incident field, and the contribution of the scattered field is

ignored).

The directly scattered signal arriving at the receiver from a scattering centre at position $\mathbf{R}$ may be represented by a scaled and delayed copy of the transmitted signal, having the general form

$$b_n(t - D_n(\mathbf{R})) \cdot g(\mathbf{R})\mathrm{d}\mathbf{R}, \tag{2.5}$$

where $D_n(\mathbf{R})$ is the total propagation delay from the transmitter to the scattering centre to the receiver, $g(\mathbf{R})$ is the complex reflectivity function of the the scene and $\mathrm{d}\mathbf{R}$ represents an infinitesimal volume element (so the product $g(\mathbf{R})\,\mathrm{d}\mathbf{R}$ is the differential reflectivity of the elementary scattering element under consideration). Note that strictly speaking, $g(\mathbf{R})$ is also dependent on the positions of the transmitter and receiver relative to that of the scatterer but, for simplicity, we will ignore this effect in these calculations. The total scattered signal arriving at the receiver will be simply the sum (integral) of the returns from all elementary scattering centres within the volume occupied by the scene being imaged $\mathcal{V}$: this can be written as

$$\iiint_{\mathcal{V}} \mathrm{d}\mathbf{R}\; g(\mathbf{R})\, b_n(t - D_n(\mathbf{R})). \tag{2.6}$$

It should be noted that other scaling factors may also be included in the model for the returned signal in (2.5), e.g. factors to account for the beampatterns of the transmitting and receiving antennas, $1/R$-like factors to account for free space attenuation of the signal as it propagates between the transmitter and scatterer and between the scatterer and the receiver, factors to account for effects from propagation through the intervening medium, etc.—in general, the overall effect of such factors is to apply a slowly varying, position-dependent scaling factor $A(\mathbf{R})$ to the terrain reflectivity, i.e. we would have $g(\mathbf{R}) = A(\mathbf{R})\, g_0(\mathbf{R})$ in the signal model, where $g_0(\mathbf{R})$ represents the true terrain reflectivity (which is, as noted above, dependent on the transmitter and receiver positions relative to the scatterer's, but this effect is being ignored here). Although the scaling $A(\mathbf{R})$ will need to be accounted for when absolute measurements of reflectivity are required, for simplicity, we opt not to explicitly consider it in the present discussion.

In SAR, a common demodulation technique for scattered chirp signals arriving at the receiver is to mix them with a replica of the original transmitted chirp: this demodulation technique is referred to as *dechirp-on-receive* or *stretch-mode processing*. Hence, as depicted in Figure 2.1 and Figure 2.2, the signal of (2.6) which arrives at the receiver is demodulated by mixing it with a dechirping signal $d_n(t)$ which is generated in a similar manner to the transmitted pulse $b_n(t)$ by modulating a copy of the basic waveform $a(t)$ generated at time $T_{\mathrm{d},n}$ onto the carrier signal which is generated in the receiver. Analogously to (2.3), this carrier may be represented by

$$c_2(t) = e^{j2\pi f_c t} e^{j\phi_2(t)}, \tag{2.7}$$

where $\phi_2(t)$ represents the phase noise in the receiver's oscillator. In the monostatic system, the transmitter and receiver share a common oscillator, so $\phi_2(t) = \phi_1(t)$ and $c_2(t) = c_1(t)$ for the monostatic case; in the bistatic system, independent and separate oscillators are used by the transmitter and receiver, so $\phi_2(t) \neq \phi_1(t)$ and $c_2(t) \neq c_1(t)$ in general for the bistatic case. As the signal generation process is essentially the same for $b_n(t)$ and $d_n(t)$, the dechirping signal has a form analogous to that of the transmitted signal (cf. (2.4)), viz.

$$\begin{aligned} d_n(t) &= a\left(t - T_{\mathrm{d},n}\right)\, c_2(t) \\ &= \mathrm{rect}\left(\frac{t - T_p/2 - T_{\mathrm{d},n}}{T_p}\right) e^{j\pi\gamma(t - T_p/2 - T_{\mathrm{d},n})^2} e^{j2\pi f_c t} e^{j\phi_2(t)}. \end{aligned} \tag{2.8}$$

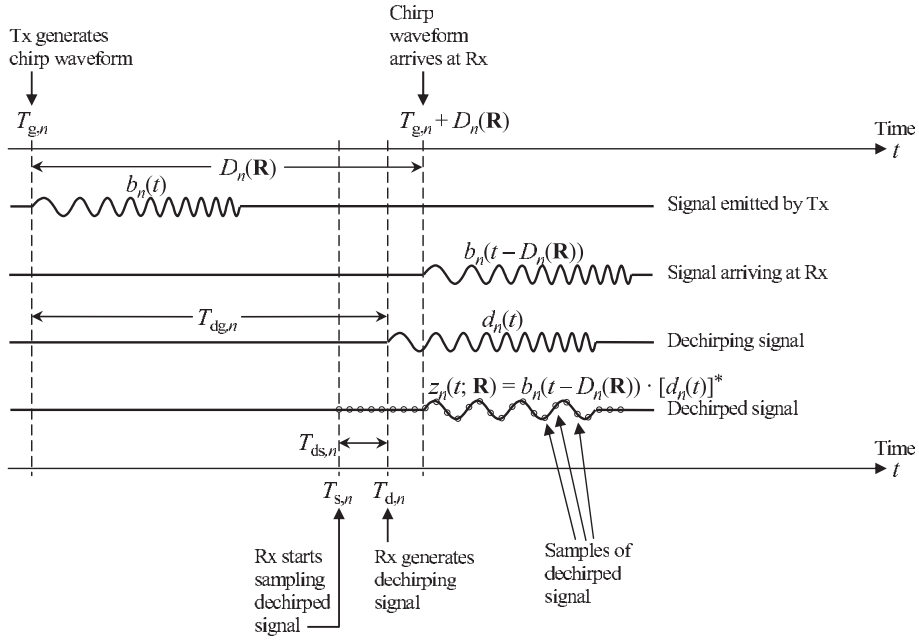

Figure 2.2: Temporal representation of signals involved in pulse transmission and reception processes. For simplicity, only the normalised scattered signal from a single scattering centre is depicted.

The resultant signal after mixing the scattered signal (2.6) with the dechirping signal $d_n(t)$ and low-pass filtering the result is thus

$$\begin{aligned}\zeta_n(t) &= \iiint_{\mathcal{V}} \mathrm{d}\mathbf{R}\; g(\mathbf{R})\, b_n(t - D_n(\mathbf{R}))[d_n(t)]^* \\ &= \iiint_{\mathcal{V}} \mathrm{d}\mathbf{R}\; g(\mathbf{R})\, z_n(t; \mathbf{R}),\end{aligned} \tag{2.9}$$

where $z_n(t; \mathbf{R})$ represents the normalised (i.e. independent of scatterer reflectivity $g(\mathbf{R})\,\mathrm{d}\mathbf{R}$) dechirped return from a scattering centre at $\mathbf{R}$, viz.

$$\begin{aligned}z_n(t; \mathbf{R}) &= b_n(t - D_n(\mathbf{R}))[d_n(t)]^* \\ &= \mathrm{rect}\left(\frac{t - T_p/2 - D_n(\mathbf{R}) - T_{\mathrm{g},n}}{T_p}\right) \mathrm{rect}\left(\frac{t - T_p/2 - T_{\mathrm{d},n}}{T_p}\right) \\ &\quad \cdot e^{j\pi\gamma(D_n(\mathbf{R}) + T_{\mathrm{g},n} - T_{\mathrm{d},n})(D_n(\mathbf{R}) + T_{\mathrm{g},n} + T_{\mathrm{d},n} - 2(t - T_p/2))} e^{-j2\pi f_c D_n(\mathbf{R})} e^{j\phi_{\mathrm{T}}(t; D_n(\mathbf{R}))},\end{aligned} \tag{2.10}$$

where $\phi_{\mathrm{T}}(t; D) = \phi_1(t - D) - \phi_2(t)$. For each pulse, the dechirped signal $\zeta_n(t)$ is sampled and recorded, with the first sample taken at the time $T_{\mathrm{s},n}$: it will thus be useful to define the variable

$$\tau = t - T_{\mathrm{s},n}, \tag{2.11}$$

being the time after the start of sampling for each pulse. Now, in the technique of SAR, an aperture is synthesised through the motion of the transmitting and receiving antennas relative to the scene over a time interval, and the data from the multiple consecutive pulses collected during this interval are coherently processed together. For signal processing purposes, it is helpful to think of the collected data from the pulses in

such a coherent processing interval as filling a two-dimensional data array with the intra-pulse 'fast' time τ running down one axis and the inter-pulse 'slow' time index n running across the other axis. This is facilitated by re-expressing the dechirped signal $\zeta_n(t)$ as a function of the variables τ and n as follows:

$$\begin{aligned} \upsilon_n(\tau) &= \zeta_n(\tau + T_{\mathrm{s},n}) \\ &= \iiint_{\mathcal{V}} \mathrm{d}\mathbf{R}\; g(\mathbf{R})\, y_n(\tau; \mathbf{R}) \end{aligned} \tag{2.12}$$

in which

$$\begin{aligned} y_n(\tau; \mathbf{R}) &\triangleq z_n(\tau + T_{\mathrm{s},n}; \mathbf{R}) \\ &= \mathrm{rect}\left(\frac{\tau - T_p/2 - D_n(\mathbf{R}) + T_{\mathrm{sg},n}}{T_p}\right) \mathrm{rect}\left(\frac{\tau - T_p/2 - T_{\mathrm{ds},n}}{T_p}\right) \\ &\quad \cdot e^{-j2\pi(f_c + \gamma(\tau - T_p/2 - T_{\mathrm{ds},n}))(D_n(\mathbf{R}) - T_{\mathrm{dg},n})} e^{j\pi\gamma(D_n(\mathbf{R}) - T_{\mathrm{dg},n})^2} \\ &\quad \cdot e^{j\phi_T(\tau + T_{\mathrm{s},n}; D_n(\mathbf{R}))} e^{-j2\pi f_c T_{\mathrm{dg},n}}, \end{aligned} \tag{2.13}$$

where $T_{\mathrm{dg},n} = T_{\mathrm{d},n} - T_{\mathrm{g},n}$, $T_{\mathrm{sg},n} = T_{\mathrm{s},n} - T_{\mathrm{g},n}$ and $T_{\mathrm{ds},n} = T_{\mathrm{dg},n} - T_{\mathrm{sg},n} = T_{\mathrm{d},n} - T_{\mathrm{s},n}$.

Observe that the support of $y_n(\tau; \mathbf{R})$ is determined by the overlap of the rectangular functions on the right-hand-side of (2.13): when $|D_n(\mathbf{R}) - T_{\mathrm{dg},n}| \geq T_p$, the two rectangular functions do not overlap and $y_n(\tau; \mathbf{R}) = 0$; when $|D_n(\mathbf{R}) - T_{\mathrm{dg},n}| < T_p$, there *will* be an overlap and the product of the two rectangular functions can be re-written as a single indicator function

$$\mathbb{I}_n(\tau; \mathbf{R}) = \begin{cases} \mathrm{rect}\left(\dfrac{\tau - V_n(\mathbf{R})}{T_p - |W_n(\mathbf{R})|}\right) & \text{if } |W_n(\mathbf{R})| < T_p, \\ 0 & \text{otherwise,} \end{cases} \tag{2.14}$$

where, for notational brevity, we have defined

$$V_n(\mathbf{R}) \triangleq \frac{1}{2}\left\{T_p + D_n(\mathbf{R}) - T_{\mathrm{sg},n} + T_{\mathrm{ds},n}\right\}, \tag{2.15}$$

$$W_n(\mathbf{R}) \triangleq D_n(\mathbf{R}) - T_{\mathrm{dg},n}. \tag{2.16}$$

Also, in the *Ingara* system, the transmitted centre frequency is $f_c = 10.1\,\mathrm{GHz}$ and the intervals $T_{\mathrm{dg},n}$ between the generation of each transmitted pulse and the corresponding dechirping pulse are constrained by the design of the system to be integer multiples of 20 ns: hence, we have $e^{-j2\pi f_c T_{\mathrm{dg},n}} = 1$. These two facts allow us to simplify the model for the normalised dechirped echo signal from a single scatterer to

$$y_n(\tau; \mathbf{R}) = \mathbb{I}_n(\tau; \mathbf{R})\, e^{j\Theta_n(\tau; \mathbf{R})}, \tag{2.17}$$

where the phase is given by

$$\begin{aligned} \Theta_n(\tau; \mathbf{R}) = &-2\pi(f_c + \gamma(\tau - T_p/2 - T_{\mathrm{ds},n}))(D_n(\mathbf{R}) - T_{\mathrm{dg},n}) \\ &+ \pi\gamma(D_n(\mathbf{R}) - T_{\mathrm{dg},n})^2 + \phi_T(\tau + T_{\mathrm{s},n}; D_n(\mathbf{R})). \end{aligned} \tag{2.18}$$

2.4 Signal preprocessing

From the results of the previous section, it may be observed that the position of a scattering centre at $\mathbf{R}$ is encoded in the phase $\Theta_n(\tau; \mathbf{R})$ of the corresponding dechirped echo signal $y_n(\tau; \mathbf{R})$: it is precisely this encoding of the scatterer position in the phase which is exploited to form an image of the scene. For successful image formation, however, some pre-processing of the signal is required to remove components in the phase which are detrimental to the image formation process: the pre-processing operations which are applied to the data are the subject of this section.

In Section 2.4.1, we discuss the compensation of the signal phase for platform motion and timing offsets during the data collection process. This is followed in Section 2.4.2 by a discussion of the procedure for the removal of a phase artefact from the dechirp-on-receive demodulation process employed during data collection. These pre-processing stages suffice to correct the deterministic phase distortions predicted by the signal model (2.18). However, the phase noise term $\phi_T(\tau + T_{\mathrm{s},n}; D_n(\mathbf{R}))$ is random in nature and cannot be so easily dismissed. In practice, although some mitigation is possible through autofocus techniques, the detrimental effects of phase noise must largely be controlled by careful hardware design (particularly with regard to the oscillators used in the radar system) rather than signal processing measures: hence, in the interests of simplicity, we shall ignore the phase noise term in the present discussion on signal processing.

2.4.1 Motion compensation

SAR image formation exploits the encoding of the position of the scattering centres $\mathbf{R}$ in the phase of the echo signal $\Theta_n(\tau; \mathbf{R})$. Indeed, the PFA is based on the assumption of a linear relationship between the phase and position. However, this underlying linearity is obscured in the raw data by undesired offsets in the radar timing which occur during data collections: if left uncorrected, these will result in a poorly focussed image. By estimating these timing offsets from measurements of platform motion and the recorded timestamps, the phase of the signal can be corrected for these effects. Since the result of this procedure can be interpreted as the stabilisation of the signal phase from a specific reference point against distortions introduced by unintended platform motion, this procedure is termed *motion-compensation to a point*.

For the *Ingara* system, the specific background to this procedure is as follows: during SAR data collection in spotlight-mode, the *Ingara* hardware dynamically adjusts each pulse's transmit-to-dechirp interval $T_{\mathrm{dg},n}$ and transmit-to-sampling interval $T_{\mathrm{sg},n}$ in an attempt to match the propagation delay for a signal scattered from a fixed reference point. (This collection reference point is essentially the centre of the scene being imaged.) If this were perfectly achieved, the phase of the signal from the reference point would be constant. However, system design limitations in the allowed triggering times of the hardware components, various system hardware delays, and errors in the real-time measurements of the airborne radar's motion make it impossible to precisely match this desired delay. As a result, the phase of the collected raw signal contains artefacts introduced by the consequent timing offsets.

A procedure for correcting these phase artefacts can be obtained by specifically considering the propagation delay $D_n(\mathbf{R})$ in the phase of the previously obtained signal model $\Theta_n(\tau; \mathbf{R})$ (see (2.18)). Without loss of generality, let the reference point used for data collection be the origin of coordinates, i.e. the point at position vector $\mathbf{0}$. As discussed above, ideally, we desire that $T_{\mathrm{dg},n} = T_{\mathrm{sg},n} = D_n(\mathbf{0})$ but, as this is not

achieved in practice, we actually have

$$T_{\mathrm{dg},n} = D_n(\mathbf{0}) + E_{\mathrm{d},n}, \tag{2.19}$$

$$T_{\mathrm{sg},n} = D_n(\mathbf{0}) + E_{\mathrm{s},n}, \tag{2.20}$$

where $E_{\mathrm{d},n}$ and $E_{\mathrm{s},n}$ are undesired timing offsets in the dechirp and sampling delays respectively. By substituting (2.19) and (2.20) into (2.18), we obtain the following expression for the signal phase:

$$\begin{aligned}\Theta_n(\tau;\mathbf{R}) = &\left\{-2\pi(f_c + \gamma(\tau - T_p/2 + E_{\mathrm{s},n}))U_n(\mathbf{R}) + \pi\gamma[U_n(\mathbf{R})]^2\right\} \\ &+ \left\{2\pi(f_c + \gamma(\tau - T_p/2 + E_{\mathrm{s},n}))E_{\mathrm{d},n} - \pi\gamma E_{\mathrm{d},n}^2\right\},\end{aligned} \tag{2.21}$$

in which $U_n(\mathbf{R})$ is the differential delay for a scattering centre at $\mathbf{R}$ relative to one at $\mathbf{0}$, viz.

$$U_n(\mathbf{R}) \triangleq D_n(\mathbf{R}) - D_n(\mathbf{0}). \tag{2.22}$$

Observe that the first term (in braces) on the right-hand-side of (2.21) contains information about the scatterer position $\mathbf{R}$, whereas the second term does not. Instead, the second term essentially involves only the undesired timing offsets $E_{\mathrm{d},n}$ and $E_{\mathrm{s},n}$ and, if these vary during a coherent processing interval, the result will be cross-range defocussing of the SAR image, as previously mentioned.

The undesired offsets $E_{\mathrm{d},n}$ and $E_{\mathrm{s},n}$ can be calculated from smoothed estimates of the transmitter and receiver positions and knowledge of the intervals $T_{\mathrm{dg},n}$ and $T_{\mathrm{sg},n}$ (transmitter and receiver position measurements and the various timestamps $T_{\mathrm{g},n}$, $T_{\mathrm{d},n}$ and $T_{\mathrm{s},n}$ are all recorded by the system during data collection): this permits the second term to be calculated and subtracted away from the data. Hence, the motion-compensated signal $\xi_n(\tau)$ may be obtained from the raw echo signal $\upsilon_n(\tau)$ by

$$\begin{aligned}\xi_n(\tau) &= \upsilon_n(\tau)e^{-j\left\{2\pi(f_c+\gamma(\tau-T_p/2+E_{\mathrm{s},n}))E_{\mathrm{d},n}-\pi\gamma E_{\mathrm{d},n}^2\right\}} \\ &= \iiint_{\mathcal{V}} \mathrm{d}\mathbf{R}\; g(\mathbf{R})\, x_n(\tau;\mathbf{R}),\end{aligned} \tag{2.23}$$

where

$$\begin{aligned}x_n(\tau;\mathbf{R}) &= y_n(\tau;\mathbf{R})e^{-j\left\{2\pi(f_c+\gamma(\tau-T_p/2+E_{\mathrm{s},n}))E_{\mathrm{d},n}-\pi\gamma E_{\mathrm{d},n}^2\right\}} \\ &= \mathbb{I}_n(\tau;\mathbf{R})\, e^{j\Omega_n(\tau;\mathbf{R})}\end{aligned} \tag{2.24}$$

and

$$\Omega_n(\tau;\mathbf{R}) = -2\pi(f_c + \gamma(\tau - T_p/2 + E_{\mathrm{s},n}))U_n(\mathbf{R}) + \pi\gamma[U_n(\mathbf{R})]^2. \tag{2.25}$$

The quantities $V_n(\mathbf{R})$ and $W_n(\mathbf{R})$ of (2.14) can also be re-expressed in terms of $U_n(\mathbf{R})$, $E_{\mathrm{d},n}$ and $E_{\mathrm{s},n}$: the result is

$$V_n(\mathbf{R}) = \frac{1}{2}\left\{T_p + U_n(\mathbf{R}) + E_{\mathrm{d},n} - 2E_{\mathrm{s},n}\right\}, \tag{2.26}$$

$$W_n(\mathbf{R}) = U_n(\mathbf{R}) - E_{\mathrm{d},n}. \tag{2.27}$$

2.4.2 Deskew processing

Inspection of the right-hand-side of (2.25) reveals that the expression for the motion-compensated signal phase contains the term $\pi\gamma\left[U_n\left(\mathbf{R}\right)\right]^2$. This phase term is an artefact of the dechirp-on-receive demodulation process, sometimes referred to as the *residual video phase*: it does not appear if the incoming scattered signal is processed with a matched-filter instead of dechirping. Its presence causes a spatially varying defocussing of the final SAR image with a severity dependent on the scatterer position $\mathbf{R}$: however, as this phase term is comprised of second or higher order terms in $|\mathbf{R}|$, it is typically negligible for positions near the scene centre, and may quite feasibly be simply ignored in practice, especially for small scene sizes. Nevertheless, a relatively simple pre-processing procedure is applied to the *Ingara* data to compensate for it.

This procedure has been termed *range-deskew processing*, because of its effect of aligning the skewed envelopes of the motion-compensated dechirped signals from scatterers at different ranges from the radar: a comprehensive discussion of this procedure may be found in Appendix C of the text by Carrara et al. [44]. However, that discussion postulates that the dechirping signal is of sufficiently long duration that scattered signals from the near and far range extremes of the scene will overlap completely with it: this differs from the *Ingara* system, where the dechirping signal has identical duration to the transmitted chirp. Hence, for thoroughness, we present below a brief discussion of the deskew processing procedure as it pertains to the *Ingara* data.

To begin, we calculate the Fourier transform of the motion-compensated signal $\xi_n(\tau)$: this is given by

$$\begin{aligned}\Xi_n(f) &= \int_{-\infty}^{\infty}\mathrm{d}\tau\ \ e^{-j2\pi f\tau}\xi_n(\tau)\\ &= \iiint_{\mathcal{V}}\mathrm{d}\mathbf{R}\ g(\mathbf{R})\,X_n(f;\mathbf{R})\end{aligned}\tag{2.28}$$

in which

$$\begin{aligned}X_n(f;\mathbf{R}) &= \int_{-\infty}^{\infty}\mathrm{d}\tau\ \ e^{-j2\pi f\tau}x_n(\tau;\mathbf{R})\\ &= \begin{cases}(T_p-|W_n(\mathbf{R}|)\,\mathrm{sinc}\left[(f+\gamma U_n(\mathbf{R}))(T_p-|W_n(\mathbf{R})|)\right]e^{j\phi} & \text{if } |W_n(\mathbf{R})|<T_p,\\ 0 & \text{otherwise,}\end{cases}\end{aligned}\tag{2.29}$$

where $\mathrm{sinc}(x)=\sin(\pi x)/(\pi x)$ and, for brevity of notation, we have defined

$$\phi \triangleq -2\pi(f+\gamma U_n(\mathbf{R}))V_n(\mathbf{R})-2\pi(f_c-\gamma(T_p/2-E_{\mathrm{s},n}))U_n(\mathbf{R})+\pi\gamma[U_n(\mathbf{R})]^2.\tag{2.30}$$

As discussed by Carrara et al. [44], the essence of the deskew procedure is the application of a quadratic phase shift to the data in the frequency domain: specifically, the phase of $\Xi_n(f)$ is adjusted by an amount $-\pi f^2/\gamma$, so the result for each scattering centre is the new signal frequency spectrum

$$S_n(f;\mathbf{R}) = X_n(f;\mathbf{R})e^{-j\pi f^2/\gamma}.\tag{2.31}$$

To obtain the deskewed signal back in the time domain, we must calculate the inverse Fourier transform of $S_n(f;\mathbf{R})$, viz.

$$s_n(\tau;\mathbf{R}) = \int_{-\infty}^{\infty}\mathrm{d}f\ e^{j2\pi f\tau}\,S_n(f;\mathbf{R}).\tag{2.32}$$

For scatterers at positions $\mathbf{R}$ such that $|W_n(\mathbf{R})|\geq T_p$, the result is trivial: $s_n(\tau;\mathbf{R})=0$. However, for

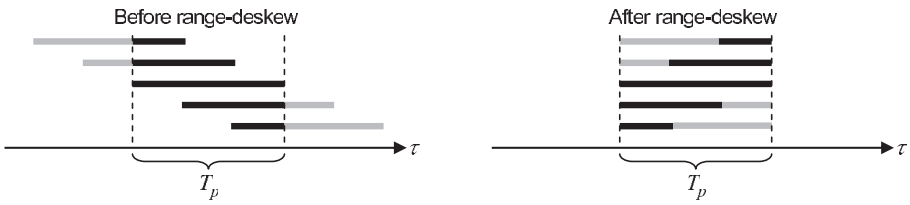

Figure 2.3: Effect of range-deskew on envelopes of dechirped signals. Illustrated case is where transmitted and dechirping signals have equal duration T_p. Grey indicates those parts of scattered signal envelopes lost due to non-overlap with dechirping signal. Returns from near and far range are at top and bottom respectively.

scatterers at $\mathbf{R}$ such that $|W_n(\mathbf{R})| < T_p$, we have

$$\begin{aligned} s_n(\tau;\mathbf{R}) = {} & e^{-j2\pi(f_c+\gamma(\tau-T_p/2+E_{\mathrm{s},n}))U_n(\mathbf{R})} \\ & \cdot \int_{-\infty}^{\infty} \mathrm{d}f \; e^{j2\pi f(\tau-(V_n(\mathbf{R})-U_n(\mathbf{R})))}(T_p - |W_n(\mathbf{R})|)\,\mathrm{sinc}(f(T_p - |W_n(\mathbf{R})|))e^{-j\pi f^2/\gamma}. \end{aligned} \tag{2.33}$$

To evaluate the integral, observe that in the integrand, $\mathrm{sinc}(f(T_p - |W_n(\mathbf{R})|))$ only has significant magnitude for values of $|f|$ under an upper bound on the order of $1/(T_p - |W_n(\mathbf{R})|)$. Hence, the maximum absolute phase of the term $e^{-j\pi f^2/\gamma}$ will be on the order of $\pi/\gamma(T_p - |W_n(\mathbf{R})|)^2$. For small values of $|\mathbf{R}|$, the value of $W_n(\mathbf{R})$ is approximately zero and so the maximum absolute phase is approximately $\pi/\gamma T_p^2$. Now, γT_p^2 is the product of the duration of the transmitted pulse T_p and the pulse bandwidth γT_p and, in practical situations, this time-bandwidth product is deliberately chosen to be numerically large: hence the maximum absolute phase is small and we can approximate $e^{-j\pi f^2/\gamma}$ in the integral by unity. Thus, the integral approximately evaluates to

$$\begin{aligned} & \int_{-\infty}^{\infty} \mathrm{d}f \; e^{j2\pi f(\tau-(V_n(\mathbf{R})-U_n(\mathbf{R})))}(T_p - |W_n(\mathbf{R})|)\,\mathrm{sinc}(f(T_p - |W_n(\mathbf{R})|)) \\ & \qquad = \mathrm{rect}\left(\frac{\tau - (V_n(\mathbf{R}) - U_n(\mathbf{R}))}{T_p - |W_n(\mathbf{R})|}\right). \end{aligned} \tag{2.34}$$

Hence, we have the result

$$s_n(\tau;\mathbf{R}) = \mathbb{I}_n(\tau + U_n(\mathbf{R});\mathbf{R})\, e^{j\Psi_n(\tau;\mathbf{R})} \tag{2.35}$$

where

$$\Psi_n(\tau;\mathbf{R}) = -2\pi(f_c + \gamma(\tau - T_p/2 + E_{\mathrm{s},n}))U_n(\mathbf{R}), \tag{2.36}$$

so the total deskewed signal from all the scattering centres is given by

$$\chi_n(\tau) = \iiint_{\mathcal{V}} \mathrm{d}\mathbf{R}\; g(\mathbf{R})\, s_n(\tau;\mathbf{R}). \tag{2.37}$$

Comparison of (2.35) and (2.36) with (2.24) and (2.25) reveals that the effect of the deskew processing operation is to remove the term $\pi\gamma\,[U_n(\mathbf{R})]^2$ from the phase and to shift the rectangular envelope by an amount $-U_n(\mathbf{R})$ (see Figure 2.3).

2.5 Polar Format Algorithm

In the deskewed motion-compensated signal $\chi_n(\tau)$ representing the return from a scene, the position $\mathbf{R}$ of each elementary scattering centre comprising the scene $\mathbf{R}$ is encoded in the phase $\Psi_n(\tau;\mathbf{R})$ of each elementary signal $s_n(\tau;\mathbf{R})$. SAR image formation exploits this phase-encoded information by matched-filtering of the total return $\chi_n(\tau)$ with a bank of filters, each matched to the elementary signal $s_n(\tau;\mathbf{R}')$ for a particular position $\mathbf{R}'$: this process essentially seeks to concentrate the energy in each of the various elementary signals $s_n(\tau;\mathbf{R})$, which is spread out over a surface parametrised by n and τ, into a single point in the space parametrised by $\mathbf{R}'$ at the location $\mathbf{R}' = \mathbf{R}$. Although such a bank of space-variant matched-filters produces the optimum solution to the image formation problem, such a brute-force approach is time-consuming and computationally intensive. Thus, in practice, various approximations are made to obtain approximate solutions through more computationally efficient methods.

The Polar Format Algorithm (PFA) is one such method. It exploits the fact that the phase $\Psi_n(\tau;\mathbf{R})$ is, to a good approximation for small $|\mathbf{R}|$, a linear function of $\mathbf{R}$ in a space parametrised by vectors $\mathbf{K}_n(\tau)$. The signals $s_n(\tau;\mathbf{R})$ are thus well-approximated by plane waves of the form $\exp(j\mathbf{K}_n(\tau)\cdot\mathbf{R})$, albeit with limited support imposed by the indicator functions $\mathbb{I}_n(\tau+U_n(\mathbf{R});\mathbf{R})$ (ref. right-hand-side of (2.35)). Hence, a Fourier transform from the space of vectors $\mathbf{K}_n(\tau)$ to a space parametrised by $\mathbf{R}'$ suffices to gather the energy from each $s_n(\tau;\mathbf{R})$ around the point $\mathbf{R}' = \mathbf{R}$ as required, thus forming the desired SAR image.

Various texts expounding on the PFA for the case of monostatic SAR have been available in the literature for over a decade [39, 44], and, in more recent years, dissertations on the PFA for bistatic SAR have also appeared [6, 45]—a good general discussion of the concepts underlying the PFA and its implementation may be found in these sources. In this section, however, we discuss the application of the PFA to the monostatic and bistatic data collected in the *Ingara* circular spotlight-mode SAR collection geometry. In Section 2.5.1, the essential theory behind the PFA is presented in a unified way, applicable to both the monostatic and bistatic *Ingara* data sets. Section 2.5.2 discusses the resampling of the data onto a suitable parallelogram grid on which the Fast Fourier Transform may be applied, and a method for the computation of this transform is covered in Section 2.5.3.

2.5.1 Theoretical basis

In this section, we demonstrate the key idea behind the PFA: that the data $\chi_n(\tau)$ can be *essentially* interpreted (with qualifications as discussed below) as samples of a spatial Fourier transform of the scene reflectivity $g(\mathbf{R})$. Our starting point is the delay $D_n(\mathbf{R})$: recall that this is the total propagation delay for the signal travelling from the transmitter to a scattering centre at the position $\mathbf{R}$ to the receiver at the instant of the nth pulse. If the instantaneous positions of the transmitter and receiver at the nth pulse are denoted by $\mathbf{P}_{1,n}$ and $\mathbf{P}_{2,n}$ respectively (see Figure 2.4), then the *range sum* is given by

$$R_{\mathrm{s},n} = |\mathbf{P}_{1,n} - \mathbf{R}| + |\mathbf{P}_{2,n} - \mathbf{R}|, \tag{2.38}$$

whereupon $D_n(\mathbf{R})$ can be obtained as the quotient of $R_{\mathrm{s},n}$ and the speed of propagation c, viz.

$$D_n(\mathbf{R}) = \frac{|\mathbf{P}_{1,n} - \mathbf{R}| + |\mathbf{P}_{2,n} - \mathbf{R}|}{c}. \tag{2.39}$$

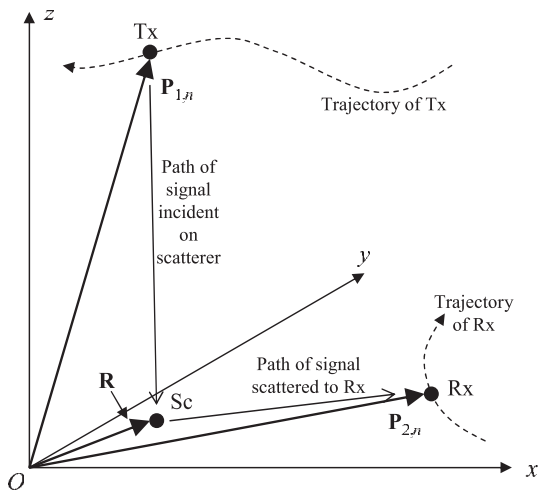

Figure 2.4: General collection geometry for bistatic radar signals.

Hence, substituting (2.39) into (2.22) yields the following expression for the differential delay:

$$U_n(\mathbf{R}) = \frac{1}{c}\sum_{i=1}^{2}\left\{|\mathbf{P}_{i,n} - \mathbf{R}| - |\mathbf{P}_{i,n}|\right\}. \tag{2.40}$$

Now, from the definition of the length of a vector and the dot (scalar) product of two vectors, we have

$$\begin{aligned} |\mathbf{P}_{i,n} - \mathbf{R}| &= \sqrt{(\mathbf{P}_{i,n} - \mathbf{R})\cdot(\mathbf{P}_{i,n} - \mathbf{R})} \\ &= \sqrt{|\mathbf{P}_{i,n}|^2 - 2|\mathbf{P}_{i,n}||\mathbf{R}|\cos\theta_{i,n} + |\mathbf{R}|^2}, \end{aligned} \tag{2.41}$$

where $\theta_{i,n}$ is the angle between the vectors $\mathbf{P}_{i,n}$ and $\mathbf{R}$. This can be expanded as a power series in $|\mathbf{R}|$: the result is

$$|\mathbf{P}_{i,n} - \mathbf{R}| = |\mathbf{P}_{i,n}| - \hat{\mathbf{P}}_{i,n}\cdot\mathbf{R} + \frac{|\mathbf{R}_{\perp\mathbf{P}_{i,n}}|^2}{2|\mathbf{P}_{i,n}|} + \ldots \tag{2.42}$$

where only terms up to second order in $|\mathbf{R}|$ have been displayed. In (2.42) and the following equations, the notation $\mathbf{U}_{\perp\mathbf{V}}$ will be employed to denote the component of a generic vector $\mathbf{U}$ which is perpendicular to a generic vector $\mathbf{V}$, i.e.

$$\mathbf{U}_{\perp\mathbf{V}} \triangleq \mathbf{U} - \left(\hat{\mathbf{V}}\cdot\mathbf{U}\right)\hat{\mathbf{V}} \tag{2.43}$$

and the notation $\hat{\mathbf{V}}$ will be employed to denote the unit vector in the direction of $\mathbf{V}$, i.e.

$$\hat{\mathbf{V}} \triangleq \frac{\mathbf{V}}{|\mathbf{V}|}. \tag{2.44}$$

Substituting (2.42) into (2.40) yields the power series representation of $U_n(\mathbf{R})$,

$$U_n(\mathbf{R}) = -\frac{1}{c}\sum_{i=1}^{2}\left\{\hat{\mathbf{P}}_{i,n}\cdot\mathbf{R} - \frac{|\mathbf{R}_{\perp\mathbf{P}_{i,n}}|^2}{2|\mathbf{P}_{i,n}|} + \ldots\right\}, \tag{2.45}$$

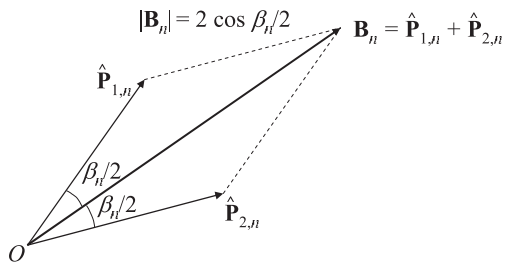

Figure 2.5: Geometric relationship between $\hat{\mathbf{P}}_{1,n}$, $\hat{\mathbf{P}}_{2,n}$ and $\mathbf{B}_n$.

whereupon, by substituting (2.45) into (2.36), we obtain the phase of the signal from a single scattering centre as

$$\Psi_n(\tau;\mathbf{R}) = \mathbf{K}_n(\tau)\cdot\mathbf{R} - \frac{|\mathbf{K}_n(\tau)|}{2|\mathbf{B}_n|}\left(\frac{|\mathbf{R}_{\perp\mathbf{P}_{1,n}}|^2}{|\mathbf{P}_{1,n}|} + \frac{|\mathbf{R}_{\perp\mathbf{P}_{2,n}}|^2}{|\mathbf{P}_{2,n}|}\right) + O\left(|\mathbf{R}|^3\right), \tag{2.46}$$

where

$$\mathbf{B}_n = \hat{\mathbf{P}}_{1,n} + \hat{\mathbf{P}}_{2,n} \tag{2.47}$$

and

$$\mathbf{K}_n(\tau) = \frac{2\pi}{c}\left[f_c + \gamma\left(\tau - \frac{T_p}{2} + E_{\mathrm{s},n}\right)\right]\mathbf{B}_n. \tag{2.48}$$

The expression (2.46) has the form of a power series but $\Psi_n(\tau;\mathbf{R})$ can also be expressed more compactly: by substituting (2.40) and (2.48) into (2.36), we obtain

$$\Psi_n(\tau;\mathbf{R}) = -\frac{|\mathbf{K}_n(\tau)|}{|\mathbf{B}_n|}\sum_{i=1}^{2}\left(|\mathbf{P}_{i,n} - \mathbf{R}| - |\mathbf{P}_{i,n}|\right). \tag{2.49}$$

From (2.47) and Figure 2.5, it may be observed that the vector $\mathbf{B}_n$ points along the instantaneous bisector of the bistatic angle β_n for a target at the origin of coordinates, and has length

$$|\mathbf{B}_n| = 2\cos(\beta_n/2). \tag{2.50}$$

(This is true in general: the monostatic case is simply a special case where the bistatic angle is zero.) Now, the magnitude of the vector $\mathbf{K}_n(\tau)$ is determined by the fast-time τ and the direction is determined by $\mathbf{B}_n$ so, as τ and $\mathbf{B}_n$ vary in the course of data collection, the tip of $\mathbf{K}_n(\tau)$ sweeps out a surface which is oriented radially to the origin. Hence, the collected radar echo data effectively contains measurements of the phases $\Psi_n(\tau;\mathbf{R})$ on this surface.

Although the present discussion is explicitly concerned with the bistatic case, it is worth noting that the monostatic case is fully accommodated in the formulation given and can be easily derived by setting the bistatic angle β_n to zero. By doing so, it can be observed that a monostatic SAR which is always (i.e. for each and every pulse) positioned along the bisector of the bistatic angle (i.e. along a line with direction given by $\mathbf{B}_n$) will collect phase data on the same surface as the bistatic SAR (although, as may be seen from (2.48) and (2.50), the radial distance of the collected data in the two data sets will differ by a factor of $\cos(\beta_n/2)$). Thus, within the present first-order approximation, it is possible to view the collected bistatic SAR data in terms of an approximation to an equivalent monostatic SAR collection [94].

The presence of the indicator function $\mathbb{I}_n(\tau + U_n(\mathbf{R});\mathbf{R})$ on the right-hand-side of (2.35) results in the

support of the measurements of $\Psi_n(\tau;\mathbf{R})$ on the collection surface having a dependence on $\mathbf{R}$. There are two cases to consider:

- **Case 1:** $|W_n(\mathbf{R})| \geq T_p$**.** In this case, this indicator function is zero and there is no support.
- **Case 2:** $|W_n(\mathbf{R})| < T_p$**.** In this case, the support of this indicator function may be determined[1] to be over those values of τ which satisfy

$$-\frac{T_p}{2} - \min\{0, W_n(\mathbf{R})\} < \tau - \frac{T_p}{2} + E_{\mathrm{s},n} < \frac{T_p}{2} - \max\{0, W_n(\mathbf{R})\}. \tag{2.51}$$

Thus, from (2.48), (2.50) and (2.51), we find that the corresponding range of vector lengths $|\mathbf{K}_n(\tau)|$ is given by

$$-\frac{\Delta K(n)}{2} + h_1(n;\mathbf{R}) < |\mathbf{K}_n(\tau)| - K_0(n) < \frac{\Delta K(n)}{2} - h_2(n;\mathbf{R}), \tag{2.52}$$

where

$$K_0(n) = \frac{4\pi\cos(\beta_n/2)}{c} f_c \tag{2.53}$$

$$\Delta K(n) = \frac{4\pi\cos(\beta_n/2)}{c}\gamma T_p \tag{2.54}$$

and

$$h_1(n;\mathbf{R}) = -\frac{4\pi\cos(\beta_n/2)}{c}\gamma \cdot \min\{0, W_n(\mathbf{R})\} \tag{2.55}$$

$$h_2(n;\mathbf{R}) = \frac{4\pi\cos(\beta_n/2)}{c}\gamma \cdot \max\{0, W_n(\mathbf{R})\}. \tag{2.56}$$

For compactness, it is desirable to obtain a single expression for the $|\mathbf{K}_n(\tau)|$ which accommodates both cases: this can be easily done by modifying the limits in (2.52) so that they keep sensible values as $|W_n(\mathbf{R})|$ increases beyond T_p. Hence, we obtain

$$-\frac{\Delta K(n)}{2} + k_1(n;\mathbf{R}) < |\mathbf{K}_n(\tau)| - K_0(n) < \frac{\Delta K(n)}{2} - k_2(n;\mathbf{R}), \tag{2.57}$$

where

$$k_1(n;\mathbf{R}) = \min\{h_1(n;\mathbf{R}), \Delta K(n)\} \tag{2.58}$$

$$k_2(n;\mathbf{R}) = \min\{h_2(n;\mathbf{R}), \Delta K(n)\}. \tag{2.59}$$

Plots of the functions $k_1(n;\mathbf{R})$ and $k_2(n;\mathbf{R})$ against $W_n(\mathbf{R})$ for a fixed value of n, as the scatterer position $\mathbf{R}$ is allowed to vary, are shown in Figure 2.6: observe that both vanish simultaneously when $W_n(\mathbf{R}) = 0$, i.e. when $U_n(\mathbf{R}) = E_{\mathrm{d},n}$. Hence, we can see that for each pulse, the radial support on the collection surface of the available phase measurements $\Psi_n(\tau;\mathbf{R})$ is greatest for scatterers at positions $\mathbf{R}$ satisfying $W_n(\mathbf{R}) = 0$: in this case, the radial support will be centred at $K_0(n)$ and have the maximum possible width of $\Delta K(n)$. The support for scatterers at other positions such that $W_n(\mathbf{R}) \neq 0$ will have a margin missing: if $W_n(\mathbf{R}) < 0$, then a margin of width $4\pi\cos(\beta_n/2)\gamma W_n(\mathbf{R})/c$, up to a maximum width of $\Delta K(n)$, will be missing at the

[1] From (2.2), (2.14), (2.26) and (2.27), when $|W_n(\mathbf{R})| < T_p$, the support of $\mathbb{I}_n(\tau + U_n(\mathbf{R});\mathbf{R})$ will be over those τ satisfying $(-T_p + |W_n(\mathbf{R})| - W_n(\mathbf{R}))/2 < \tau - T_p/2 + E_{\mathrm{s},n} < (T_p - |W_n(\mathbf{R})| - W_n(\mathbf{R}))/2$: by simplifying this inequality in each of the separate cases $0 \leq W_n(\mathbf{R}) < T_p$ and $-T_p < W_n(\mathbf{R}) < 0$ then amalgamating the results, we obtain (2.51).

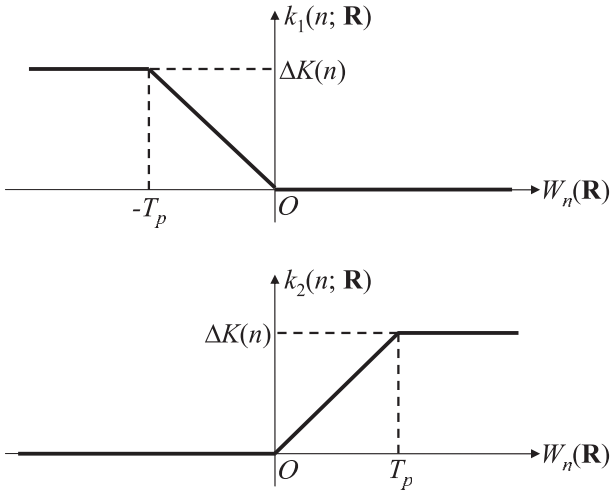

Figure 2.6: Graphs of functions $k_1(n; \mathbf{R})$ and $k_2(n; \mathbf{R})$.

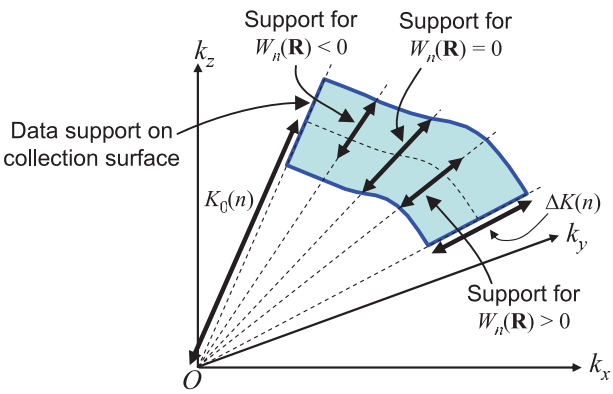

Figure 2.7: Support on data collection surface for scatterers at various $\mathbf{R}$.

edge closest to the origin; if $W_n(\mathbf{R}) > 0$, then a margin of similar width $4\pi\cos(\beta_n/2)\gamma|W_n(\mathbf{R})|/c$, up to a maximum of $\Delta K(n)$, will be missing at the edge farthest from the origin.[2] This is illustrated in Figure 2.7, in which k_x, k_y, k_z have been introduced as the Cartesian coordinates describing points of the three-dimensional space in which $\mathbf{K}_n(\tau)$ resides (we will shortly interpret this space as the spatial frequency domain which is conjugate to the spatial domain described by $\mathbf{R} = (x, y, z)^T$). Hence, for all scatterers taken together, the overlapping support of their data on the collection surface is contained within a region which is radially centred at $K_0(n)$ and has width $\Delta K(n)$, i.e. the overall radial support on the collection surface is given by those $|\mathbf{K}_n(\tau)|$ satisfying

$$-\frac{\Delta K(n)}{2} < |\mathbf{K}_n(\tau)| - K_0(n) < \frac{\Delta K(n)}{2}. \tag{2.60}$$

(This is the same region as for the special case where $W_n(\mathbf{R}) = 0$.)

In the general bistatic case where the transmitter and receiver are free to move along independent and arbitrary trajectories, the shape of the resultant collection surface traced out by the $\mathbf{K}_n(\tau)$ may be extremely complicated.[3] Fortunately, for the case of the *Ingara* circular spotlight-SAR mode collection geometry, the

[2] This is for range-deskewed signals: without range-deskewing, the positions of the margins would be reversed (cf. Figure 2.3).
[3] Indeed, pathological cases can easily be constructed by assigning to the transmitter and receiver angular velocities about the

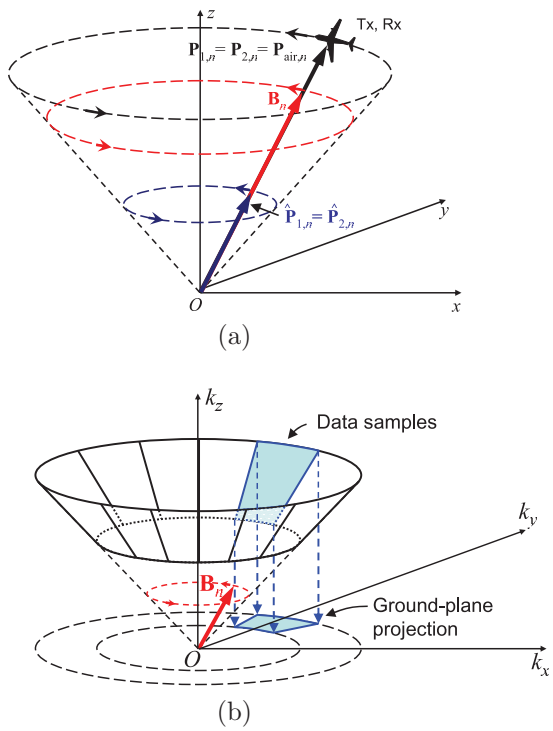

Figure 2.8: (a) Circling-Tx-fixed-Rx collection geometry for monostatic data; (b) resultant collection surface.

collection surfaces can be calculated quite simply by considering the regular trajectories traced by the vectors $\mathbf{P}_{1,n}$ and $\mathbf{P}_{2,n}$ in the monostatic and bistatic cases. For the monostatic data collected by the airborne receiver, we have $\mathbf{P}_{1,n} = \mathbf{P}_{2,n} = \mathbf{P}_{\mathrm{air},n}$, where $\mathbf{P}_{\mathrm{air},n}$ is the position of the circling airborne antenna (Figure 2.8(a)): hence the vector $\mathbf{B}_n$ circles around the vertical axis and the $\mathbf{K}_n(\tau)$ lie on the surface of an upright cone (Figure 2.8(b)). However, for the bistatic data from the stationary ground-based receiver, we have $\mathbf{P}_{1,n} = \mathbf{P}_{\mathrm{air},n}$ as before but now $\mathbf{P}_{2,n} = \mathbf{P}_{\mathrm{gnd}}$, being the fixed (constant) position of the ground-based antenna: thus, in this case, the $\mathbf{B}_n$ vectors are tilted towards the receiver and the $\mathbf{K}_n(\tau)$ in this case lie on the surface of an oblique cone (Figure 2.9).

From (2.46), observe that, to first order in $|\mathbf{R}|$, the elementary signal phase $\Psi_n(\tau;\mathbf{R})$ consists solely of the linear term $\mathbf{K}_n(\tau)\cdot\mathbf{R}$. This first-order approximation will be valid when $|\mathbf{R}| \ll |\mathbf{P}_{i,n}|$ for $i = 1, 2$: thus, near the origin, the normalised signal from each elementary scattering centre is well-approximated by a plane wave, viz.

$$s_n(\tau;\mathbf{R}) = \mathbb{I}_n(\tau + U_n(\mathbf{R});\mathbf{R})\, e^{j\mathbf{K}_n(\tau)\cdot\mathbf{R}}. \tag{2.61}$$

This is just the spatial Fourier transform of a Dirac delta function centred at $\mathbf{R}$ with a limited support imposed by the indicator function. Hence, for small scene sizes $\mathcal{V}$ such that the first-order phase approximation holds, since the SAR data $\chi_n(\tau)$ is just the sum (integral) over all $\mathbf{R} \in \mathcal{V}$ of the scaled plane waves $s_n(\tau;\mathbf{R})\, g(\mathbf{R})\mathrm{d}\mathbf{R}$, the measured values of $\chi_n(\tau)$ may be (somewhat loosely) interpreted as samples of a spatial Fourier transform

origin of equal magnitude but opposite sign: the direction of $\mathbf{B}_n$ will then be constant and a surface will not even be swept out!

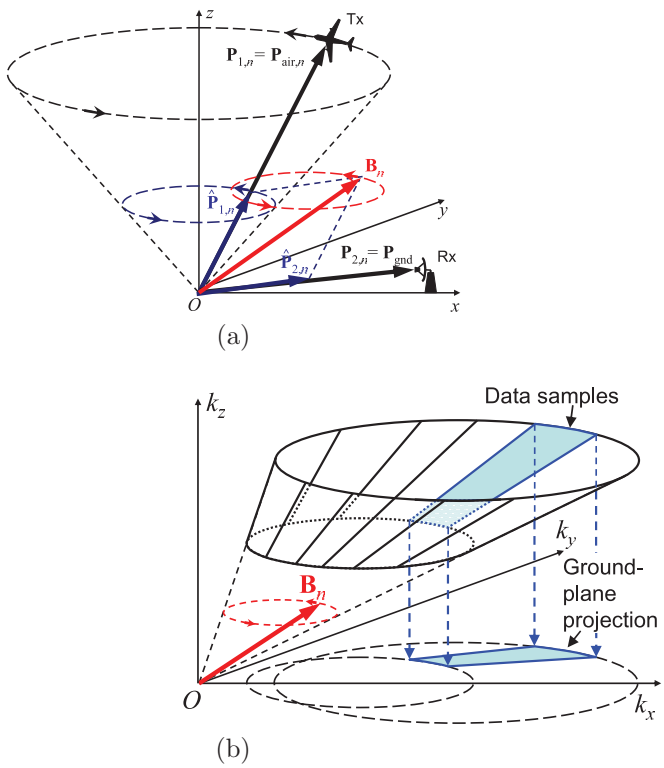

Figure 2.9: (a) Circling-Tx-fixed-Rx collection geometry for bistatic data; (b) resultant collection surface.

of the truncated complex reflectivity function of the scene,

$$g_{\mathcal{V}}(\mathbf{R}) = \begin{cases} g(\mathbf{R}) & \text{if } \mathbf{R} \in \mathcal{V}, \\ 0 & \text{otherwise.} \end{cases} \tag{2.62}$$

More formally, under this first-order phase approximation, the relationship between $\chi_n(\tau)$ and $g_{\mathcal{V}}(\mathbf{R})$ is given by

$$\chi_n(\tau) = \int_{\mathbb{R}^3} \mathrm{d}\mathbf{R}\; e^{j\mathbf{K}_n(\tau)\cdot\mathbf{R}} g_{\mathcal{V}}(\mathbf{R})\; \mathbb{I}_n(\tau + U_n(\mathbf{R}); \mathbf{R}). \tag{2.63}$$

Although the right-hand-side of (2.63) is very similar to an inverse Fourier transform,[4] it is not strictly one because of the presence of the indicator function, which introduces a dependency between the conjugate variables $\mathbf{R}$ and $\mathbf{K}_n(\tau)$. In fact, the linkage of $\mathbf{R}$ and $\mathbf{K}_n(\tau)$ by the indicator function is a consequence of the relatively short duration of the dechirping signal $d_n(t)$ employed by the *Ingara* hardware (ref. (2.8)): if the dechirping signal were of sufficient duration to overlap completely with returns from *all* parts of the scene

[4] A common convention is to define the forward and inverse Fourier transforms with negative and positive signs in the argument of the kernel of integration respectively, e.g.

$$G(\mathbf{K}) = \int_{\mathbb{R}^3} \mathrm{d}\mathbf{R}\; e^{-j\mathbf{K}\cdot\mathbf{R}} g(\mathbf{R})$$

is the *forward* (analysis) Fourier transform of $g(\mathbf{R})$ and

$$g(\mathbf{R}) = \frac{1}{(2\pi)^3} \int_{\mathbb{R}^3} \mathrm{d}\mathbf{K}\; e^{+j\mathbf{K}\cdot\mathbf{R}} G(\mathbf{K})$$

is the *inverse* (synthesis) Fourier transform of $G(\mathbf{K})$. Hence, by this convention, the spatial transform referred to in the text is an inverse Fourier transform (albeit one which has been scaled by $(2\pi)^3$), and it is the negative sign in the integration kernel which should be used for its inversion.

(and not just those from positions $\mathbf{R}$ satisfying $|W_n(\mathbf{R})| = 0$), no such linkage would arise and $\chi_n(\tau)$ would formally be the inverse spatial Fourier transform of $g_{\mathcal{V}}(\mathbf{R})$. Nevertheless, the relationship between $\chi_n(\tau)$ and $g_{\mathcal{V}}(\mathbf{R})$ is sufficiently similar to an inverse Fourier transform that image formation can be achieved by applying a Fourier transform to the data to recover a version of $g_{\mathcal{V}}(\mathbf{R})$ that has been convolved with a spatially varying impulse response. (As discussed later in Section 2.7, this impulse response is basically the Fourier transform of a function which indicates the support of the data in the space of vectors $\mathbf{K}_n(\tau)$ over the coherent processing interval.)

Image formation from the *Ingara* data is thus achieved by Fourier transformation of the deskewed, motion-compensated dechirped data $\chi_n(\tau)$. This procedure essentially multiplies the complex signals $\exp(j\mathbf{K}_n(\tau) \cdot \mathbf{R})$ in the $s_n(\tau; \mathbf{R})$ by a signal $\exp(-j\mathbf{K}_n(\tau) \cdot \mathbf{R}')$ and sums up the results: when $\mathbf{R}' = \mathbf{R}$, the multiplication cancels out the phase in $s_n(\tau; \mathbf{R})$ so that the summation gathers the energy which is spread out in the space of vectors $\mathbf{K}_n(\tau)$ and concentrates it around the point $\mathbf{R}$ in the space of vectors $\mathbf{R}'$.

Theoretically, in the most general case, the Fourier transform employed is three-dimensional: it takes, as input, the original data samples in a three-dimensional space of vectors $\mathbf{K}_n(\tau)$ and produces, as output, a three-dimensional image in a space of spatial position vectors $\mathbf{R}'$. However, in practice, it is a two-dimensional Fourier transform which is commonly employed: the main reasons for this are as follows.

1. A coherent processing interval is generally brief, with the result that the trajectories of the transmitter and receiver during the interval are well-approximated by straight lines. Consequently, the collection surface is effectively a plane (the *slant plane*), so the space of vectors $\mathbf{K}_n(\tau)$ in which the collected data samples are embedded is two-dimensional.[5]

2. The scene of interest which is imaged by the SAR is generally a large area of ground: hence, the z-coordinate displacement of scatterers above the ground-plane is of secondary interest to their xy-coordinate displacement within the ground-plane. Thus, the 'volume' $\mathcal{V}$ of scatterers comprising the scene is well-represented by a two-dimensional surface, in which the z-coordinate is suppressed by projection into the xy-plane: for the representation of such a surface, a two-dimensional image suffices.

Three-dimensional imaging is certainly feasible by: employing highly non-linear platform trajectories so the collection surface of the SAR data will be non-planar [117,118]; and/or combining data from multiple collection surfaces so that the resultant combined data set fills a three-dimensional collection volume [119–121]. However, three-dimensional SAR is currently still a subject of research interest and not routinely performed; moreover, if required, three-dimensional information can be partially recovered from two-dimensional images by scatterer height estimation through well-established interferometric or stereoscopic techniques. Hence, in the interests of simplicity, we shall confine our discussion to the case of two-dimensional images.

As the imaged scene is generally a patch of terrain comprising scatterers distributed about a ground-plane, to aid image interpretability, it is generally desirable that the plane of the image should coincide with the ground-plane. This can be achieved by simply projecting the data samples from the collection surface onto the ground-plane before applying the Fourier transform. Other image-display-planes are, of course, possible: e.g. it may occasionally be helpful to display the image in the slant-plane. The procedure for generating images in any other arbitrary choice of image-plane is similar: the data samples are projected from the the collection surface onto the chosen plane. However, as the ground-plane is the most common choice of image-plane, we

[5] As depicted in Figures 2.8(b) and 2.9(b), the circular flight trajectory of the airborne radar in the *Ingara* collection geometry produces a collection surface which is intrinsically curved (rather than planar as desired): as discussed by Jakowatz et al. [39, Section 3.8], such surface curvature reduces focus quality for targets outside the focus plane. For simplicity, however, we shall assume that the coherent processing interval is always sufficiently brief that the local surface for a given synthetic aperture is effectively planar.

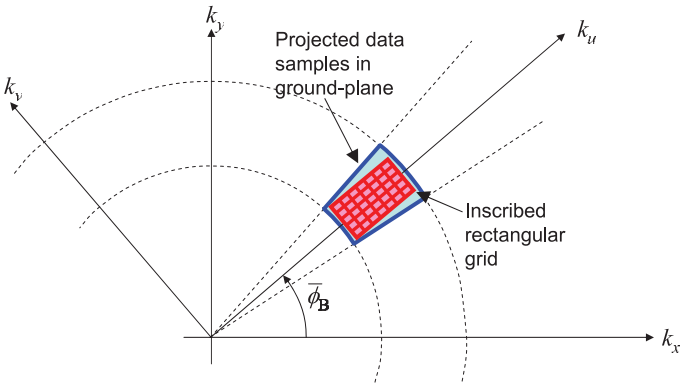

(a) Monostatic data

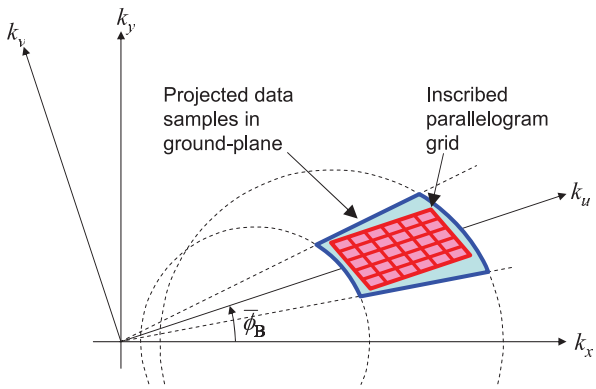

(b) Bistatic data

Figure 2.10: Shape of support in ground-plane of projected data samples collected in the *Ingara* circular spotlight-mode SAR geometry by: (a) the orbiting airborne receiver; and (b) the stationary ground-based receiver.

shall, without loss of generality, simply equate the image-plane with the ground-plane in the discussion, unless stated otherwise.

2.5.2 Resampling

As discussed in the preceding section, a Fourier transform of the data $\chi_n(\tau)$ suffices to generate a SAR image. When performing the Fourier transform, it is highly advantageous to exploit the computational speed and efficiency of Fast Fourier Transform (FFT) routines. However, FFTs require that the data they operate upon be evenly sampled on regular grids. This is not the case for the projected samples in the ground-plane, which lie on an irregular polar grid: hence, it is necessary to resample the projected data onto a regular rectangular or parallelogram grid before the FFT can be applied. Although rectangular grids are commonly employed for the monostatic case, the shape of the data support in the bistatic case is such that, generally, more effective use is made of the phase history extents by using a suitably oriented parallelogram grid (see Figure 2.10). It should be noted that a rectangular grid is really just a special case of parallelogram grid: indeed, as the angle between the axes of the parallelogram grid is dependent on the collection geometry, for certain geometries (not necessarily monostatic), a right angle will result and the parallelogram grid will actually be rectangular. In this section, we discuss the resampling procedure used to process the *Ingara* data.

We begin the discussion by considering the input to the resampling procedure: this will be an M-by-N block of data samples $\chi_n(\tau_m)$, where M is the number of samples collected per pulse, N is the number of pulses to be coherently processed, the indices m and n take values according to $m = 0, 1, \ldots, M-1$ and $n = 0, 1, \ldots, N-1$ respectively, and the continuous fast time τ has been discretised to

$$\tau_m = m/f_s, \tag{2.64}$$

in which f_s is the sampling rate. The positions of the projected samples in the ground-plane $\mathbf{k}_{m,n}$ are obtained by projecting their corresponding vectors $\mathbf{K}_n(\tau_m)$ (see Figure 2.11). From (2.48), we have

$$\mathbf{K}_n(\tau_m) = \frac{2\pi}{c}\left[f_c + \gamma\left(\tau_m - \frac{T_p}{2} + E_{\mathrm{s},n}\right)\right]\mathbf{B}_n, \tag{2.65}$$

where

$$\mathbf{B}_n = B_n \sin\theta_{\mathbf{B},n}\cos\phi_{\mathbf{B},n}\,\mathbf{a}_x + B_n \sin\theta_{\mathbf{B},n}\sin\phi_{\mathbf{B},n}\,\mathbf{a}_y + B_n\cos\theta_{\mathbf{B},n}\,\mathbf{a}_z, \tag{2.66}$$

in which B_n, $\theta_{\mathbf{B},n}$ and $\phi_{\mathbf{B},n}$ denote the lengths, polar angles and azimuth angles of the vectors $\mathbf{B}_n$, and $\mathbf{a}_x$, $\mathbf{a}_y$ and $\mathbf{a}_z$ are unit vectors in the directions of the positive x, y and z axes respectively. Hence, if we take the xy-plane as the ground-plane, then the projected sample positions are given by

$$\mathbf{k}_{m,n} = \frac{2\pi}{c}\left[f_c + \gamma\left(\tau_m - \frac{T_p}{2} + E_{\mathrm{s},n}\right)\right]\mathbf{b}_n, \tag{2.67}$$

in which the $\mathbf{b}_n$ are the projections of the $\mathbf{B}_n$, viz.

$$\mathbf{b}_n = b_n\cos\phi_{\mathbf{B},n}\,\mathbf{a}_x + b_n\sin\phi_{\mathbf{B},n}\,\mathbf{a}_y. \tag{2.68}$$

where b_n is the length of $\mathbf{b}_n$:

$$b_n = B_n\sin\theta_{\mathbf{B},n} \tag{2.69}$$

The output grid has to be specified before the projected data can be resampled. In determining an appropriate grid, we seek to balance the competing objectives of achieving fine resolution and large spatial coverage in the final SAR image against the minimisation of the resampling workload and computer memory requirements. Fine image resolution is achieved by a grid with large extents while large image spatial coverage is achieved by a grid with small sampling intervals. Ultimately, the extent of the grid is determined by the support of the data: in order to achieve the finest feasible image resolution, the desired grid should cover as much of the data support as possible but, for reasons of economy, the grid should preferably not extend beyond it. (In fact, ensuring that the grid is tightly trimmed to remain within the support of the data may also be desirable for other reasons, e.g. to avoid oddly shaped point-spread functions in the image.) The grid sampling interval is determined by the frequency content of the data: to achieve the largest feasible image coverage, the grid sample spacing should be sufficiently small to sample the highest frequency present in the data in compliance with the Nyquist criterion, but for economy, the sample spacing should be no smaller. In practice, however, as the collected data is already sampled, it will suffice to simply choose grid sampling intervals which are compatible with the existing intervals in the data. Hence, with these considerations in mind, the grid is determined as follows.

- First, new orthogonal axes k_u and k_v are defined which are aligned with the data support: the direction of the k_u-axis is specifically chosen so that it is evenly straddled by the support of the projected data.

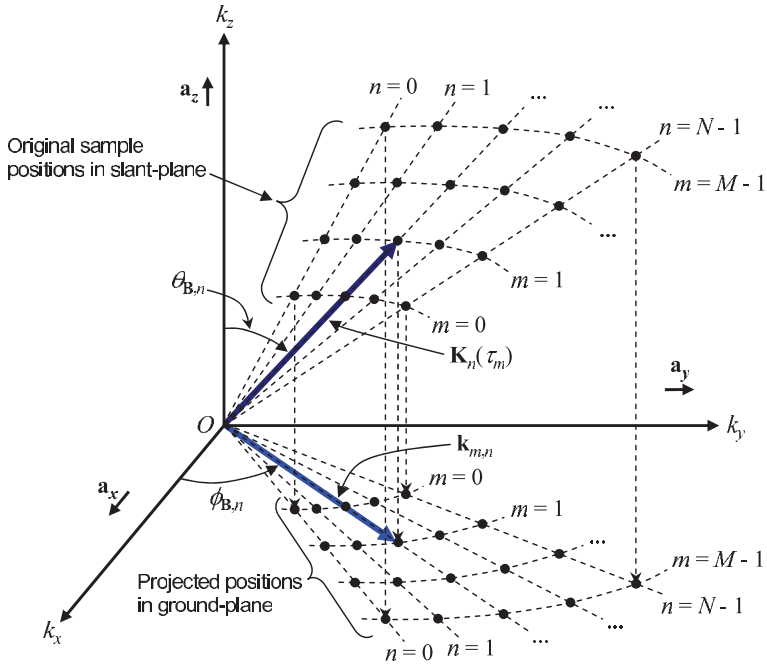

Figure 2.11: Projection of data samples from slant-plane to ground-plane.

From Figure 2.12, the required orientation of the k_u-axis relative to the x-axis, denoted by $\bar{\phi}_{\mathbf{B}}$, satisfies

$$b_{N-1} \sin\left(\phi_{\mathbf{B},N-1} - \bar{\phi}_{\mathbf{B}}\right) = b_0 \sin\left(\bar{\phi}_{\mathbf{B}} - \phi_{\mathbf{B},0}\right). \tag{2.70}$$

This can be re-arranged to give

$$\tan \bar{\phi}_{\mathbf{B}} = \frac{b_{N-1} \sin \phi_{\mathbf{B},N-1} + b_0 \sin \phi_{\mathbf{B},0}}{b_{N-1} \cos \phi_{\mathbf{B},N-1} + b_0 \cos \phi_{\mathbf{B},0}}, \tag{2.71}$$

whereupon the required value of $\bar{\phi}_{\mathbf{B}}$ can be obtained by inverting the tangent. Hence, relative to the k_u-axis, the azimuth angles of the $\mathbf{B}_n$ and $\mathbf{b}_n$ are then

$$\Delta\phi_{\mathbf{B},n} = \phi_{\mathbf{B},n} - \bar{\phi}_{\mathbf{B}} \tag{2.72}$$

so, in the $k_u k_v$-coordinate system, (2.68) becomes

$$\mathbf{b}_n = b_n \cos \Delta\phi_{\mathbf{B},n}\, \mathbf{a}_u + b_n \sin \Delta\phi_{\mathbf{B},n}\, \mathbf{a}_v, \tag{2.73}$$

where $\mathbf{a}_u$ and $\mathbf{a}_v$ are unit vectors in the directions of the k_u and k_v axes respectively.

- Second, the angle α between the axes of the parallelogram grid (see Figure 2.13) is determined by fitting a line to the projected vectors $\mathbf{b}_n$ (ref. Figure 2.14): the slope of this line gives the required value of α. Specifically, a least-squares regression line of the form $u = av + b$ is fitted to the data points (u_n, v_n),

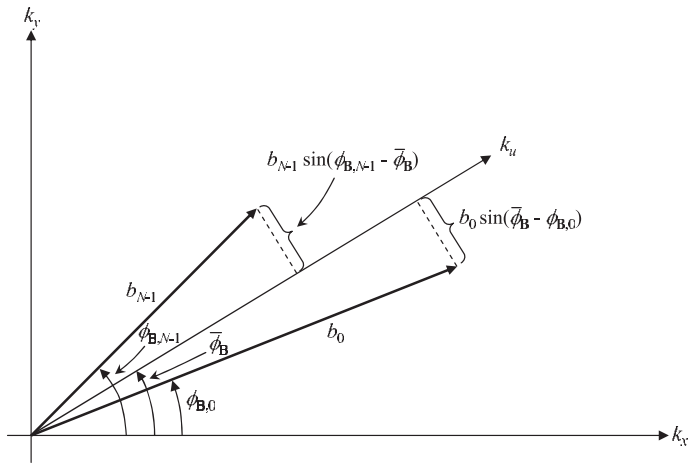

Figure 2.12: Calculating orientation of k_u-axis.

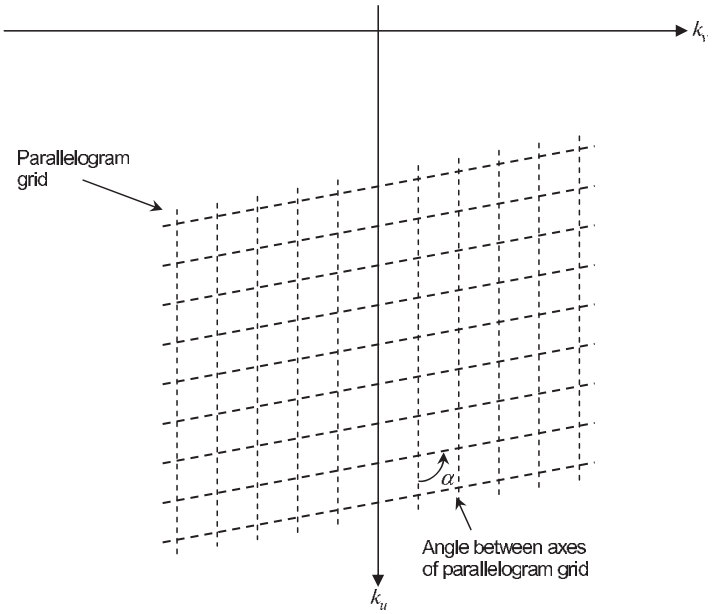

Figure 2.13: Angle α between axes of parallelogram grid.

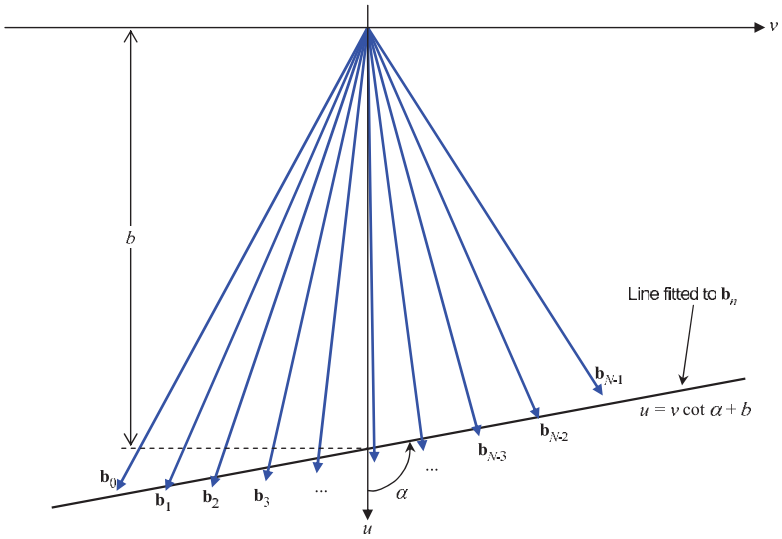

Figure 2.14: Determining angle α by fitting line to vectors $\mathbf{b}_n$.

where, from (2.73), we have

$$u_n = b_n \cos \Delta\phi_{\mathbf{B},n}, \tag{2.74}$$

$$v_n = b_n \sin \Delta\phi_{\mathbf{B},n}. \tag{2.75}$$

The required value of α can then be obtained from the parameter a through the relationship $\cot \alpha = a$.

- Third, the radial size of the support of the projected data is found. For each pulse, this support is determined by the intersection of two sets of radial distances from the origin. The first set represents the time interval when there was valid signal data available for sampling during the dechirp-on-receive process, and is determined by the overlap of the returning signals and the dechirping signal. The second set represents the time interval when sampling of the data was actually occurring, and is determined by when the sampling began and the duration over which samples were collected. Clearly, the support of the data must correspond to both when valid signal data was available *and* when the data was also being sampled: this is given by the intersection of these two sets.

  The elements of the first set are determined by the overlapping indicator functions $\mathbb{I}_n(\tau + U_n(\mathbf{R}); \mathbf{R})$ for various $\mathbf{R}$ and, as previously discussed, this leads to (2.60): when projected into the ground-plane (Figure 2.15), the result is

$$-\frac{\Delta k(n)}{2} < k_r(n) - k_0(n) < \frac{\Delta k(n)}{2}, \tag{2.76}$$

  where $k_r(n)$ is the radial distance from the origin along the direction of $\mathbf{b}_n$, and[6]

$$k_0(n) = \frac{2\pi b_n}{c} f_c, \tag{2.77}$$

$$\Delta k(n) = \frac{2\pi b_n}{c} \gamma T_p. \tag{2.78}$$

[6]Essentially, $k_r(n)$, $k_0(n)$ and $\Delta k(n)$ can be thought of as the respective projections of $|\mathbf{K}_n(\tau)|$, $K_0(n)$ and $\Delta K(n)$ onto the ground-plane, i.e. $k_r(n) = |\mathbf{K}_n(\tau)| \sin \theta_{\mathbf{B},n}$, $k_0(n) = K_0(n) \sin \theta_{\mathbf{B},n}$ and $\Delta k(n) = \Delta K(n) \sin \theta_{\mathbf{B},n}$: (2.77) and (2.78) follow from (2.53) and (2.54) respectively since $b_n = 2\cos(\beta_n/2) \sin \theta_{\mathbf{B},n}$ (ref. (2.50) and (2.69)).

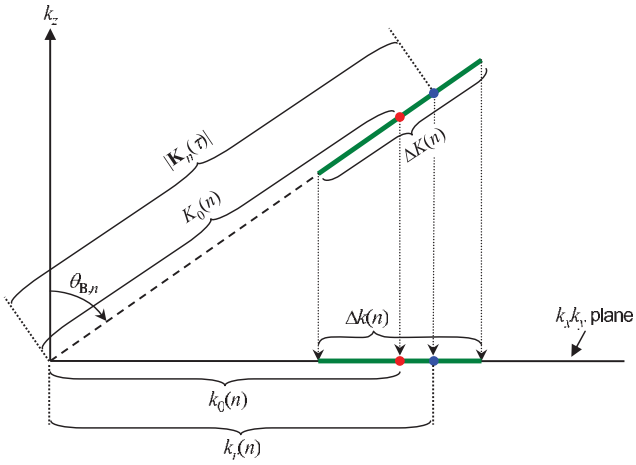

Figure 2.15: Projection of radial data support onto ground-plane.

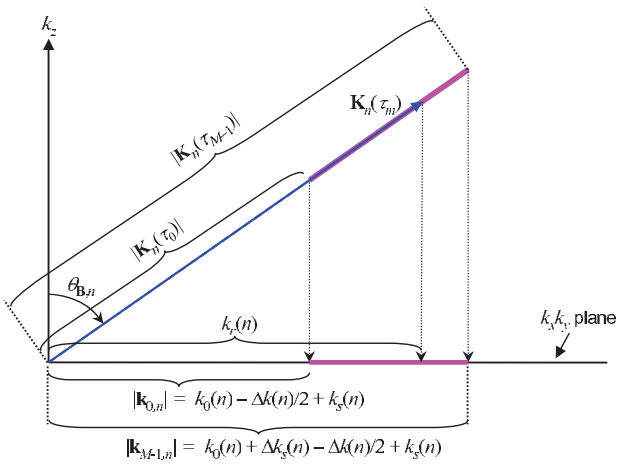

Figure 2.16: Projection of sampling positions onto ground-plane.

Hence, the elements of the first set are the $k_r(n)$ satisfying (2.76).

The elements of the second set are the $k_r(n)$ corresponding to the range of sampling times for each pulse: as depicted in Figure 2.16, by substituting $m = 0$ and $m = M - 1$ (corresponding to the first and last samples) into (2.67), we find that these are given by[7]

$$0 < k_r(n) - \left(k_0(n) - \frac{\Delta k(n)}{2} + k_s(n)\right) < \Delta k_s(n), \tag{2.79}$$

[7]Substituting $m = 0$ and $m = M - 1$ into (2.67) (recall (2.64)) and using the definitions in (2.77), (2.78), (2.80), (2.81) gives $|\mathbf{k}_{0,n}| = k_0(n) - \Delta k(n)/2 + k_s(n)$ and $|\mathbf{k}_{M-1,n}| = k_0(n) + \Delta k_s(n) - \Delta k(n)/2 + k_s(n)$ respectively: for pulse n, these are the minimum and maximum values of the projected wavevector magnitudes $|\mathbf{k}_{m,n}|$ corresponding to the set of collected samples (ref. Figure 2.11). Hence, to restrict $k_r(n)$ to this range, we set $|\mathbf{k}_{0,n}| < k_r(n) < |\mathbf{k}_{M-1,n}|$ from which (2.79) follows.

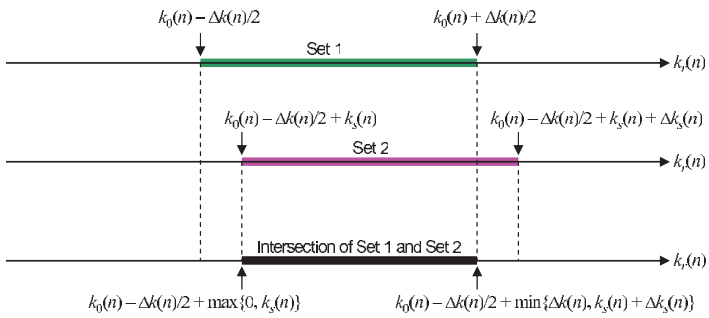

Figure 2.17: Intersections of first and second sets.

where

$$k_{\mathrm{s}}(n) = \frac{2\pi b_n}{c}\gamma E_{\mathrm{s},n}, \tag{2.80}$$

$$\Delta k_{\mathrm{s}}(n) = \frac{2\pi b_n}{c}\gamma \frac{M-1}{f_s}. \tag{2.81}$$

Thus, as shown in Figure 2.17, from the intersection of the sets of $k_r(n)$ specified by (2.76) and (2.79), the radial support of the data for each pulse is given by

$$k_r^{(\mathrm{i})}(n) < k_r(n) < k_r^{(\mathrm{o})}(n), \tag{2.82}$$

in which

$$k_r^{(\mathrm{i})}(n) = k_0(n) - \frac{\Delta k(n)}{2} + \max\left\{0, k_{\mathrm{s}}(n)\right\}, \tag{2.83}$$

$$k_r^{(\mathrm{o})}(n) = k_0(n) - \frac{\Delta k(n)}{2} + \min\left\{\Delta k(n), k_{\mathrm{s}}(n) + \Delta k_{\mathrm{s}}(n)\right\}. \tag{2.84}$$

- Fourth, a parallelogram is inscribed into the data support. The positions of the edges of the inscribed parallelogram may be specified by four parameters: the abscissa of the intersections of the inner and outer edges of the parallelogram with the k_u-axis, denoted by $k_u^{(\mathrm{i})}$ and $k_u^{(\mathrm{o})}$ respectively; and the ordinates of the left and right edges of the parallelogram, denoted by $k_v^{(\mathrm{l})}$ and $k_v^{(\mathrm{r})}$ respectively (see Figure 2.18). One possible choice for these parameters may be found by projecting the $k_r^{(\mathrm{i})}(n)$ and $k_r^{(\mathrm{o})}(n)$ obliquely (along the direction of the oblique sides of the parallelogram) onto the k_u-axis and orthogonally onto the k_v-axis:

$$k_u^{(\mathrm{i})} = \max\left\{k_r^{(\mathrm{i})}(n) \cdot \frac{\sin(\alpha - \Delta\phi_{\mathbf{B},n})}{\sin\alpha} : n = 0, 1, \ldots, N-1\right\}, \tag{2.85}$$

$$k_u^{(\mathrm{o})} = \min\left\{k_r^{(\mathrm{o})}(n) \cdot \frac{\sin(\alpha - \Delta\phi_{\mathbf{B},n})}{\sin\alpha} : n = 0, 1, \ldots, N-1\right\}, \tag{2.86}$$

$$k_v^{(\mathrm{l})} = k_r^{(\mathrm{i})}(0) \cdot \sin\Delta\phi_{\mathbf{B},0}, \tag{2.87}$$

$$k_v^{(\mathrm{r})} = k_r^{(\mathrm{i})}(N-1) \cdot \sin\Delta\phi_{\mathbf{B},N-1}. \tag{2.88}$$

In the above equations, the factors $\sin(\alpha - \Delta\Phi_{\mathbf{B},n})/\sin\alpha$ and $\sin\Delta\phi_{\mathbf{B},n}$ arise from the various projections (ref. Figure 2.19).

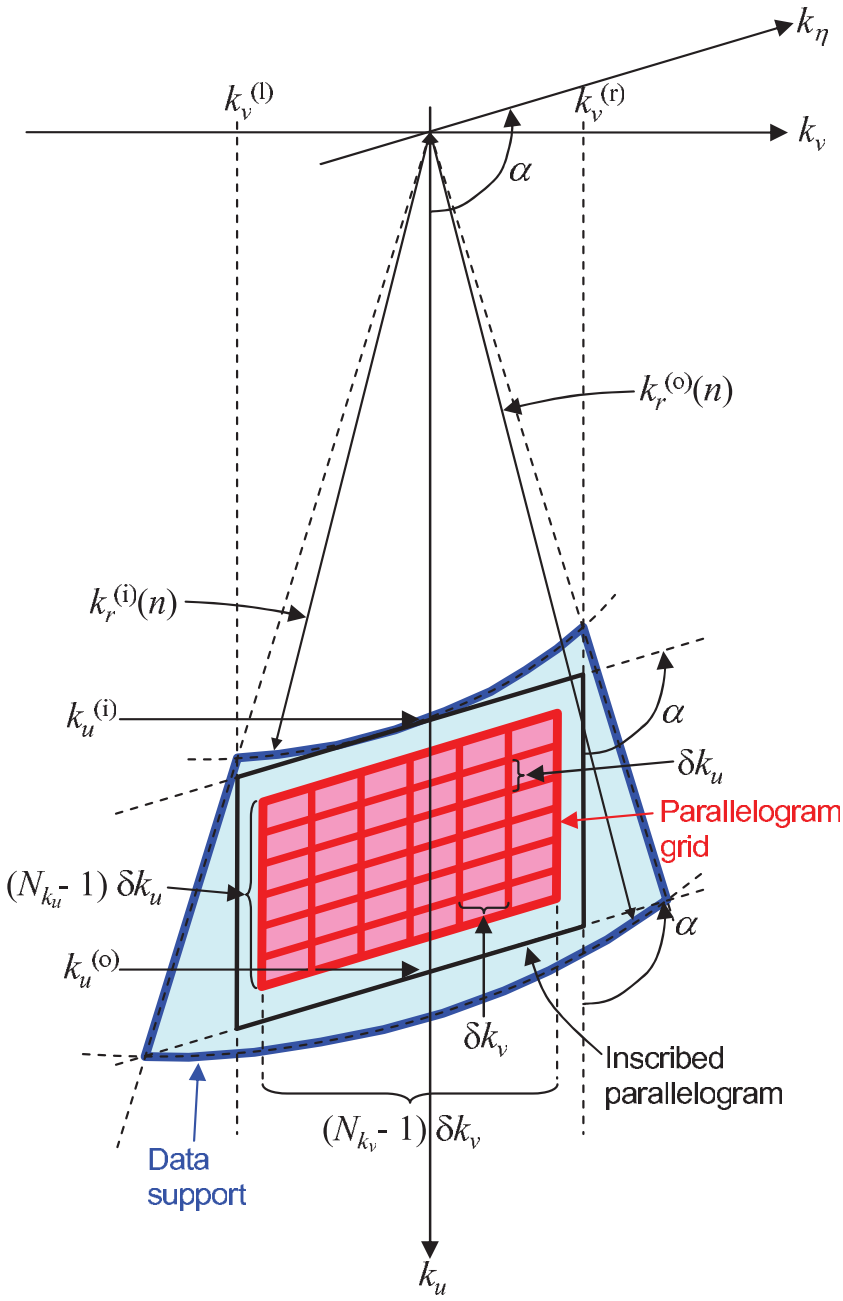

Figure 2.18: Inscribing a parallelogram grid into the data support in the ground-plane.

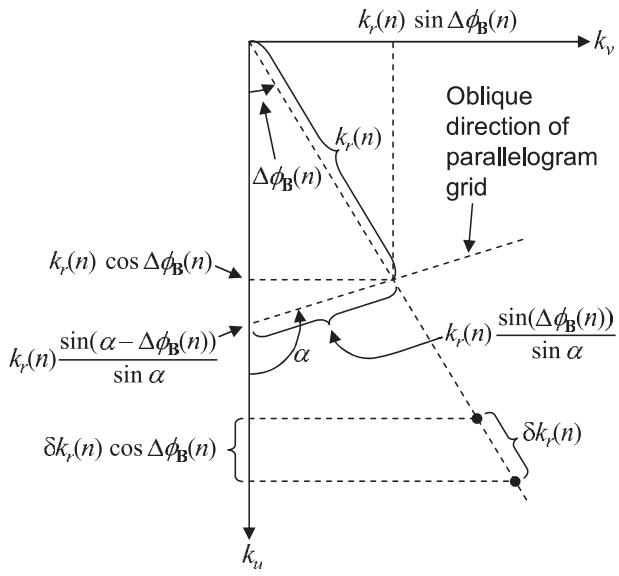

Figure 2.19: Projections of $k_r(n)$ and $\delta k_r(n)$.

- Fifth, the sampling intervals for the parallelogram grid are determined. To choose the sampling interval in the direction of the k_u-axis, first observe that, for the nth pulse, the sampling interval along the radial direction can be calculated from the difference $|\mathbf{k}_{m+1,n} - \mathbf{k}_{m,n}|$ (this is constant and defined for any m from 0 to $M-2$): using (2.67) (and (2.64)) gives the sampling interval as

$$\delta k_r(n) = \frac{2\pi b_n}{c}\frac{\gamma}{f_s}. \tag{2.89}$$

The corresponding sampling interval along the k_u-axis direction for each pulse is the orthogonal projection of the $\delta k_r(n)$ onto the k_u-axis, i.e. $\delta k_r(n)\cos\Delta\phi_{\mathbf{B},n}$. Observe that these projections may potentially vary in size from pulse to pulse (i.e. with n).

In choosing the sampling interval of the parallelogram grid along the k_u-axis, it is desirable to make a choice which is reasonably matched to these projections so that we do not excessively oversample or reduce the bandwidth of the data (oversampling increases demands on computational and memory resources while bandwidth reduction reduces the coverage area of the final SAR image). As the optimum choice requires a careful consideration of the orientations of the $\mathbf{k}_{m,n}$ vectors which can lead to complicated calculations, we will instead accept a non-optimal choice based on quick and simple rules. Some possible options are to choose the minimum or the mean of the set of projections but, for our purposes, we arbitrarily choose to use the maximum of the set of projections: this has the advantage of minimising the number of samples in the parallelogram grid, which lightens both memory and computational loads albeit at a risk of reducing image coverage. In practice, however, since the SAR signals are usually oversampled during collection and the range of the projected sampling intervals is small, the coverage reduction (along the range direction) from this choice of grid sampling interval is usually negligible. Thus, we take as the sampling interval of the parallelogram grid along the k_u-axis the maximum of these projections, viz.

$$\delta k_u = \max\left\{\delta k_r(n)\cos\Delta\phi_{\mathbf{B},n} : n = 0, 1, \ldots, N-1\right\}. \tag{2.90}$$

For reasons similar to those just presented for choosing δk_u, we will also choose δk_v, the sampling interval along the k_v-axis of the parallelogram grid, by picking a value commensurate with the largest intervals projected onto the k_v-axis occurring in the original polar grid. As larger intervals are encountered farther from the origin, we focus our attention on the intervals along the edge of the data support farthest from the origin: these are approximately given by $k_u^{(\mathrm{o})}\left(\tan\Delta\phi_{\mathbf{B},n+1} - \tan\Delta\phi_{\mathbf{B},n}\right)$ for n from 0 to $N-2$. Hence, our choice for the sampling interval of the parallelogram grid along the k_v direction is thus arbitrarily set to be

$$\delta k_v = k_u^{(\mathrm{o})} \max\left\{\tan\Delta\phi_{\mathbf{B},n+1} - \tan\Delta\phi_{\mathbf{B},n} : n = 0, 1, \ldots, N-2\right\}. \tag{2.91}$$

Like that for δk_u, this choice for δk_v is by no means optimal but, given that the signal is often oversampled in practice and the range of variation of $\tan\Delta\phi_{\mathbf{B},n+1} - \tan\Delta\phi_{\mathbf{B},n}$ is typically small, any reduction of azimuthal coverage in the final SAR image is usually insignificant.

- Sixth, the number of samples along each axis of the parallelogram grid are determined. To do this, we first estimate the dimensions of the parallelogram grid along the k_u and k_v directions. These will be given by the size of the inscribed parallelogram, less an appropriate margin to avoid any transient effects caused by attempting to calculate resampled values which are too close to the edge of the data support. The size of the inscribed parallelogram can be easily obtained from the differences between the parallelogram-edge-position parameters $k_u^{(\mathrm{o})}$ and $k_u^{(\mathrm{i})}$, and between $k_v^{(\mathrm{r})}$ and $k_v^{(\mathrm{l})}$. As discussed below and in Appendix A, the resampling operation is carried out using one-dimensional windowed-sinc filters: the required margin is thus simply the width of the one-dimensional filter which is employed in the resampling process. From Section A.2, the filter width is given by $2N_z/b$, where N_z is the number of zero-crossings and b is the filter's bandwidth parameter, chosen as $b = f_{s,\min}/\beta$ where $f_{s,\min}$ is the minimum of the old and new sampling frequencies and β is the bandwidth reduction factor. Since, in the previous step, we have chosen the new sampling frequencies of the parallelogram grid to be no higher than the original sampling frequencies present in the projected polar grid, we effectively have $f_{s,\min} = 1/\delta k_u$ and $f_{s,\min} = 1/\delta k_v$ along the k_u and k_v axes respectively. Thus, the calculated dimensions of the parallelogram grid are

$$L_{k_u} = \left(k_u^{(\mathrm{o})} - k_u^{(\mathrm{i})}\right) - 2\beta N_z \delta k_u, \tag{2.92}$$

$$L_{k_v} = \left(k_v^{(\mathrm{r})} - k_v^{(\mathrm{l})}\right) - 2\beta N_z \delta k_v. \tag{2.93}$$

The number of grid points along the k_u and k_v directions, denoted by N_{k_u} and N_{k_v} respectively, are then readily obtained by dividing these dimensions by the corresponding sampling interval: the result is

$$N_{k_u} = \left\lfloor \frac{L_{k_u}}{\delta k_u} \right\rfloor + 1, \tag{2.94}$$

$$N_{k_v} = \left\lfloor \frac{L_{k_v}}{\delta k_v} \right\rfloor + 1. \tag{2.95}$$

The above procedure suffices to define the parallelogram grid: if we set the centre of the grid to be at the

point with coordinates $(\bar{k}_u, \bar{k}_v)$, e.g.

$$\bar{k}_u = \frac{k_u^{(\mathrm{i})} + k_u^{(\mathrm{o})}}{2}, \tag{2.96}$$

$$\bar{k}_v = 0, \tag{2.97}$$

then the coordinates of each grid point are

$$k_u(p,q) = \bar{k}_u + \left(p - \left\lfloor \frac{N_{k_u}}{2} \right\rfloor\right) \delta k_u + \left(q - \left\lfloor \frac{N_{k_v}}{2} \right\rfloor\right) \delta k_v \cot\alpha, \tag{2.98}$$

$$k_v(q) = \bar{k}_v + \left(q - \left\lfloor \frac{N_{k_v}}{2} \right\rfloor\right) \delta k_v, \tag{2.99}$$

where $p = 0, 1, \ldots, N_{k_u} - 1$, $q = 0, 1, \ldots, N_{k_v} - 1$. The sizes of the grid along the k_u and k_v dimensions respectively are given by

$$\Delta k_u = (N_{k_u} - 1)\delta k_u \tag{2.100}$$

$$\Delta k_v = (N_{k_v} - 1)\delta k_v. \tag{2.101}$$

With the parallelogram grid to which the data will be resampled now specified, we now proceed to discuss the mechanics of the resampling operation. The two-dimensional polar-to-parallelogram-grid resampling procedure can be implemented as a series of one-dimensional resampling operations: this greatly simplifies the resampling process and allows simple one-dimensional filters to be employed. For processing the *Ingara* data, the interpolation filter used was a Blackman-windowed-sinc filter with support spanning eight zero-crossings on either side of the centre of the filter's impulse response, having a pass-band ripple of 0.0024 dB and stop-band attenuation of 71.8 dB. Although conceptually reasonably straightforward, the implementation of resampling in one-dimension can nevertheless be quite involved. Hence, to avoid detracting from the present discussion, the details of the one-dimensional resampling operation have been relegated to Appendix A: here, we will simply provide a high-level discussion of the two major stages of the overall resampling process.

- In the first stage, the original polar grid is resampled along the radial direction of the polar grid (see Figure 2.20 (a)). Hence, for this stage, it suffices to specify the grid positions by their radial distances from the origin: in the input grid, along each radial line, the sample radial positions are given by

  $$k_r(m,n) = k_0(n) - \frac{\Delta k(n)}{2} + k_{\mathrm{s}}(n) + m\,\delta k_r(n), \tag{2.102}$$

  and in the output grid, the desired sample positions are given by

  $$k_r'(p,n) = k_u\left(p, \left\lfloor \frac{N_{k_v}}{2} \right\rfloor\right) \frac{\sin\alpha}{\sin(\alpha - \Delta\phi_{\mathbf{B},n})}. \tag{2.103}$$

  The result of the radial resampling stage is a set of samples on an intermediate grid having a keystone shape.

- In the second stage, the keystone grid is resampled along the oblique azimuthal direction to produce the final parallelogram grid (see Figure 2.20 (b)). As the sample positions must be specified along the oblique azimuthal direction, we have introduced an oblique k_η-axis, as shown in the figure: the positions

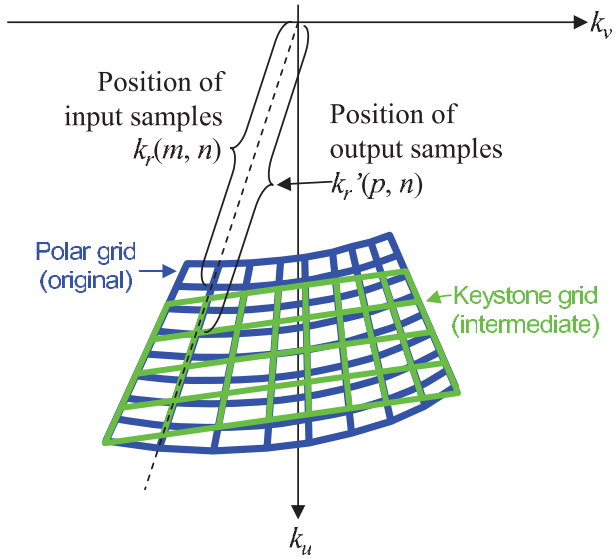

(a) Radial resampling

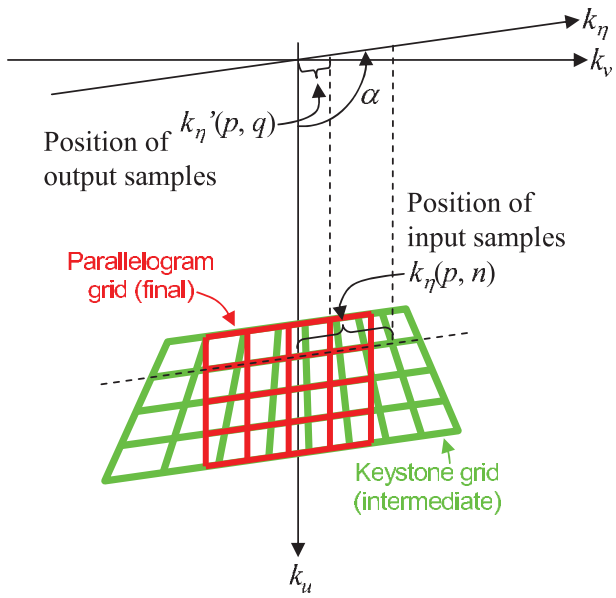

(b) Azimuthal resampling

Figure 2.20: Polar-to-parallelogram resampling: (a) from original polar grid to intermediate keystone grid; (b) from intermediate keystone grid to final parallelogram grid.

of the samples on the input grid measured along this oblique axis are thus given by

$$k_\eta(p,n) = k_u\left(p, \left\lfloor \frac{N_{k_v}}{2} \right\rfloor\right) \frac{\sin \Delta\phi_{\mathbf{B},n}}{\sin(\alpha - \Delta\phi_{\mathbf{B},n})}, \tag{2.104}$$

while the desired positions on the output grid are given by

$$k'_\eta(p,q) = \frac{k_v(q)}{\sin\alpha}. \tag{2.105}$$

The result of the azimuthal resampling stage is the desired set of samples on the parallelogram grid.

It may be observed that for the radial resampling procedure, the input sampling grid is determined by the sampling instants in 'fast' time τ: since these samples are collected by an analogue-to-digital converter (ADC) operating at a fixed sampling rate, the sample points on the input sampling grid are evenly spaced. However, for the azimuth resampling procedure, the input sampling grid is determined by the pulse repetition frequency (PRF) and the trajectories of the transmitter and receiver: in general, the result is that the sample positions on the input sampling grid are unevenly spaced. (The spacing between output samples in both the radial and azimuthal resampling procedures is constant by design.) As a result, radial resampling is suited to an approach based on output-centred convolution, while azimuth resampling is better-suited to an approach based on input-centred convolution [44].

As a check of the polar-to-Cartesian resampling implementation used for processing the *Ingara* data, the errors arising from interpolating between the various grids were assessed by calculating the signal $e^{j\mathbf{K}\cdot\mathbf{R}}$, which represents the ideal phase history of a point target at $\mathbf{R}$, at the points $\mathbf{K}$ in the original polar grid for a typical imaging geometry, then resampling the signal to obtain the values on the final parallelogram grid. For comparison, the same signal was calculated directly (without resampling) at the points on the final parallelogram grid, and the impulse responses corresponding to each of the two signals were then obtained by FFT and compared. In general, for various $\mathbf{R}$, the peak-to-side-lobe-ratio (PSLR) and the integrated-side-lobe-ratio (ISLR) for the resampled and directly calculated signals were found to be in close agreement, suggesting the effect of resampling errors to be minimal and verifying that the resampling was correctly implemented.

2.5.3 Fourier transform

We discuss, in this section, the computation of the Discrete Fourier Transform (DFT) of the data, resampled on the parallelogram grid. As previously discussed, such parallelogram grids (with non-orthogonal axes) are better suited to processing bistatic data than are the traditional rectangular grids (with orthogonal axes) usually employed for monostatic data. However, rectangular grids may be regarded as simply a special case of the parallelogram grids in which the angle between the axes happens to be 90°. Hence, the two-dimensional parallelogram grid-based DFT discussed here may be regarded as a generalisation of the familiar simple two-dimensional rectangular grid-based DFT.

In the previous section, the parallelogram grid was treated as being of finite extent while the support of the signal being sampled was considered infinite. However, for mathematical convenience, we shall adopt a slightly different viewpoint in this section, in which the parallelogram grid is treated as being of infinite extent while the signal, which is sampled on this grid, is considered to have limited support only over the finite extents of the previous grid. Both approaches are mathematically equivalent.

As the starting point for this discussion, consider the two-dimensional sampling (Dirac comb) function

describing the sampling process on the infinite parallelogram grid (ref. (2.98) and (2.99)): this is given by

$$\begin{aligned} c\left(k_u, k_v\right) &= \sum_{p=-\infty}^{\infty} \sum_{q=-\infty}^{\infty} \delta\left(k_u - k_u(p,q)\right) \cdot \delta\left(k_v - k_v(q)\right) \\ &= \sum_{p'=-\infty}^{\infty} \sum_{q'=-\infty}^{\infty} \delta\left(k_u - \bar{k}_u - p'\,\delta k_u - q'\,\delta k_v \cot\alpha\right) \cdot \delta\left(k_v - \bar{k}_v - q'\,\delta k_v\right), \end{aligned} \tag{2.106}$$

where $(\bar{k}_u, \bar{k}_v)$ are the coordinates of the grid centre,[8] and the offset indices p' and q' are related to p and q by

$$p' \triangleq p - \left\lfloor \frac{N_{k_u}}{2} \right\rfloor, \tag{2.107}$$

$$q' \triangleq q - \left\lfloor \frac{N_{k_v}}{2} \right\rfloor. \tag{2.108}$$

Since the grid is periodic, $c(k_u, k_v)$ may also be expressed as a Fourier series. This can be done by first transforming (k_u, k_v) on the right-hand-side of (2.106) into parallelogram coordinates (k_ζ, k_η): using the coordinate transformation shown in Figure 2.21, we obtain the result

$$\begin{aligned} c\left(k_u, k_v\right) &= \sum_{p'=-\infty}^{\infty} \sum_{q'=-\infty}^{\infty} \delta\left(k_\zeta - \bar{k}_u - p'\,\delta k_u + \left(k_\eta \sin\alpha - q'\delta k_v\right)\cot\alpha\right) \cdot \delta\left(k_\eta \sin\alpha - \bar{k}_v - q'\,\delta k_v\right) \\ &= \sum_{p'=-\infty}^{\infty} \sum_{q'=-\infty}^{\infty} \delta\left(k_\zeta - \bar{k}_u - p'\,\delta k_u + \bar{k}_v \cot\alpha\right) \cdot \delta\left(k_\eta \sin\alpha - \bar{k}_v - q'\,\delta k_v\right) \end{aligned} \tag{2.109}$$

where the second line follows from the first since the summand vanishes unless $k_\eta \sin\alpha - q'\delta k_v = \bar{k}_v$. The right-hand-side of (2.109) is separable into the product of two one-dimensional trains of delta-functions along the k_ζ and k_η dimensions with periods of δk_u and δk_v respectively –each of these can be written as a Fourier series, giving the result

$$c\left(k_u, k_v\right) = \frac{1}{\delta k_u} \sum_{p=-\infty}^{\infty} e^{j\frac{2\pi p\left(k_\zeta - \bar{k}_u + \bar{k}_v \cot\alpha\right)}{\delta k_u}} \cdot \frac{1}{\delta k_v} \sum_{q=-\infty}^{\infty} e^{j\frac{2\pi q\left(k_\eta \sin\alpha - \bar{k}_v\right)}{\delta k_v}}, \tag{2.110}$$

whereupon, by using the transformation shown in Figure 2.21 to transform the coordinates (k_ζ, k_η) back to (k_u, k_v), we obtain

$$c\left(k_u, k_v\right) = \frac{1}{\delta k_u\, \delta k_v} \sum_{p=-\infty}^{\infty} \sum_{q=-\infty}^{\infty} e^{j\frac{2\pi p\left(\tilde{k}_u - \tilde{k}_v \cot\alpha\right)}{\delta k_u}} e^{j\frac{2\pi q \tilde{k}_v}{\delta k_v}} \tag{2.111}$$

where

$$\tilde{k}_u = k_u - \bar{k}_u \tag{2.112}$$

$$\tilde{k}_v = k_v - \bar{k}_v. \tag{2.113}$$

Let the projected data in the ground-plane be represented by a two-dimensional function $h(k_u, k_v)$. The support of the projected data lies at an offset $(\bar{k}_u, \bar{k}_v)$ from the origin, and it is convenient to ignore this

[8] In the interests of generality, the quantities $\bar{k}_u$ and $\bar{k}_v$ will simply be referred to here without specifying their values. Of course, when processing data resampled according to the procedure in Section 2.5.2, $\bar{k}_u$ and $\bar{k}_v$ should be set according to (2.96) and (2.97).

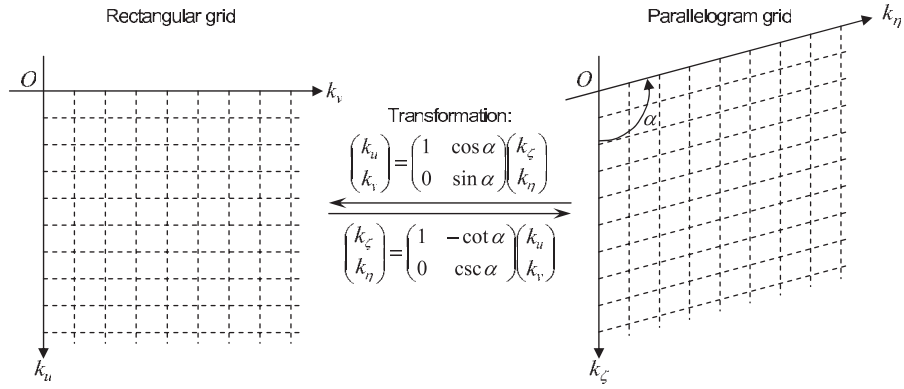

Figure 2.21: Transformations between parallelogram Cartesian coordinates (k_ζ, k_η) and rectangular Cartesian coordinates (k_u, k_v).

offset when processing the data with a Fourier transform. Hence, the resampled data is effectively shifted so that the centre of the parallelogram grid lies at the origin before the Fourier transform is calculated: this has the effect of applying a deterministic phase ramp to the transformed data which is of little practical significance for a given SAR image.[9] Equivalently, we may calculate the Fourier transform with respect to the local offset variables $\tilde{k}_u$ and $\tilde{k}_v$ instead of the original variables k_u and k_v. Hence, if $H(u, v)$ denotes the Fourier transform of a version of $h(k_u, k_v)$ shifted by $-\bar{k}_u$ and $-\bar{k}_v$ along the k_u and k_v axes respectively, being $h_{\text{shift}}(k_u, k_v) = h(k_u + \bar{k}_u, k_v + \bar{k}_v)$, then we can write[10]

$$H(u, v) = \int_{-\infty}^{\infty} \mathrm{d}\tilde{k}_u \int_{-\infty}^{\infty} \mathrm{d}\tilde{k}_v \; e^{-j\left(\tilde{k}_u u + \tilde{k}_v v\right)} \, h(\bar{k}_u + \tilde{k}_u, \bar{k}_v + \tilde{k}_v). \tag{2.114}$$

Let $h_{\text{s}}(k_u, k_v)$ be the result of sampling $h(k_u, k_v)$ on the parallelogram grid:

$$h_{\text{s}}(k_u, k_v) = c(k_u, k_v) \cdot h(k_u, k_v). \tag{2.115}$$

The Fourier transform of the shifted sampled data $h_{\text{s}}(k_u + \bar{k}_u, k_v + \bar{k}_v)$ is then

$$H_{\text{s}}(u, v) = \int_{-\infty}^{\infty} \mathrm{d}\tilde{k}_u \int_{-\infty}^{\infty} \mathrm{d}\tilde{k}_v \; e^{-j(\tilde{k}_u u + \tilde{k}_v v)} \, c(\bar{k}_u + \tilde{k_u}, \bar{k}_v + \tilde{k}_v) \, h(\bar{k}_u + \tilde{k_u}, \bar{k}_v + \tilde{k}_v). \tag{2.116}$$

By substituting (2.106) into (2.116), it is straightforward to obtain

$$H_{\text{s}}(u, v) = \sum_{p'=-\infty}^{\infty} \sum_{q'=-\infty}^{\infty} e^{-j\left(p' \, \delta k_u + q' \, \delta k_v \cot\alpha\right) u} e^{-jq' \, \delta k_v v} h_{p' + \lfloor N_{k_u}/2 \rfloor, q' + \lfloor N_{k_v}/2 \rfloor}, \tag{2.117}$$

where $h_{p,q}$ are the samples of $h(k_u, k_v)$ on the parallelogram grid (recall (2.98), (2.99), (2.107) and (2.108)),

[9] As the phase of the pixels of a complex SAR image is essentially random, such a phase modulation is of little concern when analysing images in isolation. However, if the phases of two or more SAR images are to be compared, e.g. in interferometry, then this phase ramp (which may vary from image to image) should be duly taken into account, e.g. through calculation/estimation and removal.

[10] By definition, the Fourier transform of $h_{\text{shift}}(k_u, k_v)$ is $\int_{-\infty}^{\infty} \mathrm{d}\xi \int_{-\infty}^{\infty} \mathrm{d}\omega \; e^{-j(\xi u + \omega v)} h(\bar{k}_u + \xi, \bar{k}_v + \omega)$ where ξ and ω are just dummy variables of integration. In the term $h(\bar{k}_u + \xi, \bar{k}_v + \omega)$ which appears in the integrand, the variables ξ and ω can be readily interpreted as deviations from $\bar{k}_u$ and $\bar{k}_v$ respectively. From (2.112) and (2.113), a similar interpretation is applicable to $\tilde{k}_u$ and $\tilde{k}_v$: this suggests that we replace ξ and ω in the integrals with $\tilde{k}_u$ and $\tilde{k}_v$ respectively to obtain (2.114).

i.e.

$$h_{p,q} = h\left(k_u(p,q), k_v(q)\right). \tag{2.118}$$

Now, as discussed earlier, we consider $h(k_u, k_v)$ to have finite support, such that the support of the array of data samples $h_{p,q}$ is only over $p = 0, 1, \ldots, N_{k_u} - 1$ and $q = 0, 1, \ldots, N_{k_v} - 1$ (this corresponds to the limiting extents of the previous parallelogram grid). Hence, the nested sums on the right-hand-side of (2.117) will be finite so, by using these finite limits in the summations and making the substitutions (2.107) and (2.108), we readily obtain

$$\begin{aligned} H_{\mathrm{s}}(u,v) = {} & e^{j\left(\left\lfloor \frac{N_{k_u}}{2} \right\rfloor \delta k_u + \left\lfloor \frac{N_{k_v}}{2} \right\rfloor \delta k_v \cot\alpha\right)u} e^{j\left(\left\lfloor \frac{N_{k_v}}{2} \right\rfloor \delta k_v\right)v} \\ & \cdot \sum_{p=0}^{N_{k_u}-1} \sum_{q=0}^{N_{k_v}-1} e^{-j(p\,\delta k_u + q\,\delta k_v \cot\alpha)u} e^{-jq\,\delta k_v v} h_{p,q}. \end{aligned} \tag{2.119}$$

Equation (2.119) is essentially a defining equation for the two-dimensional Discrete Time Fourier Transform (DTFT)[11] on a parallelogram grid (in the rectangular grid limit as the angle $\alpha \to \pi/2$, it is easily verified that it reduces to the familiar two-dimensional DTFT case, albeit with a constant phase term reflecting the choice of grid origin). Although (2.119) is useful in precisely specifying the computation operations, it provides little insight into the properties of the Fourier-transformed result. Hence, let us consider an alternative (but equivalent) representation of $H_{\mathrm{s}}(u,v)$ obtained by substituting (2.111) (instead of (2.106)) into (2.116): the result is

$$\begin{aligned} H_{\mathrm{s}}(u,v) &= \int_{-\infty}^{\infty} \mathrm{d}\tilde{k}_u \int_{-\infty}^{\infty} \mathrm{d}\tilde{k}_v \; e^{-j(\tilde{k}_u u + \tilde{k}_v v)} \left(\frac{1}{\delta k_u\, \delta k_v} \sum_{p=-\infty}^{\infty} \sum_{q=-\infty}^{\infty} e^{j\frac{2\pi p(\tilde{k}_u - \tilde{k}_v \cot\alpha)}{\delta k_u}} e^{j\frac{2\pi q \tilde{k}_v}{\delta k_v}} \right) h(\bar{k}_u + \tilde{k}_u, \bar{k}_v + \tilde{k}_v) \\ &= \frac{1}{\delta k_u\, \delta k_v} \sum_{p=-\infty}^{\infty} \sum_{q=-\infty}^{\infty} \int_{-\infty}^{\infty} \mathrm{d}\tilde{k}_u \int_{-\infty}^{\infty} \mathrm{d}\tilde{k}_v \; e^{-j\tilde{k}_u\left(u - \frac{2\pi}{\delta k_u} p\right)} e^{-j\tilde{k}_v\left(v + \frac{2\pi \cot\alpha}{\delta k_u} p - \frac{2\pi}{\delta k_v} q\right)} h(\bar{k}_u + \tilde{k}_u, \bar{k}_v + \tilde{k}_v). \end{aligned} \tag{2.120}$$

Observe that the double integral above has the same form as the right-hand-side of (2.114): we can thus write the result (2.120) more simply as

$$H_{\mathrm{s}}(u,v) = \frac{1}{\delta k_u\, \delta k_v} \sum_{p=-\infty}^{\infty} \sum_{q=-\infty}^{\infty} \tilde{H}_{p,q}(u,v), \tag{2.121}$$

where

$$\tilde{H}_{p,q}(u,v) = H\left(u - \frac{2\pi}{\delta k_u} p, v + \frac{2\pi}{\delta k_u \tan\alpha} p - \frac{2\pi}{\delta k_v} q\right). \tag{2.122}$$

From these equations, it may be seen that $H_{\mathrm{s}}(u,v)$ consists of repeated versions of the function $\tilde{H}_{p,q}(u,v)$ tiled over the uv-plane (see Figure 2.22). Each version of $\tilde{H}_{p,q}(u,v)$ is simply a shifted copy of the Fourier transform of the signal of interest $H(u,v)$ centred at points in a grid specified by $(u(p), v(p,q)) = (2\pi p/\delta k_u, 2\pi q/\delta k_v - 2\pi p/\delta k_u \tan\alpha)$. These points thus specify the centres of the various tiles, so each tile is of size $2\pi/\delta k_u$-by-$2\pi/\delta k_v$. These results may be directly compared to the results from the familiar two-dimensional DTFT case

[11] "Time" here should not be interpreted literally: its use merely reflects a common convention in the basic theory of Fourier transforms whereby one domain is designated as "time" and the other as "frequency". In the present context, (2.119) actually describes a Fourier transformation from the discrete spatial frequency domain to the continuous spatial position domain.

(see Figure 2.23): the essential difference between the present parallelogram grid case and the more familiar rectangular grid case is that a non-orthogonal sampling grid angle α distorts the usual regular arrangement of the Fourier transform repetitions in the rectangular grid case (Figure 2.23(b)) into an unusual sheared arrangement (Figure 2.22(b)).

Just as in the familiar rectangular grid DTFT case, it is possible to reconstruct the sampled signal if the support of $H(u,v)$ fits within each tile, i.e. in the absence of aliasing. Aliasing can be avoided by employing an anti-aliasing filter, and the raw SAR data is indeed passed through such a filter during the resampling process. This ensures that the support of $H(u,v)$ is well confined within the boundaries of each tile so, as a result, there will be no overlap between the various $\tilde{H}_{p,q}(u,v)$ for $p \neq q$: hence, for the tile centred at the origin, we have $H_{\mathrm{s}}(u,v) = H(u,v)/\delta k_u \delta k_v$ for $|u| < \pi/\delta k_u, |v| < \pi/\delta k_v$. Thus, the desired SAR image $H(u,v)$ can be obtained (to within a constant scaling factor $\delta k_u \delta k_v$) from just the values of $H_{\mathrm{s}}(u,v)$ within the tile centred at the origin.

In modern practice, digital computers are employed for signal processing, so only a discretised version of the desired SAR image (i.e. $H_{\mathrm{s}}(u,v)$ sampled at discrete values of u and v) can be obtained. We now consider the calculation of these discrete samples: to this end, let $H_{\mathrm{s}}(u,v)$ be evenly sampled within the tile centred at the origin at the sampling points (u_k, v_l) where

$$u_k = \frac{k - \lfloor N_u/2 \rfloor}{N_u} \frac{2\pi}{\delta k_u}, \tag{2.123}$$

$$v_l = \frac{l - \lfloor N_v/2 \rfloor}{N_v} \frac{2\pi}{\delta k_v}, \tag{2.124}$$

in which $N_u \geq N_{k_u}$ and $N_v \geq N_{k_v}$ are the number of sample points along the u and v directions respectively, and $k = 0, 1, \ldots, N_u - 1$ and $l = 0, 1, \ldots, N_v - 1$. By substituting u_k and v_l from (2.123) and (2.124) for u and v respectively in (2.119) and regrouping terms, we find that the resulting samples $H_{k,l} \triangleq H_{\mathrm{s}}(u_k, v_l)$ are given by

$$H_{k,l} = A_{k,l} \sum_{q=0}^{N_{k_v}-1} e^{-j\frac{2\pi l q}{N_v}} \cdot e^{-j\frac{2\pi \chi k q}{N_u}} \sum_{p=0}^{N_{k_u}-1} e^{-j\frac{2\pi k p}{N_u}} \tilde{h}_{p,q}, \tag{2.125}$$

where

$$\chi = \frac{\delta k_v}{\delta k_u} \cot \alpha, \tag{2.126}$$

$$A_{k,l} = e^{j2\pi\left(\left\lfloor \frac{N_{k_u}}{2} \right\rfloor + \left\lfloor \frac{N_{k_u}}{2} \right\rfloor \chi\right) \frac{k - \lfloor N_u/2 \rfloor}{N_u}} e^{j2\pi \left\lfloor \frac{N_{k_v}}{2} \right\rfloor \frac{l - \lfloor N_v/2 \rfloor}{N_v}}, \tag{2.127}$$

$$\tilde{h}_{p,q} = e^{j2\pi \frac{\lfloor N_u/2 \rfloor}{N_u} p} \cdot e^{j2\pi\left(\frac{\lfloor N_u/2 \rfloor}{N_u}\chi + \frac{\lfloor N_v/2 \rfloor}{N_v}\right) q} \cdot h_{p,q}. \tag{2.128}$$

From (2.125) to (2.128), we may observe that the SAR image samples $H_{k,l}$ can be efficiently calculated from the spatial frequency domain samples $h_{p,q}$ by

1. applying a suitable two-dimensional phase ramp to obtain $\tilde{h}_{p,q}$ (ref. (2.128)),
2. transforming $\tilde{h}_{p,q}$ with an FFT having p as the input variable and k as the output variable (ref. (2.125)),
3. multiplying the result by a two-dimensional phase ramp $\exp(-j2\pi\chi kq/N_u)$ (ref. (2.125)),
4. transforming the result with an FFT with q as the input variable and l as the output variable (ref. (2.125)), and
5. finally, applying a two-dimensional phase ramp $A_{k,l}$ to the result (ref. (2.127)).

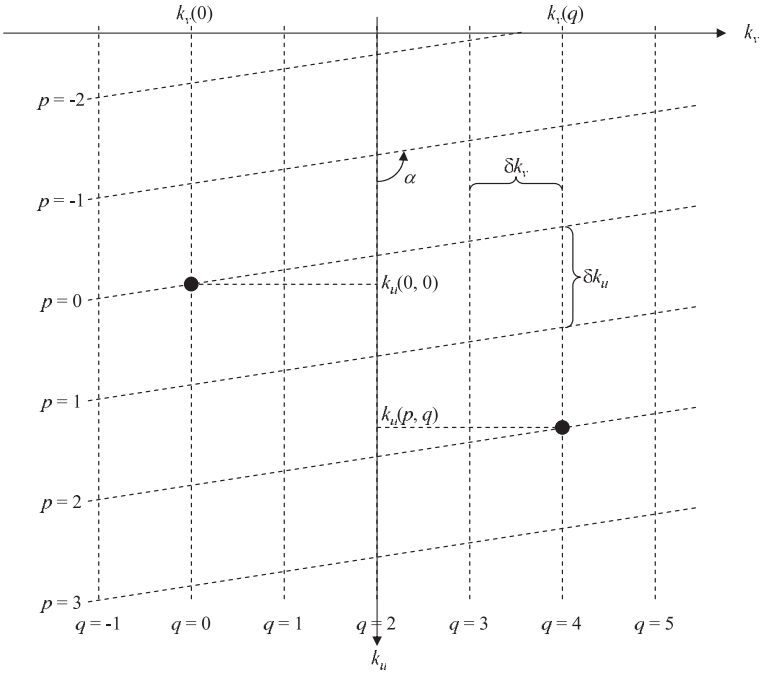

(a) Parallelogram grid on which $h(k_u, k_v)$ is sampled.

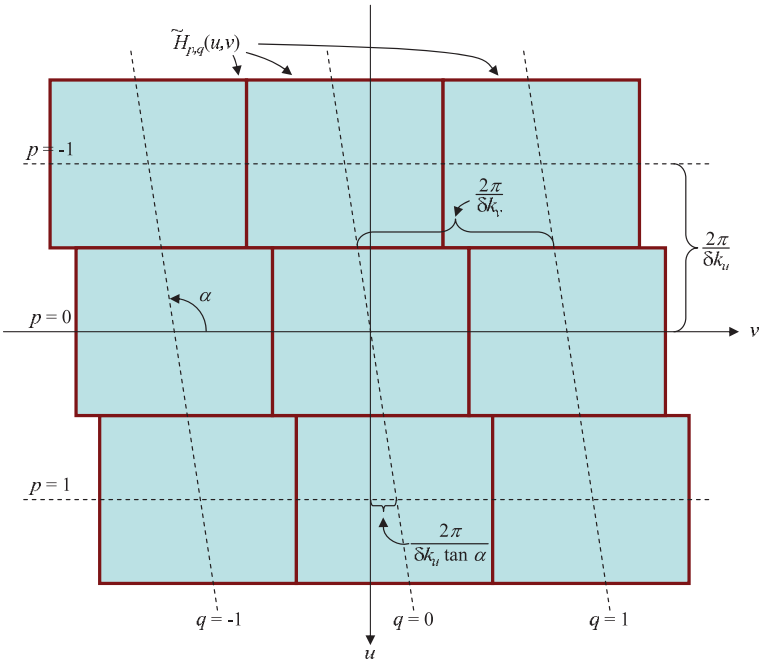

(b) Tiled repetitions of $\tilde{H}_{p,q}(u, v)$ after parallelogram-grid Fourier transform.

Figure 2.22: Fourier transform of function sampled on parallelogram grid.

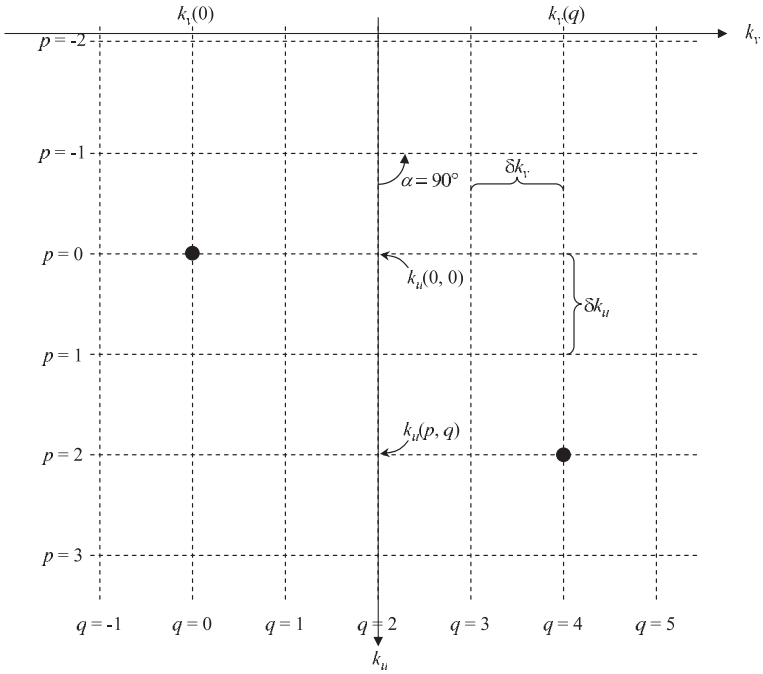

(a) Rectangular grid on which $h(k_u, k_v)$ is sampled.

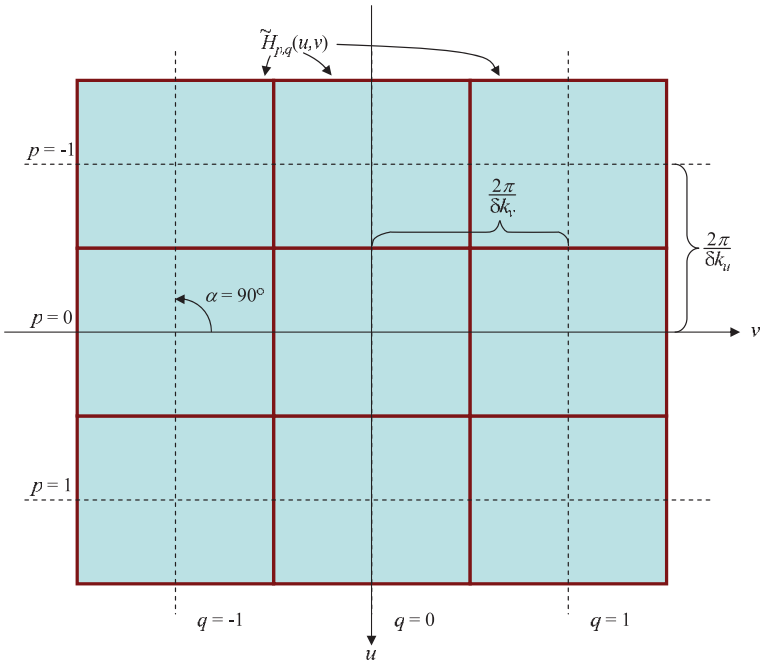

(b) Tiled repetitions of $\tilde{H}_{p,q}(u, v)$ after rectangular-grid Fourier transform.

Figure 2.23: Corresponding case for rectangular grid (cf. Figure 2.22).

In general, for the control of side-lobe levels, the resampled data will be multiplied by a two-dimensional window just prior to the calculation of the discrete Fourier transform as discussed above. Such window weighting should be considered an integral part of the Fourier transform step of the PFA processing used to process the *Ingara* data: even if it is elected not to explicitly apply a window, an implicit rectangular window has already been applied to the data as a result of its finite support.

To summarise, in this and the preceding sub-sections, we have discussed the Polar Format Algorithm (PFA) for processing dechirped-on-receive monostatic and bistatic data sets. The theoretical ideas underlying the PFA were presented in Section 2.5.1: by considering a general signal model encompassing both monostatic and bistatic cases, it was shown how in either case the collected SAR raw echo data could be interpreted as samples of the complex-valued spatial reflectivity function of the imaged scene sampled at points on a radially oriented surface in the spatial frequency domain. This enables a ground-plane SAR image to be efficiently formed by projecting the samples onto the ground-plane, resampling them onto a regular grid, and applying a Fourier transformation. Section 2.5.2 considered this SAR data resampling process: there, the determination of the resampling grid was covered in detail and the iterative use of simple one-dimensional resampling procedures to implement the required two-dimensional polar-to-parallelogram (or -rectangular) resampling was discussed. Finally, in Section 2.5.3, the theory behind a two-dimensional Discrete Fourier Transform of data sampled on a regular parallelogram grid was presented: essentially, the discussion there extended the familiar theory of two-dimensional Fourier transforms along orthogonal axes to the somewhat less familiar case of non-orthogonal axes. Ideally, applying the PFA as discussed above to SAR raw echo data would produce a well-focussed SAR image but, in practice, significant phase errors will not infrequently be present in the data, leading to azimuthal defocussing: a procedure for mitigating the effects of such phase errors is the topic of the next section.

2.6 Autofocus

In practice, the image obtained by Fourier transformation of the resampled data is not uncommonly poorly focussed along the cross-range (v-axis) direction. This is generally attributable to the presence in the data of uncompensated pulse-to-pulse phase errors, mainly arising from unknown platform position measurement errors and drifts in the phase relationship between the local oscillators in the transmitting and receiving elements of the bistatic system.

Mathematically, the aforementioned pulse-to-pulse phase errors may be collectively represented by a one-dimensional function $\psi_{\mathrm{e},n}$ added to the phase $\Psi_n(\tau;\mathbf{R})$ of each elementary signal $s_n(\tau;\mathbf{R})$ (ref. (2.35) and (2.36)): all the samples in each pulse are thus subject to the same value of the phase error $\psi_{\mathrm{e},n}$. Since the data samples in each pulse lie along radial lines in the polar grid, resampling to the parallelogram grid causes the one-dimensional phase error to assume a two-dimensional form $\psi_{\mathrm{e}}(k_u, k_v)$ in the resampled data [122]. For narrow relative bandwidths and short coherent processing intervals, however, the polar and parallelogram grids will be very similar, so only a weak dependence on k_u is introduced by the resampling process. Thus, the two-dimensional resampled phase error is frequently approximated by a one-dimensional function $\theta_{\mathrm{e}}(k_v) = \psi_{\mathrm{e}}(\bar{k}_u, k_v)$, where $\bar{k}_u$ is the centre of the span of k_u values in the grid (see (2.96)).

Methods for correcting one-dimensional phase errors of the form $\theta_{\mathrm{e}}(k_v)$ are well-established in the literature: these are generally termed *autofocus* methods as they seek to correct the phase-error-induced defocussing automatically. In PFA-based SAR processing, autofocus methods are interposed between the resampling and the Fourier transformation stages, but they are not strictly considered to be a part of the PFA itself. Broadly,

autofocus methods may be grouped into the categories of parametric and non-parametric approaches. The former involves a postulated form for the phase error function, generally taking the form of a low-order polynomial in k_v. Consequently, these are suited only to low-frequency phase errors. The latter group of approaches seek to estimate the phase error function without postulating a specific model: hence, they are more general in their applicability. An important example of the non-parametric approaches is the Phase Gradient Autofocus (PGA) algorithm: this is well covered in two major reference works on spotlight-mode SAR [39, 44]. The discussion of the PGA in these sources is focussed on monostatic SAR and thus implicitly assumes a rectangular sampling grid, but, as will be shortly demonstrated, the PGA may be applied to the parallelogram grid-sampled data without modification.

We now present a brief discussion illustrating the conceptual basis of the PGA. To begin, recall that, from (2.61), the elementary signal $s_n(\tau; \mathbf{R})$ for an isolated point scatterer for which $|\mathbf{R}|$ is small may be represented by a plane wave: upon projection into the ground-plane and introducing the phase error model $\theta_{\mathrm{e}}(k_v)$, the resultant signal may be written as

$$s(k_u, k_v; \mathbf{R}) = \iota(k_u, k_v; \mathbf{R})\, e^{j(k_u u_{\mathrm{p}} + k_v v_{\mathrm{p}})}\, e^{j\theta_{\mathrm{e}}(k_v)}, \tag{2.129}$$

where $\iota(k_u, k_v; \mathbf{R})$ is the projected indicator function, which takes unity value within the projected support of the signal, and $(u_{\mathrm{p}}, v_{\mathrm{p}})$ is the projected position of the elementary scattering centre (ref. (2.170) and (2.171)). As discussed in Section 2.5.2, this signal is resampled onto a parallelogram grid before processing with FFTs: by employing (2.98) and (2.99), we obtain the values of the samples on the parallelogram grid for index values $p = 0, 1, \ldots, N_{k_u} - 1$ and $q = 0, 1, \ldots, N_{k_v} - 1$ as

$$\begin{aligned} s_{p,q} &\triangleq s(k_u(p,q), k_v(q); \mathbf{R}) \\ &= A\, \iota_{p,q}\, e^{j(p\, C_1 + q\, C_2 + \phi_{\mathrm{e}}(q))}, \end{aligned} \tag{2.130}$$

in which

$$C_1 = \delta k_u u_{\mathrm{p}}, \tag{2.131}$$

$$C_2 = \delta k_v \left(u_{\mathrm{p}} \cot\alpha + v_{\mathrm{p}}\right), \tag{2.132}$$

and

$$A = e^{j\left(\bar{k}_u u_{\mathrm{p}} + \bar{k}_v v_{\mathrm{p}}\right)}\, e^{-j\left(\left\lfloor \frac{N_{k_u}}{2} \right\rfloor C_1 + \left\lfloor \frac{N_{k_v}}{2} \right\rfloor C_2\right)} \tag{2.133}$$

$$\iota_{p,q} = \iota(k_u(p,q), k_v(q); \mathbf{R}), \tag{2.134}$$

$$\phi_{\mathrm{e}}(q) = \theta_{\mathrm{e}}(k_v(q)). \tag{2.135}$$

Now let us consider the result of directly applying to these data samples successive one-dimensional Discrete Fourier transforms (DFTs) along each indexed dimension. Although such Fourier transforms could indeed be used to produce a SAR image from this data if the k_u and k_v axes were orthogonal, in the present case, as no account is being taken of the parallelogram (not necessarily rectangular) shape of the sampling grid, the result will be a geometrically distorted representation of the scene reflectivity, which may not be easily interpretable visually as a SAR image, but is nevertheless well-suited to the requirements of SAR autofocus algorithms. A DFT with p as the index of summation (corresponding to a transformation along the k_ζ direction shown in Figure 2.21) achieves range-compression of the data. By definition, an M-point DFT on $s_{p,q}$, where we allow

$M \geq N_{k_u}$ to accommodate cases where it might be desired to zero-pad the data to interpolate the signal in the transform domain, is given by

$$\bar{s}_{k,q} = \sum_{p=0}^{N_{k_u}-1} e^{-j\frac{2\pi kp}{M}} s_{p,q} \tag{2.136}$$

for $k = 0, 1, \ldots, M-1$. By substituting in (2.130) and regrouping terms, this may be rewritten as

$$\bar{s}_{k,q} = A\,\kappa_{k,q}\, e^{j(qC_2+\phi_{\mathrm{e}}(q))}, \tag{2.137}$$

where $\kappa_{k,q}$ is a convolution along the range-dimension of the DFTs (also along the range-dimension) of $\iota_{p,q}$ and e^{jpC_1},[12] viz.

$$\kappa_{k,q} = \frac{1}{M}\sum_{k'=0}^{M-1} \bar{\iota}_{k-k',q}\, D_{N_{k_u}}\left(\frac{k'}{M} - \frac{C_1}{2\pi}\right), \tag{2.138}$$

in which $\bar{\iota}_{k,q}$ is the DFT of $\iota_{p,q}$, viz.

$$\bar{\iota}_{k,q} = \sum_{p=0}^{N_{k_u}-1} e^{-j\frac{2\pi kp}{M}} \iota_{p,q}, \tag{2.139}$$

and $D_{N_{k_u}}(k/M - C_1/2\pi)$ is the DFT of e^{jpC_1}, where the function $D_N(x)$ is a Dirichlet kernel-like function defined by

$$D_N(x) \triangleq \sum_{n=0}^{N-1} e^{-j2\pi nx} = e^{-j\pi(N-1)x}\,\frac{\sin(\pi N x)}{\sin(\pi x)}. \tag{2.140}$$

Hence, from (2.138) and (2.131), we see that the scatterer's energy in the range-dimension has been gathered around u_{p} with a point spread function (PSF) width (resolution) determined by the indicator function: this is precisely the familiar result from applying a range-compression operation.

Similarly, a discrete Fourier transform with q as the index of summation (corresponding to a transformation along the oblique k_η direction shown in Figure 2.21) achieves azimuth-compression of the data: an N-point DFT of $\bar{s}_{k,q}$, where we similarly allow $N \geq N_{k_v}$ to accommodate cases where zero-padding is desired, is

$$\begin{aligned}\hat{s}_{k,l} &= \sum_{q=0}^{N_{k_v}-1} e^{-j\frac{2\pi lq}{N}} \bar{s}_{k,q} \\ &= A\sum_{q=0}^{N_{k_v}-1} e^{-j\frac{2\pi lq}{N}} \kappa_{k,q} e^{jqC_2} e^{j\phi_{\mathrm{e}}(q)}.\end{aligned} \tag{2.141}$$

This may be written as a double convolution between the DFTs of $\kappa_{k,q}$, e^{jqC_2} and $e^{j\phi_{\mathrm{e}}(q)}$, viz.

$$\hat{s}_{k,l} = \frac{A}{N^2}\sum_{l'=0}^{N-1} \hat{\kappa}_{k,l'} \sum_{l''=0}^{N-1} \epsilon_{l''} D_{N_{k_v}}\left(\frac{l-l'-l''}{N} - \frac{C_2}{2\pi}\right), \tag{2.142}$$

[12] If x_p and y_p are two length-N sequences, so that $X_k = \sum_{p=0}^{N-1} e^{-j2\pi kp/M} x_p$ and $Y_k = \sum_{p=0}^{N-1} e^{-j2\pi kp/M} y_p$ are their M-point DFTs (allowing $M \geq N$ for potential zero-padding), then, via inverse DFTs, we have $x_p = \frac{1}{M}\sum_{k=0}^{M-1} e^{j2\pi kp/M} X_k$ and $y_p = \frac{1}{M}\sum_{k=0}^{M-1} e^{j2\pi kp/M} Y_k$. The M-point DFT of the product $x_p y_p$ is then $\sum_{p=0}^{N-1} e^{-j2\pi kp/M} x_p y_p = \sum_{p=0}^{N-1} e^{-j2\pi kp/M} x_p \frac{1}{M}\sum_{k'=0}^{M-1} e^{j2\pi k'p/M} Y_{k'} = \frac{1}{M}\sum_{k'=0}^{M-1} Y'_k \sum_{p=0}^{N-1} e^{-j2\pi(k-k')p/M} x_p = \frac{1}{M}\sum_{k'=0}^{M-1} X_{k-k'} Y_{k'}$ which is a convolution of X_k and Y_k.

where

$$\hat{\kappa}_{k,l} = \sum_{q=0}^{N_{k_v}-1} e^{-j\frac{2\pi lq}{N}} \kappa_{k,q}, \tag{2.143}$$

$$\epsilon_l = \sum_{q=0}^{N_{k_v}-1} e^{-j\frac{2\pi lq}{N}} e^{j\phi_{\mathrm{e}}(q)} \tag{2.144}$$

are the DFTs of $\kappa_{k,q}$ and $e^{j\phi_{\mathrm{e}}(q)}$ respectively, and $D_{N_{k_v}}(l/N - C_2/2\pi)$ is the DFT of e^{jqC_2}. The right-hand-side of (2.142) is a double convolution of three signals which can be usefully interpreted in the following order. First, a Dirichlet kernel centred at the scatterer's azimuthal position v_{p} is convolved with the azimuth-Fourier-transformed indicator function $\hat{\kappa}_{k,l}$, producing a signal in which the scatterer's energy in the azimuth dimension is gathered around v_p with a width (resolution) determined by the indicator function: this is precisely the desired result from azimuth compression. Second, this azimuth-compressed signal from the first convolution is convolved with the signal ϵ_l, being the Fourier transform of the phase error function $e^{j\phi_{\mathrm{e}}(q)}$, so the effect of this second convolution is to smear out the energy which was previously concentrated around v_p by an amount corresponding to the width of the defocussing kernel ϵ_l: this is the mechanism by which the phase errors $\phi_{\mathrm{e}}(q)$ cause azimuthal-defocussing. Observe that the defocussing is one-dimensional and confined to only one of the two indexed dimensions (i.e. the one indexed by l): this conforms perfectly to the assumption made by autofocus algorithms and permits their direct application to the data array $\hat{s}_{k,l}$ without modification.

The PGA essentially seeks to estimate the one-dimensional phase error $\phi_{\mathrm{e}}(q)$ by isolating the defocussing kernel ϵ_l: it achieves this by centre-shifting and windowing the data in the azimuth direction. The centre-shifting operation involves shifting $\hat{s}_{k,l}$ in azimuth so that the centre of the Dirichlet kernel lies at the origin of the index-coordinate l: the result is

$$\begin{aligned} \tilde{s}_{k,l} &= \hat{s}_{k,l+C_2N/2\pi} \\ &= \frac{A}{N^2} \sum_{l'=0}^{N-1} \hat{\kappa}_{k,l'} \sum_{l''=0}^{N-1} \epsilon_{l''} D_{N_{k_v}} \left(\frac{l - l' - l''}{N} \right). \end{aligned} \tag{2.145}$$

Windowing involves applying a window w_l of finite-width to the centre-shifted signal $\tilde{s}_{k,l}$: this gives the result

$$\check{s}_{k,l} = \tilde{s}_{k,l} w_l. \tag{2.146}$$

The width of the window w_l is chosen to be sufficiently wide as to cover the support of the defocussing kernel ϵ_l, but sufficiently narrow as to adequately reject energy from other clutter. Applying an inverse DFT to transform the windowed signal $\check{s}_{k,l}$ back to the q-indexed domain and invoking the convolution theorem[13]

[13] The inverse DFT (transforming from the l- to q-indexed domains) of $\check{s}_{k,l} = A \cdot w_l \times \hat{\kappa}_{k,l} \star \epsilon_l \star D_{N_{k_v}}(l/N)$ (ref. (2.145) and (2.146)) is $g_{k,q} = A \cdot W_q \star \kappa_{k,q} \times e^{j\phi_{\mathrm{e}}(q)} \times 1$ where $\times$ and $\star$ denote multiplication and convolution respectively and W_q, $\kappa_{k,q}$, $e^{j\phi_{\mathrm{e}}(q)}$ and 1 are the respective inverse DFTs of w_l, $\hat{\kappa}_{k,l}$, ϵ_l and $D_{N_{k_v}}(l/N)$ (ref. (2.140), (2.143), (2.144), (2.148)).

produces

$$\begin{aligned} g_{k,q} &= \frac{1}{N}\sum_{l=0}^{N-1} e^{j\frac{2\pi lq}{N}}\check{s}_{k,l} \\ &= A\sum_{q'=0}^{N_{k_v}-1} W_{q'}\kappa_{k,q-q'}e^{j\phi_{\mathrm{e}}(q-q')}, \end{aligned} \tag{2.147}$$

where

$$W_q = \frac{1}{N}\sum_{l=0}^{N-1} e^{j\frac{2\pi lq}{N}} w_l. \tag{2.148}$$

As w_l is sufficiently wide to cover the bandwidth of $e^{j\phi_{\mathrm{e}}(q)}$, the transformed window W_q will be relatively narrow, so, to a good approximation, we have,

$$g_{k,q} \approx A\,\kappa_{k,q}\,e^{j\phi_{\mathrm{e}}(q)}. \tag{2.149}$$

Observe that, for $q = 1, 2, \ldots, N-1$,

$$\begin{aligned} \widehat{\Delta\phi_{\mathrm{e}}}(q) &\triangleq \arg\sum_{k=0}^{M-1} g^*_{k,q-1}g_{k,q} \\ &\approx \phi_{\mathrm{e}}(q) - \phi_{\mathrm{e}}(q-1), \end{aligned} \tag{2.150}$$

since the phase of $\kappa_{k,q}$ is slowly varying with q. As discussed by Jakowatz et al. [39], $\widehat{\Delta\phi_{\mathrm{e}}}(q)$ is actually the maximum-likelihood estimate of the phase difference $\Delta\phi_{\mathrm{e}}(q) = \phi_{\mathrm{e}}(q) - \phi_{\mathrm{e}}(q-1)$. Thus, $\phi_{\mathrm{e}}(q)$ can be estimated to within an additive constant by the estimator

$$\hat{\phi}_{\mathrm{e}}(q) = \sum_{q'=1}^{q} \widehat{\Delta\phi_{\mathrm{e}}}(q'). \tag{2.151}$$

In addition to the PGA method discussed above, other autofocus methods for estimating and correcting the phase error function $\phi_{\mathrm{e}}(q)$ also exist [39, 44].

The above illustrates the essential concepts underlying the implementation of the PGA used to process the *Ingara* data. The PGA as implemented in practice follows the outline above with some minor differences. One is that, as it is not known a priori where the centre of the Dirichlet kernel in azimuth for a defocussed target is, the centre-shifting operation which is implemented shifts each row (indexed by k) of the data $\hat{s}_{k,l}$ along the column index l to bring the sample with the highest energy into the $l = 0$ azimuth column. Also, as accurate centre-shifting of a defocussed target is difficult to achieve in practice, the major PGA steps of centre-shifting, windowing, applying the inverse DFT and phase error estimation are iterated to converge on the correct centre-shift and target isolation: this is done by applying the phase error estimate at each iteration to the range-compressed data $\bar{s}_{k,q}$ to give the phase-corrected range-compressed data

$$\bar{s}'_{k,q} = \bar{s}_{k,q}e^{-j\hat{\phi}_{\mathrm{e}}(q)} \tag{2.152}$$

and using $\bar{s}'_{k,q}$ as input to the next iteration.

The basis of the above discussion has been a consideration of the elementary signal from just a single

scatterer but, in practice, signals from multiple scatterers will be present in the SAR data. Nevertheless, the PGA as discussed above will still be applicable to the multiple scatterer case if we assume that the scene return is dominated by a number of relatively strong discrete targets which are well separated in range and azimuth. This assumption is not uncommonly met in real SAR imagery (e.g. multiple lamp-posts lining roads), especially when radar targets (e.g. corner reflectors) have been deliberately deployed in the scene. Under this assumption, the contributions to the range- and azimuth-compressed signal $\hat{s}_{k,l}$ from the various targets can be separated to a large degree: the centre-shifting operation picks out and shifts to the $l = 0$ position the strongest target at a given range (k index) and the windowing operation suppresses (filters out) the signals from any other targets at this range. Moreover, the presence of multiple targets at different ranges effectively produces multiple observations of the defocussing kernel and these are employed in the summation over k in (2.150) which combines the information in the defocussed azimuth profiles from multiple scatterers at different ranges to calculate the estimator $\widehat{\Delta\phi_{\mathrm{e}}}(q)$: generally, such pooling of the signals from multiple targets is likely to produce a result superior to that from using a single target alone.

2.7 Image model

SAR image formation via the PFA has previously been discussed in Section 2.5: in this section, we develop a model for the image so obtained.

To begin, observe that the vector $\mathbf{K}_n(\tau)$ of (2.48) is function of the intra-pulse time τ and the pulse index n. For most practical SAR collection scenarios, this function is invertible, i.e. it is possible to determine values τ' and n' corresponding to an arbitrary vector $\mathbf{K}$ which lies on the data collection surface, such that $\mathbf{K}_{n'}(\tau') = \mathbf{K}$. Hence, we may rewrite the pre-processed dechirped signal $\chi_n(\tau)$, representing the total return from a scene (ref. (2.37)), and the elementary signal $s_n(\tau; \mathbf{R})$, which represents the signal from a point scatterer (ref. (2.35)), to explicitly display their dependence on the vector $\mathbf{K} = \mathbf{K}_n(\tau)$: the respective results are

$$\chi(\mathbf{K}) = \iiint_{\mathcal{V}} \mathrm{d}\mathbf{R}\; g(\mathbf{R})\, s(\mathbf{K}; \mathbf{R}) \tag{2.153}$$

and

$$s(\mathbf{K}; \mathbf{R}) = \mathcal{I}(\mathbf{K}; \mathbf{R}) e^{j\Psi(\mathbf{K};\mathbf{R})}, \tag{2.154}$$

where $\Psi(\mathbf{K}; \mathbf{R})$ is simply the earlier phase function $\Psi_n(\tau; \mathbf{R})$ and $\mathcal{I}(\mathbf{K}; \mathbf{R})$ is an indicator function which indicates the support of the signal, i.e. it vanishes unless $\mathbf{K}$ lies on the data collection surface, whereupon it takes the value of the earlier indicator function $\mathbb{I}_n(\tau + U_n(\mathbf{R}); \mathbf{R})$.

Now, in the ideal case, the collection surface for a coherent processing interval is effectively planar and defines the slant plane. Hence, the vectors $\mathbf{K}$ will have the form

$$\mathbf{K} = k_u\, \mathbf{a}_u + k_v\, \mathbf{a}_v + (k_u \tan\psi + k_v \tan\eta)\, \mathbf{a}_w, \tag{2.155}$$

where ψ and η are angles specifying the slopes of the slant plane relative to the k_u and k_v axes respectively (see Figure 2.24), $\mathbf{a}_u$ and $\mathbf{a}_v$ are unit vectors along the k_u and k_v directions (ref. (2.66)) and $\mathbf{a}_w = \mathbf{a}_u \times \mathbf{a}_v$. Hence, after projection into the ground plane and resampling onto the parallelogram grid, the signals $\chi(\mathbf{K})$ and $s(\mathbf{K}; \mathbf{R})$ assume the respective forms

$$\omega(\mathbf{k}) = \iiint_{\mathcal{V}} \mathrm{d}\mathbf{R}\; g(\mathbf{R})\, h(\mathbf{k}; \mathbf{R}) \tag{2.156}$$

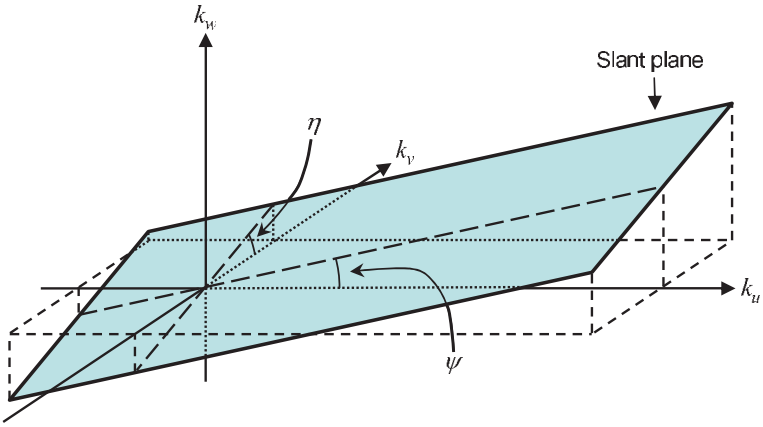

Figure 2.24: Orientation of slant plane and the angles ψ and η.

and

$$h(\mathbf{k};\mathbf{R}) = \iota(\mathbf{k};\mathbf{R})e^{j\phi(\mathbf{k};\mathbf{R})}, \tag{2.157}$$

where $\mathbf{k} \triangleq k_u\,\mathbf{a}_u + k_v\,\mathbf{a}_v$ is the projection of $\mathbf{K}$ onto the ground-plane, $\phi(\mathbf{k};\mathbf{R}) = \Psi(\mathbf{K};\mathbf{R})$, and $\iota(\mathbf{k};\mathbf{R})$ is an indicator function which indicates the support of the projected *and* resampled signal, i.e. it is zero unless $\mathbf{k}$ lies within the extents of the resampled parallelogram grid, whereupon it is simply the value of $\mathbb{I}_n(\tau + U_n(\mathbf{R});\mathbf{R})$ as before.

As discussed in Section 2.5.3, the image is formed by a Fourier transform centred at the point $\bar{\mathbf{k}} = \bar{k}_u\,\mathbf{a}_u + \bar{k}_v\,\mathbf{a}_v$: hence, if $\tilde{\mathbf{k}} = \tilde{k}_u\,\mathbf{a}_u + \tilde{k}_v\,\mathbf{a}_v$ represents the local offsets from the grid centre $\bar{\mathbf{k}}$, i.e.

$$\tilde{\mathbf{k}} = \mathbf{k} - \bar{\mathbf{k}}, \tag{2.158}$$

then a model for the image will be

$$\begin{aligned}\Omega(\mathbf{r}') &= \iint_{\mathbb{R}^2} \mathrm{d}\tilde{\mathbf{k}}\, e^{-j\tilde{\mathbf{k}}\cdot\mathbf{r}'}\,\omega(\bar{\mathbf{k}} + \tilde{\mathbf{k}}) \\ &= \iiint_{\mathcal{V}} \mathrm{d}\mathbf{R}\; g(\mathbf{R})\, H(\mathbf{r}';\mathbf{R}),\end{aligned} \tag{2.159}$$

in which

$$\begin{aligned}H(\mathbf{r}';\mathbf{R}) &= \iint_{\mathbb{R}^2} \mathrm{d}\tilde{\mathbf{k}}\, e^{-j\tilde{\mathbf{k}}\cdot\mathbf{r}'}\, h(\bar{\mathbf{k}} + \tilde{\mathbf{k}};\mathbf{R}) \\ &= e^{j\phi(\bar{\mathbf{k}};\mathbf{R})} \iint_{\mathbb{R}^2} \mathrm{d}\tilde{\mathbf{k}}\, e^{-j\tilde{\mathbf{k}}\cdot\mathbf{r}'}\,\kappa(\tilde{\mathbf{k}};\bar{\mathbf{k}},\mathbf{R}) e^{j\tilde{\phi}(\tilde{\mathbf{k}};\bar{\mathbf{k}},\mathbf{R})},\end{aligned} \tag{2.160}$$

where

$$\kappa(\tilde{\mathbf{k}};\bar{\mathbf{k}},\mathbf{R}) = \iota(\bar{\mathbf{k}} + \tilde{\mathbf{k}};\mathbf{R}), \tag{2.161}$$

$$\tilde{\phi}(\tilde{\mathbf{k}};\bar{\mathbf{k}},\mathbf{R}) = \phi(\bar{\mathbf{k}} + \tilde{\mathbf{k}};\mathbf{R}) - \phi(\bar{\mathbf{k}};\mathbf{R}). \tag{2.162}$$

From (2.159), we see that the SAR image $\Omega(\mathbf{r}')$ may be interpreted as the superposition of the responses from each elementary scatterer in the scene: each response consists of the product of the scatterer's reflectivity

$\mathrm{d}\mathbf{R}\, g(\mathbf{R})$ and the function $H(\mathbf{r}';\mathbf{R})$. As the $\mathrm{d}\mathbf{R}\, g(\mathbf{R})$ term is dependent on the physical properties of the scattering centre while the $H(\mathbf{r}';\mathbf{R})$ term is dependent on its geometric position, these two types of information which characterise the scatterer are conveyed separately by these two terms. Hence, by analysing the properties of $H(\mathbf{r}';\mathbf{R})$ alone, we can study the general, scatterer-independent properties of the SAR image.

By applying the convolution theorem to the integral on the right-hand-side of (2.160), we obtain

$$H(\mathbf{r}';\mathbf{R}) = \frac{e^{j\phi(\bar{\mathbf{k}};\mathbf{R})}}{(2\pi)^2} \iint_{\mathbb{R}^2} \mathrm{d}\mathbf{r}''\, \hat{\kappa}(\mathbf{r}'';\bar{\mathbf{k}},\mathbf{R}) \iint_{\mathbb{R}^2} \mathrm{d}\tilde{\mathbf{k}}\, e^{-j\tilde{\mathbf{k}}\cdot\left(\mathbf{r}'-\mathbf{r}''\right)} e^{j\tilde{\phi}(\tilde{\mathbf{k}};\bar{\mathbf{k}},\mathbf{R})}, \tag{2.163}$$

where $\hat{\kappa}(\mathbf{r}';\bar{\mathbf{k}},\mathbf{R})$ is the Fourier transform of $\kappa(\tilde{\mathbf{k}};\bar{\mathbf{k}},\mathbf{R})$, i.e.

$$\hat{\kappa}(\mathbf{r}';\bar{\mathbf{k}},\mathbf{R}) = \iint_{\mathbb{R}^2} \mathrm{d}\tilde{\mathbf{k}}\, e^{-j\tilde{\mathbf{k}}\cdot\mathbf{r}'}\ \kappa(\tilde{\mathbf{k}};\bar{\mathbf{k}},\mathbf{R}), \tag{2.164}$$

and the innermost integral represents the Fourier transform of $e^{j\tilde{\phi}(\tilde{\mathbf{k}};\bar{\mathbf{k}},\mathbf{R})}$. Now, by expressing the phase function $\tilde{\phi}(\tilde{\mathbf{k}};\bar{\mathbf{k}},\mathbf{R})$ in terms of the earlier phase functions $\phi(\mathbf{k};\mathbf{R}) = \Psi(\mathbf{K};\mathbf{R})$ and substituting in the previously calculated series expansion of (2.46), we obtain

$$\begin{aligned}\tilde{\phi}(\tilde{\mathbf{k}};\bar{\mathbf{k}},\mathbf{R}) &= \Psi(\bar{\mathbf{K}}+\tilde{\mathbf{K}};\mathbf{R}) - \Psi(\bar{\mathbf{K}};\mathbf{R}) \\ &= \tilde{\mathbf{K}}\cdot\mathbf{R} + \ldots,\end{aligned} \tag{2.165}$$

where $\tilde{\mathbf{k}}$ and $\bar{\mathbf{k}}$ have been projected back up to the slant plane as per (2.155) to give

$$\bar{\mathbf{K}} = \bar{k}_u\, \mathbf{a}_u + \bar{k}_v\, \mathbf{a}_v + \left(\bar{k}_u \tan\psi + \bar{k}_v \tan\eta\right)\, \mathbf{a}_w, \tag{2.166}$$

$$\tilde{\mathbf{K}} = \tilde{k}_u\, \mathbf{a}_u + \tilde{k}_v\, \mathbf{a}_v + \left(\tilde{k}_u \tan\psi + \tilde{k}_v \tan\eta\right)\, \mathbf{a}_w. \tag{2.167}$$

Hence, if $\mathbf{R}$ is specified in terms of its coordinates by

$$\mathbf{R} = u_0\, \mathbf{a}_u + v_0\, \mathbf{a}_v + w_0\, \mathbf{a}_w, \tag{2.168}$$

then (2.165) yields

$$\tilde{\phi}(\tilde{\mathbf{k}};\bar{\mathbf{k}},\mathbf{R}) = \tilde{\mathbf{k}}\cdot\mathbf{r} + \ldots, \tag{2.169}$$

in which $\mathbf{r}$ is the projected position of the scatterer in the image, and is given by $\mathbf{r} = u_\mathrm{p}\, \mathbf{a}_u + v_\mathrm{p}\, \mathbf{a}_v$, where

$$u_\mathrm{p} = u_0 + w_0 \tan\psi \tag{2.170}$$

$$v_\mathrm{p} = v_0 + w_0 \tan\eta \tag{2.171}$$

are the image coordinates. Observe that the scatterer's height w_0 causes the position of the scatterer in the image to be displaced by $w_0(\tan\psi\, \mathbf{a}_u + \tan\eta\, \mathbf{a}_v)$ from the direct orthogonal projection of $\mathbf{R}$ onto the ground-plane $u_0\, \mathbf{a}_u + v_0\, \mathbf{a}_v$: this effect is termed *layover*. By employing (2.169), we may evaluate the integral

$$\begin{aligned}\iint_{\mathbb{R}^2} \mathrm{d}\tilde{\mathbf{k}}\, e^{-j\tilde{\mathbf{k}}\cdot\left(\mathbf{r}'-\mathbf{r}''\right)} e^{j\tilde{\phi}(\tilde{\mathbf{k}};\bar{\mathbf{k}},\mathbf{R})} &= \iint_{\mathbb{R}^2} \mathrm{d}\tilde{\mathbf{k}}\, e^{-j\tilde{\mathbf{k}}\cdot\left(\mathbf{r}'-\mathbf{r}''-\mathbf{r}\right)} \\ &= (2\pi)^2 \delta(\mathbf{r}'-\mathbf{r}''-\mathbf{r})\end{aligned} \tag{2.172}$$

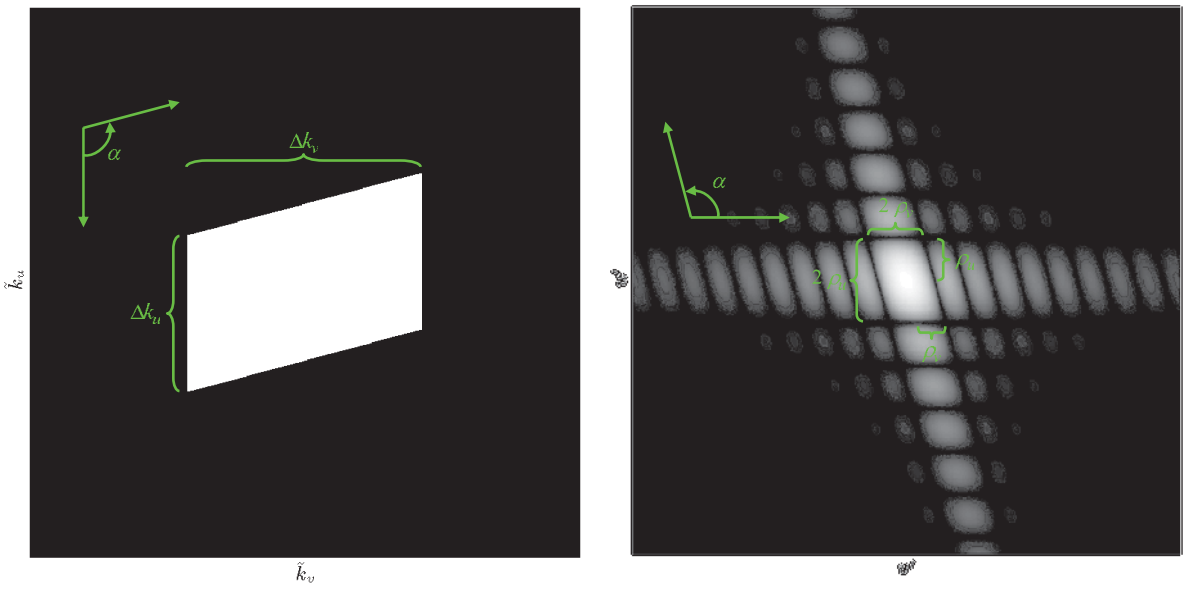

(a) $\kappa(\tilde{\mathbf{k}};\bar{\mathbf{k}},\mathbf{R})$ (b) $\log\left(\left|\hat{\kappa}(\mathbf{r}'-\mathbf{r};\bar{\mathbf{k}},\mathbf{R})\right|^2\right)$

Figure 2.25: Illustrative shapes of (a) indicator function and (b) point-spread function, as given by (2.174) and (2.175).

whereupon, by substituting the above into (2.163), we obtain the result

$$H(\mathbf{r}';\mathbf{R}) = e^{j\phi(\bar{\mathbf{k}};\mathbf{R})}\hat{\kappa}(\mathbf{r}'-\mathbf{r};\bar{\mathbf{k}},\mathbf{R}). \tag{2.173}$$

The function $H(\mathbf{r}';\mathbf{R})$ may be regarded as the image of a generic elementary scattering centre at position $\mathbf{R}$: it consists of two major components. The first is a constant phase term $\phi(\bar{\mathbf{k}};\mathbf{R})$ which depends on the three-dimensional scatterer position $\mathbf{R}$ and the centre of the parallelogram grid: as will be discussed in Chapter 3, this term can be exploited via interferometric techniques to recover the height w_0 of the scattering centre. The second component is the function $\hat{\kappa}(\mathbf{r}'-\mathbf{r};\bar{\mathbf{k}},\mathbf{R})$, which represents a spatially varying point spread function (this spatial variance is a result of the coupling between $\mathbf{K}$ and $\mathbf{R}$ imposed by the indicator functions $\mathcal{I}(\mathbf{K};\mathbf{R})$, $\iota(\mathbf{k};\mathbf{R})$ and $\kappa(\tilde{\mathbf{k}};\bar{\mathbf{k}},\mathbf{R})$, which, as previously discussed in Section 2.5.1, is ultimately a consequence of the relatively short duration of the dechirping signal). For scatterers at positions such that $U_n(\mathbf{R})$ and $E_{\mathrm{d},n}$ are effectively equal, the projected indicator function $\kappa(\tilde{\mathbf{k}};\bar{\mathbf{k}},\mathbf{R})$ will fill the entire parallelogram grid and the spatial dependence on $\mathbf{R}$ will be suppressed: we will then have

$$\kappa(\tilde{\mathbf{k}};\bar{\mathbf{k}},\mathbf{R}) = \mathrm{rect}\left(\frac{k_u-\bar{k}_u-(k_v-\bar{k}_v)\cot\alpha}{\Delta k_u}\right)\mathrm{rect}\left(\frac{k_v-\bar{k}_v}{\Delta k_v}\right), \tag{2.174}$$

whereupon the PSF will be

$$\hat{\kappa}(\mathbf{r}'-\mathbf{r};\bar{\mathbf{k}},\mathbf{R}) = \Delta k_u \Delta k_v\ \mathrm{sinc}\left(\frac{\Delta k_u}{2\pi}u'\right)\mathrm{sinc}\left(\frac{\Delta k_v}{2\pi}\left(u'\cot\alpha+v'\right)\right). \tag{2.175}$$

An example of the shapes of this indicator function and the corresponding PSF is shown in Figures 2.25: observe that the orientation of the side-lobe axes of the PSF appears to be rotated by 90° relative to those of the original parallelogram-shaped indicator function—this effect may appear somewhat counter-intuitive to

the uninitiated. The resolution of the image can be specified by the peak-to-null width of the main-lobe of the PSF: this is given by

$$\rho_u = \frac{2\pi}{\Delta k_u}, \tag{2.176}$$

$$\rho_v = \frac{2\pi}{\Delta k_v}. \tag{2.177}$$

In the case of scatterers at other positions such that $\kappa(\tilde{\mathbf{k}}; \bar{\mathbf{k}}, \mathbf{R})$ does not fill the entire parallelogram grid, the main difference will be that the support along k_u will be less than Δk_u so the corresponding range-resolution ρ_u will be coarser than $2\pi/\Delta k_u$.

It is not necessary to determine the parallelogram grid dimensions Δk_u and Δk_v via the steps given in Section 2.5.2 to estimate the expected image resolution: by considering the shape of the projected data support in the ground-plane, the following approximate expressions for Δk_u and Δk_v may be obtained

$$\Delta k_u = \frac{2\pi}{c} \gamma T_p \left|\bar{\mathbf{b}}\right| \tag{2.178}$$

$$\Delta k_v = \frac{2\pi}{c} f_c \Delta\phi_{\mathbf{B}} \left|\bar{\mathbf{b}}\right|, \tag{2.179}$$

where $\bar{\mathbf{b}} = \mathbf{b}(\bar{\mathbf{K}})$ is the vector $\mathbf{b}(\mathbf{K})$ evaluated at the centre of the coherent processing interval ($\bar{\mathbf{b}}$ will be parallel to the chosen k_u-axis) and $\Delta\phi_{\mathbf{B}}$ is the range of azimuthal angles spanned by the $\mathbf{b}(\mathbf{K})$ vectors over the synthetic aperture. Hence, the estimated image resolutions are

$$\rho_u = \frac{c}{\gamma T_p \left|\bar{\mathbf{b}}\right|}, \tag{2.180}$$

$$\rho_v = \frac{\lambda_c}{\Delta\phi_{\mathbf{B}} \left|\bar{\mathbf{b}}\right|} \tag{2.181}$$

in which $\lambda_c = c/f_c$ is the wavelength. These results are in agreement with expressions for bistatic SAR resolutions previously derived by Cardillo [38].[14]

The expressions for the resolutions can be rewritten in a more useful form: since

$$\left|\bar{\mathbf{b}}\right| = 2\cos\frac{\bar{\beta}}{2}\sin\bar{\theta}_{\mathbf{B}}, \tag{2.182}$$

where $\bar{\beta}$ is the bistatic angle at aperture centre and $\bar{\theta}_{\mathbf{B}}$ is the polar angle of the vector $\mathbf{B}(\bar{\mathbf{K}})$, (2.180) and (2.181) can be rewritten as

$$\rho_u = \frac{c}{2\gamma T_p \sin\bar{\theta}_{\mathbf{B}} \cos\left(\bar{\beta}/2\right)}, \tag{2.183}$$

$$\rho_v = \frac{\lambda_c}{2\,\Delta\phi_{\mathbf{B}} \sin\bar{\theta}_{\mathbf{B}} \cos\left(\bar{\beta}/2\right)}. \tag{2.184}$$

[14] The range resolution as presented in Cardillo's equation (3) [38] can be directly compared with (2.180). However, the cross-range resolution in Cardillo's (7) is presented in a form involving the gradient of a Doppler shift function projected into the ground-plane ∇f_{G} which makes comparison with (2.181) difficult: the key is to observe that

$$\dot{\mathbf{B}} = \sum_{i=1}^{2} \frac{\mathbf{V}_i - (\mathbf{V}_i \cdot \hat{\mathbf{P}}_i)\hat{\mathbf{P}}_i}{|\mathbf{P}_i|}$$

where $\mathbf{V}_i$ are the velocities of the transmitter and receiver, so that $\dot{\mathbf{b}} = \lambda_c \nabla f_{\mathrm{G}}$, whereupon the agreement of the two expressions becomes clear with a little geometry.

Table 2.1: Window functions and corresponding Fourier transform widths as determined numerically.

Window name	Time-domain formula	Freq. domain -3 dB width	Freq. domain peak-to-null width
Rectangular	$\mathrm{rect}(t)$	0.8859	1.0000
Hamming	$\mathrm{rect}(t)(0.54 - 0.46\cos(2\pi(t+0.5)))$	1.3030	2.0000
Hann	$\mathrm{rect}(t)(0.5 - 0.5\ \cos(2\pi(t+0.5)))$	1.4406	2.0000
Blackman	$\mathrm{rect}(t)(0.42 - 0.5\ \cos(2\pi(t+0.5)) + 0.08\cos(4\pi(t+0.5)))$	1.6437	3.0000

These expressions for the expected image resolutions reduce to the familiar monostatic form when $\bar{\beta} = 0$. It is worth emphasising, however, that $\Delta\phi_{\mathbf{B}}$ in the expression for ρ_v refers to the azimuthal span of the $\mathbf{b}(\mathbf{K})$ vectors over the coherent processing interval, and *not* to the spans $\Delta\phi_{\mathbf{P}_1}$ and $\Delta\phi_{\mathbf{P}_2}$ of the projections into the ground plane of the transmitter or receiver position vectors $\mathbf{P}_1(\mathbf{K})$ and $\mathbf{P}_2(\mathbf{K})$: in the monostatic case, $\Delta\phi_{\mathbf{B}} = \Delta\phi_{\mathbf{P}_1} = \Delta\phi_{\mathbf{P}_2}$ but, in the general bistatic case where the transmitter and receiver may be moving independently, there may be no obvious relationship between them.

Finally, it should be noted that the expressions for the peak-to-null resolutions ρ_u and ρ_v derived above apply only when no additional window (other than the implicit rectangular window) is applied to the data before the Fourier transform. If a different window is used, the resolutions need to be scaled by appropriate factors (see Table 2.1). Multiplicative factors specific to the window used are also required if it is desired to transform the peak-to-null resolutions to the corresponding -3 dB resolutions.

2.8 PFA limitations

In calculating the image PSF $\hat{\kappa}(\mathbf{r};\mathbf{k},\mathbf{R})$ in Section 2.7, the series expansion of the phase $\tilde{\phi}(\tilde{\mathbf{k}};\bar{\mathbf{k}},\mathbf{R})$ was truncated at the first-order term in $|\mathbf{R}|$. Hence, under this approximation, the expression for the PSF obtained in (2.175) is only valid for scatterer positions near the origin: the higher-order terms in the series which were ignored in this approximation cause increasingly severe geometric distortion and defocussing, which imposes limits on the size of the region which will be represented acceptably in the SAR image. In this section, we investigate the limitations of the first-order phase approximation and determine the size of its region of validity. In our analysis, we shall focus on the second-order term in the series expansion in powers of $|\mathbf{R}|$ of the elementary signal phase $\Psi(\mathbf{K};\mathbf{R})$: from (2.46), we see that this term is given by

$$\Psi^{(2)}(\mathbf{K};\mathbf{R}) = -\frac{|\mathbf{K}|}{2|\mathbf{B}(\mathbf{K})|}\sum_{i=1}^{2}\frac{|\mathbf{R}|^2 - \left(\mathbf{R}\cdot\hat{\mathbf{P}}_i(\mathbf{K})\right)^2}{|\mathbf{P}_i(\mathbf{K})|} \tag{2.185}$$

where we have rewritten the various quantities to show their dependence on the vectors $\mathbf{K}$ which lie on the collection surface instead of τ and n (as previously discussed in Section 2.7, these are related via $\mathbf{K} = \mathbf{K}_n(\tau)$).

In the monostatic case, we will have $\mathbf{P}_1(\mathbf{K}) = \mathbf{P}_2(\mathbf{K}) = \mathbf{P}(\mathbf{K})$. Hence, from (2.47), $\mathbf{B}(\mathbf{K}) = 2\hat{\mathbf{P}}(\mathbf{K})$ so $\hat{\mathbf{P}}(\mathbf{K}) = \hat{\mathbf{B}}(\mathbf{K})$. But, from (2.48), $\hat{\mathbf{B}}(\mathbf{K}) = \hat{\mathbf{K}}$ so the vectors $\hat{\mathbf{B}}(\mathbf{K})$, $\hat{\mathbf{P}}(\mathbf{K})$ and $\hat{\mathbf{K}}$ are all equivalent. Hence, the direction to the monostatic radar $\hat{\mathbf{P}}(\mathbf{K})$ is a simple function of $\mathbf{K}$. If necessary, the exact radial distance of the radar from the origin $|\mathbf{P}(\mathbf{K})|$ can then be determined from a knowledge of the trajectory and $\hat{\mathbf{P}}(\mathbf{K})$ but, for an arbitrary trajectory, the function $|\mathbf{P}(\mathbf{K})|$ will not be simple. Hence, not uncommonly, a constant value P is used to represent $|\mathbf{P}(\mathbf{K})|$: this is valid for short coherent processing intervals over which the radial distance will not change by a large amount. Thus, the phase term in (2.185) reduces, in the monostatic case,

to the simple form

$$\Psi^{(2)}(\mathbf{K};\mathbf{R}) = = -\frac{|\mathbf{K}|}{2\times 2}\sum_{i=1}^{2}\frac{|\mathbf{R}|^2 - \left(\mathbf{R}\cdot\hat{\mathbf{K}}\right)^2}{P}$$
$$= -\frac{|\mathbf{K}|}{2\,P}\left(|\mathbf{R}|^2 - (\hat{\mathbf{K}}\cdot\mathbf{R})^2\right). \tag{2.186}$$

Now, for a general imaging geometry (whether monostatic or bistatic), $\mathbf{K}$ and $\mathbf{R}$ may be represented in terms of their components by (2.155) and (2.168) respectively. For analytical simplicity, however, we will set $\psi = \eta = 0$ and $w_0 = 0$: this corresponds to the case where the image-plane is chosen to coincide with the slant-plane and the scatterers also all lie in this plane. If we work in terms of the local offsets $\tilde{k}_u, \tilde{k}_v$ (ref. (2.112), (2.113), (2.158)) and set $\bar{k}_v = 0$ (as in (2.97)), then the zeroth-, first- and second-order terms in the power series expansion of $\Psi^{(2)}(\mathbf{K};\mathbf{R})$ in these variables may be obtained as

$$\Psi^{(2,0)} = -\frac{\bar{k}_u}{2\,P}v_0^2, \tag{2.187}$$
$$\Psi^{(2,1)} = -\tilde{k}_u\frac{v_0^2}{2\,P} + \tilde{k}_v\frac{u_0 v_0}{P}, \tag{2.188}$$
$$\Psi^{(2,2)} = -\tilde{k}_v^2\frac{u_0^2 - v_0^2/2}{2\,\bar{k}_u\,P}. \tag{2.189}$$

The above results compare well to the results in equation (B.21) of the book by Jakowatz et al. [39] except for $\Psi^{(2,2)}$—this discrepancy may be attributed to a slightly different derivation in that the aforementioned source presents a derivation based on a series expansion in angular coordinates. The term $\Psi^{(2,0)}$ depends on the position parameter v_0 but not on the spatial frequency-domain offsets $(\tilde{k}_u, \tilde{k}_v)$ and hence represents a simple spatially variant phase offset which is added to the phase of the image PSF: being constant with respect to $\tilde{k}_u$ and $\tilde{k}_v$, it has little significance in the present context where the quality of a single SAR image is being considered but should be duly taken into account in coherent applications of multi-baseline SAR data, e.g. interferometry or tomography. The term $\Psi^{(2,1)}$ is linear in the variables $\tilde{k}_u$ and $\tilde{k}_v$ which are the inputs to the image-forming Fourier transform: the effect is to cause a displacement of the image PSF by an amount equal to the coefficients of $\tilde{k}_u$ and $\tilde{k}_v$. As these coefficients are dependent on the position parameters (u_0, v_0), the overall effect is a spatially varying geometric distortion of the image's representation of the scene (see Figure 2.26(a)). The term $\Psi^{(2,2)}$ is also dependent on position and is quadratic in the variable $\tilde{k}_v$: this causes a spatially variant quadratic phase distortion of the signal in the spatial frequency $(\tilde{k}_u, \tilde{k}_v)$ domain which results in defocussing along the v' direction in the image (u', v') domain.[15] Hence, the size of the undistorted and focussed region of the image is determined by the (u_0, v_0) such that the magnitudes of the $\Psi^{(2,1)}$ and $\Psi^{(2,2)}$ terms remain below appropriate thresholds of acceptability: generally, it is the defocussing effect which places the stricter limit on the size of this 'good' region. A common criterion for acceptable image focus is that quadratic phase errors must be under $\pi/4$ radians: applying this criterion to limit the magnitude of $\Psi^{(2,2)}$ gives

$$\left|u_0^2 - \frac{v_0^2}{2}\right| < \frac{2P\rho_v^2}{\lambda_c}, \tag{2.190}$$

[15] Autofocus algorithms like the PGA (Section 2.6) assume spatially invariant phase errors and are thus inapplicable to this defocussing effect. Thus, when applying the PGA to images formed by the PFA, care should be taken to ensure that the phase error is estimated only from the central 'good' region of the image where the effect of this $\Psi^{(2,2)}$ term is negligible.

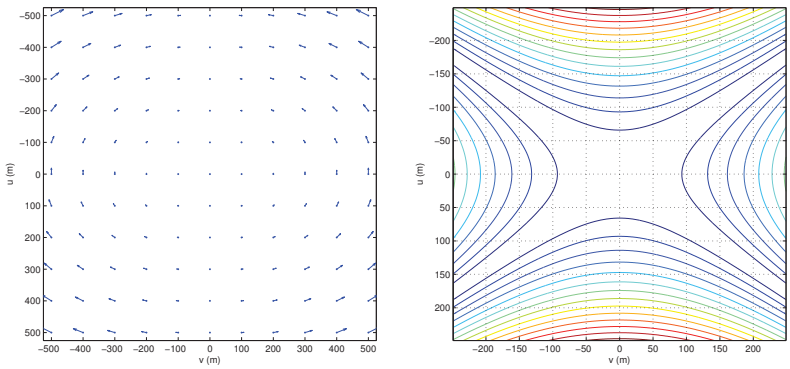

(a) (b)

Figure 2.26: (a) Displacements of scatterer positions in monostatic image as calculated from monostatic first order phase $\Psi^{(2,1)}$; (b) contour plots of magnitude of monostatic second order phase $\Psi^{(2,2)}$ with $|\tilde{k}_v| = \pi/\rho_v$ (each contour corresponds to $|\Psi^{(2,2)}| = n\pi/4$ where $n = 1, 2, \ldots$ from innermost contour outwards). Parameters were $P = 6500\,\mathrm{m}$, $\lambda_c = 0.03\,\mathrm{m}$ and $\rho_v = 0.1\,\mathrm{m}$.

since, from (2.177) and Figure 2.27, we have

$$|\tilde{k}_v| < \frac{\pi}{\rho_v} \tag{2.191}$$

and, from (2.67) with $|\mathbf{b}_n| = 2$ (since we are currently considering the monostatic case and working in the slant-plane), we have

$$\bar{k}_u \approx \frac{4\pi f_c}{c} = \frac{4\pi}{\lambda_c}. \tag{2.192}$$

The points (u_0, v_0) satisfying (2.190) above lie within a region bounded by hyperbolas (see Figure 2.26(b)): a rectangular subset of this region can be specified by the inequalities

$$\frac{|u_0|}{\rho_v} < \sqrt{\frac{2P}{\lambda_c}}, \tag{2.193}$$

$$\frac{|v_0|}{\rho_v} < \sqrt{\frac{4P}{\lambda_c}}. \tag{2.194}$$

These expressions thus give a means to estimate the undistorted and focussed region of the image for the monostatic case.

Repeating the above analysis for the general bistatic case is considerably more challenging. To begin, observe from Figure 2.5 and the equivalence relation $\hat{\mathbf{K}} = \hat{\mathbf{B}}$ (recall (2.48)) that, in the bistatic case, we have $\mathbf{B}(\mathbf{K}) = 2\left(\hat{\mathbf{P}}_1(\mathbf{K}) \cdot \hat{\mathbf{K}}\right)\hat{\mathbf{K}} = 2\left(\hat{\mathbf{P}}_2(\mathbf{K}) \cdot \hat{\mathbf{K}}\right)\hat{\mathbf{K}}$, in which the dot products satisfy $0 \leq \hat{\mathbf{P}}_i(\mathbf{K}) \cdot \hat{\mathbf{K}} \leq 1$ for $i = 1, 2$.[16] However, although $\mathbf{B}(\mathbf{K})$ is given by this relatively simple expression, it is not straightforward to obtain expressions for $\hat{\mathbf{P}}_1(\mathbf{K})$ and $\hat{\mathbf{P}}_2(\mathbf{K})$ for arbitrary transmitter and receiver trajectories. Hence, to proceed further, we must restrict the trajectories to particular cases: as our primary interest is in processing the *Ingara* data, we shall examine the case where the receiver is fixed, i.e. $\mathbf{P}_2(\mathbf{K}) = \mathbf{P}_{\mathrm{gnd}}$ being a constant. It then follows that

$$\mathbf{B}(\mathbf{K}) = 2\left(\hat{\mathbf{P}}_{\mathrm{gnd}} \cdot \hat{\mathbf{K}}\right)\hat{\mathbf{K}} \tag{2.195}$$

[16] Since $\hat{\mathbf{P}}_1(\mathbf{K}) \cdot \hat{\mathbf{K}} = \hat{\mathbf{P}}_2(\mathbf{K}) \cdot \hat{\mathbf{K}} = \cos(\beta/2)$ and $0 \leq \beta \leq \pi$ where β is the bistatic angle.

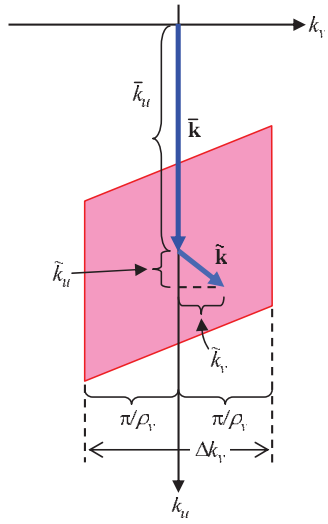

Figure 2.27: Parallelogram grid extents and $\bar{\mathbf{k}}$ and $\tilde{\mathbf{k}}$ vectors.

and, via (2.47), that

$$\begin{aligned}\hat{\mathbf{P}}_1(\mathbf{K}) &= \mathbf{B}(\mathbf{K}) - \hat{\mathbf{P}}_{\text{gnd}} \\ &= 2\left(\hat{\mathbf{P}}_{\text{gnd}} \cdot \hat{\mathbf{K}}\right)\hat{\mathbf{K}} - \hat{\mathbf{P}}_{\text{gnd}}.\end{aligned} \tag{2.196}$$

As in the monostatic case, the exact radial distance from the origin of the transmitter $|\mathbf{P}_1(\mathbf{K})|$ can be determined from $\hat{\mathbf{P}}_1(\mathbf{K})$ and a knowledge of the transmitter's trajectory, but this is unlikely to be straightforward: thus, we will assume that the variation of the distance over a coherent processing interval is slight and simply employ a constant value P_1 to represent $|\mathbf{P}_1(\mathbf{K})|$. By contrast, since the receiver is stationary, the receiver's radial distance $|\mathbf{P}_2(\mathbf{K})|$ is necessarily constant: let this be represented by $P_{\text{gnd}} = |\mathbf{P}_{\text{gnd}}|$. Thus, by substituting (2.195) and (2.196) into (2.185) then expanding and regrouping terms, we find that, for this stationary-receiver bistatic case, the second order phase term of (2.185) may be written as

$$\begin{aligned}\Psi^{(2)}(\mathbf{K};\mathbf{R}) = &-\frac{|\mathbf{K}|}{4\,\hat{\mathbf{P}}_{\text{gnd}} \cdot \hat{\mathbf{K}}}\left(|\mathbf{R}|^2 - \left(\hat{\mathbf{P}}_{\text{gnd}} \cdot \mathbf{R}\right)^2\right)\left(\frac{1}{P_1} + \frac{1}{P_{\text{gnd}}}\right) \\ &+ \frac{|\mathbf{K}|}{P_1}\left(\hat{\mathbf{K}} \cdot \mathbf{R}\right)\left(\left(\hat{\mathbf{P}}_{\text{gnd}} \cdot \hat{\mathbf{K}}\right)\left(\hat{\mathbf{K}} \cdot \mathbf{R}\right) - \hat{\mathbf{P}}_{\text{gnd}} \cdot \mathbf{R}\right).\end{aligned} \tag{2.197}$$

To analyse this further, the direction of the receiver $\hat{\mathbf{P}}_{\text{gnd}}$ must be specified: let this be given by

$$\hat{\mathbf{P}}_{\text{gnd}} = \sin\theta_2 \cos\phi_2\, \mathbf{a}_u + \sin\theta_2 \sin\phi_2\, \mathbf{a}_v + \cos\theta_2\, \mathbf{a}_w \tag{2.198}$$

where θ_2 and ϕ_2 are the polar and azimuthal angles of the receiver relative to the $k_u k_v k_w$ axes. For simplicity, in the following discussion, we shall consider only the range $0 \le \phi_2 < \pi/2$ since the results for this case can be applied to the cases where ϕ_2 lies in the other quadrants through exploitation of reflection symmetries.[17] Thus, by first substituting (2.198) into (2.197), we may then proceed as in the monostatic case above: subsequent

[17]Note that when $\phi_2 = \pi/2$, we have $\hat{\mathbf{P}}_{\text{gnd}} \cdot \hat{\mathbf{K}} = 0$ so (2.197) is inapplicable: hence, for simplicity, the case of $\phi_2 = \pi/2$ will not be explicitly considered. If needed, however, the results for this particular case can be easily inferred from those of the $0 \le \phi_2 < \pi/2$ case by examining the limit as $\phi_2 \to \pi/2$.

substitution for $\mathbf{K}$ and $\mathbf{R}$ using (2.155) and (2.168) to make explicit the dependence on $k_u, k_v, \psi, \eta, u_0, v_0, w_0$, then setting $\theta_2 = \pi/2$, $\psi = \eta = 0$ and $w_0 = 0$ (to restrict attention to the case where the image- and slant-planes coincide and the transmitter, receiver and scatterers also all lie in this plane) allows the zeroth-, first- and second-order terms in the power series expansion of $\Psi^{(2)}(\mathbf{K};\mathbf{R})$ in the offset variables $\tilde{k}_u$ and $\tilde{k}_v$ (recall (2.112), (2.113), (2.158)) with $\bar{k}_v = 0$ to be obtained as

$$\Psi^{(2,0)} = A_1 u_0^2 + 2A_2 u_0 v_0 + A_3 v_0^2 \tag{2.199}$$

$$\Psi^{(2,1)} = \tilde{k}_u \left(B_1 u_0^2 + 2B_2 u_0 v_0 + B_3 v_0^2\right) + \tilde{k}_v \left(B_4 u_0^2 + 2B_5 u_0 v_0 + B_6 v_0^2\right) \tag{2.200}$$

$$\Psi^{(2,2)} = \tilde{k}_v^2 \left(C_1 u_0^2 + 2C_2 u_0 v_0 + C_3 v_0^2\right) \tag{2.201}$$

where

$$A_1 = -\frac{\bar{k}_u \sin^2\phi_2}{4\cos\phi_2}\left(\frac{1}{P_1} + \frac{1}{P_{\text{gnd}}}\right) \tag{2.202}$$

$$A_2 = -\frac{\bar{k}_u \sin\phi_2}{4}\left(\frac{1}{P_1} - \frac{1}{P_{\text{gnd}}}\right) \tag{2.203}$$

$$A_3 = -\frac{\bar{k}_u \cos\phi_2}{4}\left(\frac{1}{P_1} + \frac{1}{P_{\text{gnd}}}\right) \tag{2.204}$$

$$B_1 = -\frac{\sin^2\phi_2}{4\cos\phi_2}\left(\frac{1}{P_1} + \frac{1}{P_{\text{gnd}}}\right) \tag{2.205}$$

$$B_2 = -\frac{\sin\phi_2}{4}\left(\frac{1}{P_1} - \frac{1}{P_{\text{gnd}}}\right) \tag{2.206}$$

$$B_3 = -\frac{\cos\phi_2}{4}\left(\frac{1}{P_1} + \frac{1}{P_{\text{gnd}}}\right) \tag{2.207}$$

$$B_4 = \frac{\sin\phi_2}{4\cos^2\phi_2}\left(\frac{4 - 3\sin^2\phi_2}{P_1} + \frac{\sin^2\phi_2}{P_{\text{gnd}}}\right) \tag{2.208}$$

$$B_5 = \frac{1}{4\cos\phi_2}\left(\frac{2 - 3\sin^2\phi_2}{P_1} - \frac{\sin^2\phi_2}{P_{\text{gnd}}}\right) \tag{2.209}$$

$$B_6 = -\frac{\sin\phi_2}{4}\left(\frac{3}{P_1} - \frac{1}{P_{\text{gnd}}}\right) \tag{2.210}$$

and

$$C_1 = -\frac{1}{4\bar{k}_u \cos^3\phi_2}\left(\frac{1 - \cos^2\phi_2(1 - 4\cos^2\phi_2)}{P_1} + \frac{\sin^2\phi_2}{P_{\text{gnd}}}\right) \tag{2.211}$$

$$C_2 = \frac{\sin\phi_2}{4\bar{k}_u \cos^2\phi_2}\left(\frac{1 + 4\cos^2\phi_2}{P_1} + \frac{1}{P_{\text{gnd}}}\right) \tag{2.212}$$

$$C_3 = -\frac{1}{4\bar{k}_u \cos\phi_2}\left(\frac{1 - 4\cos^2\phi_2}{P_1} + \frac{1}{P_{\text{gnd}}}\right). \tag{2.213}$$

As in the monostatic case, $\Psi^{(2,0)}$ is a simple phase shift applied to the PSF which is of little practical significance in the context of this discussion, the term $\Psi^{(2,1)}$ causes geometric distortion of the image, and the term $\Psi^{(2,2)}$ causes a quadratic phase shift leading to defocussing along the v direction: these effects are

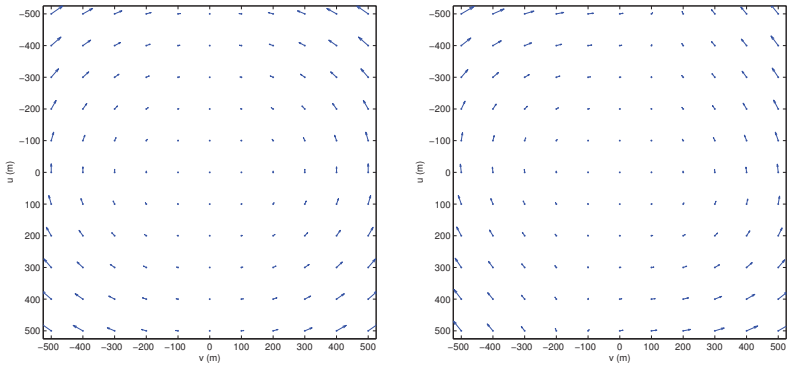

(a) $\phi_2 = 0°$

(b) $\phi_2 = 15°$

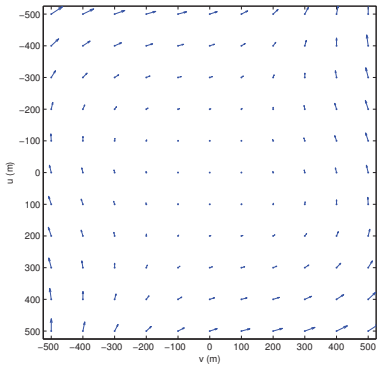

(c) $\phi_2 = 30°$

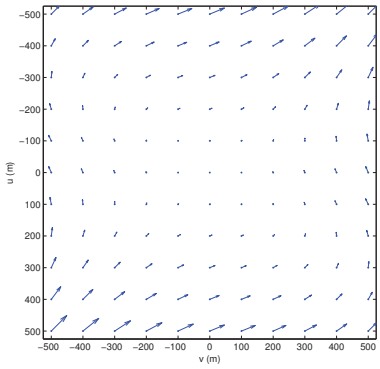

(d) $\phi_2 = 45°$

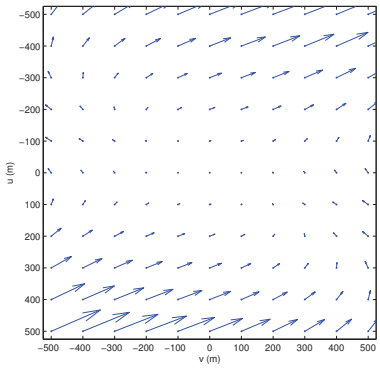

(e) $\phi_2 = 60°$

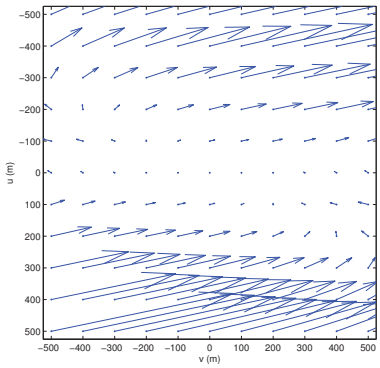

(f) $\phi_2 = 75°$

Figure 2.28: Displacements of scatterer positions in bistatic image as calculated from bistatic first order phase $\Psi^{(2,1)}$ for various receiver azimuthal positions ϕ_2. Parameters were $P_1 = 6500\,\mathrm{m}$, $P_2 = 3600\,\mathrm{m}$, $\theta_2 = \pi/2$ and $\lambda = 0.03$ m.

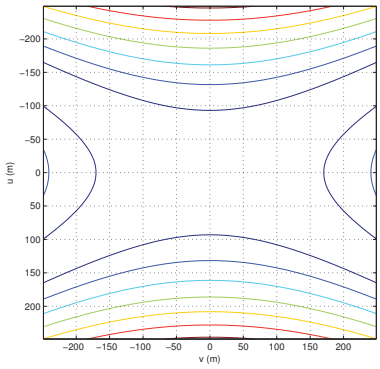

(a) $\phi_2 = 0°$, $\rho_v = 0.2\,\mathrm{m}$

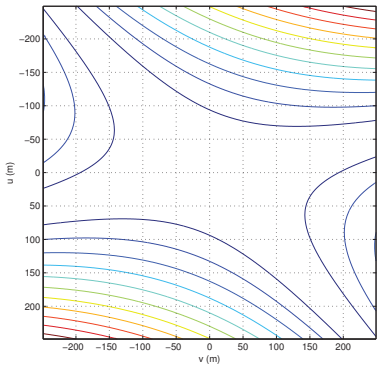

(b) $\phi_2 = 15°$, $\rho_v = 0.21\,\mathrm{m}$

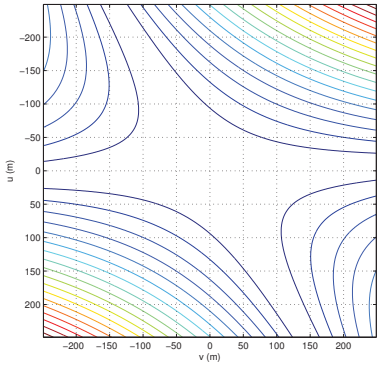

(c) $\phi_2 = 30°$, $\rho_v = 0.23\,\mathrm{m}$

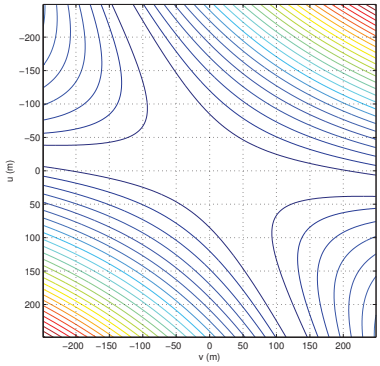

(d) $\phi_2 = 45°$, $\rho_v = 0.28\,\mathrm{m}$

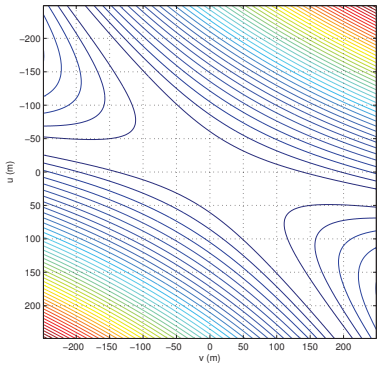

(c) $\phi_2 = 60°$, $\rho_v = 0.40\,\mathrm{m}$

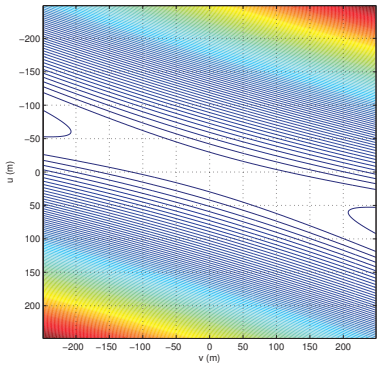

(d) $\phi_2 = 75°$, $\rho_v = 0.77\,\mathrm{m}$

Figure 2.29: Contour plots of magnitude of bistatic second order phase $\Psi^{(2,2)}$ for various receiver azimuthal positions ϕ_2 and cross-range resolutions ρ_v (each contour corresponds to $|\Psi^{(2,2)}| = n\pi/4$ where $n = 1, 2, \ldots$ from the innermost contour outwards). In each case, ρ_v has been adjusted so that $\Delta\phi_{\mathbf{B}}$ remains the same (ref. (2.184)). Parameters were $P_1 = 6500\,\mathrm{m}$, $P_2 = 3600\,\mathrm{m}$, $\theta_2 = \pi/2$ and $\lambda = 0.03$ m.

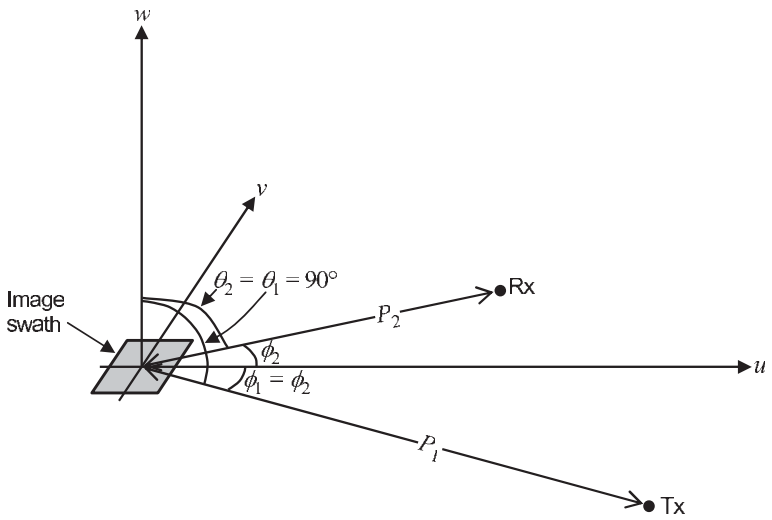

Figure 2.30: Geometry used for calculating distortions and phase terms in bistatic cases.

illustrated in Figure 2.28 and Figure 2.29 for the geometry depicted in Figure 2.30. From the figures, it can be seen that, based on the $|\Psi^{(2,2)}| < \pi/4$ criterion, once again it is the defocussing rather than the distortion effect which places the tighter constraint on the size of the 'good' region. Hence, if we apply this $\pi/4$ radian limit to (2.201), then, by using (2.191), we find that this 'good' region is given by those (u_0, v_0) satisfying

$$\left|D_1 u_0^2 + 2D_2 u_0 v_0 + D_3 v_0^2\right| < Q \tag{2.214}$$

where

$$Q = \frac{P_1 \bar{k}_u \rho_v^2}{\pi} \tag{2.215}$$

and $D_i = 4P_1 \bar{k}_u C_i$ for $i = 1, 2, 3$, viz.

$$D_1 = -\frac{1}{\cos^3 \phi_2}\left(1 - \cos^2 \phi_2 (1 - 4\cos^2 \phi_2) + \frac{P_1 \sin^2 \phi_2}{P_{\text{gnd}}}\right) \tag{2.216}$$

$$D_2 = \frac{\sin \phi_2}{\cos^2 \phi_2}\left(1 + 4\cos^2 \phi_2 + \frac{P_1}{P_{\text{gnd}}}\right) \tag{2.217}$$

$$D_3 = -\frac{1}{\cos \phi_2}\left(1 - 4\cos^2 \phi_2 + \frac{P_1}{P_{\text{gnd}}}\right) \tag{2.218}$$

To proceed further, it is useful to consider the two cases $\phi_2 = 0$ and $\phi_2 \neq 0$ separately: in the former case, the calculations are comparatively simple and the results relatively easy to interpret, while in the latter case, it is difficult to express the calculations simply and the interpretation of the resultant equations is not immediately obvious. Moreover, some insight is offered by the simpler $\phi_2 = 0$ case into the more complicated $\phi_2 \neq 0$ case, so it is doubly advantageous to consider the $\phi_2 = 0$ case first.

- **Case 1:** $\phi_2 = 0$**.** In this case, since $\sin \phi_2 = 0$ and $\cos \phi_2 = 1$, from (2.217) we may observe that $D_2 = 0$, so (2.214) assumes a simple form. By simultaneously evaluating (2.216) to (2.218) at $\phi_2 = 0$ and substituting the results into the left-hand-side of the inequality (2.214), and substituting (2.192)

and (2.215) into the right-hand-side, we obtain

$$\left|4u_0^2 - \left(3 - \frac{P_1}{P_{\text{gnd}}}\right) v_0^2\right| < \frac{4P_1\rho_v^2}{\lambda_c}. \tag{2.219}$$

This is analogous to the inequality (2.190) in the monostatic case in which the level sets of the expression $u_0^2 - v_0^2/2$ on the left-hand-side are always hyperbolas. However, a significant difference is that the level sets of the present expression $3u_0^2 - (3 - P_1/P_{\text{gnd}})\, v_0^2$ in the left-hand-side of (2.219) may be hyperbolas, lines or ellipses depending on whether the ratio

$$\rho \triangleq \frac{P_1}{P_{\text{gnd}}} \tag{2.220}$$

is less than, equal to or greater than 3. (Note that $\rho > 0$ as $P_1 > 0$ and $P_{\text{gnd}} > 0$.) Hence, we need to consider these three cases separately.

- When $\rho < 3$, the desired 'good' region is bounded by hyperbolas (Figure 2.31(a)) and we may proceed as we did previously in the monostatic case above and conclude that the size of the region may be represented by the rectangular area specified by the pair of simplified inequalities

$$\frac{|u_0|}{\rho_v} < \sqrt{\frac{P_1}{\lambda_c}} \tag{2.221}$$

$$\frac{|v_0|}{\rho_v} < \sqrt{\frac{4P_1}{\lambda_c\,|3 - P_1/P_{\text{gnd}}|}}. \tag{2.222}$$

- When $\rho = 3$, the above inequality (2.221) remains applicable while (2.222) degenerates to $|v_0|/\rho_v < \infty$ which effectively leaves v_0 unbounded (this can also be seen directly from (2.219) with $P_1/P_{\text{gnd}} = 3$): this case can be regarded as a limiting case of the $P_1/P_{\text{gnd}} < 3$ case just discussed in which two of the hyperbolas have been stretched into straight lines while the other two have receded to infinity (Figure 2.31(b)).
- Finally, when $\rho > 3$, the region is inherently elliptical (Figure 2.31(c)) so the inequalities (2.221) and (2.222) are only valid along the major and minor axes of the elliptical region, and hence do not describe this region as a whole very well: the region is then best described by the original unsimplified inequality (2.219). However, with this caveat in mind, (2.221) and (2.222) are nevertheless useful for inferring the lengths of the semi-major and semi-minor axes and hence the general size of this elliptical region: from (2.221) and (2.222), we may define

$$E_u \triangleq \rho_v \sqrt{\frac{P_1}{\lambda_c}} \tag{2.223}$$

$$E_v \triangleq \rho_v \sqrt{\frac{4P_1}{\lambda_c|3 - \rho|}} \tag{2.224}$$

  whereupon it may be seen that the semi-major and semi-minor axes are given by: E_v and E_u respectively when $\rho \leq 7$ (since in this case $E_v \geq E_u$); or E_u and E_v respectively when $\rho > 7$ (since in this case $E_u > E_v$).

It should be noted that although the quantities E_u and E_v were introduced for the specific case of the elliptical boundary, they are also generally useful as they can be interpreted as the dimension of the

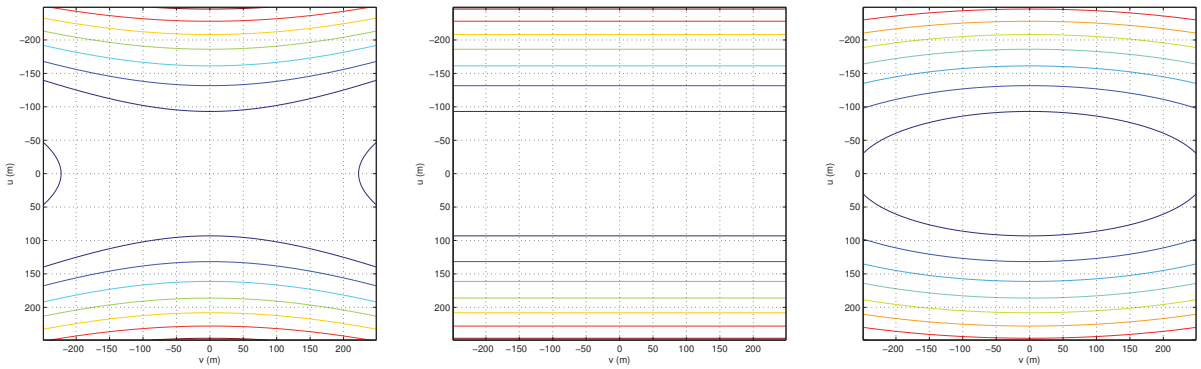

(a) $\rho = 2.3$, $E_u = 93.1$ m, $E_v = 222.5$ m (b) $\rho = 3.0$, $E_u = 93.1$ m, $E_v = \infty$ (c) $\rho = 3.5$, $E_u = 93.1$ m, $E_v = 263.3$ m

Figure 2.31: Contour plots of $|\Psi^{(2,2)}|$ for geometry shown in Figure 2.30 with variable P_1-to-P_{gnd} ratio ρ and fixed $\phi_2 = 0$, $\rho_v = 0.2$ m, $P_1 = 6500$ m (each contour corresponds to $|\Psi^{(2,2)}| = n\pi/4$ where $n = 1, 2, \ldots$ from the innermost contour outwards).

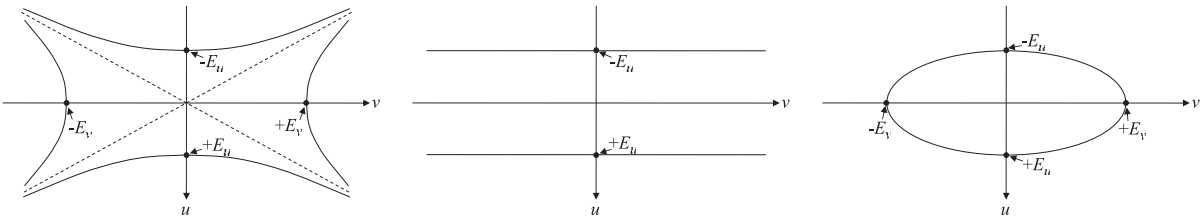

(a) $\frac{u^2}{E_u^2} - \frac{v^2}{E_v^2} = 1$ (b) $\frac{u^2}{E_u^2} = 1$ (c) $\frac{u^2}{E_u^2} + \frac{v^2}{E_v^2} = 1$

Figure 2.32: Size of region is defined by E_u and E_v.

region measured along the u and v axes in all three cases, i.e. hyperbolic, linear or elliptical boundaries (see Figure 2.32).

- **Case 2:** $\phi_2 \neq 0$**.** In this case, observe that $D_2 \neq 0$, so, to determine the size of the 'good' region, we will need to diagonalise the left-hand-side of (2.214). To do so, first observe that the expression in the left-hand-side of this inequality can be written as a simple product of vectors and matrices:

$$D_1 u_0^2 + 2D_2 u_0 v_0 + D_3 v_0^2 = \begin{pmatrix} u_0 & v_0 \end{pmatrix} \mathbf{M} \begin{pmatrix} u_0 \\ v_0 \end{pmatrix} \tag{2.225}$$

where

$$\mathbf{M} = \begin{pmatrix} D_1 & D_2 \\ D_2 & D_3 \end{pmatrix}. \tag{2.226}$$

An eigendecomposition of this symmetric matrix $\mathbf{M}$ is

$$\mathbf{M} = \mathbf{P}\mathbf{\Sigma}\mathbf{P}^T \tag{2.227}$$

where

$$\mathbf{P} = \begin{pmatrix} \frac{2D_2}{L_1} & \frac{2D_2}{L_2} \\ \frac{D_3 - D_1 - \sqrt{D}}{L_1} & \frac{D_3 - D_1 + \sqrt{D}}{L_2} \end{pmatrix} \tag{2.228}$$

$$\mathbf{\Sigma} = \begin{pmatrix} \mu_1 & 0 \\ 0 & \mu_2 \end{pmatrix} \tag{2.229}$$

in which

$$D = (D_3 - D_1)^2 + 4D_2^2, \tag{2.230}$$

$$L_1 = \sqrt{4D_2^2 + (D_3 - D_1 - \sqrt{D})^2}, \tag{2.231}$$

$$L_2 = \sqrt{4D_2^2 + (D_3 - D_1 + \sqrt{D})^2}, \tag{2.232}$$

and

$$\mu_1 = \frac{D_3 + D_1 - \sqrt{D}}{2} \tag{2.233}$$

$$\mu_2 = \frac{D_3 + D_1 + \sqrt{D}}{2}. \tag{2.234}$$

Hence, from (2.225) and (2.227), it follows that the inequality (2.214) can be written as

$$\left|\mu_1 \hat{u}_0^2 + \mu_2 \hat{v}_0^2\right| < Q \tag{2.235}$$

where $\hat{u}_0$ and $\hat{v}_0$ are related to u_0 and v_0 by

$$\begin{pmatrix} \hat{u}_0 \\ \hat{v}_0 \end{pmatrix} = \mathbf{P}^T \begin{pmatrix} u_0 \\ v_0 \end{pmatrix}. \tag{2.236}$$

Equation (2.236) suggests that we define a coordinate transformation from the (u, v) coordinates to

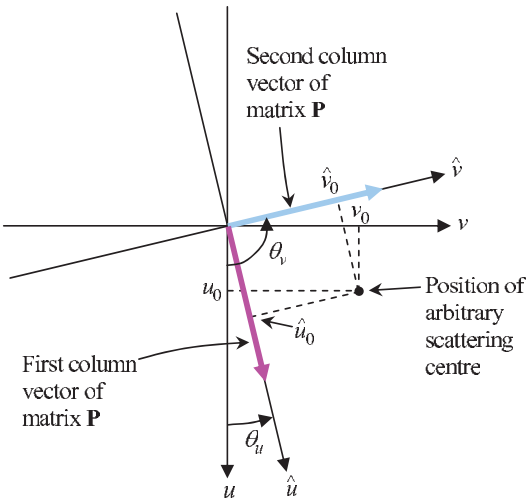

Figure 2.33: Orientations of $\hat{u}$ and $\hat{v}$ axes.

$(\hat{u}, \hat{v})$ coordinates given by

$$\begin{pmatrix} \hat{u} \\ \hat{v} \end{pmatrix} = \mathbf{P}^T \begin{pmatrix} u \\ v \end{pmatrix}. \tag{2.237}$$

Thus, just as (u_0, v_0) are the coordinates of a scattering centre in the (u, v) coordinate system, $(\hat{u}_0, \hat{v}_0)$ are the corresponding coordinates in the $(\hat{u}, \hat{v})$ coordinate system (see Figure 2.33). As the matrix $\mathbf{P}$ is orthogonal (being derived from the eigendecomposition of the symmetric matrix $\mathbf{M}$), the inverse transformation from $(\hat{u}, \hat{v})$ back to (u, v) is simply given by

$$\begin{pmatrix} u \\ v \end{pmatrix} = \mathbf{P} \begin{pmatrix} \hat{u} \\ \hat{v} \end{pmatrix}. \tag{2.238}$$

The columns of $\mathbf{P}$ thus represent vectors (in the uv coordinate system) which point along the directions of the $\hat{u}$ and $\hat{v}$ axes: since $\mathbf{P}$ is orthogonal, these vectors are orthonormal (i.e. perpendicular and of unit length) so the $\hat{u}$ and $\hat{v}$ axes are orthogonal. The orientations of the $\hat{u}$ and $\hat{v}$ axes relative to the u axes, denoted by θ_u and θ_v respectively (see Figure 2.33), can be obtained from the tangent equations

$$\tan\theta_u = \frac{D_3 - D_1 - \sqrt{D}}{2D_2} \tag{2.239}$$

$$\tan\theta_v = \frac{D_3 - D_1 + \sqrt{D}}{2D_2} \tag{2.240}$$

(in which the expressions on the right-hand-side are ratios of the v to u components of the columns of $\mathbf{P}$). The behaviour of θ_u and θ_v as θ_2 and the P_1-to-P_{gnd} ratio ρ are varied is illustrated in Figure 2.34. From these plots, it can be observed that $\theta_v = \theta_u + \pi/2$ (which is in accord with the expected orthogonality of the $\hat{u}$ and $\hat{v}$ axes) so that the $(\hat{u}, \hat{v})$ coordinate system is related to the (u, v) system by a simple rotation of the latter through the angle θ_u (recall Figure 2.33). Inspection of the plots also reveals complicated behaviour exhibited by both angles θ_u and θ_v with varying ϕ_2 and ρ. For example, the behaviour of θ_u (and hence θ_v) as ϕ_2 increases is dependent on the value of ρ: for $\rho < 7$, θ_u decreases from 0 to a minimum before increasing and returning to 0; for $\rho = 7$, θ_u increases from $-\pi/4$ to 0; and for $\rho > 7$, θ_u

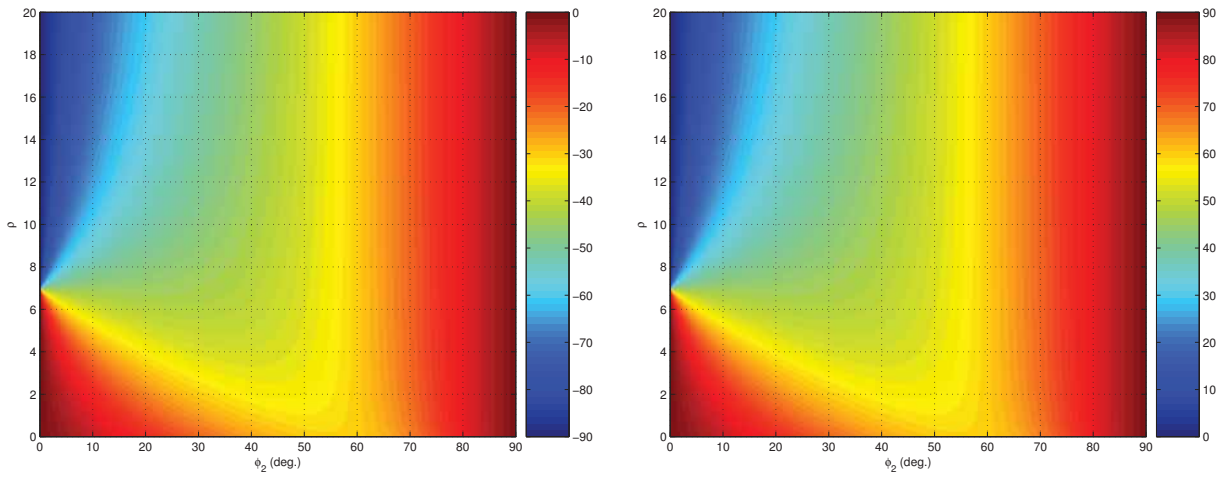

(a) θ_u (°) (b) θ_v (°)

Figure 2.34: Plots of $\hat{u}$- and $\hat{v}$-axis orientation angles θ_u and θ_v respectively (in degrees).

increases from $-\pi/2$ to 0. In contrast, when $\phi_2 = \pi/3$, we have $\tan\theta_u = -1/\sqrt{3}$ which is independent of ρ and so θ_u assumes the constant value $-\pi/6$.[18]

The left-hand-side of the inequality (2.235) is analogous to (2.219) of the $\phi_2 = 0$ case and, similarly to that case, the expression $\mu_1\hat{u}_0^2 + \mu_2\hat{v}_0^2$ in the left-hand-side of (2.235) has level sets which may be hyperbolas, lines or ellipses depending on the signs of the eigenvalues μ_1 and μ_2 of the matrix $\mathbf{M}$. By substituting (2.230) and (2.216) to (2.218) into (2.233) and (2.234), we may obtain the following expressions for μ_1 and μ_2 in terms of ϕ_2 and ρ:

$$\mu_1 = -\frac{\sqrt{\rho^2 + (-64\cos^6\phi_2 + 48\cos^4\phi_2 + 2)\,\rho + 48\cos^4\phi_2 + 1} + \rho + 1}{2\cos^3\phi_2} \tag{2.241}$$

$$\mu_2 = \frac{\sqrt{\rho^2 + (-64\cos^6\phi_2 + 48\cos^4\phi_2 + 2)\,\rho + 48\cos^4\phi_2 + 1} - \rho - 1}{2\cos^3\phi_2}. \tag{2.242}$$

From these expressions, it can be seen that $\mu_1 < 0$, $\mu_1 < \mu_2$ and $|\mu_1| > |\mu_2|$ (for the range $0 < \phi_2 < \pi/2$ currently being considered). The behaviour of μ_1 and μ_2 with varying ϕ_2 and ρ is illustrated in Figure 2.35. From the figures, we see that in the limit as $\phi_2 \to 0^+$,

$$\mu_1 = \begin{cases} -4 & \rho \le 7 \\ 3-\rho & \rho > 7 \end{cases} \tag{2.243}$$

$$\mu_2 = \begin{cases} 3-\rho & \rho \le 7 \\ -4 & \rho > 7 \end{cases} \tag{2.244}$$

(this can also be verified analytically from (2.241) and (2.242)). Also from the figures, we can see that for a given value of ρ, as ϕ_2 increases, μ_1 simply decreases (especially as ϕ_2 nears $\pi/2$) whereas μ_2 increases to a maximum value of 4 at $\phi_2 = \pi/3$ then decreases to zero as ϕ_2 approaches $\pi/2$. Hence, μ_1 is always negative (as was seen directly from (2.241)) so the shape of the level sets is determined solely

[18] These observations may be confirmed by a tedious analysis of (2.239) and (2.240) (upon substitution of (2.216) to (2.218) and (2.230)).

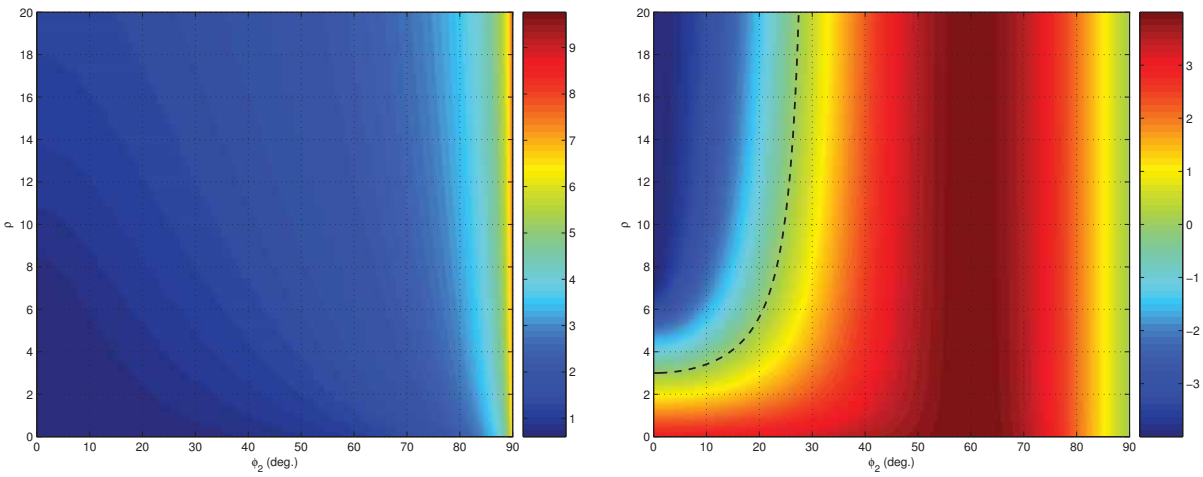

(a) $\log_{10}(-\mu_1)$ (b) μ_2

Figure 2.35: Variation of μ_1 and μ_2 with ϕ_2 and ρ. Since μ_1 is negative (see (2.241)) and varies rapidly over a large range near $\phi_2 = \pi/2$, for clarity the behaviour of μ_1 is illustrated indirectly through the proxy $\log_{10}(-\mu_1)$: transition from blue to red in plot (a) thus indicates increasingly *negative* values of μ_1. Dashed line in plot (b) is locus of $\rho = 3/(4\cos^2\phi_2 - 3)$ at which $\mu_2 = 0$.

by μ_2.

A direct analysis of the behaviour of μ_2 is difficult as (2.242) has a complicated form: instead, let us consider the determinant of the matrix $\mathbf{M}$, i.e. $\det\mathbf{M} = \mu_1\mu_2 = D_1D_3 - D_2^2$. By substituting in (2.230), (2.233), (2.234) and (2.216) to (2.218), we find that this assumes the simple form

$$\det\mathbf{M} = \frac{4}{\cos^2\phi_2}\left((4\cos^2\phi_2 - 3)\rho - 3\right). \tag{2.245}$$

Thus, it is easily seen that $\det\mathbf{M} = 0$ and hence $\mu_2 = 0$ when $(4\cos^2\phi_2 - 3)\rho - 3 = 0$ (this is shown as the dashed line in Figure 2.35(b)). Note that, as $\rho \geq 0$ (recall that ρ was defined in (2.220) as the ratio of two non-negative distances), this equation is only satisfied when $\phi_2 < \pi/6$. Thus, the following three cases may be distinguished:

- When *either* $\phi_2 < \pi/6$ and $\rho < 3/(4\cos^2\phi_2 - 3)$, *or* when $\phi_2 \geq \pi/6$, we have $\mu_2 > 0$ (as can be seen from Figure 2.35(b)) so the 'good' region will be bounded by hyperbolas and can be specified as

$$|\hat{u}_0| < \sqrt{\frac{Q}{|\mu_1|}} \tag{2.246}$$

$$|\hat{v}_0| < \sqrt{\frac{Q}{|\mu_2|}} \tag{2.247}$$

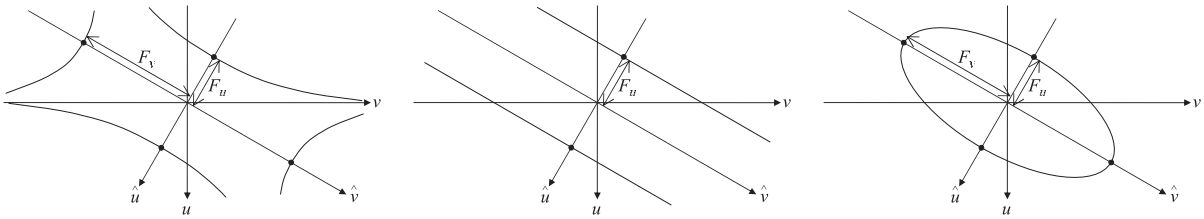

(a) $\frac{\hat{u}_0^2}{F_u^2} - \frac{\hat{v}_0^2}{F_v^2} = 1$ (b) $\frac{\hat{u}_0^2}{F_u^2} = 1$ (c) $\frac{\hat{u}_0^2}{F_u^2} + \frac{\hat{v}_0^2}{F_v^2} = 1$

Figure 2.36: Size of region is defined by F_u and F_v (c.f. Figure 2.32).

As $\bar{k}_u = (4\pi/\lambda_c)\cos\phi_2$, we have $Q = (4P_1\cos\phi_2/\lambda_c)\rho_v^2$ and hence

$$\frac{|\hat{u}_0|}{\rho_v} < \sqrt{\frac{4P_1\cos\phi_2}{\lambda_c|\mu_1|}} \tag{2.248}$$

$$\frac{|\hat{v}_0|}{\rho_v} < \sqrt{\frac{4P_1\cos\phi_2}{\lambda_c|\mu_2|}}. \tag{2.249}$$

- When $\phi_2 < \pi/6$ and $\rho = 3/(4\cos^2\phi_2 - 3)$, we have $\mu_2 = 0$ (ref. Figure 2.35(b)) and the required region will be specified by the single inequality (2.248) (since the inequality (2.249) degenerates to the tautological relation $|\hat{v}_0|/\rho_v < \infty$). This result could also have been derived directly by evaluating the inequality (2.235) with $\mu_2 = 0$.
- Finally, when $\phi_2 < \pi/6$ and $\rho > 3/(4\cos^2\phi_2 - 3)$, we have $\mu_2 < 0$ (see Figure 2.35(b)) whereupon the required region will lie within the ellipse $|\mu_1|\hat{u}_0^2 + |\mu_2|\hat{v}_0^2 = Q$, which cannot be represented well by simple inequalities of the form of (2.248) and (2.249). As in the $\phi_2 = 0$ case, however, they are useful for calculating the semi-major and semi-minor axes of the elliptical boundary: if we define

$$F_u \triangleq \rho_v\sqrt{\frac{4P_1\cos\phi_2}{\lambda_c|\mu_1|}} \tag{2.250}$$

$$F_v \triangleq \rho_v\sqrt{\frac{4P_1\cos\phi_2}{\lambda_c|\mu_2|}} \tag{2.251}$$

  then the semi-major and semi-minor axes are given by F_v and F_u respectively (since $|\mu_1| > |\mu_2|$ as was earlier seen from (2.241) and (2.242)).

The quantities F_u and F_v are the analogues of E_u and E_v discussed earlier (ref. page 73). Hence, just as for E_u and E_v, although F_u and F_v were introduced for the case of elliptical boundary shape, they can be interpreted more generally as the dimension of the region measured along the $\hat{u}_0$ and $\hat{v}_0$ axes in all three cases (see Figure 2.36).

Some examples of these three cases of hyperbolic, linear and elliptical boundaries are shown in Figure 2.37. In these plots, the receiver azimuthal position ϕ_2 was fixed at 15° while the P_1-to-P_{gnd} ratio ρ was varied: for this value of ϕ_2, the critical value of ρ at which $\det\mathbf{M} = 0$ and hence $\mu_2 = 0$ is $\rho_{\text{crit}} = 3/(4\cos^2(\pi/12) - 3) \approx 4.1$ (ref. (2.245)). Thus: in Figure 2.37(a), $\rho < \rho_{\text{crit}}$, so $\mu_2 > 0$ and the 'good' region is bounded by hyperbolas; in Figure 2.37(b), $\rho = \rho_{\text{crit}}$, so $\mu_2 = 0$ and the 'good' region is bounded by lines; and in Figure 2.37(c), $\rho > \rho_{\text{crit}}$, so $\mu_2 < 0$ and the 'good' region is bounded by

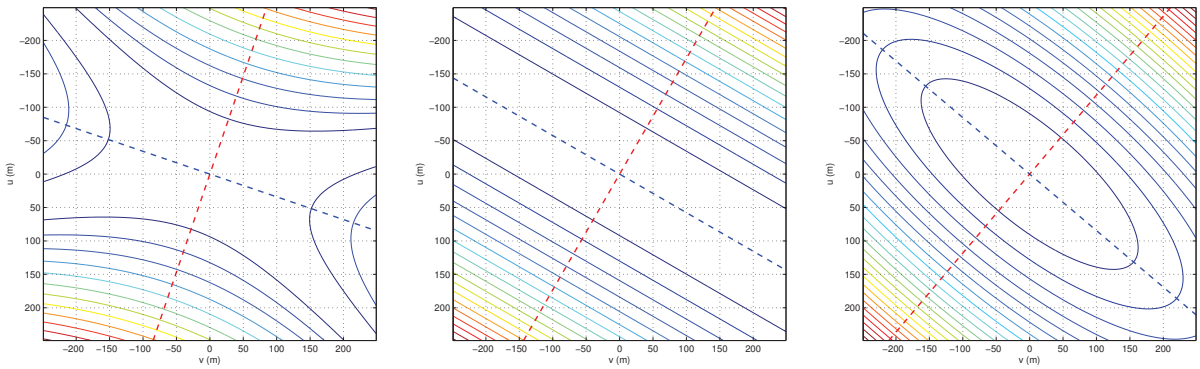

(a) $\rho = 2.0$, $\theta_u = -18.8°$, $F_u = 87.2$ m, $F_v = 160.4$ m (b) $\rho = 4.1$, $\theta_u = -30.0°$, $F_u = 79.7$ m, $F_v = \infty$ (c) $\rho = 6.0$, $\theta_u = -40.2°$, $F_u = 72.1$ m, $F_v = 203.7$ m

Figure 2.37: Contour plots of $|\Psi^{(2,2)}|$ for geometry shown in Figure 2.30 with $\phi_2 = 15°$, $\rho_v = 0.21$ m, $P_1 = 6500$ m (each contour corresponds to $|\Psi^{(2,2)}| = n\pi/4$ where $n = 1, 2, \ldots$ from the innermost contour outwards). Red and blue dashed lines indicate orientation of $\hat{u}$ and $\hat{v}$ axes respectively; calculated value of rotation angle θ_u is as shown.

an ellipse. From the figures, it can be observed that as ρ was increased, the $\hat{u}_0$ and $\hat{v}_0$ axes became increasingly rotated in a clockwise direction: this is in accord with Figure 2.34 from which we expect the angle θ_u to become increasingly negative. It may also be observed that the dimension of the 'good' region along the $\hat{u}_0$ axis F_u decreases as ρ increases: this trend is in agreement with the increasing value of $|\mu_1|$ expected from Figure 2.35(a) and the dependence of F_u on this implied by (2.250). In contrast, as ρ increases, the region's dimension along the $\hat{v}_0$ axis increases from its initial value of $F_v = 87.2$ m at $\rho = 2$ to infinity at $\rho = \rho_{\text{crit}}$ before decreasing again: this is in accord with the behaviour of μ_2 illustrated in Figure 2.35(b) which shows that μ_2 decreases and passes through zero at $\rho = \rho_{\text{crit}}$ so $|\mu_2|$ attains a minimum value of zero at $\rho = \rho_{\text{crit}}$ but otherwise increases as $|\rho - \rho_{\text{crit}}|$ increases (this affects F_v via (2.251)).

To conclude, in this section, we have addressed the problem of calculating the region of validity of the first-order (planar wavefront) phase approximation used in formulating the PFA. As we have seen, whereas an analysis of this problem for the monostatic case is relatively straightforward [39], a comparable analysis for the bistatic case is considerably more challenging. Nevertheless, expressions for the size of this region, based on limiting the defocussing effect of the second-order term in the series expansion of the elementary signal phase, were obtained for the specific case of a two-dimensional stationary-receiver bistatic imaging geometry (in which transmitter, receiver and scatterer positions are restricted to a single plane). Moreover, it was found that the boundaries of this 'good' region exhibit complicated behaviour not seen in the monostatic case: whereas the region is bounded only by hyperbolas in the monostatic case, the region in the examined bistatic case may be bounded by elliptical, linear or hyperbolic curves depending on the azimuthal separation of the transmitter and receiver and the ratio of the scene-to-transmitter and scene-to-receiver distances.

2.9 Results

The previous sections have presented a detailed discussion of the processing methods employed on the set of monostatic and bistatic SAR data which were collected in the *Ingara* bistatic SAR experimental trials. In this section, we present and discuss some representative examples of the resultant images which were obtained.

(a) Monostatic (b) Bistatic

Figure 2.38: VV-polarised (uncalibrated) (a) monostatic and (b) bistatic images of hill-top test site from simultaneously collected airborne and ground-based receiver data. Deployed targets are: D dihedral reflector; H hemisphere; T quadruple-pack trihedral reflector. Diagonal bands B_1B_2 and B_2B_3 are bare areas with no vegetation cover.

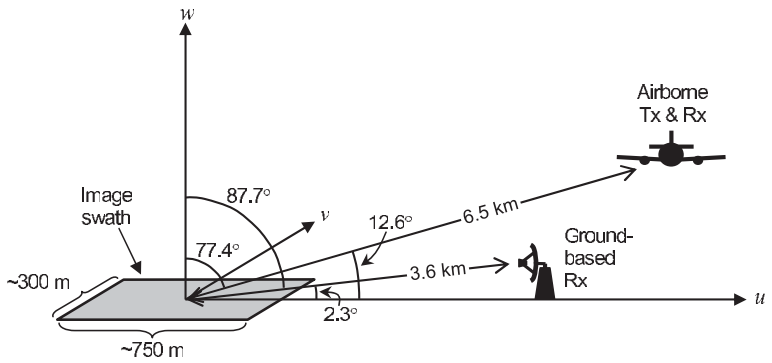

Figure 2.39: Imaging geometry for results in Figure 2.38.

Figure 2.38 shows imagery of the hill-top test site (ref. Figure 1.6) formed from monostatic and bistatic SAR data which were simultaneously collected by the airborne and ground-based receivers respectively. In forming these images, a two-dimensional Hamming window was applied to the resampled data prior to the Fourier transform, and the PGA was also applied[19] to estimate and compensate for the defocussing effect of azimuthal phase errors. For this data collection run, the collection geometry was such that the slant range and incidence angle of the aircraft, relative to the imaged site, were 6.5 km and 77.4° respectively, and the corresponding parameters for the ground-based receiver were 3.6 km and 87.7° (see Figure 2.39). The azimuthal separation angle between the aircraft and the ground-based receiver ϕ (ref. Figure 1.5) was zero at aperture centre, i.e. the aircraft, ground-based receiver and the scene focus point were all in the same vertical plane. The orientation of the images is such that the positive u-axis is directed downwards (so that near range is at the bottom) and the positive v-axis is directed rightwards; the nominal image dimensions are approximately 750 m in ground-range (vertical) by 300 m in azimuth (horizontal). The transmitted pulse length and bandwidth were 8 μs and 600 MHz respectively. Each image was formed using the echo data from 4096 consecutive pulses at a fixed effective PRF of 325 Hz; the typical aircraft speed over the collection period was 87 m/s.

The theoretical and measured range and azimuth -3 dB resolutions for these images are shown in Table 2.2: the theoretical values were calculated by scaling the results from (2.176) and (2.177) according to the FFT window used, while the measured values were obtained from cuts taken through the image of the central trihedral reflector along the u-axis (range) and v-axis (azimuth) directions (see Figure 2.40). The theoretical range resolutions are comparable for both images, but the theoretical azimuth resolution is twice as coarse in the bistatic as in the monostatic image: this is simply a consequence of the stationarity of the ground-based receiver which, unlike the *moving* airborne receiver, does not contribute to the Doppler phase-shift. Since the theoretical range resolution applies only to targets at a particular range such that the scattered signal will overlap fully with the dechirping signal during reception, the measured range resolution is likely to be coarser than the theoretical value.[20] Nevertheless, good agreement is observed between the theoretical and measured resolutions for the monostatic image along *both* range and azimuth directions. However, for the bistatic image, coarser resolutions were measured along both directions than would be expected from the theoretical values. The discrepancy between the theoretical and measured values of the range resolution of

[19] To avoid the effects of the $\Psi^{(2,2)}$ term (see footnote 15 on page 66), the PGA's error estimate was based only on the central part of the image containing the various radar reflectors.

[20] Indeed, the extent of overlap diminishes with displacement from the scene reference range (or, roughly speaking, as we go up or down from the centre of the image): for the geometry depicted in Figure 2.39 and a pulse length of 8 μs, the expected overlap at the extreme near and far ranges (bottom and top of the image respectively) is reduced by approximately 30% in both monostatic and bistatic cases, which corresponds to a coarsening of the full-overlap range resolution by a factor of 1.43.

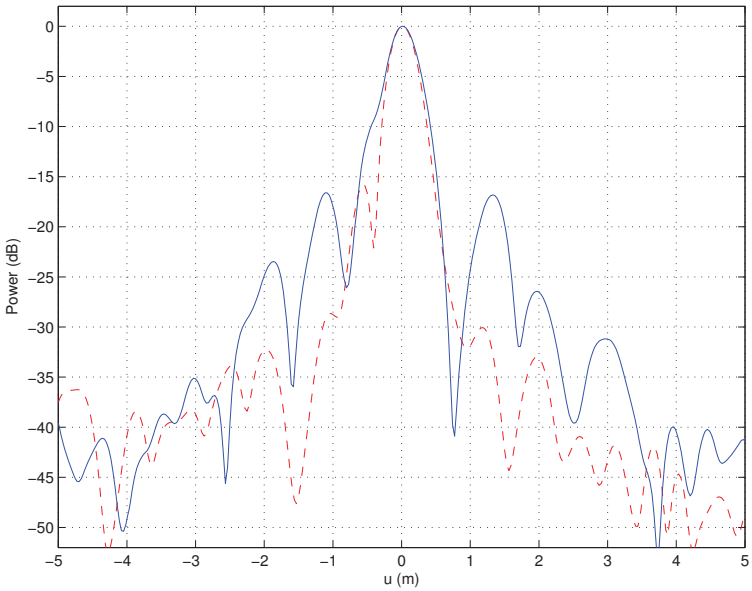

(a)

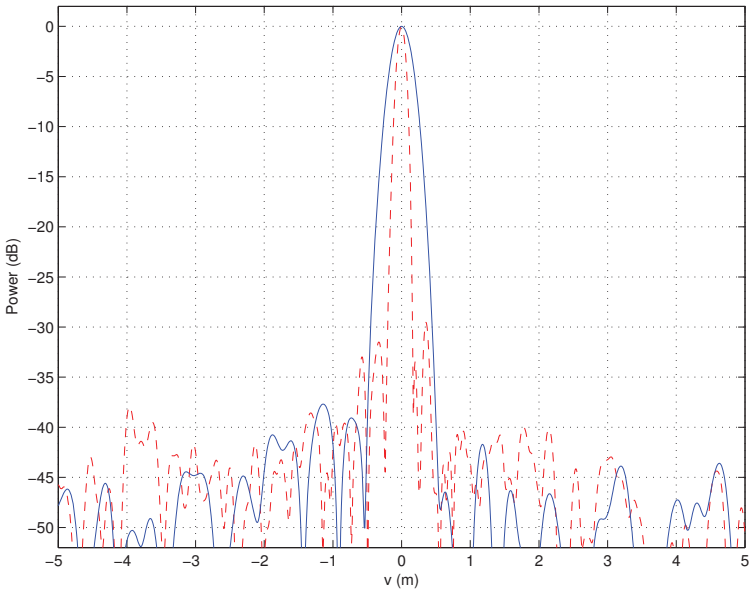

(b)

Figure 2.40: Profile of far-range centrally situated trihedral target along cuts taken through images in Figure 2.38 in: (a) vertical (range) direction; and (b) horizontal (cross-range) direction. Dashed red monostatic; solid blue bistatic.

Table 2.2: Theoretical and measured −3 dB resolutions for monostatic (airborne receiver) and bistatic (ground-based receiver) images.

Data source	Range resolution (m)		Cross-range resolution (m)	
	Theory	Measured	Theory	Measured
Airborne Rx	0.362	0.371	0.120	0.127
Ground-based Rx	0.345	0.405	0.240	0.297

the bistatic image is probably attributable to distortions introduced into the signal waveform by the RF hardware during transmission and reception: this is consistent with the high side-lobes in the range profile of the target (ref. Figure 2.40 (a)) which are present in both monostatic and bistatic images. (Higher side-lobes are observed in the bistatic than in the monostatic case, presumably because the transmitter and receiver hardware components are distinct in the former case whereas the components are common and shared in the latter.) The discrepancy between the theoretical and measured values of the azimuth resolution of the bistatic image may be the result of two factors. The first is uncompensated phase noise arising from drifts in the relative phase of the transmitter and receiver oscillators and motion measurement errors—on the whole, however, the azimuth profiles appear well-focussed, with a symmetric main-lobe and low side-lobes, which suggests successful compensation of the azimuthal phase errors by the PGA.[19] The second is the variation of the instantaneous bistatic target reflectivity with slow time, due to changes in the orientation of the reflection beampattern as the transmitter moves during aperture synthesis—since trihedral corner reflectors reflect incoming radiation monostatically, a monostatic receiver will always be on the boresight of the main-lobe of the reflection beampattern as the transmitter moves, but a bistatic receiver will be off-boresight and, consequently, may experience greater variability in its received signal.

From the discussion in Section 2.8, we expect that a degree of geometric distortion and azimuth defocussing will be present in these images, with severity increasing with distance from the centre of the images. From Figure 2.26 (b) and Figure 2.29 (a), the size of the region around the image centre in which $\left|\Psi^{(2,2)}\right| < \pi/4$ is roughly on the order of 130 m in range by 190 m in azimuth in the monostatic case and 170 m in range by 340 m in azimuth in the bistatic case. However, despite the relatively small estimated size of the focussed region, no such effects may be unambiguously detected on visual inspection of the images (there are inconclusive hints of possible azimuthal defocussing at the bottom extreme of the image). That no such effects are noticeable may be attributable to the unsuitability of the contents of this scene for revealing them: conceivably, a specially prepared scene containing a large array of regularly arranged point targets would render even mild amounts of distortion and defocussing readily apparent.

Interpretation of the images displayed in Figure 2.38 is greatly aided by reference to the photographic view of the scene from the perspective of the ground-based receiver, shown in Figure 1.6(a). In the centre of the images is the gently sloping open field in which various reflectors were deployed. The bright horizontally oriented linear features are returns from overhead power-lines crossing the field. The dark diagonally oriented bands extending down the bistatic image corresponds to areas of relatively bare earth having no vegetation cover. Vertically oriented shadows cast upon the field are also clearly visible: large shadows, arising from two groves of trees at the near edge of the field, are obvious, but multiple smaller shadows, cast by hay bales scattered through the field, may also be seen. The shadows in the monostatic image are shorter than in the bistatic image: this is attributable to the smaller incidence angle (and hence higher elevation) of the airborne radar and the larger incidence angle (and hence lower elevation) of the ground-based receiver. Careful inspection of the shadows cast by the trees reveals that the shorter shadows present in the monostatic image

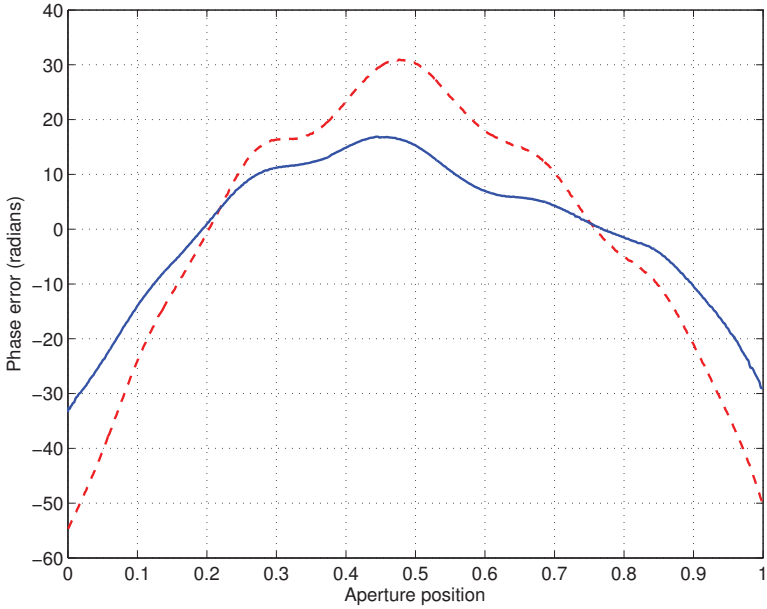

Figure 2.41: Phase error across synthetic aperture as estimated by PGA algorithm: dashed red monostatic; solid blue bistatic.

also appear in the bistatic image, where they are superimposed on the longer shadows from the low-grazing angle of the receiving dish: this is a manifestation of the double-shadow effect expected in bistatic SAR images, where the first shadow is cast by blockage of the radiation incident on the scene from reaching the shadowed area, while the second shadow is cast by blockage of the scattered radiation from the shadowed area from reaching the receiver. As a result, a greater proportion of the bistatic image is covered in shadow. These shadowing effects are presumably also the cause of the greater level of textural detail seen in the bistatic images, which is particularly evident in the ridged appearance of the field (cf. Figure 1.6(b)).

The illuminated area appears smaller in the bistatic than in the monostatic image: this is attributable to the different viewing geometries of the airborne and ground-based receivers. The narrower azimuthal extent in the bistatic image is a consequence of the shorter distance from the scene of the ground-based receiver: although both airborne and ground-based receivers have comparable azimuthal antenna beamwidths, the proximity of the ground-based receiver produces a narrower antenna azimuthal footprint than that of the farther airborne receiver, resulting in a more rapid roll-off of brightness towards the lateral edges of the bistatic image. The truncation of the illuminated area at far range in the bistatic image may be explained by the curvature of the top of the hill, which blocks the far edge of the field from the view of the lower ground-based receiver but not from the higher airborne receiver. As may be expected, however, trees in the background which are tall enough to protrude over the top of the hill remain visible in both images.

The use of separate oscillators in the transmitter and receiver of a bistatic SAR system affects the degree of synchronisation and relative phase stability achieved, and may pose a significant limitation on the quality of bistatic imagery obtained [17,33]. In particular, errors in the trigger times for the generation of the transmit and dechirp pulses and phase noise in the transmit and receive oscillators can induce severe degradation in the impulse response function (IRF), especially along the azimuth direction, by increasing the ISLR and broadening the main-lobe. To assess the impact of these error sources on the *Ingara* bistatic imagery, the PGA phase error estimates and the range and azimuth IRFs of the simultaneously acquired bistatic and

monostatic imagery were examined. Figure 2.41 shows the azimuthal phase error function across the aperture (formed over a 13 s coherent processing interval) which was estimated and corrected by the PGA. The shape of the curves for the monostatic and bistatic cases are similar, both having a large amplitude quadratic-like form on which a higher order modulation of smaller amplitude is imposed. A direct correspondence in the undulations of both curves may be seen, with the amplitude of the undulations in the monostatic curve being approximately double that in the bistatic. In general, motion measurement errors are a major contributor of azimuthal phase errors in monostatic airborne SAR, but, as previously alluded to, a significant contribution arising from drifts between the oscillators in the airborne transmitter and ground-based receiver may be expected in the case of bistatic SAR. However, the prominence of the quadratic component in the plots is consistent with motion measurement errors being the main contributor to the phase error functions in both the monostatic and bistatic data. This is supported by the geometric similarity of the undulations in the monostatic and bistatic curves, as errors in the aircraft position measurements may be expected to produce correlated phase errors in the data from both monostatic and bistatic receivers. Moreover, since both transmitter and receiver motion measurement errors contribute to the phase error in the monostatic case, but only the transmitter motion measurement error contributes in the bistatic case (the non-moving ground-based receiver has a constant position), the monostatic phase errors should be twice as large as the bistatic errors, which is consistent with the observations. Hence, these results suggest that the effect of oscillator phase noise on system performance is small compared to other factors.

The effect on the imagery of the changing transmitter-to-receiver azimuthal separation angle ϕ as the aircraft orbits during data collection is illustrated by the sequence of images presented in Figure 2.42. In this image set, the nominal dimensions of each image are 200 m in range and 200 m in azimuth. These images demonstrate a degradation as $|\phi|$ increases of the resolution of the bistatic images, even while resolution in the monostatic images remains constant. This effect is easily explained by referring to the expressions for the range and azimuth resolutions in (2.183) and (2.184): for the monostatic data, the terms on the right-hand-sides are all independent of ϕ, so ρ_u and ρ_v remain constant; however, for the bistatic data, the bistatic angle at the scene focus point $\bar{\beta}$ increases with increasing $|\phi|$, so the $\cos\left(\bar{\beta}/2\right)$ factor in the denominator decreases causing ρ_u and ρ_v to increase. Equivalently, by referring to Figures 2.8(b) and 2.9(b), it can be readily seen that in the monostatic case, the radial symmetry results in a constant-sized region of support (shown in blue) of the projected samples in the ground-plane which is independent of ϕ but, in the bistatic case, a smaller region is obtained for transmitter angular positions farther from the receiver: as resolution is directly related to the size of this region, fairly constant resolution independent of ϕ may be expected in the monostatic case, but a loss of resolution as $|\phi|$ increases would be expected in the bistatic case.

2.10 Conclusion

The processing of the *Ingara* monostatic and bistatic data sets into SAR imagery is based on a generalised version of the PFA, capable of handling both the monostatic and bistatic spotlight-mode SAR data in a unified manner. The processing steps involved have been described in this chapter. The initial step is the preprocessing of the raw echo signal to stabilise the phase of the transfer function from a reference point in the imaged scene and to remove the residual video phase. The data is then resampled from an irregular polar grid to an intermediate keystone-shaped grid to the final parallelogram-shaped grid. Once on this grid, a PGA-based autofocus procedure is applied to the data array to estimate and correct one-dimensional azimuthal phase errors which would cause defocussing of the image. A two-dimensional discrete Fourier transform which

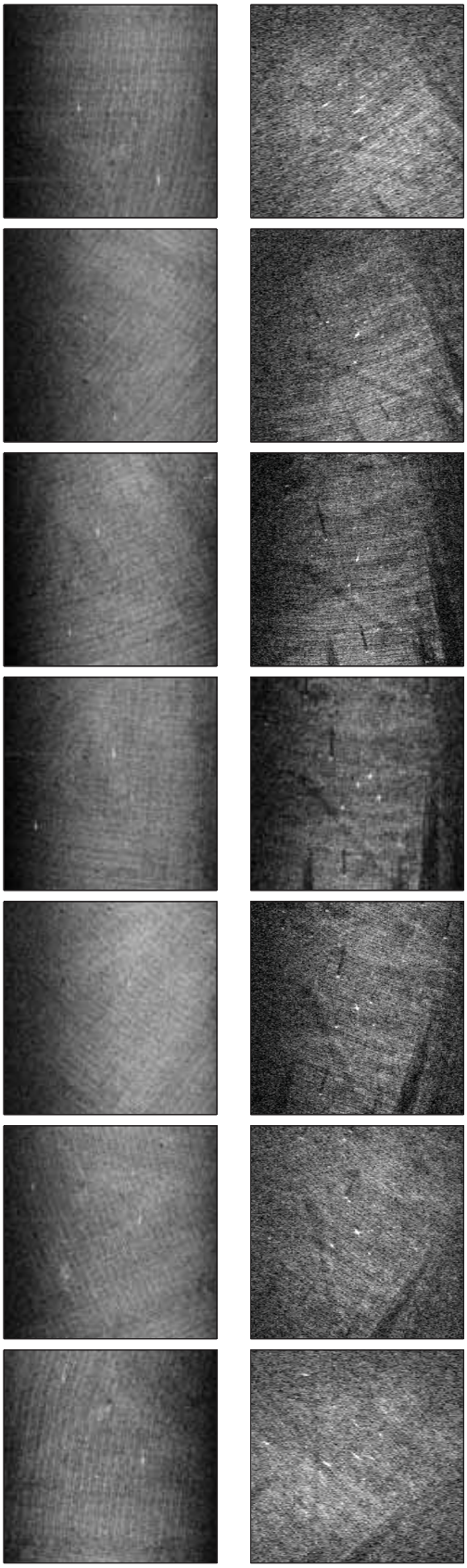

Figure 2.42: Change in monostatic (left column) and bistatic (right column) HH-polarised (uncalibrated) imagery with transmitter-to-receiver azimuthal-separation ϕ: from top to bottom row, $\phi = -90°$, $-60°$, $-30°$, $0°$, $30°$, $60°$, $90°$.

takes account of the parallelogram-shaped sampling grid is then applied to the data, which produces the final SAR image.

By deriving an analytic model for the complex SAR image, it is shown that the image is comprised of a superposition of PSFs, one for each elementary scattering centre in the scene. Information about the physical scattering properties of each scatterer is conveyed by an amplitude and phase scaling of the PSF, while the geometric position of the scatterer is encoded in a phase shift as well as the position of the PSF in the image. This phase shift which is applied to the PSF is dependent on the height of the scatterer above the image plane, and can be exploited by interferometric techniques for estimating topography. The position of the PSF is the orthogonal projection of the scatterer's position into the image plane but displaced by a height-dependent shift: this is the basis of the layover effect by which objects in the image appear unnaturally shifted towards the radar. The estimated bistatic image resolutions along orthogonal range and azimuth directions are dependent on the bandwidth and angular diversity of the bistatic line-of-sight vector respectively as well as the bistatic angle. As expected, these reduce to the familiar monostatic expressions when the bistatic angle is zero.

The useful size of the SAR image can be estimated by considering the uncompensated second order phase term, which gives rise to geometric distortion and azimuthal defocussing. Unlike the monostatic SAR case, however, this is difficult to do in the general bistatic SAR case because of extra degrees of freedom introduced into the calculations by allowing potentially independent trajectories for the transmitter and receiver. By constraining the trajectories to particular cases, however, the problem becomes more tractable. Even for the specific case of circling-transmitter-fixed-receiver spotlight-mode SAR, the complexity of the analytic expressions obtained is sufficiently great that numerical results for particular cases offer more insight into the effects present. Assuming defocussing to be the limitation on useful scene size, the results for a representative *Ingara* collection geometry indicate an expected useful scene size (range-by-azimuth) on the order of 130 m-by-190 m in the monostatic case and 170 m-by-340 m in the bistatic case for an aperture synthesised when the transmitter and bistatic receiver are in the same horizontal direction from the scene.

The image results obtained from the processing appear well-focussed with resolutions comparable to the theoretical expected values for the monostatic data but coarser for the bistatic data. The discrepancy in the range resolution is probably ascribable to a reduction in the support of the dechirped signal away from scene centre and waveform distortions introduced by the RF hardware. The discrepancy in the azimuth resolution is likely attributable to uncompensated phase noise and an aspect-dependence of the scattering response. There is no obvious defocussing or geometric distortion on visual inspection over the approximately 750 m-by-300 m extent of the images (although, due to the composite beampattern of the transmitter and receiver, the area in which objects appear illuminated and visible is smaller than this): this may simply be due to the contents of the scene which lacks strong point targets far from the centre and hence does not permit these image aberrations to be easily detected.

For the image results presented, the collection geometry was such that the airborne radar (with its monostatic receiver) was at a higher elevation than the ground-based bistatic receiver. Consequently, significant qualitative differences are apparent in the appearance of the monostatic and bistatic images, particularly shorter shadows in the monostatic than the bistatic image and a greater proportion of shadow in the bistatic image. As a result, textural details of the open terrain in the imaged scene are more easily seen in the bistatic than the monostatic image—this illustrates a potential utility of the freedom afforded by bistatic imaging to image the scene in unconventional geometries.

Chapter 3

Interferometry

3.1 Introduction

The basic product of the SAR image formation process is a complex-valued image, having both magnitude and phase. For many purposes, however, the phase is usually discarded and only the magnitude is shown. This is largely because, on casual visual observation, the phase image appears random and uninterpretable whereas, with a suitable mapping of magnitude to grey-scale values, the magnitude image can be given a similar appearance to a black-and-white aerial-reconnaissance photograph so is easily interpreted. Despite its apparent randomness, valuable information is contained in the image phase, which can be extracted by comparing the phase between a pair of SAR images: since the phase is deterministically related to the target scattering properties and the wave propagation distance, the inter-image *phase difference* encodes information about changes in the scattering properties and propagation distance between the two observations.

Interferometry is a major application of SAR data which exploits this phenomenon [47, 48]. By making use of the phase differences between two or more complex-valued SAR images collected from different viewing angles or at different times, it allows the measurement of small differences in relative range or the detection of subtle changes in the scene reflectivity function. The high sensitivity to differential range is often employed to make measurements of scattering centre height or displacement over an imaged scene on the dense sampling grid and with the wide area coverage typically afforded by SAR imagery. Indeed, the technique of SAR interferometry is now widely used with numerous applications including the topographic mapping of terrain, study of glacier and lava flow, monitoring of surface deformation (e.g. from subsidence or seismic or volcanic events), measurement of ocean currents and detection of moving objects.

Topographic terrain mapping for the production of high-quality digital elevation models (DEM) is an important application of interferometric SAR. As the topographic sensitivity obtained from interfering a pair of SAR images increases with the separation (baseline) between the cross-track antenna positions during data collection, it is desirable to employ a longer baseline (within certain limits) for DEM generation in order to increase the sensitivity to terrain height. The required long baselines can be simply achieved by repeat-pass collections, in which the SAR platform makes two separate collection passes along trajectories separated by the desired distance, while acquiring an image on each pass. However, this collection approach results in an unavoidable temporal delay between the images, during which changes in the scene or the atmospheric propagation conditions may occur: such changes hinder the accurate measurement of the phase signal of interest and hence the terrain topography. To avoid such effects, interferometric data collection in a single-

pass mode is preferred: this requires that two receiving antennas separated by the desired distance must be simultaneously operating during the collection pass. Hence, in order to achieve a long baseline with a single SAR platform, an appropriate means of maintaining the desired cross-track separation between the antennas must be found, e.g. a 60 m-long rigid mast was employed for this purpose in the Shuttle Radar Topography Mission [123]. For typical spaceborne SARs orbiting at higher altitudes, however, even longer baselines will be needed, for which maintaining antenna separation by a long rigid structure becomes unwieldy and infeasible. A natural solution is then to employ two separate platforms with each carrying one of the antennas (with either one or both platforms transmitting): a large separation can then be achieved between the two receiving antennas without a cumbersome physical connection.

Such a two-platform SAR system operates both monostatically and bistatically depending on whether the transmitter is co-located with the receiving antenna. Hence, for the bistatically operating element, the usual opportunities and challenges of bistatic SAR apply, but some additional facets are presented, however, by the interferometric combination of the monostatic and bistatic images. For example, the azimuthal phase errors caused by phase drifts between the independent transmit and receive oscillators produce a low-frequency modulation of the phase relationship between the monostatic and bistatic images [33] which must be accounted for to avoid height errors in the DEM products. This effect is more serious in stripmap-mode SAR imagery, where a low-frequency phase undulation along the lengthy azimuthal dimension will be easily noticeable but less so in spotlight-mode SAR imagery with much smaller dimensions: its main effect in the latter will be to change the phase offset between images collected at different times but this can be compensated for on an image-by-image basis when determining absolute terrain altitudes by using a known ground reference point. Azimuthal phase errors also cause azimuthal defocussing of the bistatic SAR imagery: without autofocus compensation, this can reduce the coherence between images and hinder the precise measurement of the interferometric phase. Another potential issue is raised by possible changes in scatterer reflectivity with bistatic angle, which may result in unwanted differences between the monostatic and bistatic images, thus similarly reducing their coherence and hindering interferometry.

The *Ingara* monostatic and bistatic data sets provide an opportunity for gaining insights into some of the properties and challenges of SAR interferometry employing bistatic data. This chapter discusses the application of interferometric techniques to the *Ingara* data set and presents encouraging initial results demonstrating the achievement of coherence and interference fringes. To begin, some general background to the topic of SAR interferometry is given in the Section 3.2. Then, the main stages of the interferometric processing procedure which was employed are presented: this comprises the steps of aperture trimming (Section 3.3), image registration (Section 3.4) and coherence calculation (Section 3.5). Section 3.6 discusses the information encoded in the interferogram phase, with a particular focus on topographic height. Some interferometric results are then presented in Section 3.7. Finally, some conclusions are drawn in Section 3.8.

3.2 Background

The first demonstration of topographic mapping using interferometric SAR has been credited to Graham [124], who used a two-antenna single-pass airborne SAR with optical processing: by summing the signals from the two antennas, an amplitude image with a pattern of null-lines corresponding to predetermined depression angles was produced, from which contour maps could be generated. The generation of interferometric products via this analogue processing technique has inherent limitations which render the process indirect and inflexible. The subsequent development and widespread adoption of digital SAR processing techniques, however, has

greatly expanded the ease and potential of interferometric processing, such that SAR interferometry is now a widely employed application of SAR data.

The key phenomenon underlying interferometry is the sensitivity of the phase in a SAR image to the electromagnetic propagation distance from transmitter to scattering centre to receiver: if λ is the effective wavelength of the radiation, then the range sum R_{s} contributes a term $2\pi R_{\mathrm{s}}/\lambda$ to the SAR image phase. Since the wavelengths employed by SARs are relatively short (e.g. approximately 25 cm for L-band, 6 cm for C-band and 3 cm for X-band), even though R_{s} may be on the order of several kilometres or greater, changes in R_{s} on the order of millimetres to centimetres can produce easily measurable phase changes on the order of radians. However, numerous effects affect the absolute phase of a SAR image pixel such that it effectively exhibits random behaviour and cannot be reliably predicted, so useful information can only be extracted from observed phase *differences*. Hence, a *pair* of images from which phase differences can be calculated comprises the minimum set of input data required for interferometric analysis: often, the desired phase difference between a given image pair Ω and Υ is obtained from the phase of their interferogram $\Omega\,\Upsilon^*$.

Some carefully introduced difference in the collection geometries or times between the pair of SAR images of a particular scene must be present in order to extract meaningful interferometric data. (Clearly, if two images are identical, then there can be no informative difference between their phases.) Within certain appropriate constraints, images differing only in their collection geometries are analogous to stereoscopic photography, and their phase difference corresponds to differences in R_{s} caused by differences in viewing directions, while images differing only in their collection times are analogous to time-lapse photography, and their phase difference corresponds to changes in R_{s} which have occurred between observations. In practice, for a single-platform system with a single receive-antenna, a mixture of spatial and temporal diversity will usually be present even when only one is desired: to collect two spatially separated images, two passes with different trajectories are required, hence introducing a temporal delay between the images, while to collect two temporally separated images, two passes at different times are required, and this tends to introduce a spatial difference between the images due to the difficulty of precisely replicating the collection geometry. Hence, some combination of geometry- and time-induced phase changes will be present in the interferograms. Such problems may be mitigated by having two receive-antennas separated by a baseline: with a cross-track baseline orientation, two images from slightly different grazing angles can be collected simultaneously while, with an along-track baseline orientation, two images with a short intervening delay can be collected from the same look direction. However, as previously mentioned, such a baseline implemented by a rigid structure becomes impractical for large differences in look direction or observation times whereupon, for the first case, a two-platform solution with a bistatic element may be called for. Such a two-platform solution does not greatly benefit the second case since the original navigational limitations will still likely afflict both platforms: in practice, an appropriate correction is usually made during data processing for the geometry-induced phase changes to allow the time-induced phase changes of interest to be measured.

Phase differences arising from changes in SAR observation geometry are most often exploited for topographic terrain mapping—indeed, this was the intent of the aforementioned pioneering work of Graham [124]. Topographic mapping by SAR interferometry represents a major improvement over previous optically based stereo-photogrammetric approaches as it can be largely automated and is unaffected by cloud cover or the need for solar illumination. In such cross-track interferometry applications, a cross-track difference in the receiving antenna phase centres is used so that a small grazing-angle difference is introduced between the two images. Similar (parallel) trajectories of the two antennas are desirable, which is easily achieved in a single-pass collection by a two-antenna single-platform SAR [125], but requires careful navigation in single-platform repeat-pass collections or two-platform single-pass collections. However, with appropriate effort, interferometry can still

be performed with success on data collected with non-parallel crossing trajectories [126].

Phase changes occurring between temporally separated SAR observations encode information about changes which have occurred in the region being observed. A major cause of such changes are simple bulk displacements of the surface under observation causing changes in the range sum R_s. The interval between observations must be appropriately matched to the speed of the movements: too short an interval will not record sufficient change to be detectable while too long an interval will result in decorrelation between the images and hinder phase measurements. Hence, fast ocean surface currents require a short observation interval which can be achieved by a single-pass two-antenna along-track interferometer [127, 128]. However, slower movements require longer intervals which are better achieved with repeat-pass observations but, as previously mentioned, cross-track differences in collection trajectories often introduce an unwanted phase component arising from terrain topography. Unless the cross-track baseline is small, the topographic phase will be significant and must be subtracted away to measure the surface movements of interest: this can be simply done if a DEM is available from which the topographic phase can be calculated. Otherwise, the technique of differential interferometric SAR can be employed [129]: essentially, a third SAR image is used to generate a second interferogram containing the topographic phase whereupon, by differencing the phases between the two interferograms, a 'double-difference interferogram' is then produced from which the topographic phase contribution has been removed leaving only the phase component arising from surface movement. The ability to measure slow surface movements over a wide area at a high sampling density has proven invaluable to a multitude of Earth science applications, e.g. in observing and monitoring co-seismic displacements [49], volcanic deformation [50], land subsidence [130], ice-sheet motion [131], glacier flows [132], etc.

Apart from bulk surface displacements, another cause of phase changes between temporally separated observations are changes in the positions of scattering centres within a resolution cell. Such changes may occur naturally, e.g. from the movement of wind-blown leaves or seasonal changes in vegetation, but may also arise from human activities, e.g. vehicle movements or battle damage. For subtle changes, the magnitude of the scattering process may not be appreciably affected, so such changes may not be detectable in conventional magnitude-only SAR imagery, but can be easily detectable when the phase is taken into account. This interferometric phenomenon can thus be usefully exploited for the coherent detection of scene changes [51, 133–135]. For spaceborne SARs, a further cause of inter-image phase differences is changes in the propagation conditions of the radar signals through the atmosphere: phase delays due to refractive changes can impose unwanted artefacts on the phase signal of interest [136]. For repeat-pass topographic mapping, this effect can be mitigated by increasing the baseline (and hence the amplitude of the topographic signal relative to the atmospheric phase artefact) or by averaging of multiple interferometric DEMs. In an interesting reversal of the problem, however, it has been demonstrated that, by accounting for the phase signal from surface topography and deformation, the atmospheric phase artefacts can be used to map atmospheric water vapour distributions [137].

In addition to interferometry, cross-track SAR image pairs may also be employed for range-resolution enhancement [57, 59]. Due to the wavenumber shift effect [56], a relative offset is present between the support of such pairs in the range spatial frequency domain (this gives rise to baseline decorrelation as discussed below). This effect can be exploited by coherently combining suitable image pairs to synthesise a new image with wider support along the range spatial frequency domain: since spatial resolution is inversely proportional to the spatial frequency support width, the range-resolution of the combined image should be finer than that of the original images. This technique may thus be of value in achieving improved range-resolution without increasing the transmitted bandwidth: hence, although distinct from (but still related to) classical SAR interferometry, it may still be considered as another potentially useful application of cross-track SAR data

sets collected for interferometric purposes.

The accurate measurement of the phase difference between an interferometric pair of images is dependent on the correlation between the two images: a high correlation suggests that a valid correspondence exists between the resolution elements in the two images so that their phase difference can be meaningfully interpreted. This correlation can be usefully measured by the magnitude of the complex correlation coefficient γ, and the interferometric phase is related to the phase of γ such that $|\gamma|$ strongly affects the accuracy of phase measurement [138]. Hence, a reduction in correlation between the images should be minimised as far as practicable. Such decorrelation may arise from a variety of sources [139], e.g. thermal noise, image misregistration and defocussing will all affect the essential similarity between the images and reduce their correlation, but these are basically engineering-related factors and can be mitigated by careful radar hardware and processing software design. Other sources of decorrelation are more intimately related to the physics and phenomenology of SAR, e.g. shifts in the phase relationships between multiple scattering centres in a resolution element when viewed from different directions give rise to spatial baseline decorrelation, volume decorrelation and decorrelation due to rotation [139] while random changes in the scatterer arrangement between observations give rise to temporal decorrelation. Although baseline decorrelation is explicable in terms of the fading phenomenon [140], it can also be understood in terms of a shift in the transduced wavenumber spectra of the return signal from a scene: mitigation measures thus include the use of larger bandwidths and/or offset centre frequencies during SAR data acquisition or, at the expense of resolution, through frequency-offset filtering of the SAR signals prior to image formation [56]. Volume and rotation decorrelation is not easily mitigated other than by employing longer wavelengths or smaller differences in the look directions. Since most surfaces naturally undergo changes with time (e.g. wave patterns over lakes, grass waving in the wind, abscission by deciduous forests, etc.), temporal decorrelation is generally unavoidable and represents a limiting factor for successful repeat-pass interferometry [141, 142]: possible mitigation measures are the reduction of the temporal interval between observations or the use of longer wavelengths.

Significant enhancements to the utility of interferometric data are afforded by polarimetry: as target polarimetric signatures are sensitive to the scattering mechanisms, the availability of fully polarimetric measurements permits the selection of mechanisms to optimise the interferometric coherence [62]. The combination of polarimetry and interferometry provides sensitivity to the vertical distribution of scattering mechanisms such that a direct phase-difference between interferograms can be employed as a crude estimator of tree height [62]. More accurate results may be obtained by using the techniques of polarimetric interferometry in conjunction with suitable models of the scattering behaviour of vegetation layers over ground [143, 144]. Polarimetric interferometric SAR techniques are thus of value for forest biomass estimation as well as other potential applications.

As may be inferred from the above, spaceborne SAR systems are a major source of interferometric SAR data. Yet, currently the availability of data suitable for SAR interferometry from spaceborne platforms is limited. For example, it may not be feasible to immediately image an area of interest to fulfil an urgent new collection requirement. Alternatively, if opportunistic use is being made of previously collected archival data instead, it may be that the area in question has not been previously imaged or, if it has, the spatial baseline separation or temporal delay between images may be excessive and unsuitable for interferometric analysis. A further difficulty is that, for two-pass differential SAR interferometry, an appropriate high-quality DEM may not be available for topographic phase removal. Consequently, efforts have been underway to address these deficiencies by deploying new spaceborne SAR systems specifically designed for interferometry: these generally take the form of multi-satellite systems operating in bistatic and multistatic modes in which a conventional spaceborne SAR is supplemented by additional receivers on accompanying satellites. Various configurations

have been proposed and studied for such satellite systems [8], ranging from a simple adjunct satellite to complex multi-satellite constellations: examples include the twin-satellite TOPSAT configuration [145],[1] the RADARSAT-2/3 tandem mission [146–148], the soon-to-be-deployed TanDEM-X mission [13], the TanDEM-L mission proposal [149] and the multisatellite Interferometric Cartwheel [10, 11]. In addition, some paired satellite missions with large orbital separations, such as the satellite supplement to ENVISAT-1 [7], and the passive SABRINA/BISSAT companion to COSMO/Sky-Med [12,150–152], have also been proposed which are primarily intended for making bistatic observations rather than interferometry: as topography estimation by coherent interferometric processing is precluded by the large baselines, non-coherent stereoscopic techniques have been proposed instead [7, 153]. Of course, with a different choice of orbits giving suitable baselines, conventional interferometric operation should also be possible.

Such multisatellite interferometric constellations present various challenges and are a not insignificant motivating factor for the current research interest in bistatic SAR. A simple, flexible and cost-effective way for investigating these challenges before the costly final deployment of the spaceborne platforms is through the conduct of airborne and ground-based experiments: these provide important opportunities to identify, understand and solve some of the problems posed by bistatic SAR operation and interferometry in order to better inform the planning and design of the operational mission. Some examples of bistatic SAR interferometry experiments which have been performed to date include the ONERA-DLR bistatic SAR experiments employing their airborne RAMSES and E-SAR systems [54, 154] and the Polytechnic University of Catalonia's (UPC) work with their ground-based SABRINA receiver [18, 155].[2] Although the interferometric aspect of these experiments is the main interest in the present context, such work is, of course, also of value in developing experience with bistatic SAR in general.

An interferometric analysis of the data collected in the *Ingara* bistatic SAR experiments may thus be of potential interest. In the next three sections, we discuss the processing procedures employed for an initial interferometric analysis of the *Ingara* data, starting with the topic of aperture trimming.

3.3 Aperture trimming

Interferometry involves the coherent analysis of a pair of SAR images to extract phase-sensitive information. Generally, the quality of the results obtained is greatly dependent on the correlation between the pair of images being analysed. One source of decorrelation is poor overlap of the phase histories in the spatial frequency domain: in order to minimise this effect, due account must be taken of the spatial frequency extents of the two data sets so as to 'trim away' regions which will contribute uncorrelated signals to the SAR images. Such trimming is especially important in cases where the two SAR data sets were collected with highly disparate viewing geometries: this includes the case of data simultaneously collected by a moving airborne monostatic receiver and a stationary ground-based bistatic receiver (e.g. the *Ingara* system).

The three-dimensional positions of two SAR data sets in the spatial frequency domain is largely dictated by the radar centre frequency, the bandwidth and the direction of the bisector of the bistatic angle. In general, even with a fixed radar centre frequency and bandwidth, due to differences in the collection geometry, these positions will not coincide. In interferometric collections, usually a difference in the grazing angles ψ_i of the two collections will be present (Figure 3.1), where the collection grazing angle may be defined as the grazing

[1] TOPSAT should not be confused with the United Kingdom's optically instrumented TopSat microsatellite launched in October 2005.

[2] The UPC's ground-based receiver SABRINA (SAR Bistatic Receiver for Interferometric Applications) should not be confused with the Italian Space Agency's proposed orbiting satellite mission SABRINA/BISSAT (System for Advanced Bistatic and Radar Interferometric Application/Bistatic and Interferometric SAR Satellite).

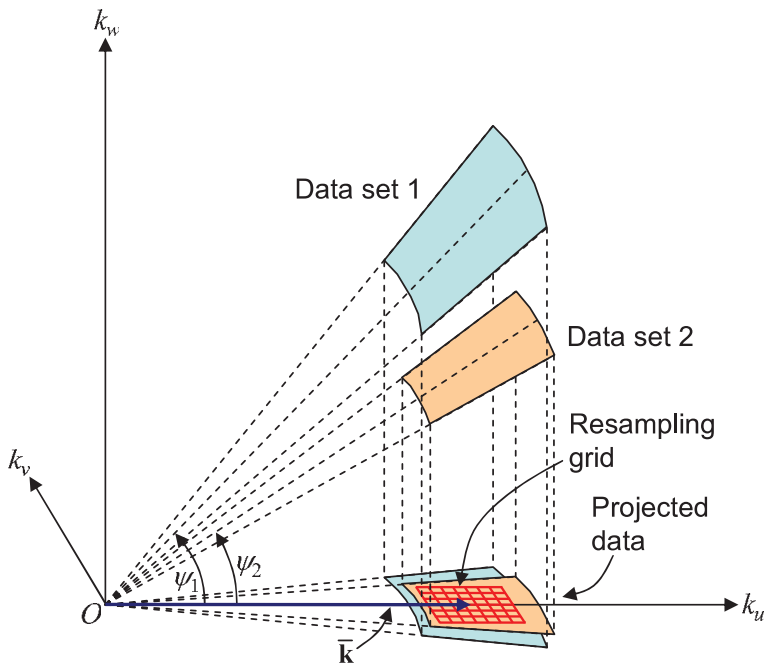

Figure 3.1: Illustrative phase history positions in the three-dimensional spatial frequency domain of *Ingara* monostatic (blue) and bistatic (beige) data sets.

angle of the bisector of the bistatic angle at aperture centre (for a monostatic collection, it is the actual grazing angle of the SAR platform while for a bistatic collection, it is the mean of the grazing angles of the transmitter and receiver). In the case of topographic mapping, where a non-zero cross-track baseline is desired for height sensitivity, such differences will be deliberate. However, in the cases of coherent change detection and terrain motion mapping, where an identical grazing angle is desirable, such grazing angle differences may still inadvertently arise due to navigational limitations in replicating the collection geometry in two separate data collection passes. As a result of this difference, the projected supports of the two phase histories in the spatial frequency domain will be shifted relative to each other along the ground range direction [56]. Along the cross-range direction, differences in the azimuthal direction of the bistatic bisector during the two collections result in shifts or otherwise poor overlap of the two data sets. Moreover, for a fixed bistatic receiver configuration like that used in the *Ingara* experiments, the radial vector $\mathbf{B}_n$ (recall (2.47)) changes its azimuthal direction at a higher rate for the monostatic data from the moving airborne receiver than for the bistatic data from the ground-based receiver: this results in the monostatic data covering a larger range of azimuthal angles than the bistatic data (see Figure 3.1). Generally, then, along both range and azimuth, the resultant projections will have a common region of overlap as well as various non-overlapping regions (Figure 3.2).

The presence of the non-overlapping regions has an adverse effect on the quality of the interferometric results by reducing the correlation between the images from the two data sets. The reason for this can be understood from the statistical properties of the spatial reflectivity function of natural rough terrain. This function can be modelled as a wide sense stationary (WSS) random process with independent samples: as a result, its Fourier transform is also WSS and also has independent samples. Thus, the non-overlapping regions of the two SAR phase histories will be statistically independent, so the contributions to the SAR images made by the Fourier transform of each of these non-overlapping regions will also be independent of each other.

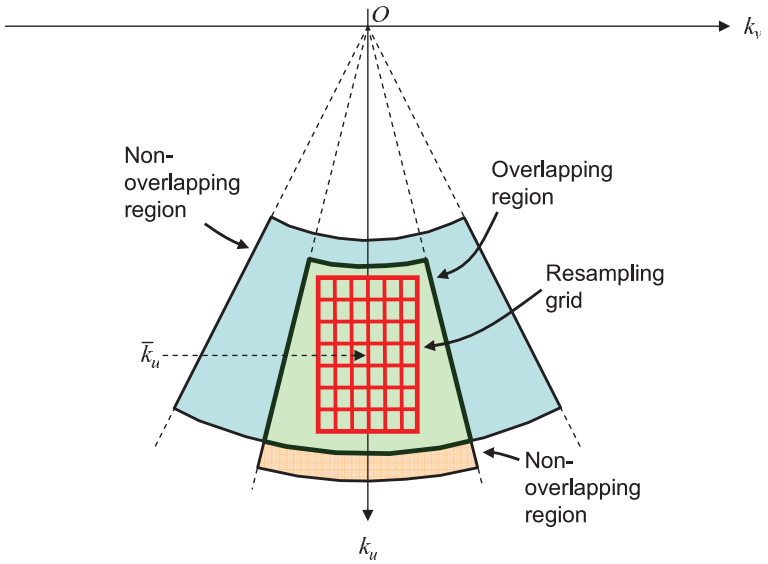

Figure 3.2: Projected phase history supports of data sets, showing overlapping and non-overlapping regions. Resampling grid is chosen to lie in the common region of overlap.

By contrast, however, only the contributions from the common area of support in the two data sets will be correlated in both images. Hence, to maximise the image cross-correlation, only the contribution made to the images by their common area of support in the spatial frequency domain is desired: contributions from the non-overlapping regions simply contribute uncorrelated 'nuisance' signals which hinder interferometric analysis.

Thus, in forming SAR images for subsequent interferometric processing, the spectral envelopes of the data sets should be well-aligned [138], i.e. only the common area of support in the spatial frequency domain of the data sets should be used. This can be achieved by *aperture trimming*, in which the non-overlapping regions are discarded and only the common overlapped region is retained for image formation [39]. Such trimming effectively processes the data with bandwidth reduction filters to retain only common spectral components: although this reduces the spatial resolution of the resultant imagery, the decorrelation can be significantly reduced [56].

In practice, for processing the *Ingara* data, the aperture trimming procedure was implemented by judiciously choosing a common resampling (parallelogram) grid lying within the common region of support of both data sets (ref. Figure 3.2). Upon resampling each data set to this common grid, both of the resampled data sets will have the same projected indicator function $\kappa(\tilde{\mathbf{k}}; \bar{\mathbf{k}}, \mathbf{R})$ and projected reference vector $\bar{\mathbf{k}} = \bar{k}_u \, \mathbf{a}_u$. As $\bar{\mathbf{k}}$ is common and the coupling between $\bar{\mathbf{k}} + \tilde{\mathbf{k}}$ and $\mathbf{R}$ in $\kappa(\cdot)$ is weak, we will simplify the notation and write $\kappa(\tilde{\mathbf{k}}; \bar{\mathbf{k}}, \mathbf{R})$ as $\kappa(\tilde{\mathbf{k}})$: its Fourier transform will then be denoted by $\hat{\kappa}(\mathbf{r}')$. This result will shortly be used in Section 3.6.

3.4 Image registration

Ideally, for the purposes of interferometric processing of a pair of SAR images, each scattering centre should appear at identical positions in each image. Generally, however, different scatterer displacements are often encountered, so that the pixels corresponding to the scatterer have different indices in each image. Various

sources contribute to this effect, including differences in layover, errors in platform position measurement, frequency differences and phase drifts between the transmit and receive oscillators, and geometric distortions from the image formation algorithm. In addition to these effects, differences in apparent scatterer position may also arise between images formed from data simultaneously collected by different receivers (e.g. the airborne monostatic and ground-based bistatic receivers employed in the *Ingara* data collections) as a result of differences in the RF delays of the distinct receiver hardware. Hence, when two SAR images are being interferometrically processed, it is necessary to account for these displacement effects to ensure that corresponding points of the ground reflectivity function are being compared. This can be done by determining a suitable warp which maps positions in one image (the source image) onto corresponding positions in the other image (the target image), then resampling the source image so that the resampled pixels directly correspond to the pixels in the target image. This procedure is referred to as *image registration* and we discuss a method (based on that of Jakowatz et al. [39]) for its implementation in this section.

We begin, in the next sub-section, by introducing the fundamental ideas underlying the image registration procedure. This is followed by a discussion of the process by which the mapping required to warp the source image onto the target image is determined. Finally, we discuss the procedure for image resampling, by which the mapping which was determined is used to produce a registered version of the source image.

3.4.1 Basic idea

Let $\Omega(u, v)$ and $\Upsilon(u, v)$ represent the source and target images respectively. Since the images are produced via DFTs, we will actually have samples (i.e. pixels) of the two underlying continuous images, i.e. for indices $k = 0, 1, \ldots, N_u - 1$ and $l = 0, 1, \ldots, N_v - 1$, we will have the sample values

$$\Omega_{k,l} = \Omega(u_k, v_l), \tag{3.1}$$

$$\Upsilon_{k,l} = \Upsilon(u_k, v_l), \tag{3.2}$$

at the corresponding sample positions (u_k, v_l) in each image given by

$$u_k = u_0 + k\,\delta u, \tag{3.3}$$

$$v_l = v_0 + l\,\delta v, \tag{3.4}$$

in which δu and δv are the sampling intervals along the u and v directions. As previously discussed, a given scatterer appearing at a location (k', l') in image $\Upsilon_{k,l}$ may well appear at a different location (k'', l'') in image $\Omega_{k,l}$: to facilitate processing, it is necessary to determine the relationship between the positions of scattering centres (k'', l'') in image $\Omega_{k,l}$ and their corresponding positions (k', l') in image $\Upsilon_{k,l}$. Then, by employing this relationship between the positions, $\Omega_{k,l}$ can be resampled to produce a new image $\hat{\Omega}_{k,l}$ such that a scatterer appearing at (k', l') in $\Upsilon_{k,l}$ also appears at the same position (k', l') in $\hat{\Omega}_{k,l}$. The image $\hat{\Omega}_{k,l}$ thus represents the result of registering the source image $\Omega_{k,l}$ onto the target image $\Upsilon_{k,l}$.

The relationship between the corresponding positions in the two images may be represented by a pair of functions $\hat{k}(k, l)$ and $\hat{l}(k, l)$ such that the resampled image

$$\hat{\Omega}_{k,l} = \Omega_{\hat{k}(k,l),\hat{l}(k,l)} \tag{3.5}$$

corresponds directly to $\Upsilon_{k,l}$ on a pixel-by-pixel basis. The functions $\hat{k}(k, l)$ and $\hat{l}(k, l)$ thus specify how the source image $\Omega_{k,l}$ should be distorted or *warped* so as to register it onto the target image $\Upsilon_{k,l}$. The

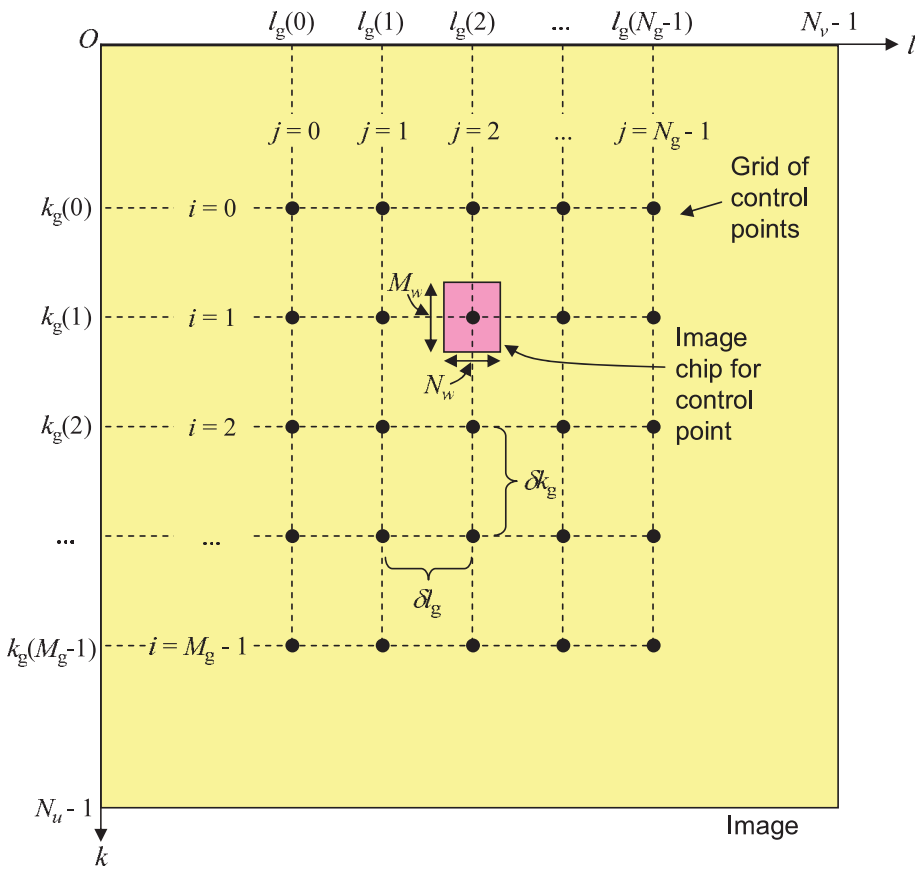

Figure 3.3: Grid of control points.

determination of suitable warp functions is key to successful image registration: once these warp functions are specified, it is relatively easy to resample the original source image $\Omega_{k,l}$ at the new sample positions $\hat{k}(k,l)$ to produce the registered image $\hat{\Omega}_{k,l}$.

3.4.2 Warp function determination

For simplicity, let the warp functions be approximated by second-order polynomials (these are generally sufficient to represent global displacement effects between corresponding points in the two images with non-crossed-ground-track collection geometries [39]). Hence, we may represent the warp functions by:

$$\hat{k}(k,l) = A_1k^2 + A_2l^2 + A_3kl + A_4k + A_5l + A_6 \tag{3.6}$$

$$\hat{l}(k,l) = B_1k^2 + B_2l^2 + B_3kl + B_4k + B_5l + B_6 \tag{3.7}$$

where the A_i and B_i are constants to be determined.

Our procedure for determining these constants will be to calculate the local displacement vectors between the images at various control points and then fit the warp functions to them by the method of least squares. To this end, let us define an M_g-by-N_g regular grid of control points to be overlaid on the images: the (i,j)

control point will have pixel index coordinates $(k, l) = (k_{\mathrm{g}}(i), l_{\mathrm{g}}(j))$ given by

$$k_{\mathrm{g}}(i) = k_{\mathrm{g}}(0) + i\,\delta k_{\mathrm{g}} \tag{3.8}$$

$$l_{\mathrm{g}}(j) = l_{\mathrm{g}}(0) + j\,\delta l_{\mathrm{g}} \tag{3.9}$$

where i and j are indices into the grid of control points, viz. $i = 0, 1, \ldots, M_{\mathrm{g}} - 1$ and $j = 0, 1, \ldots, N_{\mathrm{g}} - 1$ (see Figure 3.3). Observe that the placement, density and size of the grid are controlled by the (u, v) position of the first control point $(k_{\mathrm{g}}(0), l_{\mathrm{g}}(0))$, the spacing between the points along the u and v directions δk_{g} and δl_{g}, and the number of rows and columns of the grid M_{g} and N_{g} respectively: these must be chosen to ensure the grid of control points adequately samples the region of interest in the images. In particular, the grid should be restricted to the central illuminated area (within the composite beampattern of the transmitter and receiver) of the images: there is no benefit in placing a control point outside this area (or in any dark region with low SNR) as there will be insufficient signal to calculate the local displacement vector. To ensure a well-conditioned data set suitable for least squares fitting, the grid should sample a large spatial area at a reasonably high density; for computational efficiency, however, the grid density should also be chosen so that the fewest grid points are used which will still give an acceptable result.

Once the grid of control points is defined, the local relative displacement between the images at each point can be determined by the following sub-image correlation procedure. Around each control point, a image chip of size M_{w}-by-N_{w} pixels is extracted from each image: each chip comprises the pixels

$$\omega_{k',l'}(i, j) = \Omega_{k_{\mathrm{g}}(i)+k'-\lfloor M_{\mathrm{w}}/2\rfloor, l_{\mathrm{g}}(j)+l'-\lfloor N_{\mathrm{w}}/2\rfloor}, \tag{3.10}$$

$$\upsilon_{k',l'}(i, j) = \Upsilon_{k_{\mathrm{g}}(i)+k'-\lfloor M_{\mathrm{w}}/2\rfloor, l_{\mathrm{g}}(j)+l'-\lfloor N_{\mathrm{w}}/2\rfloor}, \tag{3.11}$$

where the intra-chip pixel indices k' and l' take values according to $k' = 0, 1, \ldots, M_{\mathrm{w}} - 1$ and $l' = 0, 1, \ldots, N_{\mathrm{w}} - 1$. The chip sizes M_{w} and N_{w} must be sufficiently large to accommodate the local relative displacement around the control point of the two images: this ensures that both image chips will have some element of the scene in common which can be detected by cross-correlation. However, the chips should also be small enough that a first-order linear displacement is the dominant difference between them, so that a sharp correlation peak will be produced and the local displacement can be easily determined: large chip sizes in which non-linear higher-order distortions are significant should be avoided, as this will result in smearing of the correlation peak and hence pose difficulties in determining the displacement.

The extracted image chips from the two SAR images contain complex-valued pixels. While a cross-correlation between these chips can be calculated directly from this complex data, an alternative approach is to first calculate the absolute value of the data and then calculate the cross-correlation between the real-valued magnitude-only image chips. While the first approach is capable of producing results superior to that of the second, particularly in eliminating spurious correlation peaks from bright targets, it is not nearly as straightforward to implement. Not uncommonly, errors will be present in the measurement of the collection geometry, which will cause a misplacement of the phase history data in the spatial frequency domain, resulting in an undesired relative displacement between the phase history data of the two interferometric data sets—this produces a phase ramp between the two images, which reduces the magnitude of the correlation peak and hinders the determination of the local displacement by a complex correlation-based approach. Although these problems can be mitigated by shifting the phase history data of one image and calculating multiple complex correlations at different shifts, the nett result remains that correlating the complex-valued image chips is a more complicated process than correlating the real-valued magnitude-only chips. For this reason, it was opted

to only correlate the magnitude-only data for the work reported in this thesis: this approach was found to give adequate results for the data analysed.

To calculate the cross-correlation between the magnitude-only chips, it is advantageous to employ FFTs for efficiency: this was done as follows. First the magnitude-only image chips were transformed into the two-dimensional frequency domain, viz.

$$\hat{\omega}_{p,q}(i,j) = \sum_{k'=0}^{M_\mathrm{w}-1} e^{-j\frac{2\pi p k'}{M_\mathrm{w}}} \sum_{l'=0}^{N_\mathrm{w}-1} e^{-j\frac{2\pi q l'}{N_\mathrm{w}}} \left|\omega_{k',l'}(i,j)\right| \tag{3.12}$$

$$\hat{\upsilon}_{p,q}(i,j) = \sum_{k'=0}^{M_\mathrm{w}-1} e^{-j\frac{2\pi p k'}{M_\mathrm{w}}} \sum_{l'=0}^{N_\mathrm{w}-1} e^{-j\frac{2\pi q l'}{N_\mathrm{w}}} \left|\upsilon_{k',l'}(i,j)\right|, \tag{3.13}$$

where $p = 0, 1, \ldots, M_\mathrm{w} - 1$ and $q = 0, 1, \ldots, N_\mathrm{w} - 1$. Next, the cross-correlation was calculated in the frequency-domain:

$$\hat{R}_{p,q}(i,j) = \begin{cases} \hat{\omega}_{p,q}(i,j)\,\hat{\upsilon}^*_{p,q}(i,j) & p \neq 0, q \neq 0 \\ 0 & p = q = 0, \end{cases} \tag{3.14}$$

where, because we are correlating non-negative magnitude-only data, we have specially set the zero-frequency term to zero to avoid a DC bias (this simplifies calculation of the quality factor $q(i,j)$ discussed below). Finally, the cross-correlation is inverse Fourier transformed back to the spatial-domain, viz.

$$R_{k',l'}(i,j) = \frac{1}{M_\mathrm{w} N_\mathrm{w}} \sum_{p=0}^{M_\mathrm{w}-1} e^{j\frac{2\pi p k'}{M_\mathrm{w}}} \sum_{q=0}^{N_\mathrm{w}-1} e^{j\frac{2\pi q l'}{N_\mathrm{w}}} \hat{R}_{p,q}(i,j). \tag{3.15}$$

The local displacement between the image chips is directly related to the position of the correlation peak. To determine the correlation peak position, an initial estimate is first obtained by noting the indices (k'_0, l'_0) of the maximum value in the array of cross-correlation values $R_{k',l'}(i,j)$. This estimate is then refined by fitting a quadratic polynomial to a local 3×3 array of pixels surrounding (k'_0, l'_0) by the method of least squares: if we denote the indices of the pixels in this local neighbourhood by k_n and l_n, where $n = 1, 2, \ldots, 9$ (see Figure 3.4), and the corresponding cross-correlation values by R_n, then the quadratic polynomial

$$z = ak^2 + bl^2 + ckl + dk + el + f \tag{3.16}$$

can be fitted by solving the matrix equation

$$\begin{bmatrix} \sum_n k_n^4 & \sum_n k_n^2 l_n^2 & \sum_n k_n^3 l_n & \sum_n k_n^3 & \sum_n k_n^2 l_n & \sum_n k_n^2 \\ \sum_n k_n^2 l_n^2 & \sum_n l_n^4 & \sum_n k_n l_n^3 & \sum_n k_n l_n^2 & \sum_n l_n^3 & \sum_n l_n^2 \\ \sum_n k_n^3 l_n & \sum_n k_n l_n^3 & \sum_n k_n^2 l_n^2 & \sum_n k_n^2 l_n & \sum_n k_n l_n^2 & \sum_n k_n l_n \\ \sum_n k_n^3 & \sum_n k_n l_n^2 & \sum_n k_n^2 l_n & \sum_n k_n^2 & \sum_n k_n l_n & \sum_n k_n \\ \sum_n k_n^2 l_n & \sum_n l_n^3 & \sum_n k_n l_n^2 & \sum_n k_n l_n & \sum_n l_n^2 & \sum_n l_n \\ \sum_n k_n^2 & \sum_n l_n^2 & \sum_n k_n l_n & \sum_n k_n & \sum_n l_n & \sum_n 1 \end{bmatrix} \begin{bmatrix} a \\ b \\ c \\ d \\ e \\ f \end{bmatrix} = \begin{bmatrix} \sum_n k_n^2 R_n \\ \sum_n l_n^2 R_n \\ \sum_n k_n l_n R_n \\ \sum_n k_n R_n \\ \sum_n l_n R_n \\ \sum_n R_n \end{bmatrix} \tag{3.17}$$

(in which all summations are over $n = 1, 2, \ldots 9$) for the coefficients a to f. By determining the stationary points of (3.16), we find that the position of the quadratic peak is at the pixel intra-chip index coordinates

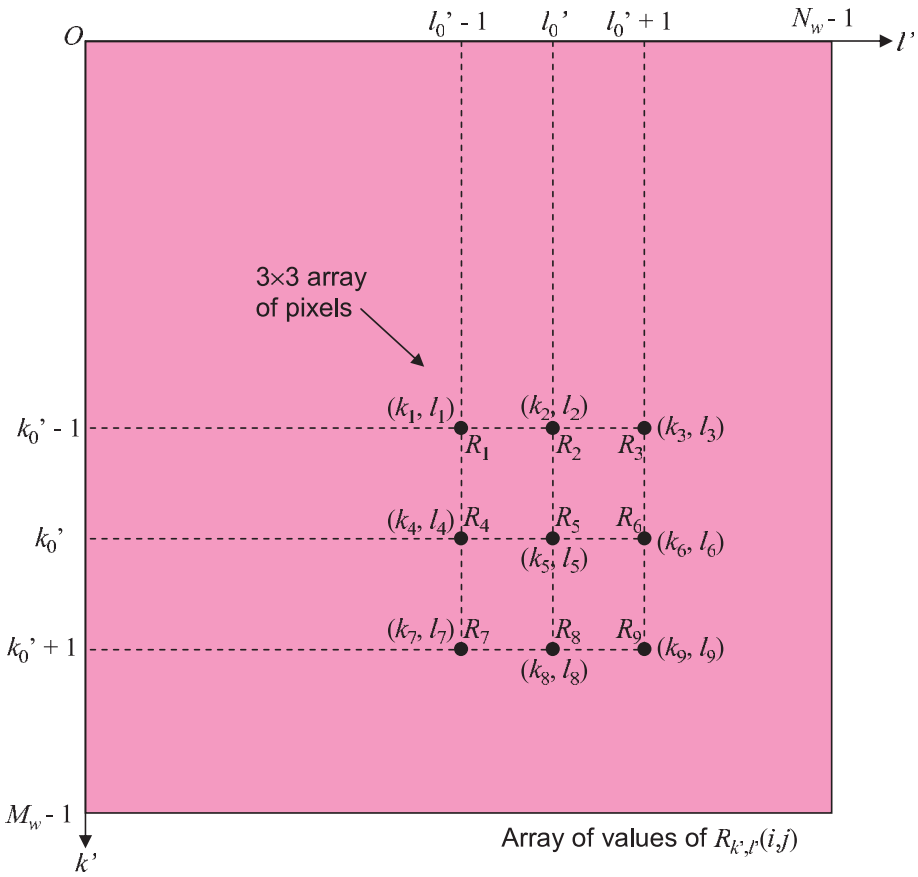

Figure 3.4: 3×3-pixel array centred at maximum value of image chip correlation samples $R_{k',l'}(i,j)$.

$(k'_{\mathrm{p}}(i,j), l'_{\mathrm{p}}(i,j))$ given by

$$k'_{\mathrm{p}}(i,j) = \frac{2bd - ce}{c^2 - 4ab} \tag{3.18}$$

$$l'_{\mathrm{p}}(i,j) = \frac{2ae - cd}{c^2 - 4ab} \tag{3.19}$$

whereupon, by substituting these results back into (3.16), the peak value may be calculated to be

$$R_{\max}(i,j) = \frac{ae^2 + bd^2 - cde}{c^2 - 4ab} + f. \tag{3.20}$$

Observe that the intra-chip coordinates $k'_{\mathrm{p}}(i,j)$ and $l'_{\mathrm{p}}(i,j)$ currently assume non-negative values, i.e.

$$0 \leq k'_{\mathrm{p}}(i,j) \leq M_{\mathrm{w}} - 1 \tag{3.21}$$

$$0 \leq l'_{\mathrm{p}}(i,j) \leq N_{\mathrm{w}} - 1 \tag{3.22}$$

However, for later calculations, it will be helpful if they instead assumed values in a zero-centred interval: this can be achieved by adjusting their values according to

$$k'_{\mathrm{p}}(i,j) := k'_{\mathrm{p}}(i,j) - \left\lfloor \frac{k'_{\mathrm{p}}(i,j)}{M_{\mathrm{w}}} + \frac{1}{2} \right\rfloor M_{\mathrm{w}} \tag{3.23}$$

$$l'_{\mathrm{p}}(i,j) := l'_{\mathrm{p}}(i,j) - \left\lfloor \frac{l'_{\mathrm{p}}(i,j)}{N_{\mathrm{w}}} + \frac{1}{2} \right\rfloor N_{\mathrm{w}} \tag{3.24}$$

so that these adjusted values will then satisfy

$$-\left\lfloor \frac{M_{\mathrm{w}}}{2} \right\rfloor \leq k'_{\mathrm{p}}(i,j) \leq \left\lceil \frac{M_{\mathrm{w}}}{2} \right\rceil - 1 \tag{3.25}$$

$$-\left\lfloor \frac{N_{\mathrm{w}}}{2} \right\rfloor \leq l'_{\mathrm{p}}(i,j) \leq \left\lceil \frac{N_{\mathrm{w}}}{2} \right\rceil - 1 \tag{3.26}$$

as required. The correlation peak position and value are then taken to be the adjusted $(k'_{\mathrm{p}}(i,j), l'_{\mathrm{p}}(i,j))$ and $R_{\max}(i,j)$ respectively.

In practice, the local displacements determined for the various control points will not all be of equal reliability: some control points will inevitably fall within areas of low SNR for which there will be insufficient signal to produce a valid correlation peak. In such cases, the $R_{k',l'}(i,j)$ values represent the result of attempting to correlate uncorrelated random noise, so the 'peak' value $R_{\max}(i,j)$ will not stand out very strongly from the background values of $R_{k',l'}(i,j)$. Since the DC bias in the values of $R_{k',l'}(i,j)$ has been removed (see (3.14)), the ratio of the peak to the standard deviation provides a simple means of assessing the strength of the correlation peak. Hence, the reliability of the control points may be measured by a quality factor

$$q(i,j) = \frac{R_{\max}(i,j)}{\sigma_R(i,j)} \tag{3.27}$$

where $\sigma_R(i,j)$ is the standard deviation of the $R_{k',l'}(i,j)$: a reliable control point will be one with a large value of $q(i,j)$, signifying that the peak stands out strongly from the background. Hence, to determine the warp function, the quality measures $q(i,j)$ of the various control points are thresholded against a suitable value q_{lo} and those that exceed this threshold are admitted for use in determining the warp function. This

simple threshold test can be misled by bright artificial targets however, so, in practice, it was generally found useful to also test the $q(i,j)$ against a maximum threshold q_{hi} to cull such cases. Thus, the admissible set of control points can be represented by

$$\mathcal{S} = \{(i,j) : q_{\mathrm{lo}} < q(i,j) < q_{\mathrm{hi}}\}\,. \tag{3.28}$$

Having thus obtained a suitable set of control points, the required warp functions $\hat{k}(k,l)$ and $\hat{l}(k,l)$ can now be determined by a least-squares fit of the warp function values at the control points $\hat{k}(k_{\mathrm{g}}(i,j), l_{\mathrm{g}}(i,j))$ and $\hat{l}(k_{\mathrm{g}}(i,j), l_{\mathrm{g}}(i,j))$ to the warp measurements $k_{\mathrm{g}}(i,j) + k'_{\mathrm{p}}(i,j)$ and $l_{\mathrm{g}}(i,j) + l'_{\mathrm{p}}(i,j)$, employing only the data which satisfies $(i,j) \in \mathcal{S}$. The required coefficients A_i and B_i of (3.6) and (3.7) respectively can be determined by solving a matrix equation analogous to (3.17), viz.

$$\begin{bmatrix} \sum_n k_n^4 & \sum_n k_n^2 l_n^2 & \sum_n k_n^3 l_n & \sum_n k_n^3 & \sum_n k_n^2 l_n & \sum_n k_n^2 \\ \sum_n k_n^2 l_n^2 & \sum_n l_n^4 & \sum_n k_n l_n^3 & \sum_n k_n l_n^2 & \sum_n l_n^3 & \sum_n l_n^2 \\ \sum_n k_n^3 l_n & \sum_n k_n l_n^3 & \sum_n k_n^2 l_n^2 & \sum_n k_n^2 l_n & \sum_n k_n l_n^2 & \sum_n k_n l_n \\ \sum_n k_n^3 & \sum_n k_n l_n^2 & \sum_n k_n^2 l_n & \sum_n k_n^2 & \sum_n k_n l_n & \sum_n k_n \\ \sum_n k_n^2 l_n & \sum_n l_n^3 & \sum_n k_n l_n^2 & \sum_n k_n l_n & \sum_n l_n^2 & \sum_n l_n \\ \sum_n k_n^2 & \sum_n l_n^2 & \sum_n k_n l_n & \sum_n k_n & \sum_n l_n & \sum_n 1 \end{bmatrix} \begin{bmatrix} A_1 & B_1 \\ A_2 & B_2 \\ A_3 & B_3 \\ A_4 & B_4 \\ A_5 & B_5 \\ A_6 & B_6 \end{bmatrix} = \begin{bmatrix} \sum_n k_n^2 K_n & \sum_n k_n^2 L_n \\ \sum_n l_n^2 K_n & \sum_n l_n^2 L_n \\ \sum_n k_n l_n L_n & \sum_n k_n l_n L_n \\ \sum_n k_n K_n & \sum_n k_n L_n \\ \sum_n l_n K_n & \sum_n l_n L_n \\ \sum_n K_n & \sum_n L_n \end{bmatrix} \tag{3.29}$$

where the summation is over $n = 1, 2, \ldots, |\mathcal{S}|$, in which $|\mathcal{S}|$ denotes the number of elements of $\mathcal{S}$, and k_n denotes the various $k_{\mathrm{g}}(i,j)$, l_n denote the various $l_{\mathrm{g}}(i,j)$, K_n denotes the $k_{\mathrm{g}}(i,j) + k'_{\mathrm{p}}(i,j)$ and L_n denotes the $l_{\mathrm{g}}(i,j) + l'_{\mathrm{p}}(i,j)$.

3.4.3 Image resampling

Once the warp functions $\hat{k}(k,l)$ and $\hat{l}(k,l)$ have been determined, the source image $\Omega_{k,l}$ can then be resampled to produce $\hat{\Omega}_{k,l}$. Although this is a two-dimensional resampling operation which is similar in concept to the polar-to-Cartesian resampling employed in PFA image formation (ref. Section 2.5.2), unlike the PFA-case this image resampling is not easily implemented as a series of one-dimensional resampling operations. A fairly rigorous solution to this image resampling problem would be to convolve the image data with an appropriate two-dimensional kernel: although perfectly feasible, this is a computationally intensive process. Hence, for the preliminary interferometric analysis reported in this thesis, it was opted to employ a fast and simple bilinear interpolation procedure instead which, although crude and approximate, sufficed for quickly producing initial results. Specifically, the bilinear interpolant is given by

$$\hat{\Omega}_{k,l} = (1-\delta\hat{k})\,(1-\delta\hat{l})\,\Omega_{\lfloor\hat{k}\rfloor,\lfloor\hat{l}\rfloor} + \delta\hat{k}\,(1-\delta\hat{l})\,\Omega_{\lfloor\hat{k}\rfloor+1,\lfloor\hat{l}\rfloor} + (1-\delta\hat{k})\,\delta\hat{l}\,\Omega_{\lfloor\hat{k}\rfloor,\lfloor\hat{l}\rfloor+1} + \delta\hat{k}\,\delta\hat{l}\,\Omega_{\lfloor\hat{k}\rfloor+1,\lfloor\hat{l}\rfloor+1} \tag{3.30}$$

where $\hat{k} = \hat{k}(k,l)$, $\hat{l} = \hat{l}(k,l)$, $\delta\hat{k} = \hat{k} - \lfloor\hat{k}\rfloor$ and $\delta\hat{l} = \hat{l} - \lfloor\hat{l}\rfloor$. The result $\hat{\Omega}_{k,l}$ then represents a version of the source image $\Omega_{k,l}$ which has been registered onto the target image $\Upsilon_{k,l}$ as desired.

3.5 Coherence

An important parameter for extracting interferometric information from a pair of SAR images is the complex correlation coefficient: if $\Omega = \Omega(u, v)$ and $\Upsilon = \Upsilon(u, v)$ denote the two images, then this correlation parameter $\gamma = \gamma(u, v)$ is defined as

$$\gamma = \frac{\langle \Omega\, \Upsilon^* \rangle}{\sqrt{\langle \Omega\, \Omega^* \rangle \, \langle \Upsilon\, \Upsilon^* \rangle}} \tag{3.31}$$

where $\langle \cdot \rangle$ denotes ensemble averaging and we have suppressed the positional (u, v) dependence for notational compactness. In the literature, the magnitude of the complex correlation $|\gamma|$ reflects the degree of coherence and is often simply referred to as the 'coherence', and the complex correlation γ has also been referred to as the 'complex coherence'. From the right-hand-side of (3.31), the parameter γ may be interpreted as the averaged interferogram normalised by the square root of the product of the powers of the two images: consequently, the magnitude of γ is restricted to a standard range of values from zero to unity. However, since the normalisation factor is real-valued, the phase of the dividend (numerator) is unaffected by the division operation, so the phase of γ remains equal to the averaged interferogram phase.

The restricted range of values of $|\gamma|$, i.e. $0 \leq |\gamma| \leq 1$, facilitates its easy interpretation as an indicator of the similarity between Ω and Υ: values near zero are indicative of poorly correlated images while values near one are indicative of highly correlated images. Generally, a high level of correlation is desired for interferometric analysis in order to obtain precise phase measurements (see below), and this is usually obtained by avoiding decorrelation through careful collection planning to meet certain spatial (look-angle) and temporal constraints. Excessive differences between the look-angles of the two images may induce decorrelation through two main mechanisms: shifts in the transduced ground wavenumber ranges of the reflectivity spectra with changing grazing angle give rise to *baseline decorrelation* (this effect can be mitigated by careful aperture trimming: see Section 3.3); and changes in the phase relationships between volume-distributed elementary scattering centres with grazing angle result in *volume decorrelation*. Also, *decorrelation due to rotation* [139] can also arise due to alterations in the phase relationships between the elementary scatterers in a resolution element as the aspect (azimuth) angle changes. Excessive temporal separation between the images permits the accumulation of physical changes in the surface between the times of the two observations: this changes the surface reflectivity function, giving rise to *temporal decorrelation* effects. (Hence, all things being equal, one may generally expect that simultaneously collected interferometric data, e.g. from a monostatic and a bistatic receiver operating in conjunction, will display a higher coherence magnitude than temporally separated data.) Further sources of decorrelation include receiver thermal noise (which contributes an uncorrelated component to the two SAR images) and processing aberrations (resulting in image misregistration or defocussing), but these should normally be reduced to minor levels through careful hardware engineering and processor design.

The effects of the various sources of decorrelation can be usefully summarised as a product of correlation terms [139], e.g.

$$|\gamma| = |\gamma_{\text{thermal}}| \cdot |\gamma_{\text{spatial}}| \cdot |\gamma_{\text{temporal}}| \tag{3.32}$$

where $|\gamma_{\text{thermal}}|$ represents decorrelation due to thermal noise, $|\gamma_{\text{spatial}}|$ represents decorrelation due to spatial (look-angle) effects (including volume decorrelation), and $|\gamma_{\text{temporal}}|$ represents temporal decorrelation. The thermal noise effect can be expressed in terms of the SNRs of the two images from which the interferogram is derived [138]:

$$|\gamma_{\text{thermal}}| = \frac{1}{\sqrt{\left(1 + \text{SNR}_1^{-1}\right)\left(1 + \text{SNR}_2^{-1}\right)}} \tag{3.33}$$

where SNR_i is the SNR of the ith image.[3] In practice, the various system- and geometry-dependent decorrelating effects can generally be reduced to manageable levels, so that in this example we would have $|\gamma_{\mathrm{thermal}}| \approx 1$ and $|\gamma_{\mathrm{spatial}}| \approx 1$. This leaves only temporal scene changes as the remaining cause of significant decorrelation through the $|\gamma_{\mathrm{temporal}}|$ term. Under these circumstances, a display of the spatial variation of $|\gamma|$ can be interpreted as a crude change map, with low values indicating regions where the scene reflectivity changed between the data collections and high values indicating regions where no changes occurred: illustrative results in this vein will be presented in Section 3.7. It is worth noting, however, that the correlation magnitude per se as a statistic, although conceptually simple, may not produce adequate performance in practical change-detection applications: in such cases, more sophisticated discriminants should be employed [51].

In practice, for a given pair of SAR images, γ must be estimated from the sample coherence, an expression for which may be obtained by replacing the ensemble averaging of (3.31) with averaging over N discrete samples:

$$\hat{\gamma} = \frac{\sum_{i=1}^{N} \Omega_i \, \Upsilon_i^*}{\sqrt{\sum_{i=1}^{N} |\Omega_i|^2 \; \sum_{i=1}^{N} |\Upsilon_i|^2}}. \tag{3.34}$$

Generally, the averaging implied by the summation will be over N looks or over a local neighbourhood of N pixels. Touzi and Lopes [156] have calculated the probability density function of the sample coherence magnitude, $d = |\hat{\gamma}|$, to be

$$p(d; D, L) = 2(L-1)(1-D^2)^L d(1-d^2)^{L-2} F(L, L; 1; D^2 d^2) \tag{3.35}$$

for $L > 2$ and $D \neq 1$, where D is the (true) coherence magnitude, L is the number of independent samples (looks) and $F(\cdot)$ is the hypergeometric function. From their calculated expression for $p(d; D, L)$, Touzi and Lopes go on to demonstrate that the magnitude of the sample coherence is a biased estimator of the true coherence magnitude: $|\hat{\gamma}|$ is biased towards higher values, especially for lower values of the true coherence. Various methods for removing this bias have been proposed [157], but, as the bias decreases as the number of independent samples is increased, simply averaging over a large set of values may produce acceptable results for non-demanding applications. Such averaging also has the benefit of reducing the effects of random noise, but this is achieved at the expense of spatial resolution: an appropriate balance between these factors must often be struck in practice.

The phase of $\hat{\gamma}$ is directly related to the phase difference of the averaged interferogram:

$$\arg \hat{\gamma} = \arg \left(\sum_{i=1}^{N} \Omega_i \Upsilon_i^* \right) \tag{3.36}$$

in which the right-hand-side is a maximum-likelihood estimator of the interferogram phase [39]. As discussed in the next section, this interferometric phase contains useful information, e.g. it can be exploited to recover terrain height or monitor ground deformation. Since $\hat{\gamma}$ is a random variable, the phase estimates recovered from $\arg \gamma$ will exhibit stochastic behaviour, with the variance increasing as the coherence magnitude decreases: Just and Bamler [138] observe that the phase standard deviation rapidly increases with decreasing coherence $|\gamma|$ up to a limit of approximately 104°. Consequently, precise phase determinations are only obtained in regions of high coherence: thus for high-quality interferometric results, all appropriate efforts should be made to reduce scene decorrelation.

[3] If the complex-valued SAR images s_1, s_2 are each modelled as consisting of a common component c arising from measurements of the scattered returns and a random component n_i arising from noise such that $s_i = c + n_i$, then the signal-to-noise ratio (SNR) of each image is given by $\mathrm{SNR}_i = \langle |c|^2 \rangle / \langle |n_i|^2 \rangle$ [139].

3.6 Interferometric phase

From Section 2.7, the model for the ith SAR image in an interferometric pair (where $i = 1, 2$) can be written as

$$\Omega_i(\mathbf{r}') = \iiint_{\mathcal{V}} \mathrm{d}\mathbf{R}\, g_i(\mathbf{R})\, e^{j\Psi(\bar{\mathbf{K}}_i;\mathbf{R})}\, \hat{\kappa}(\mathbf{r}' - \mathbf{r}) \tag{3.37}$$

where we have employed the simplified notation for the point spread function (PSF) $\hat{\kappa}(\cdot)$ introduced in Section 3.3, and

$$\mathbf{R} = u_0\, \mathbf{a}_u + v_0\, \mathbf{a}_v + w_0\, \mathbf{a}_w \tag{3.38}$$

is the three-dimensional position of an elementary scattering centre,

$$\mathbf{r} = (u_0 + w_0 \tan\psi_i)\, \mathbf{a}_u + (v_0 + w_0 \tan\eta_i)\, \mathbf{a}_v \tag{3.39}$$

is the projected position of the scatterer in the image and

$$\mathbf{r}' = u\, \mathbf{a}_u + v\, \mathbf{a}_v \tag{3.40}$$

represents a generic position in the image. Equation (3.37) may be interpreted as follows: a given scattering centre at $\mathbf{R}$ is represented in the SAR image by a two-dimensional elementary signal $\mathrm{d}\mathbf{R}\, g_i(\mathbf{R})\, e^{j\Psi(\bar{\mathbf{K}}_i;\mathbf{R})}\, \hat{\kappa}(\mathbf{r}' - \mathbf{r})$, which is composed of a real-valued PSF $\hat{\kappa}(\mathbf{r}' - \mathbf{r})$ centred at $\mathbf{r}$, to which has been applied a phase shift comprising two components. The first component is the phase of the scatterer's reflectivity $\mathrm{d}\mathbf{R}\, g_i(\mathbf{R})$ which is dependent on the physical scattering properties of the scattering centre and which, as the notation suggests, may differ between the two collections. The second is the phase $\Psi(\bar{\mathbf{K}}_i;\mathbf{R})$ which is dependent on the scatterer's position $\mathbf{R}$ and the collection geometry through $\bar{\mathbf{K}}_i$. Hence, the interferometric phase difference between the scatterer's signal in the two images may potentially be exploited in three principal ways.

- First, if $g_1(\mathbf{R}) = g_2(\mathbf{R})$ and $\mathbf{R}$ is constant, then differences in the $\bar{\mathbf{K}}_i$ will contribute a height-dependent interferometric phase $\Psi(\bar{\mathbf{K}}_2;\mathbf{R}) - \Psi(\bar{\mathbf{K}}_1;\mathbf{R})$: this height-dependence of the phase can be exploited for the mapping of terrain topography.
- Second, if $\mathbf{R}$ is constant and $\bar{\mathbf{K}}_1 = \bar{\mathbf{K}}_2$, then a non-vanishing phase difference will indicate changes in the phase of the scene reflectivity $g_i(\mathbf{R})$: this effect can be exploited for the coherent detection of scene changes.
- Third, for constant scatterer reflectivity and $\bar{\mathbf{K}}_1 = \bar{\mathbf{K}}_2 = \bar{\mathbf{K}}$, a small displacement of the scatterer $\delta\mathbf{R}$ in the second image relative to the first will produce a phase change $\Psi(\bar{\mathbf{K}};\mathbf{R}+\delta\mathbf{R}) - \Psi(\bar{\mathbf{K}};\mathbf{R})$: the change in scatterer position encoded in this phase can be usefully employed for mapping terrain motion.

In practice, however, in the second and third applications above, we will usually have $\bar{\mathbf{K}}_1 \neq \bar{\mathbf{K}}_2$ due to the difficulty of exactly replicating a collection geometry. Thus the phase effects exploited in the second and third applications will generally be contaminated by a phase contribution from that of the first. This height-dependent phase offset will need to be accounted for, e.g. through the use of an existing digital elevation model (DEM) or by combining two interferograms in a differential interferometry technique [129]. In the remainder of this section, we will discuss the theoretical basis of scatterer height encoding in the interferometric phase. This discussion will thus be naturally focussed on the topographic mapping application: the other interferometric applications will not be discussed further.

From (2.49), the position-dependent phase associated with the signal of a scatterer in image i is given by

$$\Psi(\bar{\mathbf{K}}_i;\mathbf{R}) = -\frac{|\bar{\mathbf{K}}_i|}{|\mathbf{B}(\bar{\mathbf{K}}_i)|}\sum_{j=1}^{2}\left\{\left|\mathbf{P}_j(\bar{\mathbf{K}}_i)-\mathbf{R}\right| - \left|\mathbf{P}_j(\bar{\mathbf{K}}_i)\right|\right\} \tag{3.41}$$

$$= \bar{\mathbf{K}}_i\cdot\mathbf{R} - \frac{|\bar{\mathbf{K}}_i|}{2\,|\mathbf{B}(\bar{\mathbf{K}}_i)|}\sum_{j=1}^{2}\left\{\frac{|\mathbf{R}|^2 - \left(\hat{\mathbf{P}}_j(\bar{\mathbf{K}}_i)\cdot\mathbf{R}\right)^2}{|\mathbf{P}_j(\bar{\mathbf{K}}_i)|}\right\} + O(|\mathbf{R}|^3). \tag{3.42}$$

The phase of the interferogram $\Omega_1\Omega_2^*$ is thus the difference between the phases $\Psi(\bar{\mathbf{K}}_i;\mathbf{R})$ of the two images: let this be denoted by $\Delta\Psi(\mathbf{R})$, so

$$\Delta\Psi(\mathbf{R}) = \Psi(\bar{\mathbf{K}}_2;\mathbf{R}) - \Psi(\bar{\mathbf{K}}_1;\mathbf{R}). \tag{3.43}$$

To proceed further, we employ a series expansion of $\Delta\Psi(\mathbf{R})$ in powers of $|\mathbf{R}|$ up to second order and consider the terms separately. This process is aided by noting that the required terms may be simply obtained by reference to the power series expansion of $\Psi(\bar{\mathbf{K}}_i;\mathbf{R})$ displayed in (3.42). Hence, we make the following observations.

- As there is no zeroth order term of $\Psi(\bar{\mathbf{K}}_i;\mathbf{R})$ in (3.42), we conclude that the zeroth order term of $\Delta\Psi(\mathbf{R})$ vanishes, i.e.

$$\Delta\Psi^{(0)}(\mathbf{R}) = 0. \tag{3.44}$$

- The first order term of $\Delta\Psi(\mathbf{R})$ is

$$\Delta\Psi^{(1)}(\mathbf{R}) = \left(\bar{\mathbf{K}}_2 - \bar{\mathbf{K}}_1\right)\cdot\mathbf{R} \tag{3.45}$$

  which can be quite simply expressed as

$$\Delta\Psi^{(1)}(\mathbf{R}) = w_0\,\bar{k}_u(\tan\psi_2 - \tan\psi_1), \tag{3.46}$$

  since, from (2.166) with $\bar{k}_v = 0$, we have $\bar{\mathbf{K}}_i = \bar{k}_u\,\mathbf{a}_u + \bar{k}_u\tan\psi_i\,\mathbf{a}_w$ (ref. Figure 3.1). Hence, the scatterer's height w_0 is linearly encoded in the phase of this term, which may be easily inverted to recover the terrain height function from a pair of SAR images.

- The second order term is given by

$$\Delta\Psi^{(2)}(\mathbf{R}) = \\ -\frac{|\bar{\mathbf{K}}_2|}{2|\mathbf{B}(\bar{\mathbf{K}}_2)|}\sum_{j=1}^{2}\left\{\frac{|\mathbf{R}|^2 - \left(\hat{\mathbf{P}}_j(\bar{\mathbf{K}}_2)\cdot\mathbf{R}\right)^2}{|\mathbf{P}_j(\bar{\mathbf{K}}_2)|}\right\} + \frac{|\bar{\mathbf{K}}_1|}{2|\mathbf{B}(\bar{\mathbf{K}}_1)|}\sum_{j=1}^{2}\left\{\frac{|\mathbf{R}|^2 - \left(\hat{\mathbf{P}}_j(\bar{\mathbf{K}}_1)\cdot\mathbf{R}\right)^2}{|\mathbf{P}_j(\bar{\mathbf{K}}_1)|}\right\} \tag{3.47}$$

  in which, if $\hat{\mathbf{P}}_j(\bar{\mathbf{K}}_i) = p_{u,i,j}\,\mathbf{a}_u + p_{v,i,j}\,\mathbf{a}_v + p_{w,i,j}\,\mathbf{a}_w$, we have

$$|\mathbf{R}|^2 - \left(\hat{\mathbf{P}}_j(\bar{\mathbf{K}}_i)\cdot\mathbf{R}\right)^2 = (1-p_{u,i,j}^2)u_0^2 + (1-p_{v,i,j}^2)v_0^2 - 2p_{u,i,j}p_{v,i,j}u_0v_0 \\ - 2p_{w,i,j}(p_{u,i,j}u_0 + p_{v,i,j}v_0)w_0 + (1-p_{w,i,j}^2)w_0^2. \tag{3.48}$$

  Hence, it may be observed that $\Delta\Psi^{(2)}(\mathbf{R})$ is composed of a sum of various terms, some of which are dependent only on powers of u_0 and v_0 but not w_0. These contribute a spatially varying offset to $\Delta\Psi(\mathbf{R})$ which masks the height-dependence we seek to exploit in $\Delta\Psi^{(1)}(\mathbf{R})$.

Thus, to exploit the information about the height w_0 encoded in $\Delta\Psi^{(1)}(\mathbf{R})$, it is necessary to compensate for the effects of the $\Delta\Psi^{(2)}(\mathbf{R})$ term. Fortunately, these troublesome effects can be largely mitigated by subtracting away from $\Delta\Psi(\mathbf{R})$ a correction given by

$$\Delta\Psi(\mathbf{R}_{\text{proj}}) = \Psi(\bar{\mathbf{K}}_2; \mathbf{R}_{\text{proj}}) - \Psi(\bar{\mathbf{K}}_1; \mathbf{R}_{\text{proj}}) \tag{3.49}$$

where $\mathbf{R}_{\text{proj}}$ is the projection of $\mathbf{R}$ onto the xy-plane, i.e.

$$\mathbf{R}_{\text{proj}} = u_0\, \mathbf{a}_u + v_0\, \mathbf{a}_v. \tag{3.50}$$

This phase correction represents a 'flat-Earth' phase function, being the phase values present in the absence of topographic variations: applying the correction results in a corrected phase

$$\Delta\Psi_{\text{c}}(\mathbf{R}) \triangleq \Delta\Psi(\mathbf{R}) - \Delta\Psi(\mathbf{R}_{\text{proj}}). \tag{3.51}$$

This step effectively "flattens the interferogram" since, for a level surface, it removes the spatial phase variations and leaves just a flat constant phase.

We now demonstrate that subtracting the correction $\Delta\Psi(\mathbf{R}_{\text{proj}})$ away from the original phase $\Delta\Psi(\mathbf{R})$ leaves the first order height-dependent terms dominant in the phase.

- First, observe that it follows from (3.44) and (3.46) that

$$\Delta\Psi^{(0)}(\mathbf{R}_{\text{proj}}) = 0 \tag{3.52}$$

  and

$$\Delta\Psi^{(1)}(\mathbf{R}_{\text{proj}}) = 0. \tag{3.53}$$

  Hence, the zeroth and first order terms of $\Delta\Psi(\mathbf{R})$, i.e. $\Delta\Psi^{(0)}(\mathbf{R})$ and $\Delta\Psi^{(1)}(\mathbf{R})$ respectively, are unchanged by the subtraction of this phase correction $\Delta\Psi(\mathbf{R}_{\text{proj}})$: in particular, the linear height encoding in (3.46) is completely unaffected.

- Second, observe that, from (3.47), the second order term of $\Delta\Psi(\mathbf{R}_{\text{proj}})$ is

$$\Delta\Psi^{(2)}(\mathbf{R}_{\text{proj}}) = -\frac{|\bar{\mathbf{K}}_2|}{2|\mathbf{B}(\bar{\mathbf{K}}_2)|}\sum_{j=1}^{2}\left\{\frac{|\mathbf{R}_{\text{proj}}|^2 - \left(\hat{\mathbf{P}}_j(\bar{\mathbf{K}}_2)\cdot\mathbf{R}_{\text{proj}}\right)^2}{|\mathbf{P}_j(\bar{\mathbf{K}}_2)|}\right\} + \frac{|\bar{\mathbf{K}}_1|}{2|\mathbf{B}(\bar{\mathbf{K}}_1)|}\sum_{j=1}^{2}\left\{\frac{|\mathbf{R}_{\text{proj}}|^2 - \left(\hat{\mathbf{P}}_j(\bar{\mathbf{K}}_1)\cdot\mathbf{R}_{\text{proj}}\right)^2}{|\mathbf{P}_j(\bar{\mathbf{K}}_1)|}\right\} \tag{3.54}$$

  in which, from (3.48),

$$|\mathbf{R}_{\text{proj}}|^2 - \left(\hat{\mathbf{P}}_j(\bar{\mathbf{K}}_i)\cdot\mathbf{R}_{\text{proj}}\right)^2 = (1-p_{u,i,j}^2)u_0^2 + (1-p_{v,i,j}^2)v_0^2 - 2p_{u,i,j}p_{v,i,j}u_0v_0. \tag{3.55}$$

After subtraction, the corrected second order phase term is then

$$\Delta\Psi^{(2)}(\mathbf{R}) - \Delta\Psi^{(2)}(\mathbf{R}_{\text{proj}}) = -w_0 \frac{|\bar{\mathbf{K}}_2|}{2|\mathbf{B}(\bar{\mathbf{K}}_2)|} \sum_{j=1}^{2} \left\{ \frac{(1 - p_{w,2,j}^2)w_0 - 2p_{w,2,j}(p_{u,2,j}u_0 + p_{v,2,j}v_0)}{|\mathbf{P}_j(\bar{\mathbf{K}}_2)|} \right\}$$
$$+ w_0 \frac{|\bar{\mathbf{K}}_1|}{2|\mathbf{B}(\bar{\mathbf{K}}_1)|} \sum_{j=1}^{2} \left\{ \frac{(1 - p_{w,1,j}^2)w_0 - 2p_{w,1,j}(p_{u,1,j}u_0 + p_{v,1,j}v_0)}{|\mathbf{P}_j(\bar{\mathbf{K}}_1)|} \right\}, \quad (3.56)$$

where the coefficients of w_0 on the right-hand-side have been written in a form to facilitate comparison with the coefficients of w_0 in (3.46). It can be observed that, although the bulk of the strongly position-dependent quadratic terms have been removed by the subtraction, a certain dependence on position (u_0, v_0) and height w_0 still remains. However, although the terms $\left|\bar{\mathbf{K}}_i\right|/2\left|\mathbf{B}(\bar{\mathbf{K}}_i)\right|$ in (3.56) are of the order of magnitude of $\bar{k}_u$ in (3.46), the terms in the summations involve ratios of u_0, v_0 and w_0 to $\left|\mathbf{P}_j(\bar{\mathbf{K}}_i)\right|$. Hence, for sufficiently large $\left|\mathbf{P}_j(\bar{\mathbf{K}}_i)\right| \gg |u_0|, |v_0|, |w_0|$ such that these summations are negligible compared to the term $\tan\psi_2 - \tan\psi_1$ in (3.46), this corrected second order phase will be negligible compared to the first order phase.

Under these circumstances, we may conclude that, to first order in $|\mathbf{R}|$, the corrected phase difference will be

$$\Delta\Psi_{\text{c}}(\mathbf{R}) = \Delta\Psi^{(1)}(\mathbf{R}), \quad (3.57)$$

as desired.

From (3.46) and (3.57), the corrected interferogram phase $\Delta\Psi_{\text{c}}(\mathbf{R})$ is related to the terrain height w_o by

$$\Delta\Psi_{\text{c}}(\mathbf{R}) = w_0\, \bar{k}_u(\tan\psi_2 - \tan\psi_1). \quad (3.58)$$

In practice, the phase data are obtained by taking the argument of the complex-valued interferogram, and this only gives wrapped values in a 2π-wide interval. Consequently, a height-of-ambiguity δh, being the non-negative change in terrain height corresponding to a 2π change in the corrected interferometric phase, can be calculated:

$$\delta h = \frac{2\pi}{\bar{k}_u\,|\tan\psi_2 - \tan\psi_1|} \quad (3.59)$$

Smaller δh corresponds to greater height sensitivity but a higher fringe rate (from more frequent occurrences of wrapping) and hence greater ambiguity. This ambiguity must be resolved to determine unambiguous terrain heights for topographic mapping applications and various two-dimensional phase unwrapping approaches exist to accomplish this [158]. The topic of phase unwrapping is, however, outside the scope of the present discussion.

To illustrate the results of the above procedure for estimating surface topography, the expected phase $\Delta\Psi_{\text{c}}(\mathbf{R})$ was calculated for a surface consisting of a two-dimensional raised-cosine function scaled to simulate a mound of height 10 m extending over an area spanning 750 m in range and 300 m in azimuth. Power series approximations were not employed in this calculation: $\Delta\Psi_{\text{c}}(\mathbf{R})$ was ultimately obtained (via (3.43), (3.49) and (3.51)) from the original phase equation (3.41) using the range to each image pixel. The simulated collection geometry was such that the first image was monostatic with the co-located transmitter and receiver at a slant range of 6500 m and an elevation angle of 12° while the second image was bistatic and shared the same identically located transmitter but with the receiver at a slant range of 3500 m and an elevation angle of 2°. The central wavenumber $\bar{k}_u$ was set to a value of 415 rad/m. For this geometry, the height-of-ambiguity was

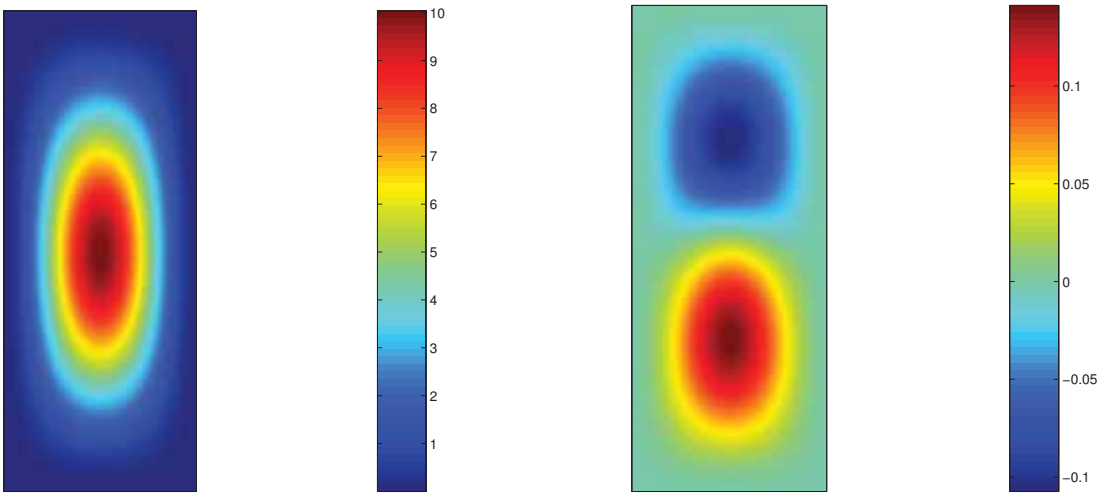

(a) Estimated height (m) (b) Height error (m)

Figure 3.5: Simulation results for 10 m high mound over a 750 m × 300 m region. Near range is at bottom of images.

calculated to be $\delta h = 0.17$ m. The height as recovered from the calculated phase is shown in Figure 3.5(a): this is in excellent agreement with the true simulated height profile. The difference between the recovered and true heights represents the contribution of the second- and higher-order terms of the corrected phase $\Delta\Psi_{\mathrm{c}}(\mathbf{R})$: as these terms are themselves dependent on the unknown height, they are not easily correctable, but, as shown in this example (Figure 3.5(b)), the error caused by these terms is small, being on the order of ± 0.1 m.

It is often convenient for (3.58) and (3.59) to be expressed in terms of an effective wavelength λ and grazing angle difference $\Delta\psi$. This may be done as follows. With the definitions

$$\psi_0 \triangleq \frac{\psi_1 + \psi_2}{2} \tag{3.60}$$

$$\Delta\psi \triangleq \psi_2 - \psi_1 \tag{3.61}$$

we can easily obtain the first-order approximation

$$\tan\psi_2 - \tan\psi_1 = \frac{\Delta\psi}{\cos^2\psi_0}. \tag{3.62}$$

An effective wavelength λ corresponding to the reference ground wavenumber $\bar{k}_u$ may be obtained by projecting from the ground plane up to the mean slant plane between the two images: this gives

$$\bar{k}_u = \frac{4\pi}{\lambda}\cos\psi_0. \tag{3.63}$$

Hence, substituting these into the previous equations gives the desired results

$$\Delta\Psi_{\mathrm{c}}(\mathbf{R}) = w_0 \frac{4\pi}{\lambda}\frac{\Delta\psi}{\cos\psi_0} \tag{3.64}$$

and

$$\delta h = \frac{\lambda}{2}\frac{\cos\psi_0}{|\Delta\psi|}. \tag{3.65}$$

Table 3.1: Parameters of interferometric pairs from Runs A and B.

Interferometric pair	ψ_1	ψ_2	$\lvert\Delta\psi\rvert$	δh
Air-air repeat-pass	12.60°	13.70°	1.10°	0.75 m
Ground-ground repeat-pass	7.46°	8.01°	0.55°	1.55 m
Air-ground single-pass	12.60°	7.46°	5.14°	0.16 m

3.7 Results

Initial interferometric results were obtained by analysing two *Ingara* SAR data collection runs: Run A was the same collection run discussed earlier in Section 2.9 (results from which were displayed in Figure 2.38) while Run B was a similar run, with a nearly identical imaging geometry, but performed approximately 100 minutes later. To form the images for interferometric processing, the uncalibrated VV-polarised data from 4096 consecutive pulses from all four receiver data sets (one each from the airborne and ground-based receivers from the two runs) were first resampled onto a common sampling grid in the spatial frequency domain, chosen to lie within the intersection of the regions of support of the projected data samples from all four receiver data sets. For this grid, the central wavenumber $\bar{k}_u$ was 414.8 rad/m. In order to more precisely account for the terrain slope-dependence of baseline decorrelation [159], for the purposes of this interferometric analysis, the data samples were projected onto a plane-of-best-fit to the local terrain slope, which was determined by analysis of GPS data collected by systematically traversing the site with a hand-held GPS receiver unit. Next, an FFT was performed on the resampled data to produce an initial set of unregistered images, having approximate theoretical -3 dB resolutions of 0.55 m in range and 0.24 m in azimuth, with pixels spaced at intervals of approximately 0.25 m in range and 0.16 m in azimuth. Finally, interferometric pairs were defined for analysis: for each pair to be analysed, a source and a target image were designated, and the source image was registered on to the target image. Once registered pairs of images were obtained, the interferometric coherence γ was calculated for each image pair by spatial averaging according to (3.34): for this data, an averaging window of 5 pixels in range by 10 pixels in azimuth was used.

In this initial data analysis, attention was concentrated on three particular interferometric pairs: an 'air-air' (monostatic-monostatic) pair, where both target and source images were formed from data monostatically collected by the airborne receivers of Runs A and B respectively; a 'ground-ground' (bistatic-bistatic) pair, where both target and source images were formed from data bistatically collected by the ground-based receivers of Runs A and B respectively; and an 'air-ground' (mixed monostatic-bistatic) pair, where the target image was from data monostatically collected by the airborne receiver of Run A and the source image was from data bistatically collected by the ground receiver also of Run A. The air-air and ground-ground pairs are thus cases of repeat-pass interferometry, in which a temporal separation exists between the two interfered images, while the air-ground pair is a case of single-pass interferometry, in which the two images were collected simultaneously. For each pair, let the grazing angles of the target and source images be denoted by ψ_1 and ψ_2 respectively (image grazing angles were defined in Section 3.3). From the discussion in Section 3.6, two important parameters characterising each interferometric pair are thus the angular difference $\Delta\psi = \psi_2 - \psi_1$ and the associated height-of-ambiguity δh: a summary of the parameters for these three image pairs is given in Table 3.1.

For these pairs, typical results from the image registration procedure are shown in Figure 3.6 and Figure 3.7. In the top row, the warp function used in registering the source image onto the target image is depicted by arrows showing the local displacement which was applied to transform the original unregistered image into

the final registered image. The median displacements shown are approximately 5.3 and 9.3 pixels respectively for the air-air and ground-ground image pairs. In the case of the air-ground pair, the median displacement is 39.6 pixels but this appears dominated by a constant offset along the vertical (range) direction. The small displacements between the images in the air-air and ground-ground cases are probably a result of minor changes in imaging geometry and motion measurement errors from pass-to-pass. However, the large displacement in the air-ground case is most likely attributable to differences in signal delays through the RF paths of the distinct airborne and ground-based receivers (this effect is not present in the first two cases as both images in each pair were obtained from the same receiver): such receiver signal-delay differences may be expected to produce a general displacement between the images along the range direction, as is observed. In the second row of the figure, the residual displacements of the registered source image are depicted by a field of arrows (like the warp function) but with zero-length arrows circled for highlighting purposes. These residual displacements were estimated by simply determining the peak location of the cross-correlation between real-valued local image chips of size 64×64 pixels from the registered source and target images: only integer values are thus obtained for these estimates of residual horizontal and vertical displacement. Inspection of the figure reveals that non-zero residual displacements systematically occur over the power-lines, presumably due to local misregistration (from inadequate accommodation of layover differences) as well as the peculiar nature of the power-line images (which, unlike speckle from a homogeneous area, have a dominant component which exhibits little change along the horizontal direction—this produces an indistinct correlation peak which hinders accurate displacement estimation). Also, large residual displacements were consistently obtained over the extreme near-range region at the bottom of the images (which was dominated by bushes, trees and shadows), in the extreme far-range region (which is shadowed from the receiver by the crest of the hill) and around the lateral edges of the images (which is outside the main-lobes of the antenna beampatterns): this is probably attributable to inaccurate or invalid displacement estimates in these regions, since temporal and volume decorrelation afflicts images of trees and bushes while SNR falls precipitously at the edges of the antenna main-lobes and in shadowed regions. However, the results generally show an even distribution of small or zero-valued residual displacements over the open field area of the scene: this suggests the achievement of a reasonably high level of successful image registration by the image registration procedure.

Figure 3.8 shows the interferometric results for the set of interferometric pairs. For display purposes, the coherence magnitudes have been mapped to grey-scale levels such that black corresponds to a coherence of zero while white corresponds to a coherence of one. Qualitatively, inspection of the third column of Figure 3.8 reveals high values of the magnitude of the interferometric coherence γ for the air-air and ground-ground interferometric pairs over the terrain, with the latter slightly higher than the former. However, lower values are observed for the air-ground pair, despite the lack of temporal decorrelation between the simultaneously collected data. To quantify this difference, a 856-row-by-388-column window, carefully positioned to avoid regions with anomalous coherence values (e.g. over the power-lines, in the tree shadows and near the edges of the images), was defined over the central portion of the coherence images covering the open field area. Histograms were then obtained of the $N = 332128$ coherence magnitudes within the window for the various interferometric pairs: the results are shown in Figure 3.9. It can be seen that the air-air and ground-ground coherences are heavily skewed and contain few low values whereas the air-ground pair is less skewed and contains a more even spread of values. Some summary statistics for these distributions are given in Table 3.2: these statistics are also consistent with the above observations, e.g. the mean air-ground coherence is 0.49 which is lower than the means of 0.64 and 0.76 for the air-air and ground-ground coherences and the standard deviation of the air-ground coherence is 0.17 which is larger than the corresponding values for the air-air and ground-ground coherences of 0.13 and 0.12. From the discussion in Section 3.5, these observed coherence

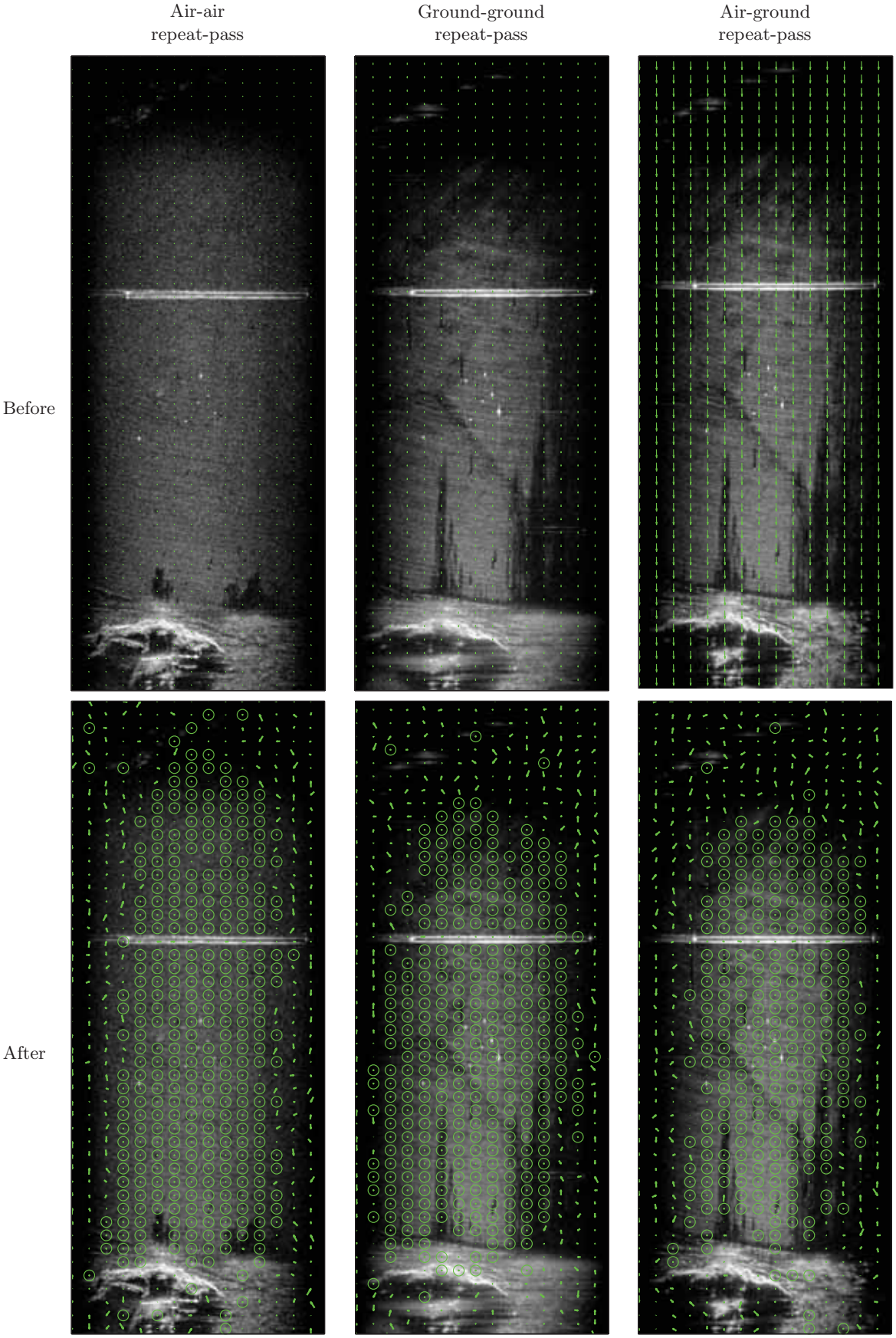

Figure 3.6: Registration results from Runs A and B, showing source images before and after registration. Top row shows warp function applied to source image before registration (see Fig. 3.7 for expanded view). Bottom row shows residual displacements after registration with zero-valued displacements circled.

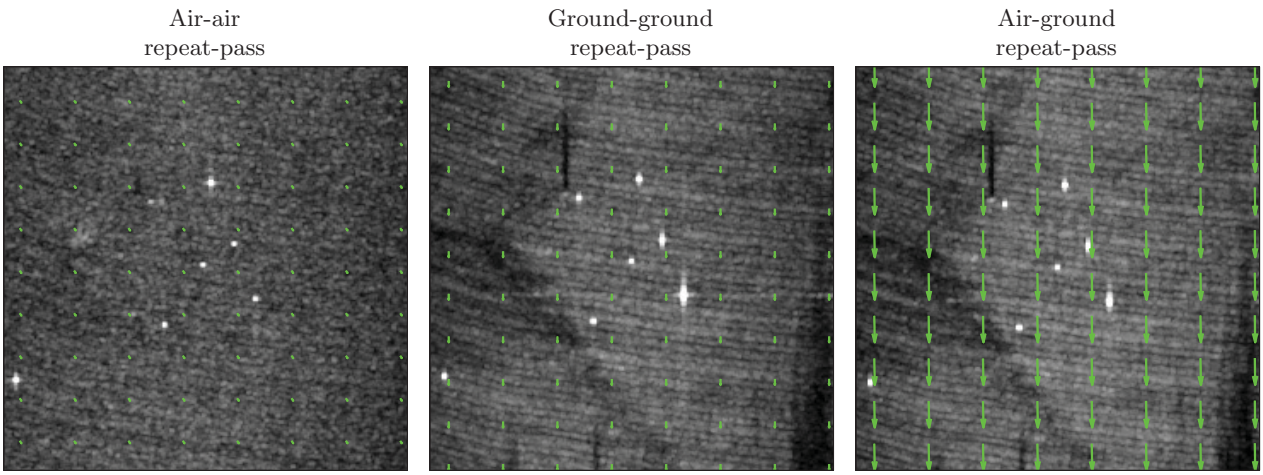

Figure 3.7: Close-up view of warp functions applied to source image before registration.

Table 3.2: Statistics of coherence estimates from Runs A and B. ('S.D.' denotes standard deviation; 'Mode' refers to statistical mode, i.e. the value occurring most frequently in a data set [which corresponds to the location of the peak of a probability distribution or histogram]; D and L are parameters of least squares fit of $p(d; D, L)$ (ref. (3.35)) to histogram.)

Interferometric pair	Mean	S.D.	Median	Mode	D	L
Air-air repeat-pass	0.64	0.13	0.66	0.68	0.63	11
Ground-ground repeat-pass	0.76	0.12	0.79	0.83	0.76	8
Air-ground single-pass	0.49	0.17	0.50	0.55	0.43	8

magnitudes d may be expected to have the probability distribution $p(d; D, L)$ shown in (3.35) which has parameters D and L representing the true coherence magnitude and number of looks respectively: hence, for each of the three interferometric pairs, the generic distribution function $p(d; D, L)$ was fitted to the observed distribution of coherence magnitudes by varying D and L to minimise the mean-squared-error between the observed and expected histogram bin counts (for simplicity, only integer values of L were examined). The resultant fitted probability density functions are shown as the red curves in Figure 3.9 and the corresponding 'best fit' values of their parameters D and L are given in Table 3.2: overall, a good fit is observed between the histograms and red curves, suggesting the general validity of using the probability density function $p(d; D, L)$ for describing this data. From Table 3.2, it may be observed that the various averages (mean, median and mode) of the observed coherence magnitudes are generally greater than or equal to the values of the parameter D, which is consistent with the bias of the sample coherence magnitude towards higher values when it is used as an estimator of the true coherence magnitude [156, 157]: this bias reduces as the true coherence increases, however, and the closer agreement between the mean and D values in the table for higher values of D is consistent with this effect. Also, from Table 3.2, it may be seen that the values of the parameter L are all considerably less than the number of pixels in the spatial averaging window, i.e. $5 \times 10 = 50$: this may be attributable to a degree of spatial correlation between adjacent pixels (see Figure 4.17) which has caused the effective number of independent samples to be less than the total number of pixels averaged.

Two possible causes of the slightly lower coherence of the air-air relative to the ground-ground repeat-pass pair are different SNRs and volume decorrelation. As the airborne receiver was farther from the scene (6.5 km) than the ground-based receiver (3.6 km), the scattered signal strength arriving at the former will be more attenuated than at the latter. Also, as the half-power beamwidth of the airborne antenna is wider (20°

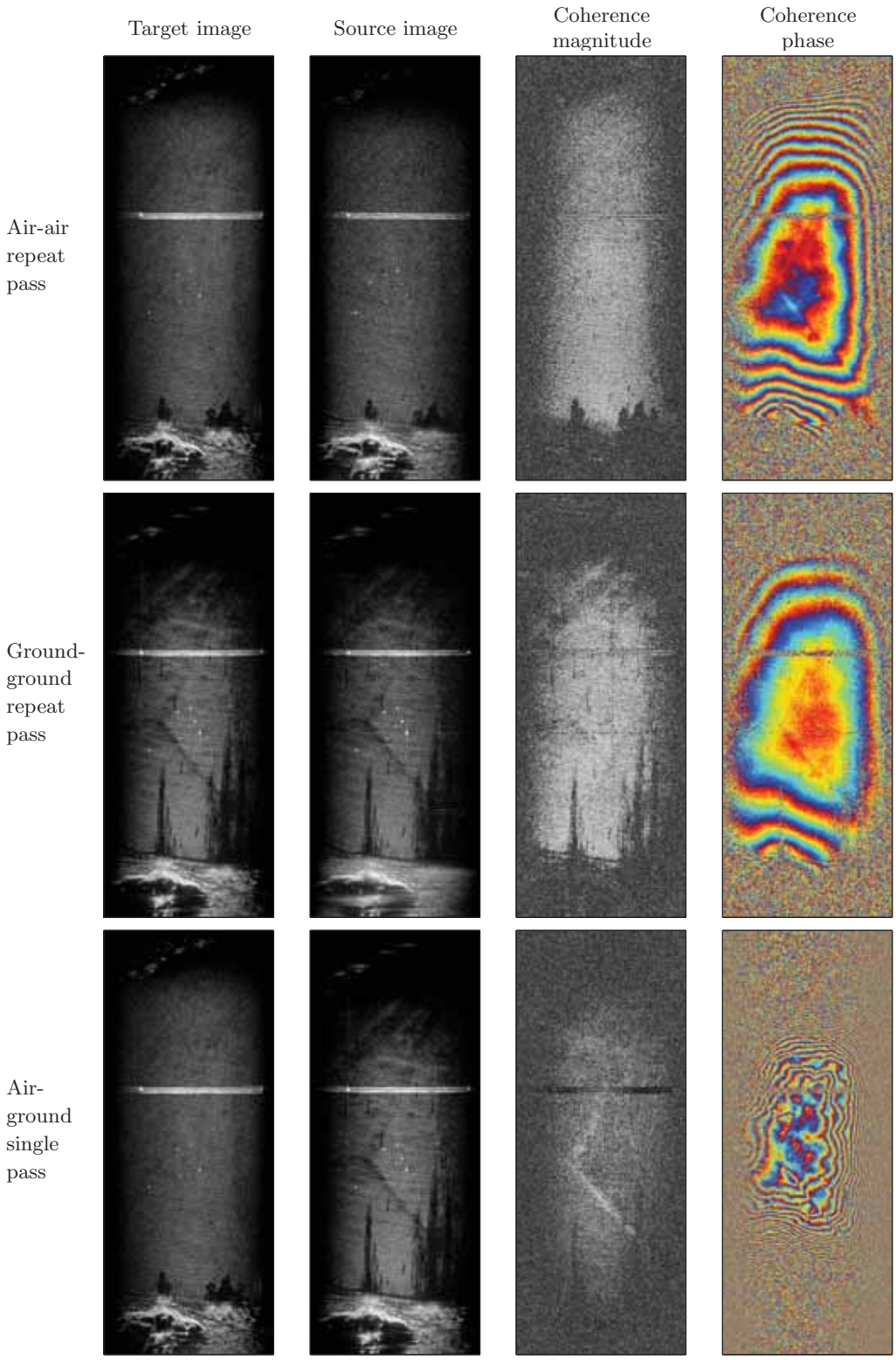

Figure 3.8: Interferometric results from Runs A and B. Source image has been registered onto target image.

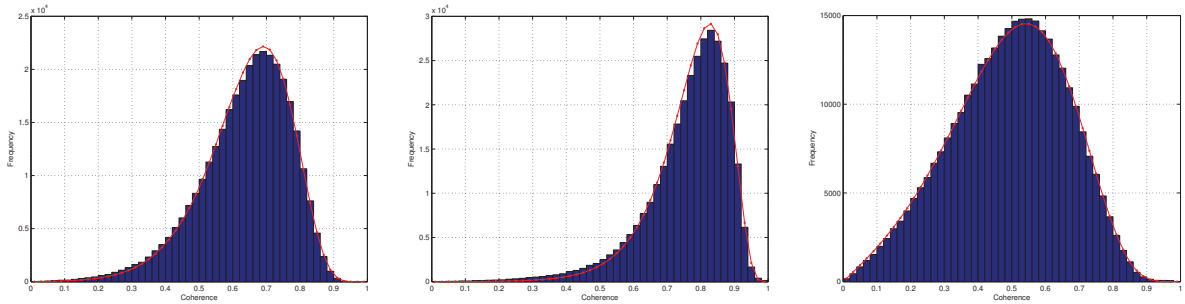

(a) Air-air repeat-pass (b) Ground-ground repeat-pass (c) Air-ground single-pass

Figure 3.9: Histograms of coherence estimates from Runs A and B. Red curves depict fitted probability density functions $p(d; D, L)$ (ref. (3.35)).

in elevation by 1.5° in azimuth) than the beamwidth of the ground-based antenna (2°), more background noise will be admitted into the received signal by the airborne antenna than by the ground-based antenna. Both these effects will tend to degrade the SNR of the data from the airborne receiver relative to data from the ground-based receiver, and a lower airborne receiver SNR would be consistent with the lower coherence observed. Crude estimates of the SNR, obtained from the ratio of the average signal intensity over the open field area to that over the shadows, are approximately 9 dB and 14 dB for the airborne and ground-based receiver images respectively. From (3.33), these SNRs produce expected decorrelations of approximately 0.89 and 0.96, the ratio of which is 0.92: this is greater than the observed ratio of the air-air to ground-ground coherences of 0.84 (calculated from the values in Table 3.2) which suggests that SNR differences are not the sole cause of the observed air-air and ground-ground coherence difference. Indeed, a significant role for volume decorrelation appears possible given the larger difference in grazing angles $|\Delta\psi|$ for the air-air than for the ground-ground interferometric pair. Moreover, a smaller air-air and ground-ground coherence difference has been obtained with a second interferometric data set (discussed below) having smaller values of $|\Delta\psi|$ for the air-air and ground-ground pairs (see Tables 3.4 and 3.5), which is consistent with an expected reduction in volume decorrelation as the difference in SAR look directions decreases: with the very small $|\Delta\psi|$ values in this second data set, the observed air-air to ground-ground coherence ratio is approximately 0.93 which is in good agreement with the value expected from SNR effects alone.

From (3.33), the SNRs of the airborne and ground-based receiver images lead to an expected correlation of 0.92 for the air-ground interferograms, which is considerably higher than the observed value of 0.49, suggesting that other factors are also involved. Some degree of decorrelation in the air-ground single-pass results may simply be due to system and processing issues, e.g. differences in the airborne and ground-based receiver range impulse responses due to RF-path signal distortion may reduce the inter-image coherence. However, various non system- or processor-related factors may also have contributed to the observed low air-ground coherence. For instance, the local terrain slope may be significant relative to the height-of-ambiguity δh, resulting in inaccurate aperture trimming, and an inadequate accounting for baseline decorrelation. Also, the calculation of γ assumes a constant phase over the averaging window used, but this will not be true if significant topographic variations are present, with the result that degradation in the coherence estimate will occur. Moreover, because of the relatively large value of $|\Delta\psi|$ for this pair, potentially significant volume decorrelation may be present—indeed, as already mentioned, the slightly higher coherence of the ground-ground pair relative to the air-air pair appears consistent with a significant contribution from this mechanism. This source of decorrelation is also suggested by the relatively higher coherence magnitudes in the air-ground

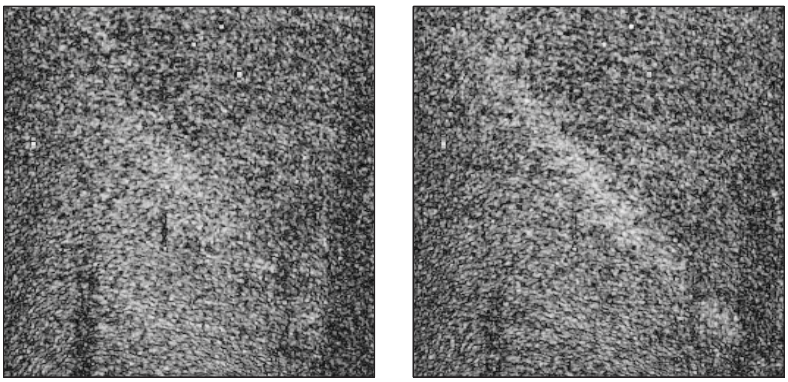

(a) HH (b) VV

Figure 3.10: Close-up views of Run A/B air-ground single-pass coherence images of diagonal band area from uncalibrated HH- and VV-polarised data.

Table 3.3: Statistics of coherence estimates over band and adjoining stubble from Run A/B air-ground single-pass uncalibrated HH- and VV-polarised data.

Region	Polarisation	Mean	S.D.	Median	Mode	D	L
Band	HH	0.56	0.16	0.58	0.59	0.52	9
Band	VV	0.60	0.16	0.62	0.67	0.58	8
Stubble	HH	0.53	0.16	0.56	0.62	0.50	9
Stubble	VV	0.52	0.16	0.53	0.55	0.47	9

pair occurring over the diagonal band of bare earth: as there is no vegetation cover over this region, volume decorrelation is minimal and higher coherence magnitudes would be expected. Further supporting observations come from a simple comparison of the coherence images from the uncalibrated HH- and VV-polarised data: as previously observed in Figure 3.8, there is noticeable contrast between the unvegetated diagonal band and the adjoining area of crop stubble just below it in the VV-polarised coherence image (Figure 3.10(b)) but there is much less contrast in the corresponding HH-polarised coherence image (Figure 3.10(a)). Histograms of coherence values obtained from regions of $N = 39560$ and $N = 38217$ pixels over the band and adjoining stubble area respectively are shown in Figure 3.11 and corresponding summary statistics are tabulated in Table 3.3 (red curves and columns labelled D and L pertain to least squares fit of $p(d; D, L)$ to histograms—recall earlier discussion of Figure 3.9 and Table 3.2): for the HH-polarised data, a similar distribution of coherence values is present in both band and stubble areas but, for the VV-polarised data, the distribution for the band is skewed to contain more high coherence values than the stubble. These observations may be interpreted as the effect of preferential scattering of vertically polarised incident radar radiation by the vertically oriented stalks of crop stubble while horizontally polarised radiation is permitted to penetrate: consequently, there is a tendency for volume scattering to occur in the VV channel from the vertically oriented stubble volume and for surface scattering to occur in the HH channel from a phase centre closer to the ground surface.

Low coherence magnitudes are also observed over the power-lines in the air-ground pair but not in the air-air or ground-ground pairs: unlike the case of the open terrain area, however, this low coherence is most likely artefactual. Due to the large difference in viewing geometries between the monostatic and bistatic images, there are significant differences in the layover of the power-lines in the two images. Such complicated local differences in layover are not easily accommodated by the simple global quadratic warp function employed in

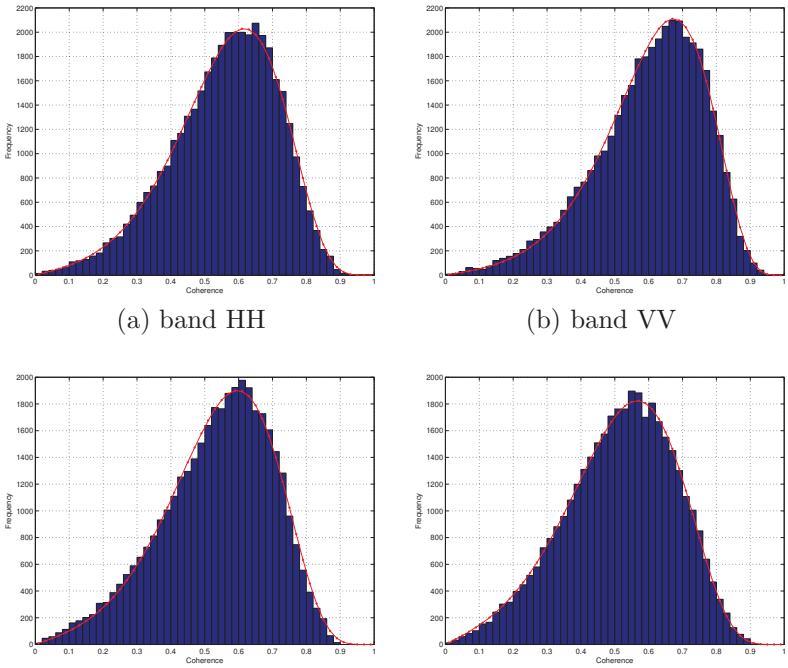

(a) band HH (b) band VV

(c) stubble HH (d) stubble VV

Figure 3.11: Histograms of coherences over diagonal band and adjoining stubble area from Run A/B air-ground single-pass uncalibrated HH- and VV-polarised data. Red curves depict fitted probability density functions $p(d; D, L)$ (ref. (3.35)).

the image registration procedure (more sophisticated warp functions, e.g. involving two-dimensional splines, would be required). Consequently, misregistration has occurred of the pixels over this region of the images, giving rise to the observed low coherence (Figure 3.12). Although having a 'nuisance' effect on the coherence, such differential layover effects between the monostatic and bistatic images may nevertheless have potential value for the interpretation of the three-dimensional structure of objects in the scene.

For display in the figures, the wrapped values of the interferogram phase have been colour-coded such that a cycle of colours from blue to red corresponds to a phase change of 2π radians. Interferometric fringes are clearly observable in the phase of the complex coherence (rightmost column of Figure 3.8) with different fringe rates occurring in each of the air-air, ground-ground and air-ground pairs. The likely cause of these fringe

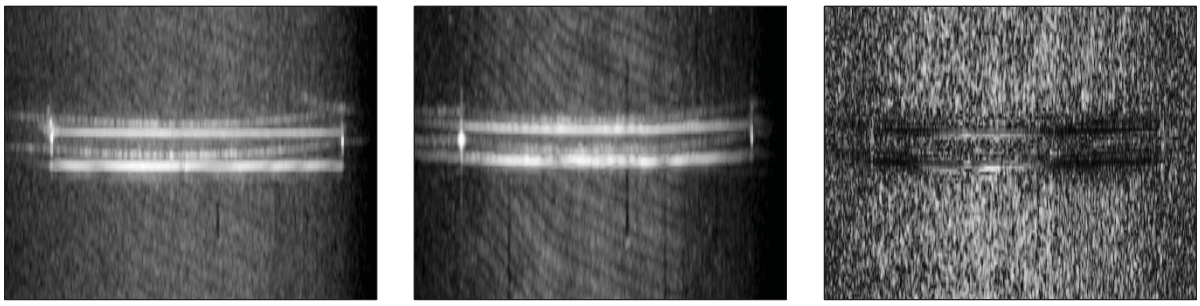

(a) Air image (b) Ground image (c) Coherence magnitude

Figure 3.12: Close-up view of power-lines in images from Run A showing misregistration. Corresponding coherence magnitude between (a) and (b) is shown in (c). (Vertical axis has been stretched for clarity.)

Table 3.4: Parameters of interferometric pairs from Runs A and C.

Interferometric pair	ψ_1	ψ_2	$\lvert\Delta\psi\rvert$	δh
Air-air repeat-pass	12.60°	12.70°	0.10°	7.92 m
Ground-ground repeat-pass	7.46°	7.52°	0.05°	16.01 m
Air-ground repeat-pass	12.60°	7.52°	5.08°	0.16 m

rate differences is the different values of $|\Delta\psi|$ in the various pairs: from (3.65), the height of ambiguity δh is inversely proportional to $|\Delta\psi|$ so, as is readily observed in the results, larger values of $|\Delta\psi|$ will be associated with higher fringe rates as the sensitivity of the phase to local topographical variations increases. The shape of the fringe pattern appears consistent between the air-air and ground-ground pairs, and the apparent fringe spacing in the former is about half that in the latter, which is consistent with the calculated value of δh being approximately half as large in the former as in the latter. The much higher fringe rate observed in the air-ground pair makes visual comparison of its fringe shape with the other two difficult but is consistent with the much smaller calculated value of δh. The overall pattern of the fringes in all three pairs is also broadly consistent with the visually observed ground-truth topography of the imaged scene.

The foregoing discussion has been concerned with the interferometric analysis of a data set comprised of Runs A and B, having a short temporal separation of just 100 minutes. However, a similar interferometric analysis has also been conducted on a data set obtained by replacing Run B with Run C, which was a similar run but performed almost a day later. The temporal separation between Run A and Run C is approximately 23 hours and 50 minutes, and during this intervening period, a utility vehicle entered and drove over part of the imaged scene. To conduct a simple preliminary investigation into the detectability of the vehicle tracks in this data, three interferometric pairs were again defined for analysis: the first two pairs were similar air-air and ground-ground repeat-pass pairs as before but the last was now an air-ground *repeat-pass* pair where the target image was from the airborne receiver of Run A and the source image was from the ground receiver of Run C. As the grazing angles of the aircraft during Runs A and C were much closer than the angles during Runs A and B, the angle difference parameter $|\Delta\psi|$ is considerably less for the air-air and ground-ground pairs of Run A/C than for the corresponding pairs of Run A/B. For all of these pairs, the wavenumber parameter $\bar{k}_u$ was 416.2 rad/m; other parameters are summarised in Table 3.4.

Figure 3.13 presents the results of the interferometric analysis of the various Run A/C pairs. Generally, similar results are obtained for the coherence magnitudes as for the data from Runs A and B: high coherence is observed for the air-air and ground-ground pairs and low coherence is observed for the air-ground pair. However, the histograms, fitted probability density function $p(d; D, L)$ and statistics given in Figure 3.14 and Table 3.5 indicate that the air-air and ground-ground coherences are higher in the Run A/C data than in the corresponding Run A/B data, with the Run A/C ground-ground coherence being slightly higher than the air-air coherence: these observations are again consistent with a reduction in volume decorrelation as a result of the smaller difference in look angles $|\Delta\psi|$. Slightly lower coherence values are present in the air-ground pairs from Runs A and C than Runs A and B: while such a trend is consistent with temporal decorrelation which will be present in the former but not the latter, it is difficult to draw firm conclusions due to the small size of the effect and the variability in the data. For the Run A/C air-air and ground-ground pairs, the fringe rate in the coherence phase is much less than previously observed for Runs A and B: this may also be attributed to the much smaller $|\Delta\psi|$ and larger δh values. In contrast, the fringe pattern for the Run A/C air-ground repeat-pass pair appears very similar to that for the air-ground single-pass pair from Runs A and B: this is consistent with the very similar $|\Delta\psi|$ values for both cases which has resulted in a similar δh and

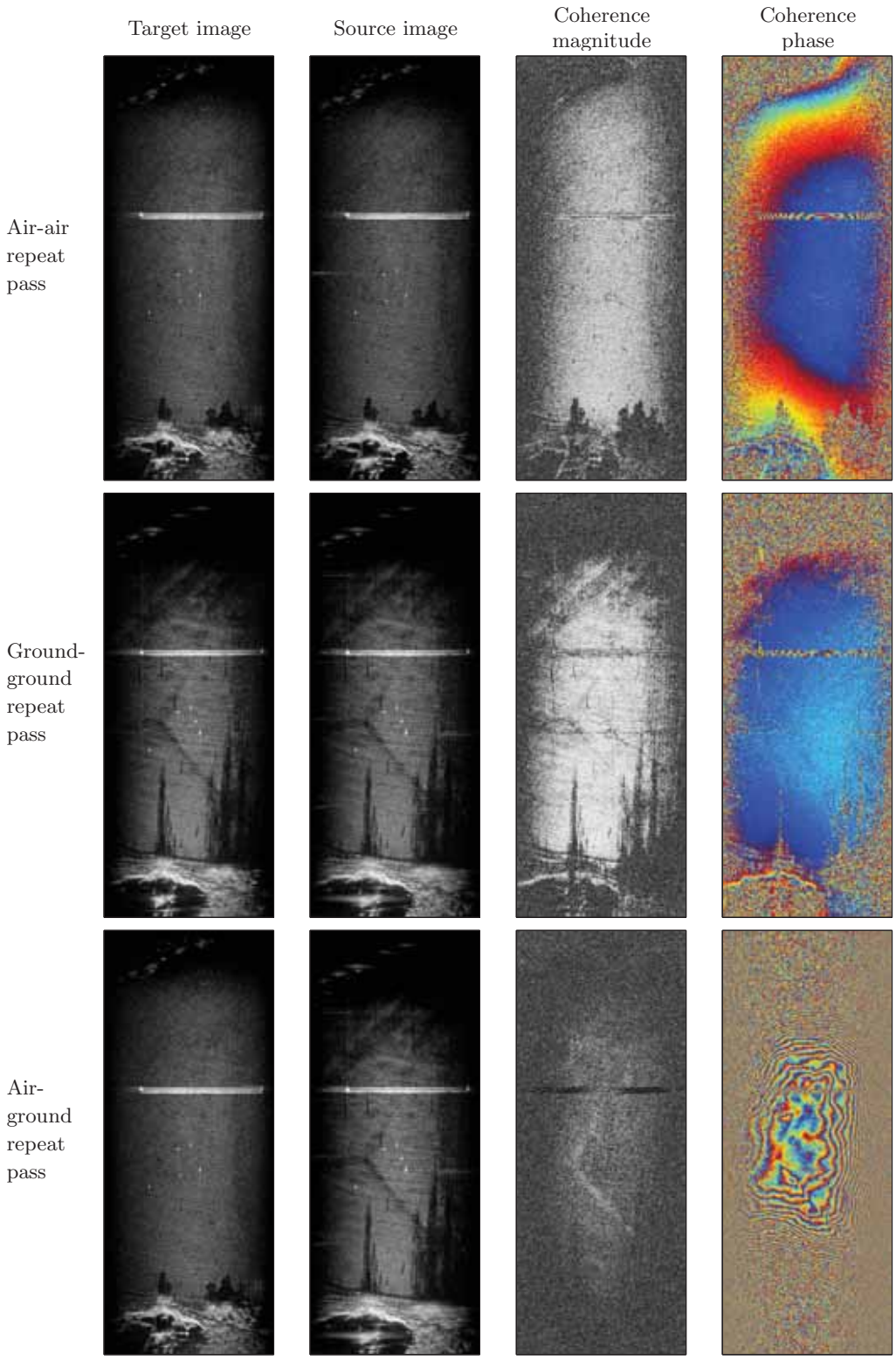

Figure 3.13: Interferometric results from Runs A and C. Source image has been registered onto target image.

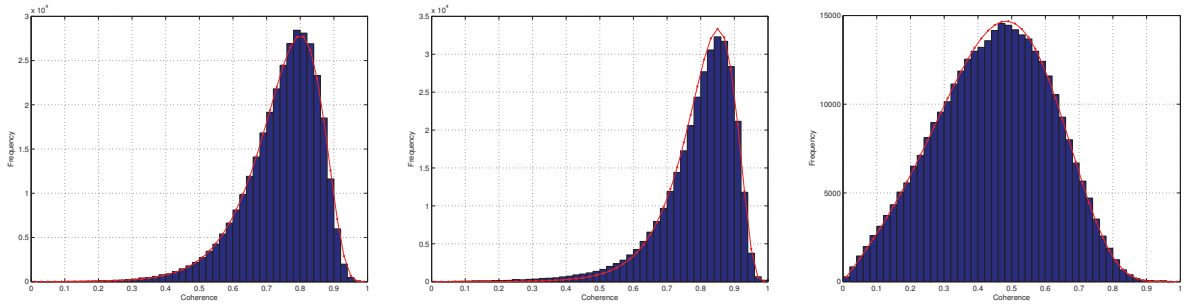

(a) Air-air repeat-pass (b) Ground-ground repeat-pass (c) Air-ground repeat-pass

Figure 3.14: Histograms of coherence estimates from Runs A and C. Red curves depict fitted probability density functions $p(d; D, L)$ (ref. (3.35)).

Table 3.5: Statistics of coherence estimates from Runs A and C.

Interferometric pair	Mean	S.D.	Median	Mode	D	L
Air-air repeat-pass	0.74	0.11	0.76	0.79	0.74	9
Ground-ground repeat-pass	0.79	0.12	0.82	0.86	0.79	8
Air-ground repeat-pass	0.45	0.17	0.46	0.49	0.38	9

hence topographic phase sensitivity.

The track of the utility vehicle is not visible in the intensity images (first two columns of Figure 3.13) but can be easily seen against the high coherence background of the coherence images of the air-air and ground-ground pairs although not against the low coherence background of the air-ground pair (third column of Figure 3.13)—this is more clearly illustrated in the magnified views given in Figure 3.15. Such observations demonstrate the subtle nature of the scene changes caused by the passage of the vehicle, which has disturbed the relative positions of the scattering centres within the SAR resolution cells: this has induced significant changes in the scattering phase but has not appreciably altered the scattering magnitude. As the coherence magnitude is sensitive to these phase differences, the vehicle tracks are visible in the coherence imagery (when the background coherence is high) but not the intensity imagery. While the air-ground background coherence in this data is insufficient for a visual detection of the vehicle track, its detectability with more sophisticated coherent change statistics may be worthy of further investigation. An increase in the utility of such monostatic-bistatic image pairs for coherent change detection may be expected if a higher coherence can be achieved: one possible measure to accomplish this may be to reduce the disparity in viewing angles.

3.8 Conclusion

An initial interferometric analysis of various single-pass and repeat-pass combinations of *Ingara* monostatic and bistatic SAR images has been conducted. High coherence (mean value 0.6 or greater) was obtained for air-air and ground-ground repeat-pass interferometric pairs, comprising either two monostatic images from the airborne receiver or two bistatic images from the ground-based receiver with temporal separations of approximately 100 minutes or 24 hours. However, low coherence (mean value less than 0.5) was found in the air-ground interferometric pairs (each comprising a monostatic and bistatic image from the airborne and ground-based receivers respectively) in cases when both images were simultaneously collected and when they were separated by nearly 24 hours.

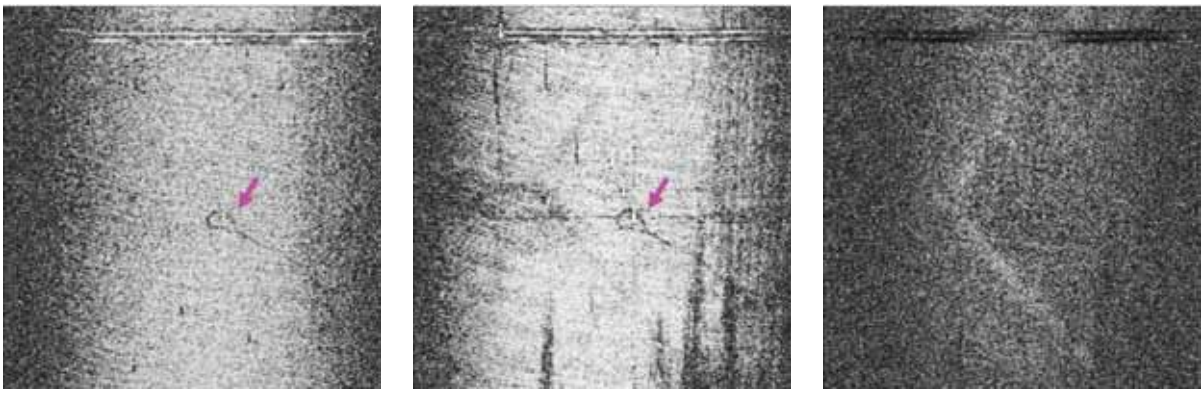

(a) Air-air repeat-pass (b) Ground-ground repeat-pass (c) Air-ground repeat-pass

Figure 3.15: Close-up views of coherence maps from Run A/C data. Arrow indicates vehicle track.

Various factors may have contributed to the low air-ground coherence, including impulse response differences, residual misregistration and baseline decorrelation. A significant role for volume decorrelation is suggested, however, by the large difference in grazing angle $|\Delta\psi|$ between the air-ground images, the overall tendency for higher coherence values to be obtained in the various interferometric pairs (air-air, ground-ground and air-ground) as the grazing angle-difference $|\Delta\psi|$ between the images is reduced, and by the lower decorrelation observed over a band of unvegetated surface in VV-polarised but not HH-polarised images. The large $|\Delta\psi|$ of more than 5° between the monostatic and bistatic images in this data set is largely due to restrictions on the collection geometry (it was not feasible to fly the aircraft much lower): in practical applications, much smaller values of $|\Delta\psi|$ would be routinely employed in order to reduce baseline decorrelation, and this would also assist in reducing volume decorrelation.

For the air-air and ground-ground interferometric pairs, vehicle tracks made in the 24 hour interval between observations are easily detected visually in the coherence maps against the high coherence background. However, the tracks cannot be seen in the air-ground pairs, presumably because of insufficient contrast against the low coherence background. Assuming volume decorrelation to be the dominant effect, this result suggests that similar radar viewing angles should be chosen to increase the air-ground coherence when coherent change detection techniques are to be applied to such pairs.

Despite the decorrelation between the monostatic and bistatic images observed in this data, potential benefits may nevertheless come from the supplementation of the monostatic data set from the airborne receiver by a bistatic data set from the ground-based receiver. One example is the visual differentiation between surface and volume scattering demonstrated by the enhanced contrast between the bare surface region and the adjoining stubble-covered region which is seen in the VV-polarised air-ground coherence images but not the air-air or ground-ground images. Another is the differential overlay of the power-lines which may be of possible utility in elucidating three-dimensional structure.

Possible future work on this topic might thus include deeper investigation into the causes of the air-ground decorrelation, the application of formal coherent change algorithms to the data, further investigation of the polarisation-dependence of the observed bare surface to stubble coherence contrast and application of stereogrammetric techniques to the power-line images.

Chapter 4

Polarimetric calibration

4.1 Introduction

The polarisation state of radar echoes carries potentially useful information for characterising the target [160]: this is exploited in the now well-established technique of radar polarimetry [63, 161]. Polarimetric techniques have been successfully employed in various applications, including crop classification [162], forest management [163], soil moisture estimation [164], sea ice monitoring [165] and oil slick observation [166]. Polarimetric information may also be usefully employed in conjunction with information from other sources: a major example is the synergistic combination of polarisation and phase information in the technique of polarimetric interferometry [62, 144].

To date, polarimetric techniques have predominantly been applied to monostatically scattered radar signals. However, the polarimetric information content of bistatically scattered signals is potentially greater: of the four coefficients $s_{\mathrm{hh}}, s_{\mathrm{hv}}, s_{\mathrm{vh}}, s_{\mathrm{vv}}$ which characterise the polarimetric scattering behaviour of a radar target, for monostatic scattering, the two cross-polarised scattering coefficients s_{hv} and s_{vh} are constrained by the reciprocity theorem to be equal [63], i.e. $s_{\mathrm{hv}} = s_{\mathrm{vh}}$; in the case of bistatic scattering, however, the reciprocity theorem does not apply and no such equivalence is imposed. Bistatic polarimetry is thus a topic of research interest [64, 66] and the collection and analysis of bistatic polarimetric SAR data is a major objective of the *Ingara* bistatic SAR research programme.

In general, to apply the techniques of radar polarimetry, all four target scattering coefficients must be measured by the radar. As this generally entails the transmission of alternating orthogonal polarisations with a consequent doubling of the overall PRF, the radar's unambiguous range in fully polarimetric operation is approximately half of that achievable when operating in a single- or dual-polarised mode in which only one fixed polarisation is transmitted. As a result, motivated by the desire to achieve the full image swath width and maintain revisit rates for space-based SARs, attention has recently been focussed on the polarimetric potential of dual- or compact-polarimetric operating modes where a restricted set comprising only two instead of all four polarisation channels is collected [167–170]. Such modes are outside the scope of the present discussion, however, and only fully polarimetric operation will be considered here.

Multi-polarimetric imaging radars are designed to measure the full quad-polarised target scattering matrix. However, no instrument is perfect and, in practice, distortions are introduced on transmit and receive, so the resulting measurements may not accurately reflect the true characteristics of the scattering process. Hence, for the valid inference of target polarimetric scattering characteristics from collected SAR data, system-introduced

polarimetric distortions must first be corrected by polarimetric calibration.

The calibration of a polarimetric radar system to obtain useful and reliable scattering measurements involves both: (a) the estimation and correction of the system polarisation impurities and channel-imbalances so that ratios between simultaneous measurements from different channels will faithfully reflect target characteristics; as well as (b) the determination and application of an overall scaling factor to the measurements made by the system so that they can be directly related to the absolute scattering characteristics (e.g. in dBm^2) of the targets being measured. The calibration step (b) is a radiometric calibration procedure essentially identical to those originally developed for non-polarimetric single-polarisation radars [171] and is subject to its own particular challenges [172]: hence, it may arguably be regarded as being separate and distinct from the actual polarimetric calibration of the system. Moreover, as polarimetric information is usually exploited by forming ratios between the simultaneous target scattering measurements in the various polarisation channels, the compensation for system polarisation impurities and channel-imbalances in the polarimetric measurements *without radiometric calibration* will suffice for such polarimetric analyses. Hence, we shall limit the scope of the polarimetric calibration problem considered in this chapter to that of step (a) only.

The polarimetric calibration of monostatic polarimetric radars has been well-studied with numerous techniques having been developed [173–182]. To date, less attention, however, has been directed towards the calibration of bistatic polarimetric radars. In particular, unlike the monostatic case where airborne and spaceborne systems have received substantial consideration [183–194], the polarimetric calibration procedures for bistatic systems are primarily intended for laboratory-type instrumentation radars operating in controlled environments [83, 195, 196]: consequently, they tend to employ calibration targets requiring precise alignment with the look-direction of the radar antennas [82]. Such an approach, although quite feasible in stationary laboratory or test-range conditions, is not well-suited to dynamic in-the-field situations (like those of *Ingara*) involving a manœuvring airborne component which is subject to navigation errors. This motivates the investigation of alternative calibration methods for the *Ingara* bistatic data.

In this chapter, we discuss the polarimetric calibration of the *Ingara*-collected data sets. By way of introduction, we begin in the next section (Section 4.2) by presenting some general background information to set the problem of SAR polarimetric calibration into context. We then discuss a model for the polarimetric distortions introduced by the radar system in Section 4.3. This is followed by a discussion of the theoretical basis of the methods to be employed for polarimetric calibration: the distributed target-based methods for the calculation of the cross-talk parameters are discussed in Section 4.4, followed by methods for the estimation of the channel-imbalance in Section 4.5. The actual application of these methods to the collected *Ingara* data are the subject of Section 4.6: first an overview is given of the data which is available for calculating the calibration solution; then results from the application of the calibration algorithms are presented. Finally, we draw some conclusions.

4.2 Background

In earlier times, single-polarisation SAR systems were the norm and SAR images were only analysed qualitatively, so SAR instrument calibration was not accorded a high priority. However, the proliferation of multi-polarimetric systems and the growth of interest in quantitative techniques for SAR image exploitation has now firmly established its importance. The goal of calibration is essentially to ensure the stability, repeatability, accuracy and hence reliability of measurements derived from SAR imagery, thus enabling the full value of SAR data to be realised. Generally, full SAR calibration involves multiple varied aspects of the SAR

images, including geometric and radiometric as well as polarimetric calibration: a comprehensive overview of the SAR calibration problem may be found in the paper by Freeman [80]. In accordance with the remarks in the previous section, however, in this discussion, our interest will be restricted only to polarimetric calibration.

Fundamentally, polarimetric calibration involves the comparison of special polarimetric test measurements made by the radar system against the expected results: by employing a suitable mathematical model, the polarimetric distortion which was introduced by the radar, comprising interchannel cross-talk polarisation impurities and amplitude and phase imbalances between channels, is determined and can then be corrected in other measurements. To obtain a suitable set of "expected results" with which to compare the measurements, radar targets with known scattering properties are commonly employed. These may be classified into two categories: point targets (e.g. trihedral and dihedral corner reflectors, spheres, cylinders/dipoles, etc.) and distributed targets (e.g. agricultural fields, forests, etc.). Correspondingly, there are two major approaches to polarimetric calibration: point target-based methods and distributed target-based methods. Numerous examples of these have been described in the published literature, the majority of which were developed with monostatic polarimetric radars in mind and with only a minority specifically addressing the case of bistatic radars (nevertheless, techniques developed specifically for the monostatic case may still be applicable to the bistatic case if a nearly monostatic geometry is employed during the calibration procedure). In the following two paragraphs, the examples discussed will mainly relate to monostatic rather than bistatic calibration: bistatic-specific techniques will be the focus towards the end of this section.

The point target-based methods generally employ a set of known reference targets for gathering measurements with which to calculate the system polarimetric distortion parameters. These calibration methods were generally developed with instrumented anechoic chamber-based point target measuring radars in mind (for which clutter levels are low and accurate target alignment with the radar antennas is easily achieved) but they may also be used for imaging radars if appropriate measures are taken (such as using high RCS targets with low alignment sensitivity deployed in a low-return area). In general, a set of three measurements of suitably chosen targets are required: a sphere, a horizontal cylinder and a cylinder tilted at 45° were utilised in the work of Whitt et al. [195]; a sphere or circular disk, an upright dihedral and a dihedral tilted at 45° were employed by Wiesbeck and Riegger [197] and also by Wiesbeck and Kähny [178]; a flat plate, an upright dihedral and a dihedral tilted at an arbitrary angle were used by Chen et al. [198, 199]; while a sphere and two arbitrary passive targets are required in the approach of Whitt and Ulaby [176]—the use of various more general triplets of targets for polarimetric calibration has been extensively investigated by Yueh et al. [173]. Under certain conditions, however, a smaller target set can suffice: with the assumption of negligible cross-talk, Sarabandi et al. [174] required only a sphere and a tilted cylinder; and by assuming reciprocity of the transmit and receive distortions, Gau and Burnside [181] needed only an upright and tilted dihedral, while Sarabandi and Ulaby [175] could calibrate with just a single sphere or trihedral. However, while such an assumption of radar distortion reciprocity may be valid for some monostatic radars where the same hardware is used for both transmit and receive, it is much less tenable for bistatic systems where distinct hardware is used in the separated transmitter and receiver. Interestingly, the set of point targets suitable for use in polarimetric calibration need not be restricted to passive reflecting targets: Polarimetric Active Radar Calibrators (PARCs) have been employed by Freeman et al. [183] and (for bistatic systems) the use of the direct-path signal for polarimetric calibration has even been proposed [84]: both PARC and direct-path signal measurements share similar characteristics with those of passive reflectors and may be employed in an identical manner for polarimetric calibration.

By contrast, distributed target-based polarimetric calibration methods employ as their reference targets extended homogeneous areas with known statistical scattering properties. Such targets are naturally suited

to imaging radars, which may typically cover large areas in a single image swath. Moreover, spatially varying polarimetric distortions are more easily estimated using this extended target approach, since otherwise multiple point targets must be deployed across the swath. A further advantage is that, unlike the point target method, where calibration reflectors must be deployed prior to imaging, the distributed target approach requires no such effort as the extended targets being used are already naturally present in the scene. To estimate the polarimetric distortion parameters, the covariance matrix between the variously polarised measurements is calculated and compared with the expected covariances from a knowledge of the target. In Sarabandi's approach [186], a full knowledge of the true Mueller matrix of the distributed target is employed to solve for the polarimetric distortion parameters. Generally, however, so detailed a knowledge of the distributed target is not at hand, and less stringent conditions must be substituted. Hence, rather than a specific knowledge of the covariances, most distributed target approaches simply rely on two key assumptions concerning the scattering behaviour of the distributed target: the first is that the target displays scattering reciprocity, i.e. $s_{\mathrm{hv}} = s_{\mathrm{vh}}$; and the second is that the target is azimuthally symmetric so that the co- and cross-polarised scattering is uncorrelated [200], i.e. $\langle s_{ii} s_{ij}^* \rangle = 0$. These assumptions are usually met for natural distributed targets imaged in a monostatic geometry [201], but a masking procedure for excluding regions with high co-/cross-polarised correlation can also be used [202]. With these assumptions, the four cross-talk terms and the VH-HV channel-imbalance term of the polarimetric calibration solution can be estimated, leaving just one remaining channel-imbalance term to be determined: typically, this outstanding term can be estimated using a single known point target, thus completing the determination of the polarimetric calibration solution. The earliest attempt at such distributed target-based calibration seems to be by van Zyl [184]: his approach is somewhat restrictive, however, due to an assumption of polarimetric distortion reciprocity, which is not universally valid for all radars. Such radar reciprocity is not assumed in the method of Klein [85], which is based on calculating the eigenvector corresponding to the minimum eigenvalue of the measured covariance matrix followed by iterative refinement of the calibration solution. A non-iterative method for determining the calibration parameters has been proposed by Quegan [86]. In his approach, an estimation of the VH-HV channel-imbalance is obtained based on the assumption of equal channel noise: this was subsequently improved by Kimura et al. [203] to accommodate differences between the noise levels. However, an uncorrected bias is present in Quegan's cross-talk estimators, which results in inaccurate cross-talk estimates [88]: this is corrected in an iterative modification of Quegan's method proposed by López-Martinez et al. [204]. The assumption of target azimuthal symmetry on which these methods rely is not valid in the presence of a significant azimuthal terrain slope: to accommodate such cases, Ainsworth et al. [87] allow non-zero co-/cross-polarised correlations in their method which employs an iterative procedure by which incremental corrections to the VH-HV imbalance and cross-talk parameters are estimated at each iteration. The above methods all employ linear approximations of a standard non-linear mathematical model for the effect of the system polarimetric distortion which are obtained by assuming a low cross-talk level: instead of the usual approach of applying algebra to the linearised model to estimate the calibration parameters, Xiong [182] has proposed an alternative based on the use of a genetic algorithm, while Mura et al. [191] have proposed another involving the application of a least-squares minimisation procedure to measurements of a known distributed target obtained from three independent looks.

As previously stated, the plethora of point- and distributed target-based approaches discussed above are mainly intended for monostatic radar systems: only a few authors have specifically addressed the polarimetric calibration of bistatic systems. Among these are: Kähny et al. [196] who apply a similar method to Wiesbeck and Kähny's [178] for bistatic polarimetric calibration; Bradley et al. [82, 83] who give a broad overview of targets and techniques for bistatic polarimetric calibration; McLaughlin et al. [205] who propose a bistatic

polarimetric calibration technique based on transmission-link measurements for separate calibration of the receiver and transmitter subsystems; and Daout et al. [84] who employ the direct-path signal to calibrate a bistatic system with negligible cross-talk. These techniques are all directed toward laboratory-type instrumentation radars for which precise antenna positioning is achievable: techniques using point targets tend to involve measurements made in a quasi-monostatic geometry so that monostatic calibration methods can be applied while the techniques based on the use of transmission-link and direct-path signals involve careful boresight-to-boresight alignment of transmit and receive antennas. None of the techniques specifically address the problem of polarimetrically calibrating dynamic bistatic systems with an airborne component.

For calibrating the *Ingara* bistatic SAR, an approach was employed based on collecting quasi-monostatic data so as to apply an adapted version of the distributed target algorithms which is supplemented with various point target measurements. In the next section, the groundwork is laid for discussing the method by presenting a mathematical model for the radar polarimetric distortion.

4.3 Polarimetric model

As a foundation for subsequent discussion, this section introduces a basic model for the polarimetric distortions which afflict the measurements made by a polarimetric SAR. Such a polarimetric imaging radar transmits and receives both elements of an orthogonal polarisation basis: for the linear basis, this consists of horizontally (H) and vertically (V) polarised signals. Hence, four possible combinations of transmit and receive polarisations are possible: in the linear basis, these may be denoted by the upper-case letter pairs 'HH', 'HV', 'VH' and 'VV' respectively, where the first letter in each pair refers to the polarisation being transmitted and the second to that being received. In this convention, the order of the letters is intuitive, being in accord with the temporal order of the transmit and receive processes. However, for the purposes of matrix-based calculation, it is more convenient to reverse this order, so that the receive polarisation is specified by the first letter and the transmit polarisation by the second: to avoid potential ambiguity, lower-case letters will be employed to indicate this reverse-order convention, e.g. 'hh', 'vh', 'hv', 'vv'. Although this discussion will employ the linear polarisation basis, no generality is lost as an arbitrary polarisation can be synthesised from a given basis [206].

Two conventions for specifying the orientation of the horizontal and vertical axes relative to the direction of wave propagation are widely used: the Forward-Scatter Alignment (FSA) convention and the Back-Scatter Alignment (BSA) convention [63]. As the choice of convention affects how quantities of interest should be interpreted (see Figure 4.1), it must be specified to avoid any ambiguity: although the FSA is preferred for problems involving bistatic scattering, we shall adopt the BSA as it is more convenient when making practical measurements. No generality is lost however: quantities can always be converted between the two conventions by using appropriate transformation matrices.

To completely specify the scattering characteristics of a target, the scattered signal must be measured in all four combinations of transmit and receive polarisations, resulting in a 2×2 complex matrix with entries s_{ij}, where $i, j \in \{\mathrm{h}, \mathrm{v}\}$. However, polarimetric distortions introduced by the transmit and receive processes result in an observed scattering matrix with entries o_{ij} which differ from the actual quantities of interest s_{ij}: a standard polarimetric distortion model which relates the two is

$$\begin{bmatrix} o_{\mathrm{hh}} & o_{\mathrm{hv}} \\ o_{\mathrm{vh}} & o_{\mathrm{vv}} \end{bmatrix} = \begin{bmatrix} r_{\mathrm{hh}} & r_{\mathrm{hv}} \\ r_{\mathrm{vh}} & r_{\mathrm{vv}} \end{bmatrix} \begin{bmatrix} s_{\mathrm{hh}} & s_{\mathrm{hv}} \\ s_{\mathrm{vh}} & s_{\mathrm{vv}} \end{bmatrix} \begin{bmatrix} t_{\mathrm{hh}} & t_{\mathrm{hv}} \\ t_{\mathrm{vh}} & t_{\mathrm{vv}} \end{bmatrix} + \begin{bmatrix} n_{\mathrm{hh}} & n_{\mathrm{hv}} \\ n_{\mathrm{vh}} & n_{\mathrm{vv}} \end{bmatrix} \tag{4.1}$$

where the t_{ij} and r_{ij} represent the distortions introduced by the transmit and receive processes and the n_{ij}

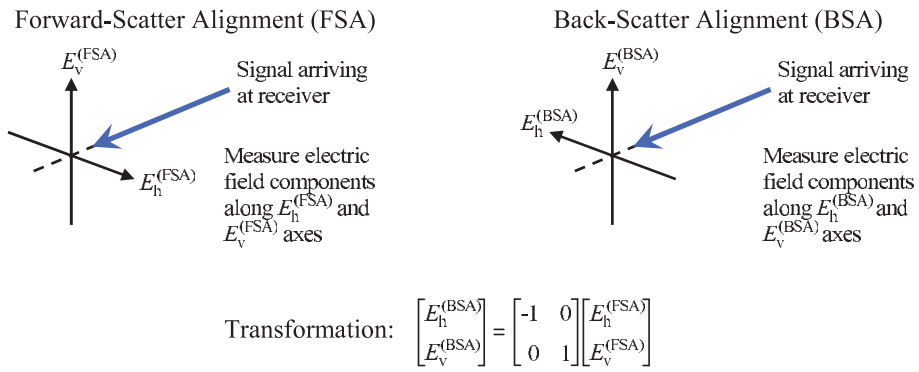

Figure 4.1: Illustrative example of Forward-Scatter and Back-Scatter Alignment and transformation between them.

represent system noise. In accordance with the notational convention being used, the quantities r_{ij} and t_{ij} refer to the response in channel i to a stimulus in channel j. Generally, polarimetric radars will be designed to have high isolation between the co- and cross-polarised channels, so we may assume that $|r_{ij}| \ll |r_{ii}|$, $|r_{ji}| \ll |r_{ii}|$, $|t_{ij}| \ll |t_{ii}|$, $|t_{ji}| \ll |t_{ii}|$.

Two points are worth keeping in mind with regard to the model above. The first is that, strictly speaking, a complex-valued scaling factor of the form e^{-jkR}/R, where R is the propagation distance from target to receiver and $k = 2\pi/\lambda$ where λ is the wavelength, should be prepended to the first (matrix product) term on the right-hand-side of (4.1). However, as polarimetric analyses generally involve only ratios of the o_{ij} (or s_{ij}) with each other, this scaling factor is of little practical significance and its display is often suppressed in the interests of clarity—we shall also adopt this policy here. The second point is that the distortion parameters may vary as a function of look direction relative to the antenna boresight (and hence scene position) so that, for high measurement precision over a large image swath, different calibration solutions should be obtained for each region of interest, e.g. by deploying multiple calibration targets across the swath, making assumptions as to the scattering behaviour of naturally occurring distributed targets or using a knowledge of the antenna beampatterns to extend a calibration solution for one viewing angle to others [207].

Equation (4.1) may be rewritten more compactly in terms of matrices, i.e.

$$\mathbf{O} = \mathbf{RST} + \mathbf{N} \tag{4.2}$$

in which each matrix has the generic form

$$\mathbf{X} = \begin{bmatrix} x_{\mathrm{hh}} & x_{\mathrm{hv}} \\ x_{\mathrm{vh}} & x_{\mathrm{vv}} \end{bmatrix}. \tag{4.3}$$

By re-expressing $\mathbf{O}$, $\mathbf{S}$ and $\mathbf{N}$ in the vector form

$$\mathbf{x} = \begin{bmatrix} x_{\mathrm{hh}} \\ x_{\mathrm{hv}} \\ x_{\mathrm{vh}} \\ x_{\mathrm{vv}} \end{bmatrix} \tag{4.4}$$

the polarimetric distortion model can also be written as

$$\mathbf{o} = \mathbf{P}\mathbf{s} + \mathbf{n} \tag{4.5}$$

in which the 4×4 complex matrix $\mathbf{P}$ is given by

$$\begin{aligned} \mathbf{P} &= \mathbf{R} \otimes \mathbf{T}^T \\ &= \begin{bmatrix} r_{\mathrm{hh}}t_{\mathrm{hh}} & r_{\mathrm{hh}}t_{\mathrm{vh}} & r_{\mathrm{hv}}t_{\mathrm{hh}} & r_{\mathrm{hv}}t_{\mathrm{vh}} \\ r_{\mathrm{hh}}t_{\mathrm{hv}} & r_{\mathrm{hh}}t_{\mathrm{vv}} & r_{\mathrm{hv}}t_{\mathrm{hv}} & r_{\mathrm{hv}}t_{\mathrm{vv}} \\ r_{\mathrm{vh}}t_{\mathrm{hh}} & r_{\mathrm{vh}}t_{\mathrm{vh}} & r_{\mathrm{vv}}t_{\mathrm{hh}} & r_{\mathrm{vv}}t_{\mathrm{vh}} \\ r_{\mathrm{vh}}t_{\mathrm{hv}} & r_{\mathrm{vh}}t_{\mathrm{vv}} & r_{\mathrm{vv}}t_{\mathrm{hv}} & r_{\mathrm{vv}}t_{\mathrm{vv}} \end{bmatrix} \end{aligned} \tag{4.6}$$

where $\cdot^T$ denotes the matrix transpose and $\otimes$ denotes the Kronecker product. The matrix $\mathbf{P}$ may also be usefully expressed as

$$\mathbf{P} = Y\,\mathbf{MAK} \tag{4.7}$$

where

$$\mathbf{M} = \begin{bmatrix} 1 & v & w & vw \\ z & 1 & wz & w \\ u & uv & 1 & v \\ uz & u & z & 1 \end{bmatrix}, \quad \mathbf{A} = \begin{bmatrix} \alpha & 0 & 0 & 0 \\ 0 & 1 & 0 & 0 \\ 0 & 0 & \alpha & 0 \\ 0 & 0 & 0 & 1 \end{bmatrix}, \quad \mathbf{K} = \begin{bmatrix} k^2 & 0 & 0 & 0 \\ 0 & k & 0 & 0 \\ 0 & 0 & k & 0 \\ 0 & 0 & 0 & 1 \end{bmatrix} \tag{4.8}$$

and the complex scalar quantities are given by

$$\begin{aligned} Y = r_{\mathrm{vv}}t_{\mathrm{vv}}, \quad k = \frac{r_{\mathrm{hh}}}{r_{\mathrm{vv}}}, \quad \alpha = k^{-1}\frac{t_{\mathrm{hh}}}{t_{\mathrm{vv}}}, \\ u = \frac{r_{\mathrm{vh}}}{r_{\mathrm{hh}}}, \quad v = \frac{t_{\mathrm{vh}}}{t_{\mathrm{vv}}}, \quad w = \frac{r_{\mathrm{hv}}}{r_{\mathrm{vv}}}, \quad z = \frac{t_{\mathrm{hv}}}{t_{\mathrm{hh}}}. \end{aligned} \tag{4.9}$$

Hence, from the above: the quantity Y represents the overall gain in the vv channel; k is the channel-imbalance ratio for receive; α is the ratio of the transmit and receive channel-imbalances; and u, v, w and z are ratios describing the cross-talk between channels. In general, especially for a well-designed polarimetric radar with high channel isolation and good channel balance, it may be assumed that $|u|, |v|, |w|, |z| \ll 1$ and $|\alpha|, |k| \approx 1$.

The general validity of the polarimetric model in (4.5) and (4.6) has been questioned by Freeman [208]. Specifically, Freeman argues that the implicit assumption of system constancy is not always applicable, particularly in the case where the H- and V-receiver gains are continually being switched to accommodate the lower cross- than co-polarised return powers typically encountered for natural targets: in such cases (of which *Ingara* is one), the standard polarimetric model is not necessarily valid unless the receiver gain differential is removed from the data. As compensation for such receiver gain changes is indeed routinely applied during processing of the *Ingara* data, we shall continue to employ this model in our discussion.

Polarimetric calibration involves the estimation of the parameters Y, k, α, and u, v, w, z so that the polarimetric distortion matrix $\mathbf{P}$ is determined and (4.5) can then be inverted to give the desired scattering response $\mathbf{s}$: neglecting the noise $\mathbf{n}$, the resultant expression is

$$\mathbf{s} = Y^{-1}\mathbf{K}^{-1}\mathbf{A}^{-1}\mathbf{M}^{-1}\mathbf{o}. \tag{4.10}$$

This suggests a logical order for transforming the uncalibrated data $\mathbf{o}$ through intermediate partially calibrated

states to the final fully calibrated state $\mathbf{s}$: first calculate the cross-talk ratios u, v, w, z, which determine $\mathbf{M}$, and calibrate for the effects of cross-talk; next, calculate the channel-imbalance ratios α and k, which determine $\mathbf{A}$ and $\mathbf{K}$, and calibrate for channel-imbalance; and finally calculate the absolute calibration parameter Y and scale the data to the correct radiometric level. As radiometric calibration is outside the scope of this discussion, only the first two steps will be discussed in the following sections.

4.4 Cross-talk calibration

Estimates of the cross-talk ratios u, v, w, z as well as the channel-imbalance ratio α can be obtained from the statistics of measurements of the back-scattering from a suitable distributed target. Such a target generally comprises an extended homogeneous area, e.g. a grassy field. For calibration purposes, some knowledge of the target's scattering properties is required: generally, an absolute quantitative knowledge is not at hand so it is usual to only require that the covariance matrix of the target's scattering vector $\mathbf{s}$ assumes a particular standard form: this known form of the covariance matrix can then be exploited to obtain the aforementioned parameter estimates, and various algorithms have previously been proposed to accomplish this [85–87]. In the following subsections, we first expound the general theoretical basis of these approaches, then discuss various distributed target-based algorithms in turn. The final subsection presents a comparison of the relative performance on simulated data of the algorithms discussed.

4.4.1 Basic theory

To begin, let the covariance matrix $\mathbf{C_x}$ of the generic random vector $\mathbf{x}$ of (4.4) be defined as

$$\begin{aligned} C_{\mathbf{x}} &\triangleq \left\langle \mathbf{x}\mathbf{x}^H \right\rangle \\ &= \begin{bmatrix} \langle x_{\mathrm{hh}} x_{\mathrm{hh}}^* \rangle & \langle x_{\mathrm{hh}} x_{\mathrm{hv}}^* \rangle & \langle x_{\mathrm{hh}} x_{\mathrm{vh}}^* \rangle & \langle x_{\mathrm{hh}} x_{\mathrm{vv}}^* \rangle \\ \langle x_{\mathrm{hv}} x_{\mathrm{hh}}^* \rangle & \langle x_{\mathrm{hv}} x_{\mathrm{hv}}^* \rangle & \langle x_{\mathrm{hv}} x_{\mathrm{vh}}^* \rangle & \langle x_{\mathrm{hv}} x_{\mathrm{vv}}^* \rangle \\ \langle x_{\mathrm{vh}} x_{\mathrm{hh}}^* \rangle & \langle x_{\mathrm{vh}} x_{\mathrm{hv}}^* \rangle & \langle x_{\mathrm{vh}} x_{\mathrm{vh}}^* \rangle & \langle x_{\mathrm{vh}} x_{\mathrm{vv}}^* \rangle \\ \langle x_{\mathrm{vv}} x_{\mathrm{hh}}^* \rangle & \langle x_{\mathrm{vv}} x_{\mathrm{hv}}^* \rangle & \langle x_{\mathrm{vv}} x_{\mathrm{vh}}^* \rangle & \langle x_{\mathrm{vv}} x_{\mathrm{vv}}^* \rangle \end{bmatrix} \end{aligned} \tag{4.11}$$

where $\mathbf{x}^H$ denotes the conjugate transpose of $\mathbf{x}$ and $\langle \cdot \rangle$ denotes averaging (in practice, $\langle \cdot \rangle$ is calculated by averaging pixels over a region of the image). If we assume that the various channel noises n_{ij} are uncorrelated with the various s_{ij} as well as with each other, then from (4.5), the covariance matrices of the random vectors $\mathbf{o}$, $\mathbf{s}$ and $\mathbf{n}$ are related by

$$\mathbf{C} \triangleq \mathbf{C_o} - \mathbf{C_n} = \mathbf{P}\mathbf{C_s}\mathbf{P}^H. \tag{4.12}$$

In the above, $\mathbf{C_s}$ represents the scattering behaviour of the distributed target. The effects of system-introduced polarimetric distortion are to pre- and post-multiply $\mathbf{C_s}$ by $\mathbf{P}$ and $\mathbf{P}^H$, giving the matrix $\mathbf{C}$, which may be regarded as a noise-corrected version of the actual observed covariance matrix $\mathbf{C_o}$, obtained by subtracting away the noise covariance matrix $\mathbf{C_n}$.

Under appropriate assumptions, the noise covariance matrix $\mathbf{C_n}$ takes a very simple form: since the noise processes in different polarisation channels may be assumed to be uncorrelated, i.e. $\left\langle n_p n_q^* \right\rangle = 0$ for different polarisations $p, q \in \{\mathrm{hh}, \mathrm{hv}, \mathrm{vh}, \mathrm{vv}\}$, the matrix $\mathbf{C_n}$ will be diagonal with non-negative diagonal entries N_{ii} representing the noise powers in the various polarisation channels, viz.

$$N_{11} = \langle n_{\mathrm{hh}} n_{\mathrm{hh}}^* \rangle, \quad N_{22} = \langle n_{\mathrm{hv}} n_{\mathrm{hv}}^* \rangle, \quad N_{33} = \langle n_{\mathrm{vh}} n_{\mathrm{vh}}^* \rangle, \quad N_{44} = \langle n_{\mathrm{vv}} n_{\mathrm{vv}}^* \rangle. \tag{4.13}$$

Moreover, as the H and V polarisations are received by distinct RF hardware in the receiver, the noise powers may be expected to vary only with the received but not the transmitted polarisations, i.e. we expect $\langle n_{\mathrm{hh}} n_{\mathrm{hh}}^* \rangle = \langle n_{\mathrm{hv}} n_{\mathrm{hv}}^* \rangle$ and $\langle n_{\mathrm{vh}} n_{\mathrm{vh}}^* \rangle = \langle n_{\mathrm{vv}} n_{\mathrm{vv}}^* \rangle$. Hence, we have $N_{11} = N_{22}$ and $N_{33} = N_{44}$, so the expected form of $\mathbf{C_n}$ is

$$\mathbf{C_n} = \begin{bmatrix} N_{22} & 0 & 0 & 0 \\ 0 & N_{22} & 0 & 0 \\ 0 & 0 & N_{33} & 0 \\ 0 & 0 & 0 & N_{33} \end{bmatrix}. \tag{4.14}$$

For the purposes of polarimetric calibration, two standard assumptions are commonly made about the scattering behaviour of distributed targets. The first is that the principle of scattering reciprocity holds, i.e. that $s_{\mathrm{hv}} = s_{\mathrm{vh}}$: as this is only expected to be the case for a bistatic angle of zero, i.e. for monostatic backscattering, this constrains the geometry for collecting distributed target measurements intended for use in polarimetric calibration to only those cases where the bistatic angle is small. The second assumption is that azimuthal-symmetry is displayed, so that the co- and cross-polarised returns are uncorrelated, i.e. $\left\langle s_{ii} s_{ij}^* \right\rangle = 0$ for $i \neq j$. Under these assumptions, the distributed target covariance matrix $\mathbf{C_s}$ will have the form

$$\mathbf{C_s} = \begin{bmatrix} \sigma_{11} & A^* & A^* & \sigma_{41}^* \\ A & \beta & \beta' & B \\ A & \beta' & \beta & B \\ \sigma_{41} & B^* & B^* & \sigma_{44} \end{bmatrix} \tag{4.15}$$

in which

$$\beta' = \beta \quad \text{and} \quad A = B = 0. \tag{4.16}$$

However, as Ainsworth et al. [87] have done, the conditions (4.16) may be relaxed to accommodate system noise and non-zero terrain orientation angles.

Now, by substituting (4.7) into (4.12), we obtain

$$\mathbf{C} = \mathbf{Q}\,\mathbf{D}\,\mathbf{Q}^H \tag{4.17}$$

where

$$\mathbf{Q} = \mathbf{MA} \tag{4.18}$$

and

$$\begin{aligned} \mathbf{D} &\triangleq |Y|^2 \mathbf{K} \mathbf{C}_s \mathbf{K}^H \\ &= \begin{bmatrix} \tau_{11} & G^* & G^* & \tau_{41}^* \\ G & \gamma & \gamma' & H \\ G & \gamma' & \gamma & H \\ \tau_{41} & H^* & H^* & \tau_{44} \end{bmatrix} \end{aligned} \tag{4.19}$$

in which

$$\begin{gathered} \tau_{11} = |Y|^2 |k|^4 \sigma_{11}, \quad \tau_{41} = |Y|^2 k^{*2} \sigma_{41}, \quad \tau_{44} = |Y|^2 \sigma_{44}, \\ \gamma = |Yk|^2 \beta, \quad \gamma' = |Yk|^2 \beta', \quad G = k^* |Yk|^2 A, \quad H = |Y|^2 k B. \end{gathered} \tag{4.20}$$

Observe that the matrix $\mathbf{D}$ has the same postulated form as $\mathbf{C_s}$ (cf. (4.15)): indeed, if the conditions (4.16) hold for $\mathbf{C_s}$, then the analogous conditions

$$\gamma' = \gamma \quad \text{and} \quad G = H = 0 \tag{4.21}$$

will apply to $\mathbf{D}$. Also observe that the quantities Y and k appear only in the expression (4.19) for matrix $\mathbf{D}$: the right-hand-side of (4.17) is thus directly analogous to that of (4.12) but with Y and k both set to 1. The matrix $\mathbf{D}$ thus represents a version of $\mathbf{C_s}$ which is subject *only to* the effects of absolute gain Y and channel-imbalance k and *not to* the effects of the channel-imbalance term α or the cross-talk ratios, and (4.17) and (4.18) can be interpreted as posing a polarimetric calibration problem similar to that of (4.12) but involving *only* the cross-talk and channel-imbalance effects described by the u, v, w, z and α parameters and *not* the gain and imbalance effects described by Y and k. Hence, this demonstrates that the problem of determining u, v, w, z and α can be separated from that of determining Y and k.

The determination of k will be discussed later in Section 4.5 while the determination of Y constitutes the process of radiometric calibration which is outside the scope of the present chapter: for now, our attention will be on the parameters u, v, w, z and α. As already mentioned, various algorithms for their determination from the covariance matrix $\mathbf{C}$ have been reported in the literature: three particular examples are the methods of Klein [85], Quegan [86] and Ainsworth et al. [87]. As differences in notation and definitions between the various sources render comparison difficult, in the following sections, we shall derive minor variants of these algorithms, denoted by K, Ka, Q, Qi, A and Az, according to their authors' approaches but with a common system of definitions and notations.

4.4.2 Algorithms *K* and *Ka*

The key idea of Klein's approach [85] is that, under assumptions (4.16), the matrix $\mathbf{C}$ has a zero eigenvalue with corresponding eigenvector $\mathbf{f}$ given by

$$\mathbf{f}^H = \mathbf{g}^H \mathbf{P}^{-1} \tag{4.22}$$

where $\mathbf{g} = (0, 1, -1, 0)^T$. To obtain $\mathbf{f}$ explicitly, observe that from (4.7) and (4.8), we have

$$\mathbf{P}^{-1} = \frac{1}{Y} \mathbf{K}^{-1} \mathbf{A}^{-1} \mathbf{M}^{-1} \tag{4.23}$$

in which

$$\mathbf{K}^{-1} = \begin{bmatrix} 1/k^2 & 0 & 0 & 0 \\ 0 & 1/k & 0 & 0 \\ 0 & 0 & 1/k & 0 \\ 0 & 0 & 0 & 1 \end{bmatrix}, \quad \mathbf{A}^{-1} = \begin{bmatrix} 1/\alpha & 0 & 0 & 0 \\ 0 & 1 & 0 & 0 \\ 0 & 0 & 1/\alpha & 0 \\ 0 & 0 & 0 & 1 \end{bmatrix},$$

$$\mathbf{M}^{-1} = \frac{1}{(1-uw)(1-vz)} \begin{bmatrix} 1 & -v & -w & vw \\ -z & 1 & wz & -w \\ -u & uv & 1 & -v \\ uz & -u & -z & 1 \end{bmatrix}. \tag{4.24}$$

Hence, (4.22) evaluates to

$$\mathbf{f}^H = \frac{1}{Yk\,(1-uw)(1-vz)}\left(\frac{u}{\alpha} - z, 1 - \frac{uv}{\alpha}, wz - \frac{1}{\alpha}, \frac{v}{\alpha} - w\right) \tag{4.25}$$

whereupon, if we denote the components of $\mathbf{f}$ according to $\mathbf{f}^H = (f_1, f_2, f_3, f_4)$, then it can be shown that

$$\frac{f_1 f_4 - f_2 f_3}{(f_3 + w f_1)(f_3 + z f_4)} = \alpha \tag{4.26}$$

$$\frac{f_1 + z f_2}{f_3 + z f_4} = -u \tag{4.27}$$

$$\frac{f_4 + w f_2}{f_3 + w f_1} = -v \tag{4.28}$$

from which, by expanding in powers of w and z, the following approximations may be obtained:

$$\alpha \approx \alpha_0 \left(1 - w\frac{f_1}{f_3} - z\frac{f_4}{f_3}\right) \tag{4.29}$$

$$u \approx -\frac{f_1}{f_3} + z\alpha \tag{4.30}$$

$$v \approx -\frac{f_4}{f_3} + w\alpha \tag{4.31}$$

where

$$\alpha_0 \triangleq \frac{f_1 f_4 - f_2 f_3}{f_3^2}. \tag{4.32}$$

Now, under the assumptions of (4.21), by calculating the matrix products in (4.17) and keeping terms to first order in the cross-talk ratios, we may obtain the linear approximations

$$C_{21} = zC_{11} + wC_{41} + \gamma(v + \alpha w)^* \tag{4.33}$$

$$C_{24} = zC_{41}^* + wC_{44} + \gamma(u + \alpha z)^* \tag{4.34}$$

where C_{ij} denotes the entry in the ith row and jth column of matrix $\mathbf{C}$. By substituting (4.30) and (4.31) into (4.33) and (4.34), we obtain the results

$$C_{21} = zC_{11} + wC_{41} + \gamma(2w\alpha - f_4/f_3)^* \tag{4.35}$$

$$C_{24} = zC_{14} + wC_{44} + \gamma(2z\alpha - f_1/f_3)^*. \tag{4.36}$$

Solving (4.35) for z gives

$$z = \frac{C_{21} - wC_{41} - \gamma\,(2w\alpha - f_4/f_3)^*}{C_{11}} \tag{4.37}$$

which, when substituted into (4.36), produces

$$w = aw + bw^* + c \tag{4.38}$$

Algorithm K

1. Input matrix $\mathbf{C}$.
2. Calculate the eigenvector of $\mathbf{C}$ with zero-eigenvalue and assign it to $\mathbf{f} = (f_1, f_2, f_3, f_4)^H$.
3. Set $\alpha := \alpha_0$, where α_0 is given in (4.32).
4. Set $\gamma := C_{22}$.
5. Initialise iteration counter $n := 0$.
6. Repeat
   (a) Set a, b, c according to (4.39), (4.40), (4.41) respectively.
   (b) Solve (4.42) for $w = \Re(w) + j\Im(w)$.
   (c) Calculate z, u, v using (4.37), (4.30), (4.31) respectively.
   (d) Set $\gamma_{\text{old}} := \gamma$ and update γ using (4.44).
   (e) Increment iteration counter, i.e. $n := n + 1$.

   until $n \geq 16$ or $|\gamma - \gamma_{\text{old}}| / |\gamma_{\text{old}}| < 10^{-8}$.
7. Output u, v, w, z, α.

Algorithm Ka

1. Input matrix $\mathbf{C}$.
2. Calculate the eigenvector of $\mathbf{C}$ with zero-eigenvalue and assign it to $\mathbf{f} = (f_1, f_2, f_3, f_4)^H$.
3. Set $\alpha := \alpha_0$, where α_0 is given in (4.32).
4. Set $\gamma := C_{22}$.
5. Initialise iteration counter $n := 0$.
6. Repeat
   (a) Set a, b, c according to (4.39), (4.40), (4.41) respectively.
   (b) Solve (4.42) for $w = \Re(w) + j\Im(w)$.
   (c) Calculate z, u, v using (4.37), (4.30), (4.31) respectively.
   (d) Update α using (4.29).
   (e) Set $\gamma_{\text{old}} := \gamma$ and update γ using (4.44).
   (f) Increment iteration counter, i.e. $n := n + 1$.

   until $n \geq 16$ or $|\gamma - \gamma_{\text{old}}| / |\gamma_{\text{old}}| < 10^{-8}$.
7. Output u, v, w, z, α.

Figure 4.2: Algorithms K and Ka.

where

$$a = \frac{|C_{41}|^2 + 4\gamma^2|\alpha|^2}{C_{11}C_{44}} \tag{4.39}$$

$$b = \frac{4\gamma\alpha^* C_{14}}{C_{11}C_{44}} \tag{4.40}$$

$$c = \frac{C_{11}\left(C_{24} + \gamma f_1^*/f_3^*\right) - C_{14}\left(C_{21} + \gamma f_4^*/f_3^*\right) - 2\gamma\alpha^*\left(C_{12} + \gamma f_4/f_3\right)}{C_{11}C_{44}}. \tag{4.41}$$

Equation (4.38) can be more usefully expressed as

$$\begin{bmatrix} \Re(w) \\ \Im(w) \end{bmatrix} = \frac{1}{(1-a)^2 - |b|^2} \begin{bmatrix} 1-a+\Re(b) & \Im(b) \\ \Im(b) & 1-a-\Re(b) \end{bmatrix} \begin{bmatrix} \Re(c) \\ \Im(c) \end{bmatrix} \tag{4.42}$$

which enables w to be calculated for given estimated values of γ and α: once w is determined, the remaining cross-talk ratios z, u and v can then be obtained from (4.37), (4.30) and (4.31).

Having obtained w, the estimate of γ can be refined as follows: from (4.17), we may obtain

$$\mathbf{D} = \mathbf{Q}^{-1}\,\mathbf{C}\,\mathbf{Q}^{-H} \tag{4.43}$$

which yields the following expression for the entry in the second row and column of $\mathbf{D}$:

$$\begin{aligned} \gamma = {} & C_{22} + |z|^2 C_{11} + |w|^2 C_{44} + |wz|^2 C_{33} \\ & + 2\Re\left(wzC_{32} + wz^*C_{41} - zC_{12} - wC_{42} - w|z|^2 C_{31} - |w|^2 zC_{34}\right). \end{aligned} \tag{4.44}$$

This enables a new estimate of γ to be obtained from the calculated value of w.

The algorithm K is essentially that proposed by Klein [85], and operates by assigning $\mathbf{f}$ to be the eigenvector

corresponding to the minimum (zero-valued) eigenvalue of the input matrix $\mathbf{C}$ and using α_0 as a fixed estimate[1] for α and C_{22} as an initial estimate for γ, then iteratively calculating estimates for w, z, u and v using (4.42), (4.37), (4.30) and (4.31) and an updated estimate of γ using (4.44); algorithm Ka is a slightly improved version of K in which the estimate of α is updated in each iteration using (4.29). In both algorithms (shown in Figure 4.2), iterations are continued until: the relative magnitude of the change in two successive estimates of γ falls below an arbitrary threshold set at 10^{-8}; or an arbitrary maximum iteration count of 16 is exceeded.

4.4.3 Algorithms *Q* and *Qi*

The approach employed by Quegan [86] is based on obtaining linear approximations to the polarimetric distortion model of (4.17) and solving them for the unknowns u, v, w, z and α. To introduce his approach, first observe that, from (4.17), the entries C_{ij} of the matrix $\mathbf{C}$ may be calculated from

$$C_{ij} = \mathbf{m}_i \, \tilde{\mathbf{D}} \, \mathbf{m}_j^H \tag{4.45}$$

where $\mathbf{m}_i$ denotes the ith row of the matrix $\mathbf{M}$ and $\tilde{\mathbf{D}} \triangleq \mathbf{A}\,\mathbf{D}\,\mathbf{A}^H$. Thus, assuming the conditions (4.21) hold, by explicitly evaluating the right-hand-side of (4.45) and keeping terms up to first order in the cross-talk ratios, it is straightforward to obtain the following two groups of linearised approximations for the C_{ij}:

$$C_{11} = |\alpha|^2 \tau_{11} \tag{4.46}$$

$$C_{41} = \alpha^* \tau_{41} \tag{4.47}$$

$$C_{44} = \tau_{44} \tag{4.48}$$

and

$$C_{21} = zC_{11} + wC_{41} + (v + w\alpha)^* \gamma \tag{4.49}$$

$$C_{24} = zC_{14} + wC_{44} + (u + z\alpha)^* \gamma \tag{4.50}$$

$$C_{31} = uC_{11} + vC_{41} + (v + w\alpha)^* \alpha\gamma \tag{4.51}$$

$$C_{34} = uC_{14} + vC_{44} + (u + z\alpha)^* \alpha\gamma. \tag{4.52}$$

Applying a similar approach to calculate approximations for C_{22}, C_{32}, C_{23} and C_{33} produces leading terms involving γ but no terms that are first order in the cross-talk ratios: however, as the magnitude of γ may itself be small, simply disregarding the second order terms in the cross-talk ratios may not be justified. By employing a less intuitive approach,[2] it is possible to obtain the following set of approximations, which are analogous to Quegan's equations (19), (20) and (21) [86]:

$$C_{22} = z^* C_{21} + w^* C_{24} + \gamma \tag{4.53}$$

$$C_{32} = z^* C_{31} + w^* C_{34} + \alpha\gamma \tag{4.54}$$

$$C_{23} = u^* C_{21} + v^* C_{24} + \alpha^* \gamma \tag{4.55}$$

$$C_{33} = u^* C_{31} + v^* C_{34} + |\alpha|^2 \gamma. \tag{4.56}$$

[1] However, due to differences in approximation, the expression for α_0 incorporates more terms than the corresponding equation (22) of Klein's paper [85].

As $\mathbf{C}$ is Hermitian, expressions for the remaining C_{ij} may be obtained from the complex conjugates of the above.

By Quegan's reasoning [86], the third terms on the right-hand-sides of equations (4.49) to (4.52) are negligible: ignoring them results in a set of simultaneous linear equations which, when solved (e.g. by Cramer's rule), gives the following estimators for the cross-talk ratios:

$$\hat{u} \triangleq \frac{C_{44}C_{31} - C_{41}C_{34}}{\Delta} \tag{4.57}$$

$$\hat{v} \triangleq \frac{C_{11}C_{34} - C_{31}C_{14}}{\Delta} \tag{4.58}$$

$$\hat{w} \triangleq \frac{C_{11}C_{24} - C_{21}C_{14}}{\Delta} \tag{4.59}$$

$$\hat{z} \triangleq \frac{C_{44}C_{21} - C_{41}C_{24}}{\Delta} \tag{4.60}$$

where

$$\Delta \triangleq C_{11}C_{44} - |C_{14}|^2. \tag{4.61}$$

The above estimators $\hat{u}$, $\hat{v}$, $\hat{w}$, $\hat{z}$ for the cross-talk ratios u, v, w, z correspond directly to those derived by Quegan [86]. However, as shown by López-Martinez et al. [204], these estimators are actually biased: by substituting (4.49) to (4.52) into (4.57) to (4.60), we may obtain

$$\hat{u} = u + \alpha\gamma\, p(u, v, w, z, \alpha) \tag{4.62}$$

$$\hat{v} = v + \alpha\gamma\, q(u, v, w, z, \alpha) \tag{4.63}$$

$$\hat{w} = w + \gamma\, q(u, v, w, z, \alpha) \tag{4.64}$$

$$\hat{z} = z + \gamma\, p(u, v, w, z, \alpha) \tag{4.65}$$

where the functions $p(\cdot)$ and $q(\cdot)$ are defined by

$$p(u, v, w, z, \alpha) = \frac{(v + w\alpha)^* C_{44} - (u + z\alpha)^* C_{41}}{\Delta} \tag{4.66}$$

$$q(u, v, w, z, \alpha) = \frac{(u + z\alpha)^* C_{11} - (v + w\alpha)^* C_{14}}{\Delta}. \tag{4.67}$$

Thus, employing $\hat{u}$, $\hat{v}$, $\hat{w}$, $\hat{z}$ as estimators for the cross-talk ratios produces biased results which may not accurately reflect the true values. To account for the bias, López-Martinez et al. propose an iterative cross-talk estimation procedure in which the estimates for the cross-talk ratios u_k, v_k, w_k, z_k at the kth iteration are refined according to the scheme

$$u_{k+1} = \hat{u} - \alpha\gamma\, p_k \tag{4.68}$$

$$v_{k+1} = \hat{v} - \alpha\gamma\, q_k \tag{4.69}$$

$$w_{k+1} = \hat{w} - \gamma\, q_k \tag{4.70}$$

$$z_{k+1} = \hat{z} - \gamma\, p_k \tag{4.71}$$

[2]Let $\mathbf{k}_2 \triangleq \mathbf{m}_2 - z\,\mathbf{m}_1 - w\,\mathbf{m}_4$ and $\mathbf{k}_3 \triangleq \mathbf{m}_3 - u\,\mathbf{m}_1 - v\,\mathbf{m}_4$. Then, to first order in z and w, the quantity $\mathbf{m}_2\,\tilde{\mathbf{D}}\,\mathbf{k}_2 = C_{22} - z^*C_{21} - w^*C_{24}$. However, it is easily verified that, again to first order, $\mathbf{k}_2 = (0, 1, 0, 0)$: this gives $\mathbf{m}_2\,\tilde{\mathbf{D}}\,\mathbf{k}_2 = \gamma$. Hence, we have (4.53). By applying similar reasoning to $\mathbf{m}_3\,\tilde{\mathbf{D}}\,\mathbf{k}_2$, $\mathbf{m}_2\,\tilde{\mathbf{D}}\,\mathbf{k}_3$ and $\mathbf{m}_3\,\tilde{\mathbf{D}}\,\mathbf{k}_3$, (4.54), (4.55) and (4.56) may be obtained.

where

$$p_k \triangleq p(u_k, v_k, w_k, z_k, \hat{\alpha}) \tag{4.72}$$

$$q_k \triangleq q(u_k, v_k, w_k, z_k, \hat{\alpha}). \tag{4.73}$$

The above discussion pertains to the estimation of the cross-talk ratios: let us now consider the channel-imbalance parameter α, for which an estimator may be obtained independently of the above as follows. Observe that

$$C_{31} - \alpha C_{21} = (u - \alpha z)C_{11} + (v - \alpha w)C_{41} \tag{4.74}$$

$$C_{34} - \alpha C_{24} = (u - \alpha z)C_{14} + (v - \alpha w)C_{44} \tag{4.75}$$

whereupon, by applying Cramer's Rule, we obtain

$$u - \alpha z = \frac{C_{31}C_{44} - C_{34}C_{41} - \alpha(C_{21}C_{44} - C_{24}C_{41})}{\Delta} \tag{4.76}$$

$$v - \alpha w = \frac{C_{11}C_{34} - C_{14}C_{31} - \alpha(C_{11}C_{24} - C_{14}C_{21})}{\Delta}. \tag{4.77}$$

Similarly, observe that

$$C_{33} - \alpha C_{23} = (u - \alpha z)C_{13} + (v - \alpha w)C_{43} \tag{4.78}$$

$$C_{32} - \alpha C_{22} = (u - \alpha z)C_{12} + (v - \alpha w)C_{42} \tag{4.79}$$

whereupon, by substituting for $u - \alpha z$ and $v - \alpha w$ from (4.76) and (4.77) respectively and solving for α, we obtain the following two estimators for the parameter α:

$$\hat{\alpha}_1 = \frac{C_{33} - \hat{u}C_{13} - \hat{v}C_{43}}{X} \tag{4.80}$$

$$\hat{\alpha}_2 = \frac{X^*}{C_{22} - \hat{z}C_{12} - \hat{w}C_{42}} \tag{4.81}$$

where

$$X = C_{23} - \hat{z}C_{13} - \hat{w}C_{43}. \tag{4.82}$$

From casual inspection of (4.80) and (4.81), the form of the estimators $\hat{\alpha}_1$ and $\hat{\alpha}_2$ appear distinct. However, when noise is negligible (i.e. $\mathbf{C_n} = \mathbf{0}$) or the values used for the C_{ij} are taken from the properly corrected covariance matrix $\mathbf{C} = \mathbf{C_o} - \mathbf{C_n}$ (this requires that $\mathbf{C_n}$ be accurately known), identical results are obtained from $\hat{\alpha}_1$ and $\hat{\alpha}_2$. When this is not the case, however, although their phases will still be the same,[3] the amplitudes of the $\hat{\alpha}_i$ will differ with $|\hat{\alpha}_1| > |\hat{\alpha}_2|$, and this is attributable to the effects of uncompensated noise on the values used for the covariance terms C_{22} and C_{33} [86] (the C_{ij} are being approximated by the entries of the observed covariance matrix $\mathbf{C_o}$ instead of being assigned their true values from the noise-compensated covariance matrix $\mathbf{C}$). Hence, it is desirable to combine the $\hat{\alpha}_i$ to produce a single final estimator $\hat{\alpha}$. The phase of $\hat{\alpha}$ is simply determined: as the phases of the $\hat{\alpha}_i$ are identical, we may simply set $\arg\hat{\alpha} = \arg\hat{\alpha}_i$. As for the magnitude of $\hat{\alpha}$, an expression for assigning $|\hat{\alpha}|$ can be derived by considering the ratio of the noise

[3] The result $\arg\hat{\alpha}_1 = \arg\hat{\alpha}_2$ follows by observing that the numerator of $\hat{\alpha}_1$ in (4.80) and the denominator of $\hat{\alpha}_2$ in (4.81) are real-valued (this can be shown by substituting in (4.57) to (4.61) and recalling that $C_{ij} = C_{ji}^*$): thus $\arg\hat{\alpha}_1 = \arg(1/X) = -\arg X$ and $\arg\hat{\alpha}_2 = \arg(X^*) = -\arg X$ as anticipated.

powers

$$m \triangleq N_{33}/N_{22} \tag{4.83}$$

where N_{ij} is the entry in the ith row and jth column of $\mathbf{C_n}$: this was originally done for the special case where $m = 1$ by Quegan [86], and subsequently extended to more general values of m by Kimura et al. [203]. Essentially, the method involves modifying (4.53) and (4.56) by adding non-negative noise covariances N_{22} and N_{33} to their right-hand-sides and replacing the cross-talk values u, v, w, z with the estimators $\hat{u}$, $\hat{v}$, $\hat{w}$, $\hat{z}$ in (4.53) to (4.56). This produces the results

$$\hat{\alpha}_1 = \alpha + \frac{N_{33}}{\alpha^* \gamma} \tag{4.84}$$

$$\hat{\alpha}_2 = \frac{\alpha}{1 + N_{22}/\gamma} \tag{4.85}$$

whereupon, solving for the N_{ii} and substituting into the definition of m gives the quadratic equation

$$|\hat{\alpha}_2||\alpha|^2 + (m - |\hat{\alpha}_1\hat{\alpha}_2|)|\alpha| - m|\hat{\alpha}_2| = 0 \tag{4.86}$$

which can be solved for $|\alpha|$ and the result assigned to $|\hat{\alpha}|$: hence we obtain

$$|\hat{\alpha}| = \frac{|\hat{\alpha}_1\hat{\alpha}_2| - m + \sqrt{(|\hat{\alpha}_1\hat{\alpha}_2| - m)^2 + 4m|\hat{\alpha}_2|^2}}{2|\hat{\alpha}_2|}. \tag{4.87}$$

As the primary focus in polarimetric calibration is on estimating the cross-talk ratios and α parameter, an estimate of γ is not strictly necessary in Quegan's original approach [86]. However, the quantity γ appears explicitly in (4.68) to (4.71) and so must be estimated in order to apply the cross-talk refinement procedure of López-Martinez et al. [204]. One possible way to estimate γ has been suggested by Quegan [86], who, presumably by comparing his analogues of (4.54) and (4.82), obtained the result

$$\gamma = \frac{X^*}{\alpha}. \tag{4.88}$$

Algorithm Q (shown in Figure 4.3) is essentially the algorithm proposed by Quegan [86], with the cross-talk ratios estimated non-iteratively by $\hat{u}$, $\hat{v}$, $\hat{w}$ and $\hat{z}$, and the parameter α by (4.80), (4.81) and (4.87). Algorithm Qi is essentially Q with the modification proposed by López-Martinez et al. [204]: the only difference between Qi and Q is that, in the former, the cross-talk estimates are iteratively refined using (4.68) to (4.71). These iterations are continued until: the change in two successive estimates of each of the cross-talk ratios is below an arbitrary threshold set at 10^{-8} or an arbitrary maximum iteration count of 16 is exceeded.

4.4.4 Algorithms A and Az

The basis of the approach of Ainsworth et al. [87] is the observation that (4.17) can be rewritten as the following two-stage transformation of $\mathbf{C}$ into $\mathbf{D}$:

$$\mathbf{L} = \mathbf{A}^{-1}\mathbf{C}\mathbf{A}^{-H} \tag{4.89}$$

$$\mathbf{D} = \tilde{\mathbf{M}}^{-1}\mathbf{L}\tilde{\mathbf{M}}^{-H} \tag{4.90}$$

where $\tilde{\mathbf{M}} \equiv \mathbf{A}^{-1}\mathbf{M}\mathbf{A}$. Calibration may thus be achieved by judiciously choosing first α, which determines $\mathbf{A}$, then u, v, w, z, which (together with α) determine $\tilde{\mathbf{M}}$, to transform $\mathbf{C}$ into the particular form given in

Algorithm Q

1. Input matrix $\mathbf{C}$.
2. Calculate Δ from (4.61).
3. Calculate $\hat{u}$, $\hat{v}$, $\hat{w}$, $\hat{z}$ from (4.57) to (4.60).
4. Calculate X from (4.82).
5. Calculate $\hat{\alpha}_1$, $\hat{\alpha}_2$ from (4.80) and (4.81).
6. Calculate $\hat{\alpha} = |\hat{\alpha}|e^{j \arg \hat{\alpha}}$ using (4.87) for $|\hat{\alpha}|$ and the mean of $\{\arg \hat{\alpha}_1, \arg \hat{\alpha}_2\}$ for $\arg \hat{\alpha}$.
7. Output $\hat{u}$, $\hat{v}$, $\hat{w}$, $\hat{z}$, $\hat{\alpha}$.

Algorithm Qi

1. Input matrix $\mathbf{C}$.
2. Calculate Δ from (4.61).
3. Calculate $\hat{u}$, $\hat{v}$, $\hat{w}$, $\hat{z}$ from (4.57) to (4.60).
4. Calculate X from (4.82).
5. Calculate $\hat{\alpha}_1$, $\hat{\alpha}_2$ from (4.80) and (4.81).
6. Calculate $\hat{\alpha} = |\hat{\alpha}|e^{j \arg \hat{\alpha}}$ using (4.87) for $|\hat{\alpha}|$ and the mean of $\{\arg \hat{\alpha}_1, \arg \hat{\alpha}_2\}$ for $\arg \hat{\alpha}$.
7. Calculate γ from (4.88).
8. Initialise iteration counter $k := 0$ and set $u_k = \hat{u}$, $v_k = \hat{v}$, $w_k = \hat{w}$, $z_k = \hat{z}$.
9. Repeat
   (a) Calculate p_k and q_k using (4.72) and (4.73) respectively.
   (b) Calculate u_{k+1}, v_{k+1}, w_{k+1}, z_{k+1} using (4.68) to (4.71).
   (c) Increment iteration counter, i.e. $k := k + 1$.

   until $k \geq 16$ or the maximum of $|u_k - u_{k-1}|$, $|v_k - v_{k-1}|$, $|w_k - w_{k-1}|$, $|z_k - z_{k-1}|$ is less than 10^{-8}.
10. Output u_k, v_k, w_k, z_k, $\hat{\alpha}$.

Figure 4.3: Algorithms Q and Qi.

(4.15) and (4.19).

The choice for α follows from (4.89), which gives the entries in the middle rows and columns of $\mathbf{L}$ as

$$L_{22} = C_{22} \tag{4.91}$$

$$L_{32} = |\alpha|^{-1} e^{-j \arg \alpha} C_{32} \tag{4.92}$$

$$L_{33} = |\alpha|^{-2} C_{33} \tag{4.93}$$

where L_{ij} is the entry in the ith row and jth column of $\mathbf{L}$. To make these match the form (4.19), we need to set L_{22} and L_{33} to be equal and L_{32} to be real, from which it follows that $|\alpha|^2 = C_{33}/C_{22}$ and $\arg \alpha = \arg C_{32}$, whereupon it is straightforward to obtain

$$\alpha = \sqrt{\frac{C_{33}}{C_{22}}} e^{j \arg C_{32}}. \tag{4.94}$$

To choose the cross-talk ratios u, v, w, z, we expand the right-hand-side of (4.90) to give linearised approximations for the entries D_{21}, D_{31}, D_{24} and D_{34} in the matrix $\mathbf{D}$, where D_{ij} denotes the entry in the ith row and jth column: as $D_{21} = D_{31} = G$ and $D_{24} = D_{34} = H$, we obtain the resulting set of equations:

$$G = -\alpha z L_{11} + L_{21} - w L_{41} - v^* L_{22}/\alpha^* - w^* L_{33} \tag{4.95}$$

$$G = -u L_{11} + L_{31} - v L_{41}/\alpha - v^* L_{32}/\alpha^* - w^* L_{33} \tag{4.96}$$

$$H = -u^* L_{22} - \alpha^* z^* L_{23} - \alpha z L_{14} + L_{24} - w L_{44} \tag{4.97}$$

$$H = -u^* L_{32} - \alpha^* z^* L_{33} - u L_{14} + L_{34} - v L_{44}/\alpha. \tag{4.98}$$

These can be collectively rewritten as

$$\begin{bmatrix} \Re(\mathbf{X}) \\ \Im(\mathbf{X}) \end{bmatrix} = \begin{bmatrix} \Re(\boldsymbol{\xi}+\boldsymbol{\tau}) & -\Im(\boldsymbol{\xi}-\boldsymbol{\tau}) \\ \Im(\boldsymbol{\xi}+\boldsymbol{\tau}) & \Re(\boldsymbol{\xi}-\boldsymbol{\tau}) \end{bmatrix} \begin{bmatrix} \Re(\boldsymbol{\kappa}) \\ \Im(\boldsymbol{\kappa}) \end{bmatrix} \tag{4.99}$$

where $\boldsymbol{\kappa} \triangleq (u, v, w, z)^T$ and

$$\mathbf{X} = (G-L_{21}, G-L_{31}, H-L_{24}, H-L_{34})^T \tag{4.100}$$

$$\boldsymbol{\xi} = -\begin{bmatrix} 0 & 0 & L_{41} & \alpha L_{11} \\ L_{11} & L_{41}/\alpha & 0 & 0 \\ 0 & 0 & L_{44} & \alpha L_{14} \\ L_{14} & L_{44}/\alpha & 0 & 0 \end{bmatrix} \tag{4.101}$$

$$\boldsymbol{\tau} = -\begin{bmatrix} 0 & L_{22}/\alpha^* & L_{23} & 0 \\ 0 & L_{32}/\alpha^* & L_{33} & 0 \\ L_{22} & 0 & 0 & \alpha^* L_{23} \\ L_{32} & 0 & 0 & \alpha^* L_{33} \end{bmatrix}. \tag{4.102}$$

Hence, for given values of the terms G and H (see below), (4.99) can be solved for $\boldsymbol{\kappa}$.

The parameters (α, u, v, w, z) can be estimated by a single iteration of the above procedure, using $\mathbf{C}$ as input and producing an estimate of $\mathbf{D}$ as output. However, in practice a single iteration will only partly correct for the cross-talk and imbalance effects, so the resultant $\mathbf{D}$ represents only a *partially*-calibrated version of the original matrix $\mathbf{C}$. Hence, for improved results, the iterations can be repeated, using the estimated $\mathbf{D}$ from each iteration as input to the next [87]. To combine the intermediate results $(\alpha_i, u_i, v_i, w_i, z_i)$, where $i = 1, 2, \ldots$, to obtain the overall parameter estimates, observe that

$$\begin{aligned} \mathbf{D}_i &= \tilde{\mathbf{M}}_i^{-1}\mathbf{A}_i^{-1} \ldots \tilde{\mathbf{M}}_1^{-1}\mathbf{A}_1^{-1}\ \mathbf{C}\ \mathbf{A}_1^{-H}\tilde{\mathbf{M}}_1^{-H} \ldots \mathbf{A}_i^{-H}\tilde{\mathbf{M}}_i^{-H} \\ &= \left(\mathbf{A}_1\tilde{\mathbf{M}}_1 \ldots \mathbf{A}_i\tilde{\mathbf{M}}_i\right)^{-1} \mathbf{C} \left(\mathbf{A}_1\tilde{\mathbf{M}}_1 \ldots \mathbf{A}_i\tilde{\mathbf{M}}_i\right)^{-H} \\ &= (\mathbf{M}_1\mathbf{A}_1 \ldots \mathbf{M}_i\mathbf{A}_i)^{-1}\, \mathbf{C}\, (\mathbf{M}_1\mathbf{A}_1 \ldots \mathbf{M}_i\mathbf{A}_i)^{-H} \end{aligned} \tag{4.103}$$

where $\mathbf{D}_i$, $\tilde{\mathbf{M}}_i$, $\mathbf{M}_i$ and $\mathbf{A}_i$ denote the values assumed by the various matrices at the ith iteration: hence, we need to re-express the chain matrix product $\mathbf{M}_1\mathbf{A}_1\mathbf{M}_2\mathbf{A}_2\mathbf{M}_3\mathbf{A}_3 \ldots$ in the form of the product $\mathbf{Q} = \mathbf{MA}$ of final $\mathbf{M}$ and $\mathbf{A}$ matrices (cf. (4.18)), so that (4.103) assumes a form consistent with (4.17). By calculating the matrix entries algebraically, it can be shown that this is possible to first order in the cross-talk ratios, and that the appropriate relations between the final (α, u, v, w, z) parameters and the intermediate results are given by

$$\alpha = \alpha_1 \times \alpha_2 \times \alpha_3 \ldots \tag{4.104}$$

$$u = u_1 + u_2 + u_3 + \ldots \tag{4.105}$$

$$v = v_1 + \alpha_1 v_2 + \alpha_1\alpha_2 v_3 + \ldots \tag{4.106}$$

$$w = w_1 + w_2 + w_3 + \ldots \tag{4.107}$$

$$z = z_1 + \alpha_1^{-1} z_2 + (\alpha_1\alpha_2)^{-1} z_3 + \ldots \tag{4.108}$$

The iterative procedure above constitutes the algorithms A and Az (shown in Figure 4.4), with their sole

Algorithm A

1. Input matrix $\mathbf{C}$.
2. Initialise variables $\alpha := 1$, $u := 0$, $v := 0$, $w := 0$, $z := 0$.
3. Initialise iteration counter $i := 0$.
4. Repeat
   (a) Calculate α_i from (4.94).
   (b) Calculate matrix $\mathbf{L}$ using α_i in (4.89).
   (c) Set G, H according to (4.109), (4.110).
   (d) Calculate $\mathbf{X}$, $\boldsymbol{\xi}$, $\boldsymbol{\tau}$ using α_i in (4.100), (4.101), (4.102) respectively and solve (4.99) for $\boldsymbol{\kappa} = (u_i, v_i, w_i, z_i)$.
   (e) Update $u := u+u_i$, $v := v+\alpha v_i$, $w := w+w_i$, $z := z + \alpha^{-1} z_i$ as per (4.105) to (4.108).
   (f) Update $\alpha := \alpha \times \alpha_i$ as per (4.104).
   (g) Calculate $\mathbf{D}$ from (4.90) and set $\mathbf{C} := \mathbf{D}$.
   (h) Increment iteration counter, i.e. $i := i + 1$.

   until $i \geq 16$ or the maximum of $|u_i|$, $|v_i|$, $|w_i|$, $|z_i|$ is less than 10^{-8}.
5. Output u, v, w, z, α.

Algorithm Az

1. Input matrix $\mathbf{C}$.
2. Initialise variables $\alpha := 1$, $u := 0$, $v := 0$, $w := 0$, $z := 0$.
3. Initialise iteration counter $i := 0$.
4. Repeat
   (a) Calculate α_i from (4.94).
   (b) Calculate matrix $\mathbf{L}$ using α_i in (4.89).
   (c) Set $G := 0$, $H := 0$.
   (d) Calculate $\mathbf{X}$, $\boldsymbol{\xi}$, $\boldsymbol{\tau}$ using α_i in (4.100), (4.101), (4.102) respectively and solve (4.99) for $\boldsymbol{\kappa} = (u_i, v_i, w_i, z_i)$.
   (e) Update $u := u+u_i$, $v := v+\alpha v_i$, $w := w+w_i$, $z := z + \alpha^{-1} z_i$ as per (4.105) to (4.108).
   (f) Update $\alpha := \alpha \times \alpha_i$ as per (4.104).
   (g) Calculate $\mathbf{D}$ from (4.90) and set $\mathbf{C} := \mathbf{D}$.
   (h) Increment iteration counter, i.e. $i := i + 1$.

   until $i \geq 16$ or the maximum of $|u_i|$, $|v_i|$, $|w_i|$, $|z_i|$ is less than 10^{-8}.
5. Output u, v, w, z, α.

Figure 4.4: Algorithms A and Az.

difference being the manner G and H are assigned: A follows the approach of Ainsworth et al. [87], which attempts to accommodate non-zero terrain orientation angles by allowing non-zero G and H, and sets

$$G = \frac{L_{21} + L_{31}}{2} \tag{4.109}$$

$$H = \frac{L_{24} + L_{34}}{2} \tag{4.110}$$

while Az follows the assumptions used in the algorithms K, Ka, Q and Qi and sets $G = H = 0$. In both A and Az, iterations are continued until the maximum value of the $|u_i|$, $|v_i|$, $|w_i|$, $|z_i|$ fall below an arbitrary tolerance of 10^{-8} or a maximum iteration count of 16 is exceeded.

4.4.5 Noise estimation

As input, the various distributed target polarimetric calibration algorithms expect the noise-corrected observed terrain covariance matrix $\mathbf{C} = \mathbf{C_o} - \mathbf{C_n}$. However, as an accurate estimate of the noise covariance matrix $\mathbf{C_n}$ is not always available, in practice $\mathbf{C_n}$ may simply be ignored and the noisy observed terrain covariance matrix $\mathbf{C_o}$ used in place of $\mathbf{C}$: this is, of course, valid when the terrain return is strong and the noise is negligible, but is less defensible when the terrain return is weak (e.g. in low-grazing angle collections). Since the matrix $\mathbf{C_n}$ is diagonal (cf. (4.14)), using $\mathbf{C_o}$ directly as input amounts to employing a version of $\mathbf{C}$ with additive biases on its main diagonal: as the observed cross-polarised power terms $\langle |o_{\mathrm{hv}}|^2 \rangle$ and $\langle |o_{\mathrm{vh}}|^2 \rangle$ are of smaller magnitude than the co-polarised power terms $\langle |o_{\mathrm{hh}}|^2 \rangle$ and $\langle |o_{\mathrm{vv}}|^2 \rangle$, these biases may significantly affect the cross-polarised terms, leading to inaccurate results. Hence, correcting $\mathbf{C_o}$ for $\mathbf{C_n}$ when the latter is available is to be preferred.

A straightforward approach for estimating $\mathbf{C_n}$ is to make special measurements of the "no-return" signal,

e.g. deeply shadowed areas or a "noise-only" image where the transmitter has been switched into a non-transmitting mode. However, Freeman [209] has proposed a different approach which uses the measured Bragg backscatter from slightly rough surfaces using symmetrised data under the assumption of radar system reciprocity. In the following, we present a potential alternative to these approaches for estimating $\mathbf{C_n}$ which is based on the assumption of scattering reciprocity: this method does not require special measurement of a "no-return" signal and does not assume radar reciprocity.

From (4.17), the covariance matrix of the partially calibrated (after correction for cross-talk and the α channel-imbalance parameter) terrain data is given by

$$\mathbf{D} = \mathbf{Q}^{-1}(\mathbf{C_o} - \mathbf{C_n})\mathbf{Q}^{-H}. \tag{4.111}$$

By substituting (4.8), (4.14) and (4.18) into the right-hand-side and evaluating the matrix product, expressions for the second and third terms along the main diagonal may be obtained as

$$D_{22} = \kappa_{22} - N_{22}\frac{(1+|w|^2)(1+|z|^2)}{|1-uw|^2|1-vz|^2} \tag{4.112}$$

$$D_{33} = \kappa_{33} - N_{33}\frac{(1+|u|^2)(1+|v|^2)}{|\alpha|^2|1-uw|^2|1-vz|^2} \tag{4.113}$$

where D_{ij} is the entry in the ith row and jth column of the matrix $\mathbf{D}$, κ_{ij} is the entry in the ith row and j column of the matrix $\mathbf{Q}^{-1}\mathbf{C_o}\mathbf{Q}^{-H}$, and N_{ii} is the noise power in channel i as previously defined (ref. (4.13) and (4.14)). Now, from (4.19), under the assumption of scattering reciprocity, the entries D_{22} and D_{33} should both be equal. Thus, by setting $D_{22} = D_{33}$, the following expression for the noise power is obtained:

$$N_{22} = \frac{(\kappa_{33} - \kappa_{22})|1-uw|^2|1-vz|^2}{m|\alpha|^{-2}(1+|u|^2)(1+|v|^2) - (1+|w|^2)(1+|z|^2)} \tag{4.114}$$

where m is as defined in (4.83).

Equation (4.114) provides a simple non-iterative means for estimating the noise powers given reasonably accurate estimates of the cross-talk ratios and α parameter: an iterative approach is also possible in which, at each iteration, the current estimates of N_{22} and N_{33} are used to correct $\mathbf{C_o}$ and new estimates of the parameters u, v, w, z, α are calculated and used to update the values of N_{22} and N_{33} to be used in the next iteration. Observe that the essential basis of the method presented here for $\mathbf{C_n}$-estimation is the noise-induced inequality of κ_{22} and κ_{33}, which motivates the calculation of suitable values for N_{22} and N_{33} in order to achieve equality of D_{22} and D_{33}, as given by (4.112) and (4.113). As a result, the distributed target algorithms A and Az are unsuitable for direct use in conjunction with this method since, if given $\mathbf{C_o}$ as input, they will (as a direct consequence of their design) produce cross-talk and, in particular, α estimates such that $\kappa_{22} = \kappa_{33}$ is assured from the start. Instead, alternative algorithms must be employed which will return faithful estimates of the calibration parameters (especially α) in a manner which is reasonably robust to noise: as discussed in the next section, a reasonable choice which exploits the strengths of the different algorithms is to use Az to estimate the cross-talk but to use Ka to estimate the α parameter.

4.4.6 Performance comparison

The set of distributed target algorithms K, Ka, Q, Qi, A and Az collectively represent a variety of approaches to solving the cross-talk estimation problem: a comparison of their relative performance, especially with

Table 4.1: Representative covariance matrix entries.

Surface	σ_{11}	$\lvert\sigma_{41}\rvert$	σ_{44}	β
Vegetation	1	0.01	1	0.25
Ocean	0.71	0.79	1.4	0.01
Geological	1	0.79	1	0.063

regard to accuracy and robustness to noise, is an obvious topic of interest. However, a rigorous theoretical approach to addressing this matter is difficult as the required calculations will be quite involved: hence, a simple approach based on the use of numerical simulations has been employed here instead.

In these simulations, the following Monte Carlo approach was used to efficiently sample the large multi-dimensional space of distortion parameters. First, the magnitudes of the entries in the covariance matrix $\mathbf{C}_s$ were set to values representative of vegetation, ocean and geological surfaces: the values used were the same as those employed by Klein [85] and are shown in Table 4.1. Next, for each surface type, uniformly distributed random phases between 0 and 2π were assigned to σ_{41}, u, v, w, z, and α, and random uniformly distributed values between 0 and 0.1 were assigned to $|u|$, $|v|$, $|w|$, $|z|$, and between 0.5 and 1.5 to $|\alpha|$. (The intent of this process is simply to produce random complex quantities with evenly distributed random phases and amplitudes appropriate to the polarimetric model: recall from Section 4.3 that we assume $|u|, |v|, |w|, |z| \ll 1$ and $|\alpha| \approx 1$.) The remaining two parameters Y and k were both set to unity value, i.e. $Y = k = 1$ (which, from (4.19), results in $\mathbf{D} = \mathbf{C_s}$). The procedure just described is similar to that in Klein's Monte Carlo simulations [85], but the magnitudes of the various parameters are here set differently. Each set of randomly assigned values gave rise to a matrix $\mathbf{P}$ by virtue of (4.7) and (4.8), which then allowed the corresponding covariance matrix $\mathbf{C} = \mathbf{P}\,\mathbf{C_s}\,\mathbf{P}^H$ to be calculated. For this work, two separate sets of simulation runs were performed: in the first set, the matrix $\mathbf{C}$ was used directly as input to the various distributed target algorithms, while in the second, the input to the algorithms was instead the noise-biased covariance matrix $\mathbf{C_o} = \mathbf{C} + \mathbf{C_n}$, in which the noise covariance matrix $\mathbf{C_n}$ had the form of (4.14) with $N_{22} = N_{33} = 0.01$. Thus, the first set of runs simulates the 'noise-free' (or perfectly noise-compensated) case while the second set simulates a 'noise-present' case where uncompensated uncorrelated noise processes are present in each polarisation channel, each having equal powers 20 dB lower than the geometric mean of the terrain co-polarised hh and vv powers, being σ_{11} and σ_{44} respectively.

A key assumption in the derivation of the algorithms is that the cross-talk ratios u, v, w and z all have small magnitudes: consequently, any set of estimates produced by the algorithms in which large cross-talk ratio magnitudes occur is of questionable validity. Hence, as suggested by Quegan [86], a simple validity test based on the rejection of cross-talk ratios with large magnitudes should be applied to screen out such cases: accordingly, in the set of results produced by the simulations, the magnitudes of the cross-talk estimates produced by the algorithms for each input covariance matrix were examined, and the result was only accepted as valid if $|u|$, $|v|$, $|w|$, $|z|$ were all below an arbitrary threshold set at 0.1. Table 4.2 shows the proportion of results produced by each algorithm which were thus accepted as valid. Generally, with the exception of Q, all algorithms produced valid results for all surface types in the vast majority ($\gtrsim 99\%$) of cases. By comparison, much lower proportions ($\approx 80\%$) of valid results were produced by Q for vegetation and geological surfaces but a greater proportion ($\approx 96\%$) was produced for the ocean surface: this may be attributable to higher accuracy in cross-talk estimation by Q for ocean than vegetation or geological surfaces (see below).

Figure 4.5 shows representative plots of the magnitudes of the relative estimation errors for the cross-talk ratios and α parameter in the noise-free case. For brevity, only the results for the cross-talk parameter w are shown, as the plots for the other cross-talk ratios u, v and z are similar. Also, as algorithms Q and Qi

Table 4.2: Percentage of valid estimates in $N = 65536$ trials by algorithm and surface type.

	Noise-free			Noise-present		
Algorithm	Vegetation	Ocean	Geological	Vegetation	Ocean	Geological
K	99.09	99.60	99.09	97.93	96.85	92.30
Ka	99.60	99.74	99.55	98.16	96.84	92.41
Q	78.12	95.98	78.57	79.92	99.30	83.38
Qi	99.49	99.69	99.46	99.97	99.96	99.92
A	97.76	96.50	98.18	98.37	98.24	99.33
Az	99.98	99.93	99.91	99.99	99.78	99.67

produce identical estimates of α, to avoid visual clutter, only the markers for Q are displayed in the plots for α. In the plots for the cross-talk ratios, a degradation of relative estimation accuracy with decreasing cross-talk magnitude is clearly observed for all algorithms except Az. Overall cross-talk estimation accuracy is very high for Az and high for K, Ka and Qi but low for Q and A where large errors on the order of the parameter itself are common. Also, lower errors were produced by K, Ka, Q and Qi for ocean surface, while A and Az appear relatively insensitive to surface type. In contrast to the cross-talk, the estimation accuracy for the α parameter is high for all algorithms with error magnitudes being no more than a few percent of $|\alpha|$, and with no apparent effect of $|\alpha|$ on the size of the error. Errors of similar magnitude were produced by K, Q/Qi and A for all surface types; however, errors produced by Az and Ka were approximately an order of magnitude lower for ocean and geological surfaces and two orders of magnitude lower for vegetation.

From Figure 4.5, the algorithm Ka performs noticeably better than its counterpart K in estimating α but only marginally better when estimating the cross-talk ratios: this may be attributed to the employment by K of a zeroth-order expression (see (4.32)) for estimating α, which contrasts with the use by Ka of a more accurate first-order expression in w and z (see (4.29)). The low accuracy observed in the cross-talk estimates produced by Q is consistent with the γ-dependent bias of the cross-talk estimators (see equations (4.62) to (4.65)): as expected, the trend in the accuracy achieved is in agreement with the relative size of the γ values for the three terrain types (cf. Table 4.1), with the lowest errors produced for the ocean surface which has the smallest value of γ. The low cross-talk estimation accuracy of A appears to be a consequence of allowing non-zero G and H, which permits specious convergence to a solution different from the true set of values: A is thus actually designed to solve a different problem from the other algorithms, for which $G = H = 0$ is assumed. However, as shown by the results, when A is modified as in Az so that $G = H = 0$ is enforced, excellent accuracy is achieved.

The relative error magnitudes for the case where noise is present are shown in Figure 4.6. By comparing this with Figure 4.5, a degradation in the estimation accuracy for the cross-talk ratios by several orders of magnitude is readily apparent for Az, K, Ka and Qi: indeed, for the ocean surface, these now achieve relative cross-talk estimation errors only marginally smaller than Q. The highest cross-talk ratio estimation accuracies are still achieved by algorithm Az, but only by a small margin: it is closely followed by Ka and Qi. For the parameter α, the accuracies of the K and Q/Qi algorithms appear little changed while that of the Ka algorithm is slightly degraded. However, the performance of the algorithms A and Az in estimating α is much more seriously compromised: a pronounced $|\alpha|$-dependence is evident with the lowest relative error occurring at $|\alpha| \approx 1$ and a strong trend of increasing error as $|\alpha|$ departs from unity. Overall, in the presence of noise, the highest accuracy in estimating α appears to be achieved by Ka, followed by Q/Qi and K.

The apparent breakdown of algorithms A and Az at estimating α when noise is present is a direct consequence of their approach to solving the polarimetric calibration problem: A and Az attempt to find suitable

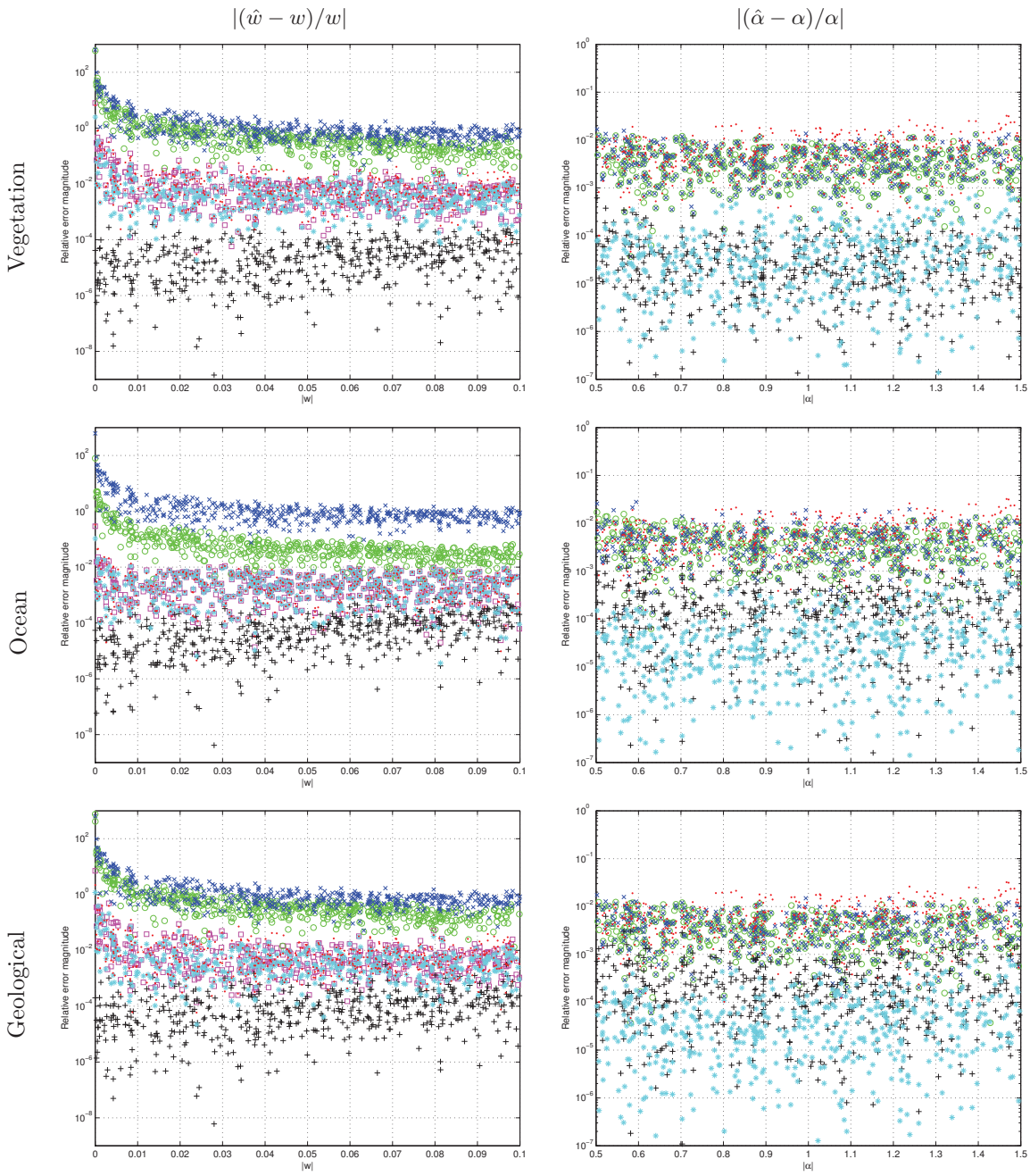

Figure 4.5: Magnitude of relative estimation errors for w and α by algorithm in noise-free case: red $\bullet$ K; cyan $*$ Ka; green $\circ$ Q; magenta $\square$ Qi; blue $\times$ A; black $+$ Az.

values for u, v, w, z and α which transform the input covariance matrix into the particular form given in (4.15) and (4.19). This works well when the noise-corrected covariance matrix $\mathbf{C}$ is given as input but is less appropriate when a significant noise-induced bias in the C_{22} and C_{33} terms is present, as this interferes with the estimation of α by (4.94). Hence, although the resultant estimate of α is still effective in equalising the 'calibrated' C_{22} and C_{33} terms, it is, however, biased by the uncorrected noise and no longer accurately estimates the true value of α. Interestingly, the relative robustness of the α estimates by Ka and K in these simulations is a direct consequence of their eigendecomposition approach: Klein and Freeman [177] note

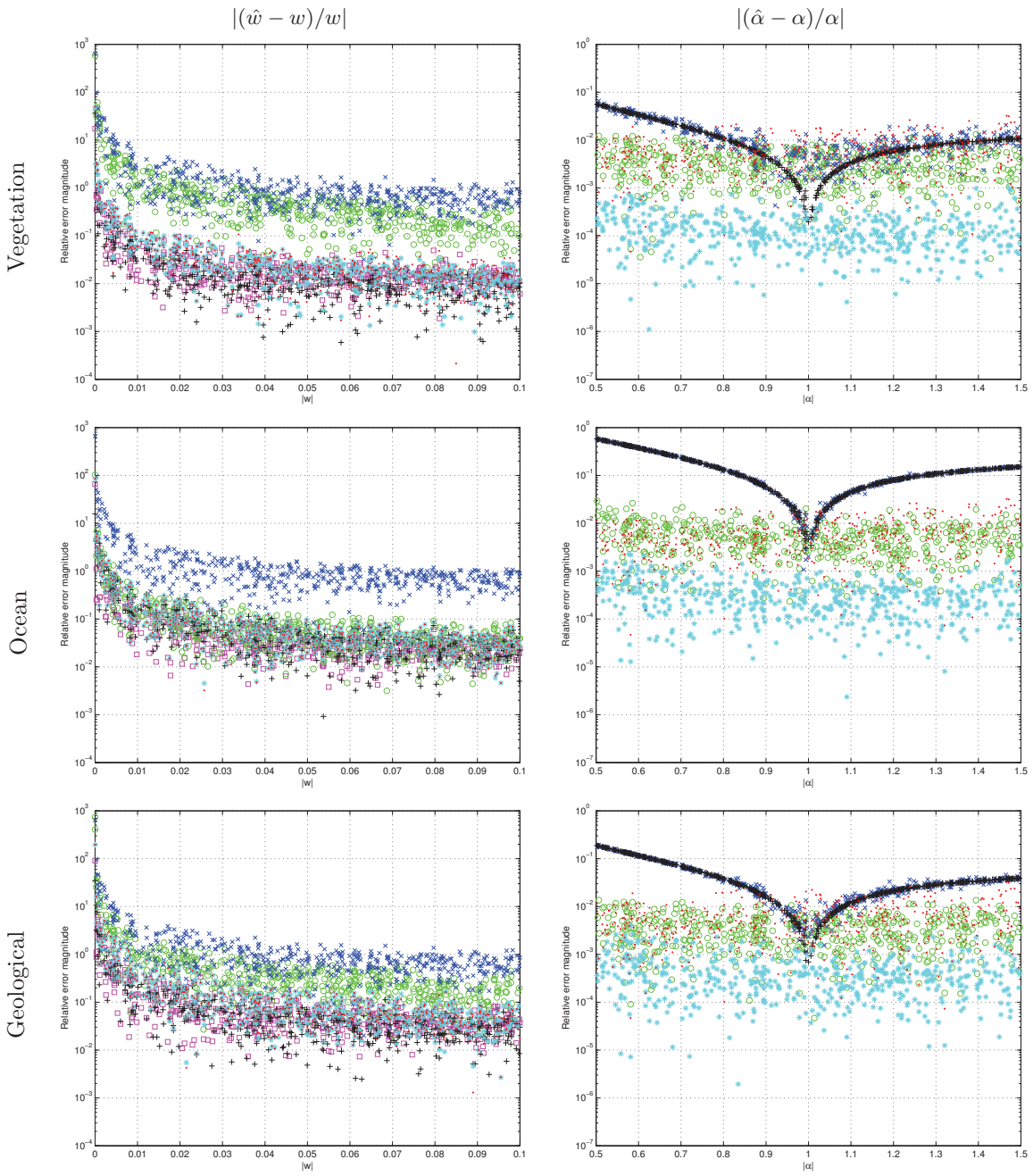

Figure 4.6: Magnitude of relative estimation errors for w and α by algorithm with noise present: red $\bullet$ K; cyan $*$ Ka; green $\circ$ Q; magenta $\square$ Qi; blue $\times$ A; black $+$ Az.

that for mutually uncorrelated noise with equal variance, $\mathbf{C}$ and $\mathbf{C_o}$ will have the same eigenvectors and the eigenvalues of $\mathbf{C_o}$ will be equal to those of $\mathbf{C}$ plus the noise variances. Hence, in such a case, it suffices to compute the eigendecomposition of $\mathbf{C_o}$ instead of $\mathbf{C}$ and use as the vector $\mathbf{f}$ (ref. Section 4.4.2) the eigenvector corresponding to the minimum eigenvalue, as was done.

As discussed in Section 4.4.5, accurate estimates of u, v, w, z and α are required to apply (4.114) and estimate the noise power. From the above results, in the presence of noise, the most accurate estimates of the cross-talk ratios are produced by Az while the most accurate estimates of α are produced by Ka. Accordingly,

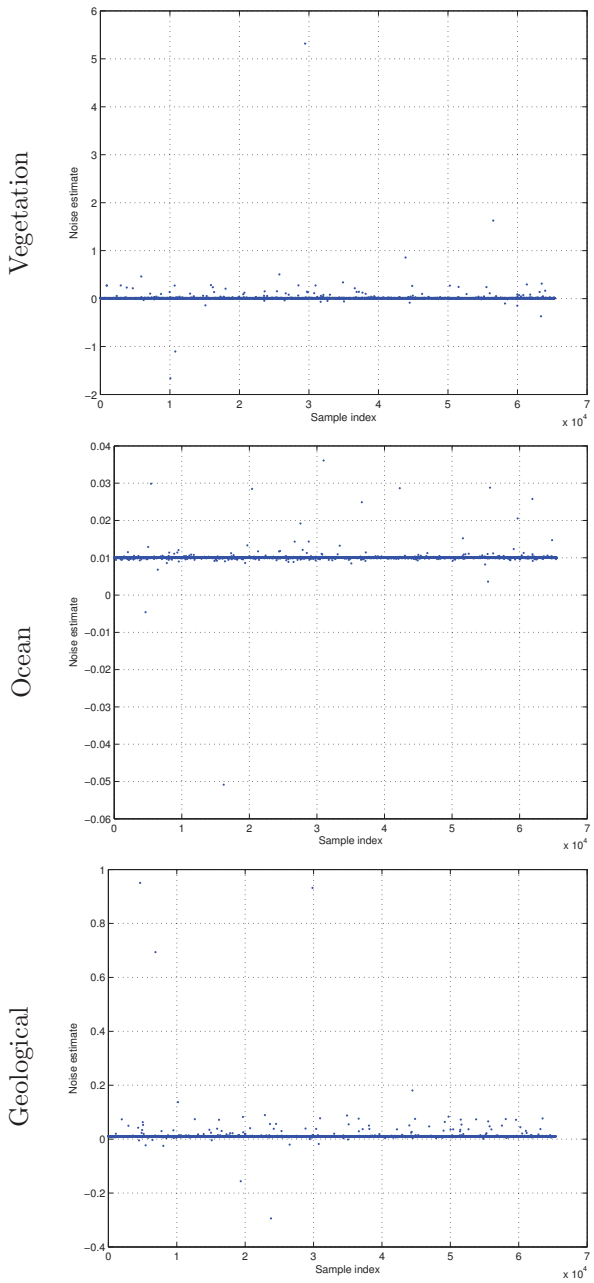

Figure 4.7: Estimates of noise power $N_{22} = N_{33}$ from iterative hybrid Ka/Az algorithm.

the following hybrid approach using Az and Ka to estimate the cross-talk ratios and α parameter respectively was iteratively employed for noise-estimation. First the noise power ratio m was set to unity, and the initial estimates of $N_{22} = N_{33}$ were set to zero. Then, at each iteration, the input covariance matrix was corrected by subtraction of the current estimates of the noise powers from the diagonal terms, and the various parameters u, v, w, z were calculated using Az while the parameter α was calculated using Ka. Equation (4.114) was then employed to estimate the incremental noise powers which were then added to the current noise estimates to produce the updated noise estimates for the next iteration. Representative plots of the resultant noise estimates as obtained by this iterative procedure are shown in Figure 4.7 and accompanying summary statistics are tabulated in Table 4.3: for all surface types, valid cross-talk estimates were obtained in a high

Table 4.3: Percentage of valid estimates and estimated noise power in $N = 65536$ trials of iterative hybrid Az/Ka algorithm.

Surface type	Percentage valid	Estimated noise (mean ± std. dev.)
Vegetation	99.78	0.0102 ± 0.0241
Ocean	99.91	0.0100 ± 0.0003
Geological	99.76	0.0101 ± 0.0062

proportion of cases and the noise estimates were in excellent agreement with the true value of 0.01. However, from Figure 4.7, it can be seen that, although the vast majority of the noise estimates were tightly clustered around the mean, a few extreme outliers were nevertheless present, indicating the need for caution. The final results of cross-talk and α parameter estimation with this hybrid algorithm are shown in Figure 4.8, along with the results from Ka and Az alone (without noise-correction) for comparison. As can be seen from this figure, estimation accuracies for cross-talk and α on the order of Az and Ka in the noise-free case are obtained (cf. Figure 4.5), indicating the accurate estimation and compensation for the noise by this procedure.

4.4.7 Summary

This section discussed the use of distributed targets for polarimetric calibration: essentially, the key idea is that by making appropriate assumptions concerning the statistics of the polarimetric scattering behaviour of a distributed target, estimates of the cross-talk ratios u, v, w, z and the channel-imbalance parameter α can be obtained. Three previously published techniques to calculate such estimates (authored by Klein [85], Quegan [86] and Ainsworth et al. [87]) were considered, and six minor variants of these algorithms (denoted K, Ka, Q, Qi, A and Az) were derived using a common system of definitions and notation to facilitate comparison. The relative performance of these six algorithms was compared through Monte Carlo numerical simulations: the results indicate cross-talk and α were most accurately estimated in the presence of noise by Az and Ka respectively. These relative strengths of Az and Ka are exploited in a proposed hybrid approach for estimating and accounting for noise when calculating the calibration solution: numerical simulations indicate this Az-Ka hybrid algorithm produces more accurate results than either Az or Ka alone.

4.5 Channel-imbalance calibration

The correction of channel-imbalance is the logical next step following cross-talk calibration. In our polarimetric distortion model (ref. Section 4.3), the effects of channel-imbalance are represented by the α and k parameters. Although an estimate of α is produced by the previously discussed cross-talk calibration procedure, both α and k can be estimated from measurements of suitable point targets, e.g. dihedral reflectors (or even the direct-path signal). This is the subject of the present section.

To begin, observe that substitution of (4.7) into the vectorised polarimetric distortion model of (4.5) and re-arranging produces the equation

$$\tilde{\mathbf{o}} \triangleq \mathbf{M}^{-1}(\mathbf{o} - \mathbf{n}) = Y\mathbf{AKs}. \tag{4.115}$$

In practice, the value of the noise $\mathbf{n}$ will be unknown but it will, generally, be of small magnitude: thus, henceforth in this discussion, we shall assume the noise is negligible and take $\mathbf{n} = \mathbf{0}$. The quantity $\tilde{\mathbf{o}}$ thus represents the partially calibrated measurements after correction for channel cross-talk: if the cross-talk ratios u, v, w, z (and hence the matrix $\mathbf{M}$) have been determined (e.g. by a distributed target technique), the $\tilde{\mathbf{o}}$ can

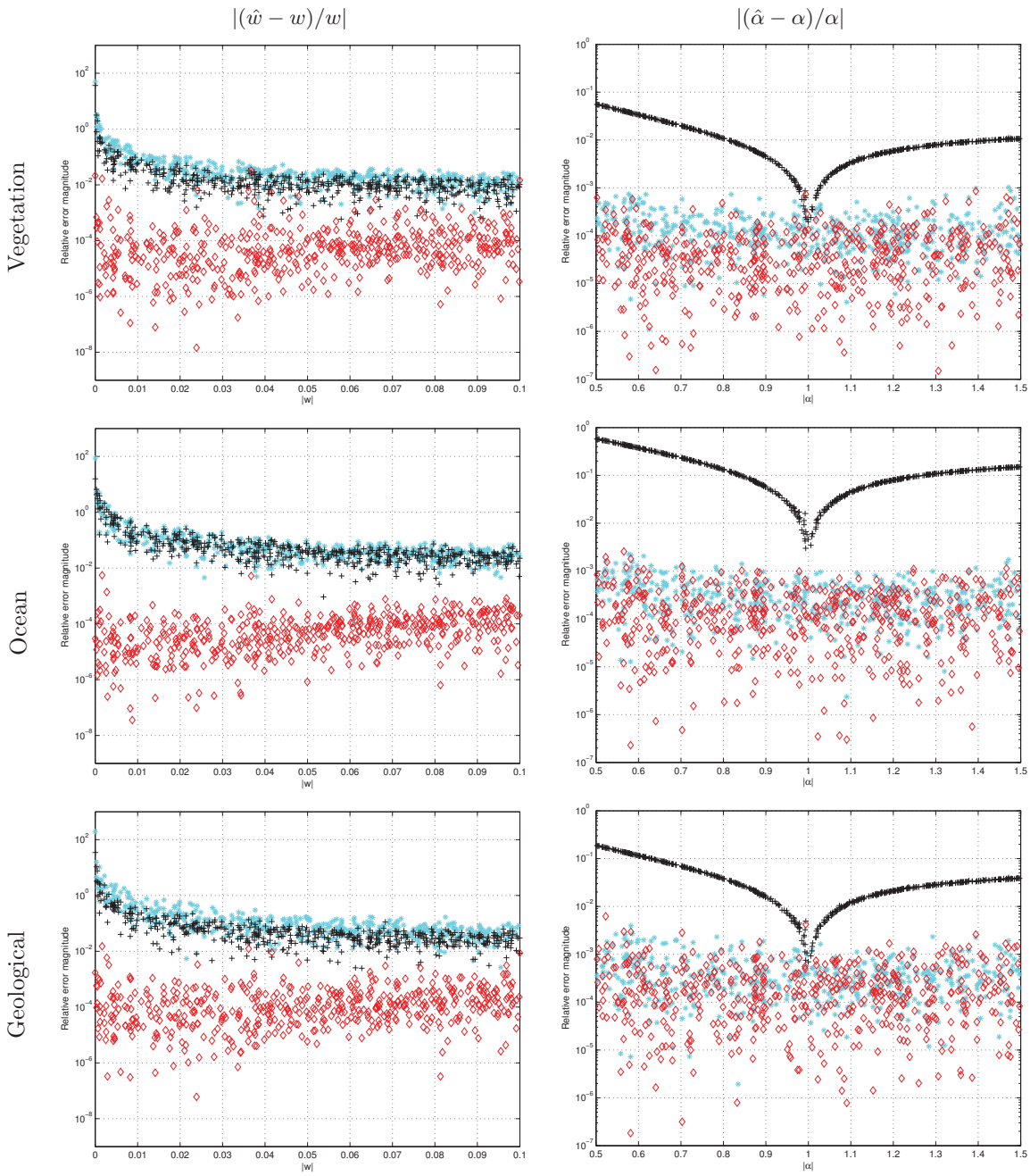

Figure 4.8: Magnitude of relative estimation errors for w and α by algorithm with noise present: cyan $*$ Ka; black $+$ Az; red $\Diamond$ hybrid Ka/Az with iterative noise-estimation.

be simply obtained as $\mathbf{M}^{-1}\mathbf{o}$. Alternatively, if estimates of the cross-talk ratios are not available but $|u|$, $|v|$, $|w|$, $|z|$ are, however, known to be negligible, then $\mathbf{M}$ will just be a 4×4 identity matrix and we can simply take $\tilde{\mathbf{o}} = \mathbf{o}$ directly.

Let the components of $\tilde{\mathbf{o}}$ be denoted by $\tilde{o}_{ij}$: then, (4.115) can be written explicitly in terms of the

components as

$$\begin{bmatrix} \tilde{o}_{\mathrm{hh}} \\ \tilde{o}_{\mathrm{hv}} \\ \tilde{o}_{\mathrm{vh}} \\ \tilde{o}_{\mathrm{vv}} \end{bmatrix} = \begin{bmatrix} Yk^2\alpha s_{\mathrm{hh}} \\ Yks_{\mathrm{hv}} \\ Yk\alpha s_{\mathrm{vh}} \\ Ys_{\mathrm{vv}} \end{bmatrix} \tag{4.116}$$

In the case of a cross-polarising target for which the cross-polarised terms s_{hv} and s_{vh} are both non-zero and the ratio $s_{\mathrm{vh}}/s_{\mathrm{hv}}$ is known, it is possible to obtain an estimate of the channel-imbalance parameter α by taking the ratio of $\tilde{o}_{\mathrm{vh}}$ to $\tilde{o}_{\mathrm{hv}}$:

$$\alpha = \frac{\tilde{o}_{\mathrm{vh}}/\tilde{o}_{\mathrm{hv}}}{s_{\mathrm{vh}}/s_{\mathrm{hv}}}. \tag{4.117}$$

The presence of a suitable cross-polarising target is required to calculate α by this means: this is usually quite a restrictive condition, necessitating the premeditated deployment of such targets. Fortunately, however, in the absence of such targets, α can also be estimated through a distributed target calibration method, as previously discussed.

With an estimate of α, the remaining channel-imbalance ratio k can be determined to within a sign ambiguity, given a suitable target (whether cross-polarising or not) for which the co-polarised terms s_{hh} and s_{vv} are both non-zero and the ratio $s_{\mathrm{hh}}/s_{\mathrm{vv}}$ is known: this can be done by forming the ratio of $\tilde{o}_{\mathrm{hh}}$ to $\tilde{o}_{\mathrm{vv}}$, which gives

$$k = \pm\sqrt{\frac{\tilde{o}_{\mathrm{hh}}/\tilde{o}_{\mathrm{vv}}}{\alpha\, s_{\mathrm{hh}}/s_{\mathrm{vv}}}}. \tag{4.118}$$

However, with a cross-polarising target, unambiguous expressions for k can be obtained from the ratios $\tilde{o}_{\mathrm{hh}}/\tilde{o}_{\mathrm{vh}}$ and $\tilde{o}_{\mathrm{hv}}/\tilde{o}_{\mathrm{vv}}$, viz.

$$k = \frac{\tilde{o}_{\mathrm{hh}}/\tilde{o}_{\mathrm{vh}}}{s_{\mathrm{hh}}/s_{\mathrm{vh}}} \tag{4.119}$$

$$k = \frac{\tilde{o}_{\mathrm{hv}}/\tilde{o}_{\mathrm{vv}}}{s_{\mathrm{hv}}/s_{\mathrm{vv}}}. \tag{4.120}$$

Calculating k from these equations requires that the co-/cross-polarised ratios $s_{\mathrm{hh}}/s_{\mathrm{vh}}$ or $s_{\mathrm{hv}}/s_{\mathrm{vv}}$ be accurately known. Typically, however, the magnitudes of these ratios will be sensitive to the relative alignment of the target and the radar antennas: as precise alignment is not always achievable (e.g. for a manœuvring airborne SAR being buffeted by wind), it is difficult to achieve high accuracy when employing (4.119) or (4.120) to calculate k. However, as the co-polarised ratio $s_{\mathrm{hh}}/s_{\mathrm{vv}}$ and the *sign* of the co-/cross-polarised ratios $s_{\mathrm{hh}}/s_{\mathrm{vh}}$ and $s_{\mathrm{hv}}/s_{\mathrm{vv}}$ are relatively insensitive to small alignment errors, k may potentially be best calculated by using (4.118) to obtain $\pm k$, then resolving the sign ambiguity with (4.119) or (4.120).

Examples of non-cross-polarising targets on which (4.118) may be applied are trihedral corner reflectors or spheres, both of which have monostatic scattering matrices of the form

$$\mathbf{S} = \begin{bmatrix} 1 & 0 \\ 0 & 1 \end{bmatrix}. \tag{4.121}$$

Observe that, conveniently, for both these targets $s_{\mathrm{hh}}/s_{\mathrm{vv}} = 1$, which simplifies the expression for k to

$$k = \pm\sqrt{\frac{\tilde{o}_{\mathrm{hh}}}{\alpha\, \tilde{o}_{\mathrm{vv}}}}. \tag{4.122}$$

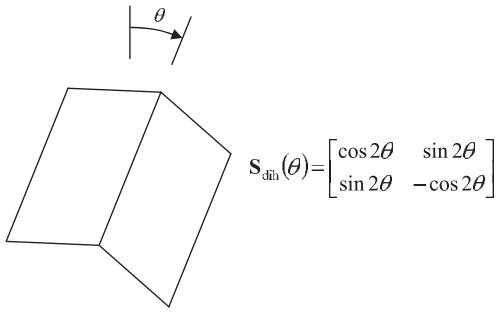

Figure 4.9: Direction of rotation of dihedral corner reflector and resultant monostatic scattering matrix.

While the symmetry of spherical targets confers the advantage of an unchanging scattering response which is independent of viewing direction, trihedral corner reflectors have a higher RCS than a comparably sized sphere, so are generally preferred for calibration. For both targets, however, the expected scattering response (4.121) is valid only for the monostatic case, which requires that the bistatic angle should be kept as close to zero as possible when calibrating a bistatic polarimeter.

An example of a suitable cross-polarising target on which (4.117), (4.118), (4.119) and (4.120) can be applied is a dihedral corner reflector tilted so that the seam makes an angle $\theta \neq n\pi/4$ with the vertical: the monostatic scattering matrix when the dihedral is viewed along its backscatter boresight direction is shown in Figure 4.9. To achieve a high degree of cross-polarisation with equal power in the four polarisation channels, an appropriate tilt angle to use would be $\theta = \pm\pi/8 = \pm 22.5°$. Observe that, conveniently, $s_{\mathrm{vh}}/s_{\mathrm{hv}} = 1$ independently of θ, so (4.117) simplifies to

$$\alpha = \frac{\tilde{\sigma}_{\mathrm{vh}}}{\tilde{\sigma}_{\mathrm{hv}}}. \tag{4.123}$$

Similarly, $s_{\mathrm{hh}}/s_{\mathrm{vv}} = -1$ which results in (4.118) becoming

$$k = \pm j\sqrt{\frac{\tilde{\sigma}_{\mathrm{hh}}}{\alpha\,\tilde{\sigma}_{\mathrm{vv}}}} \tag{4.124}$$

and, as $s_{\mathrm{hh}}/s_{\mathrm{vh}} = -s_{\mathrm{vv}}/s_{\mathrm{hv}} = \cot 2\theta$, equations (4.119) and (4.120) become

$$k = \frac{\tilde{\sigma}_{\mathrm{hh}}}{\tilde{\sigma}_{\mathrm{vh}}}\tan 2\theta \tag{4.125}$$

$$k = -\frac{\tilde{\sigma}_{\mathrm{hv}}}{\tilde{\sigma}_{\mathrm{vv}}}\cot 2\theta. \tag{4.126}$$

Note that if $\pm k$ is first obtained via (4.124) and the sign ambiguity is then resolved using (4.125) or (4.126), then a precise knowledge of θ is unnecessary. As with the previous targets, this expected scattering response is valid only for the monostatic case, so only a small bistatic angle is permissible when using dihedral corner reflectors for bistatic polarimetric calibration. A drawback of dihedral corner reflectors as calibration targets is the relatively narrow beamwidth of their scattering response. As a result, alternatives such as gridded trihedral reflectors, which also possess cross-polarising properties but have a broader backscatter beamwidth, may be preferable [210].

For bistatic radars, the direct-path signal with the transmit and receive antennas aligned so that each lies on the boresight of the other can potentially be used for polarimetric calibration. In essence, this substitutes measurements of a known cross-polarising target with measurements of the direct-path signal in which cross-

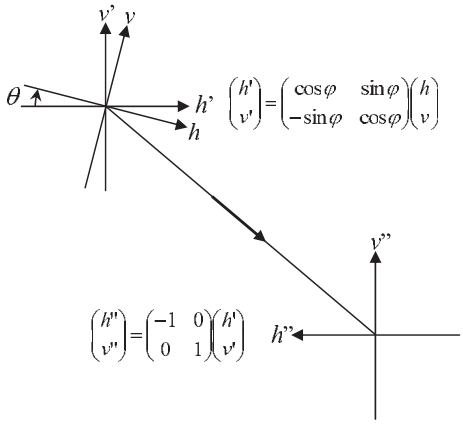

Figure 4.10: Transformations between coordinates used in calculating the expected polarimetric properties of the direct-path signal: hv are axes of the rotated transmit antenna; $h'v'$ are generic horizontal and vertical axes; and $h''v''$ are receive antenna axes in Back-Scatter Alignment (BSA) convention.

polarisation is achieved through relative rotation of the antennas: from Figure 4.10, the 'scattering matrix' for this direct-path signal may be calculated to be

$$\begin{aligned} \mathbf{S} &= \begin{bmatrix} -1 & 0 \\ 0 & 1 \end{bmatrix} \begin{bmatrix} \cos\phi & \sin\phi \\ -\sin\phi & \cos\phi \end{bmatrix} \\ &= \begin{bmatrix} -\cos\phi & -\sin\phi \\ -\sin\phi & \cos\phi \end{bmatrix}. \end{aligned} \tag{4.127}$$

As this is similar in form to the dihedral scattering matrix of Figure 4.9 (albeit with the rotation angle ϕ in place of 2θ), the corresponding formulae for α and k are identical to (4.123) and (4.124), and the analogues of (4.125) and (4.126) are easily obtained as

$$k = (\tilde{o}_{\mathrm{hh}}/\tilde{o}_{\mathrm{vh}}) \tan\phi \tag{4.128}$$

$$k = -(\tilde{o}_{\mathrm{hv}}/\tilde{o}_{\mathrm{vv}}) \cot\phi. \tag{4.129}$$

As with the dihedral, if (4.124) is used to obtain $\pm k$ and (4.128) or (4.129) is then used to disambiguate the sign, then it is unnecessary for ϕ to be accurately measured. This is fortunate as, while controlled and measured antenna rotation may be quite practicable for small laboratory-based radars, it is much less feasible for operational airborne radars: for the *Ingara* bistatic system, rotation of the airborne transmitting antenna was ultimately achieved by pitching the aircraft!

A similar direct-path-signal-based calibration technique has previously been suggested by Daout et al. [84]. Their approach requires two direct-path signal measurements, the first made with the polarisation axes of the two antennas aligned and the second with a relative rotation between them: from these measurements, the polarimetric distortion parameters are calculated and subsequently used to correct the polarimetric channel-imbalances in scattering measurements made of targets of interest. A disadvantage of the procedure stipulated by Daout et al. [84] is the requirement to take *two* separate measurements when only a single measurement is required by the method discussed above. A further deficiency is that, in their calculation of the polarimetric distortion parameters, the ambiguity introduced by the taking of a square root seems not to receive due

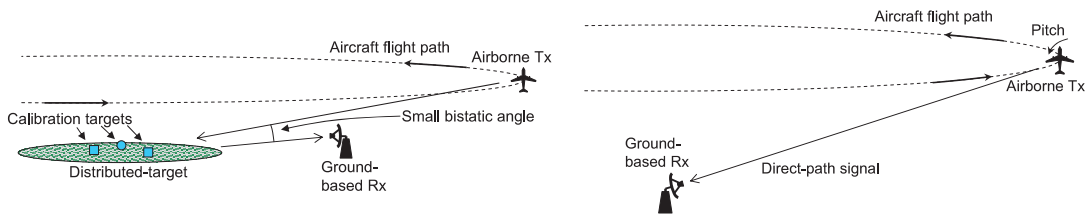

(a) Imaging collection (b) Direct-path signal collection

Figure 4.11: Geometries employed for collection of data for polarimetric calibration.

consideration. For these reasons, the method of Daout et al. will not be further considered here.

4.6 Calibration of *Ingara* data

In this section, we discuss the application of the previously discussed polarimetric calibration techniques to the monostatic and bistatic data sets collected during the March and December 2008 *Ingara* bistatic trials. The overall objective is to derive a calibration solution, i.e. a canonical set of estimates of the calibration parameters k, α, u, v, w and z, which can then be applied to calibrate the collected data. As distinct receiver hardware is employed in the airborne and ground-based systems, separate calibration solutions will be derived for the monostatic and bistatic data. In addition, due to various factors such as ageing of the electronic components and modifications made to the radar hardware, the long-term stability of the calibration parameters cannot be assumed: hence, separate calibration solutions will also be derived for the March and December 2008 data sets.

4.6.1 Data sets

Two sets of data collected by the airborne and ground-based receivers are available for calculating the polarimetric calibration solutions: the first set was collected in March 2008 while the second was collected in December 2008. Each data set largely comprises multiple spotlight-mode SAR imaging runs of the hill-top test site which were made at low aircraft altitudes in order to minimise the bistatic angle between the airborne transmitter and the ground-based receiver (see Figure 4.11(a)); prior to imaging, various calibration targets with known monostatic polarimetric signatures were deployed at the test site (see Figure 4.12). A total of 20 and 14 such collection runs are included in the March and December data sets respectively: in each set, the SAR data from runs with indices 1–7 and 8–14 was simultaneously collected on the same day by the airborne and ground-based receivers respectively within a period of approximately two hours. Runs with indices 15–20 in the March data set are an additional six runs containing data collected a day later than runs 1–14 over a period of an hour by the ground-based receiver only (due to an unfortunate hardware fault, the corresponding data which was simultaneously collected by the airborne receiver is not usable and therefore not included in this analysis). In the March 2008 imaging runs, additional discrete 20 dB attenuator components were temporarily inserted into the RF chain in the ground-based receiver hardware (this was done to reduce the receiver sensitivity as part of an abortive attempt to collect direct-path data): these attenuators were subsequently removed just prior to the December 2008 imaging runs.

The low aircraft altitudes employed during these data collection runs resulted in a low grazing angle (see Figure 4.13) and hence low backscatter power from the terrain, but this geometry was nevertheless chosen in order to obtain a near-monostatic collection geometry for the ground-based receiver data. The motivation for

D1: $-22.5°$-rotated 25 cm dihedral,
$\mathbf{S} = \begin{bmatrix} 1 & -1 \\ -1 & -1 \end{bmatrix}$

D2: upright 25 cm dihedral,
$\mathbf{S} = \begin{bmatrix} 1 & 0 \\ 0 & -1 \end{bmatrix}$

H: hemisphere,
$\mathbf{S} = \begin{bmatrix} 1 & 0 \\ 0 & 1 \end{bmatrix}$

D4: $22.5°$-rotated 50 cm dihedral,
$\mathbf{S} = \begin{bmatrix} 1 & 1 \\ 1 & -1 \end{bmatrix}$

D3: upright 50 cm dihedral,
$\mathbf{S} = \begin{bmatrix} 1 & 0 \\ 0 & -1 \end{bmatrix}$

Figure 4.12: Photographs of calibration targets taken in December 2008, showing aspect presented to ground-based receiver, and normalised expected scattering matrix $\mathbf{S}$. Set-up of targets was similar in both March and December 2008 trials.

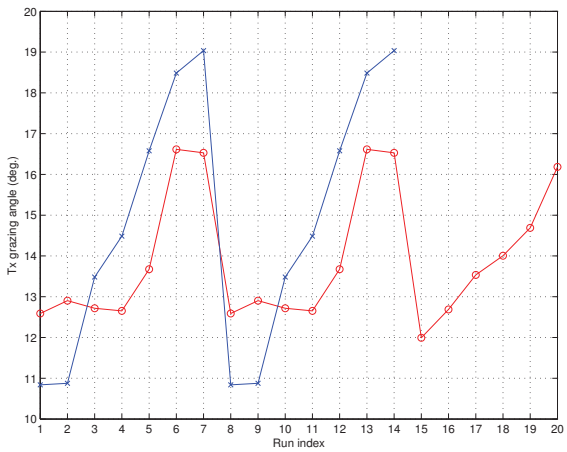

Figure 4.13: Grazing angles of airborne transmitter for the various collection runs: red ∘ March 2008; blue × December 2008. In both March and December data sets, data with run indices 1–7 was collected in a monostatic geometry by the airborne receiver while data with run indices 8 and above was collected in a bistatic geometry by the ground-based receiver.

this is two-fold: to allow the application of distributed target calibration techniques for cross-talk estimation (as previously discussed, these techniques are derived assuming cross-polarised equivalence, i.e. $s_{\mathrm{hv}} = s_{\mathrm{vh}}$, which is expected from scattering reciprocity only for a strict monostatic collection geometry), and to allow channel-imbalance estimation from measurements made of standard calibration targets from the data collected by the ground-based receiver (the familiar theoretical polarimetric responses of these targets are valid for the case of monostatic backscattering but not when a significant bistatic angle is present).

For these calibration runs, the typical slant ranges of the aircraft and ground-based receiver antennas from the calibration site were approximately 6.5 km and 3.5 km respectively. The collected data were processed to form monostatic and bistatic images with approximate resolutions (range × azimuth) of 0.4 m×0.1 m and 0.4 m×0.2 m respectively; the approximate width of the image swath was up to 1000 m. From the grazing angles, stand-off ranges and swath width, the angle subtended at the antennas can be estimated (Figure 4.16): for representative grazing angles of 13° and 2° for the airborne and ground-based antennas, the elevation angles subtended by the swath are approximately 2° and 0.6° respectively. As these angles are only a small fraction of the 3 dB elevation beamwidths of the airborne and ground-based antennas (which are approximately 20° and 2° respectively), little variation of the polarimetric distortion across the image swath would be expected. Hence, in this discussion, we shall take the distortion to be spatially constant for simplicity.

In order to apply the distributed target cross-talk calibration techniques to the data, it is first necessary to estimate the covariance matrix $\mathbf{C_o}$ of the polarimetric measurements of an appropriate distributed target. For the two data sets which were analysed, this was performed by calculating the covariances between the variously polarised measurements of the open area in the imaged scene: this calculation was done for each of the various monostatic and bistatic images formed from the data collected in each run around the point when the bistatic angle was minimal. The precise region used for the covariance estimation was carefully selected to lie near the centre of the images, while avoiding the bright returns from the power-lines and the deployed calibration targets, as well as the shadows cast by the trees in the bistatic images: the chosen region is shown in Figures 4.14 and 4.15. The sample covariance between the polarisations p and q, where

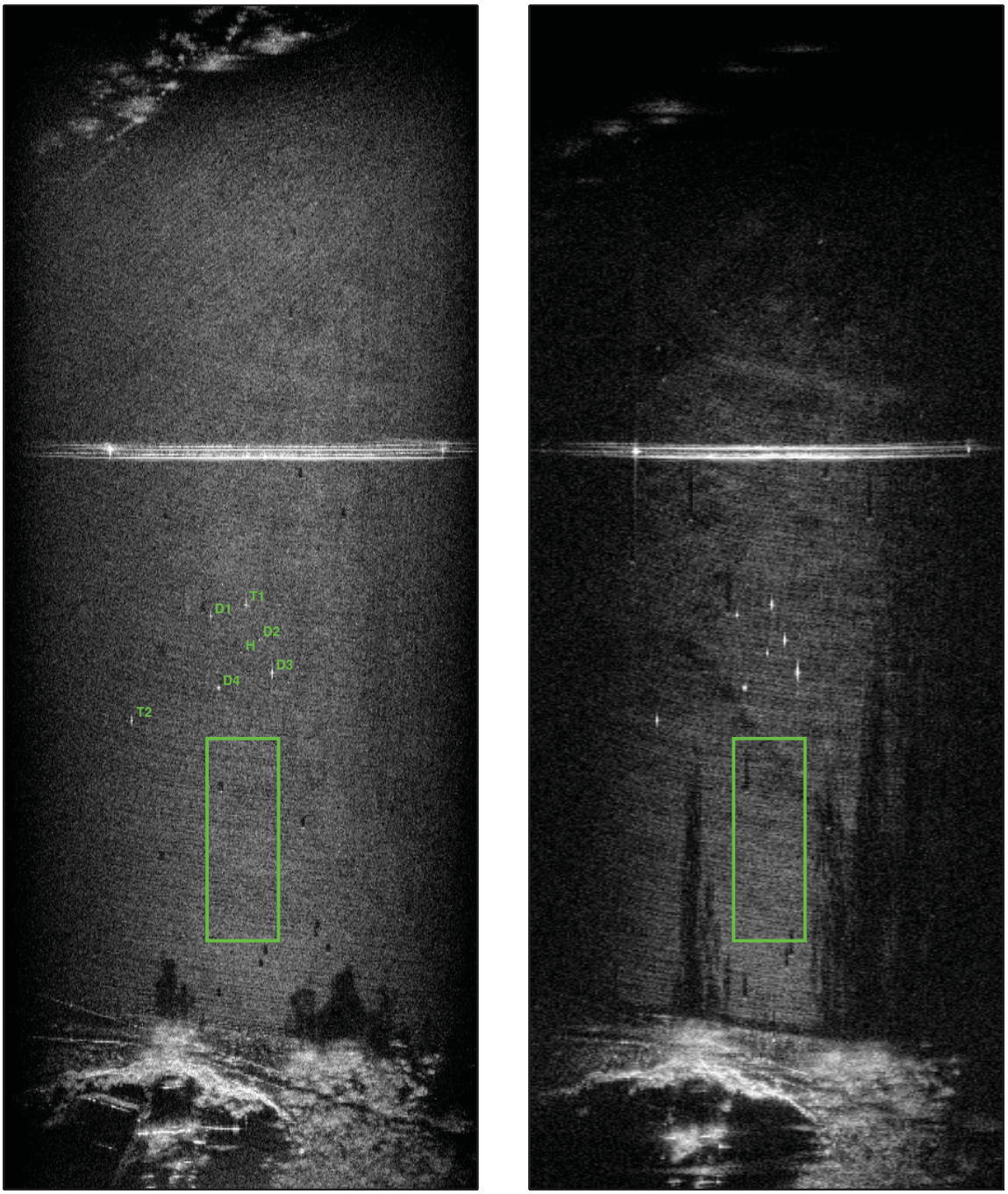

(a) Monostatic (b) Bistatic

Figure 4.14: HH-polarised (uncalibrated) (a) monostatic and (b) bistatic images of hill-top test site from data simultaneously collected in March 2008 by airborne and ground-based receivers. Deployed targets are: D1 and D2 rotated and upright 25 cm dihedral reflectors; D3 and D4 upright and rotated 50 cm dihedral reflectors; H hemisphere; T1 and T2 quadruple-pack trihedral reflectors. Rectangle indicates region used for covariance matrix estimation.

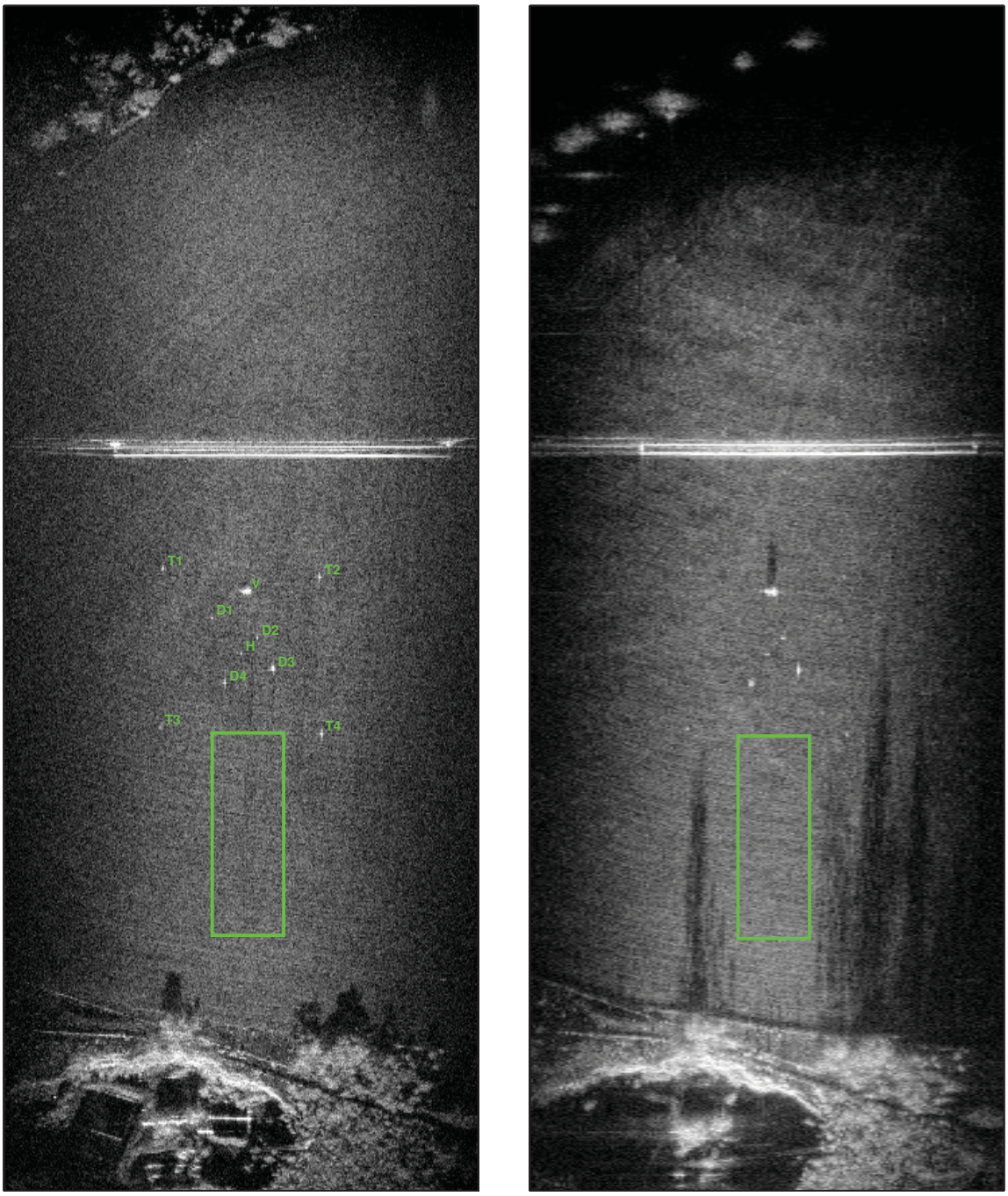

(a) Monostatic (b) Bistatic

Figure 4.15: HH-polarised (uncalibrated) (a) monostatic and (b) bistatic images of hill-top test site from data simultaneously collected in December 2008 by airborne and ground-based receivers. Deployed targets are: D1 and D2 rotated and upright 25 cm dihedral reflectors; D3 and D4 upright and rotated 50 cm dihedral reflectors; H hemisphere; T1 to T4 quadruple-pack trihedral reflectors; V utility vehicle. Rectangle indicates region used for covariance matrix estimation.

$p, q \in \{\mathrm{hh}, \mathrm{hv}, \mathrm{vh}, \mathrm{vv}\}$, was calculated according to the equation

$$\langle o_p o_q^* \rangle = \frac{1}{N} \sum_{n=1}^{N} (o_p)_n (o_q)_n^* \tag{4.130}$$

where the notation $(o_p)_n$ denotes the nth pixel from polarisation channel p in the set of N pixels being employed in the calculation. To obtain a set of independent pixels with which to calculate the covariance estimates, the correlation function of the region at various lags along the range and azimuth directions was first calculated and examined: some examples are shown in Figure 4.17. Interestingly, high side-lobes are observed in the range direction in the bistatic data from the H-polarised receiver: this effect is probably attributable to the high range side-lobes caused by waveform distortions previously discussed in Section 2.9. From these and similar plots, it was generally observed that the pixels were highly correlated only over lags of up to around three pixels in the range and azimuthal directions: hence, a three-pixel skip distance along each direction was adopted for choosing the pixels to be included in the set used in the covariance calculations.

To facilitate comparison of the covariance matrices from the various runs, each calculated covariance matrix was normalised by the geometric mean of the hh and vv channel powers, i.e. $\sqrt{\langle |o_{\mathrm{hh}}|^2 \rangle \langle |o_{\mathrm{vv}}|^2 \rangle}$. Such an overall scaling only affects the absolute radiometric parameter Y but does not affect the cross-talk ratios u, v, w, z or the channel-imbalance parameters α and k. The normalisation factors used for the various runs are shown in Figure 4.18. Large differences in the baseline power levels between the uncalibrated monostatic and bistatic data is evident: this is probably attributable to a mix of factors, including differences in the distances of the airborne and ground-based receivers from the imaged scene, differences in the gains of the airborne and ground-based antennas and differences in the operating levels of the airborne and ground-based receiver hardware. Also evident are differences in the power levels between the March and December 2008 data: these may be the result of changes in the hardware characteristics (particularly in the ground-based receiver where the temporarily inserted 20 dB attenuators were removed), changes in the collection geometries and changes in the terrain reflectivity. For the bistatic data, both March and December 2008 data sets show a systematic trend of decreasing power level with run index: this trend follows the increase in the transmitter grazing angle with run index (see Figure 4.13), and is thus consistent with a reduction in the received scattered power as the bistatic angle increases. By contrast, in the monostatic data, no systematic trend in the power level with run index is apparent (this has to be interpreted with caution, however, due to the sizable variability in the measurements), which is consistent with the constancy of the zero-valued bistatic angle in this data.

The normalised values of the various covariances comprising the entries of the covariance matrices are shown in Figures 4.19 and 4.20. As the covariance matrix is Hermitian, in the interests of clarity, only one of each conjugate pair of values is shown. As a result of the normalisation, the plotted co-polarised (hh and vv) powers in Figure 4.19 expressed in decibels lie at equal distances on opposite sides of the 0 dB line. Generally, the (calibrated) co-polarised hh and vv powers from natural terrain may be expected to be of a similar order of magnitude, while the cross-polarised hv and vh powers should be equal (by scattering reciprocity) but a few decibels less than the co-polarised powers (e.g. see Table 4.1): the plots in Figure 4.19 of the uncalibrated measured powers are broadly consistent with these expected relationships. However, it may be observed that in the airborne receiver data, the H-polarised received powers are a few decibels greater than the V-polarised received powers, while this relationship is reversed in the ground-based receiver data: this likely reflects an idiosyncratic difference in the gains of the H- and V-polarised receivers in the airborne and ground-based systems (with the airborne H-polarised receiver and ground-based V-polarised receiver having slightly higher gains than their partners) which must be compensated for by polarimetric calibration. The powers of

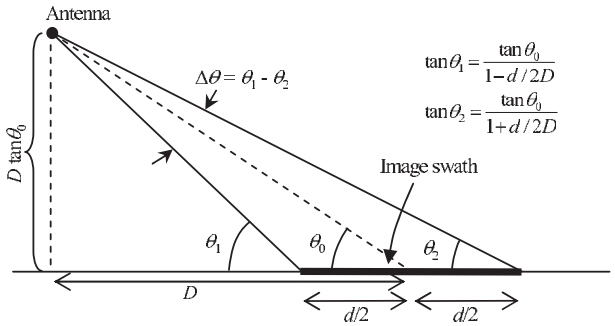

Figure 4.16: Calculation of $\Delta\theta$, being the elevation angle subtended by an image swath of width d at an antenna with stand-off distance D and grazing angle θ_0.

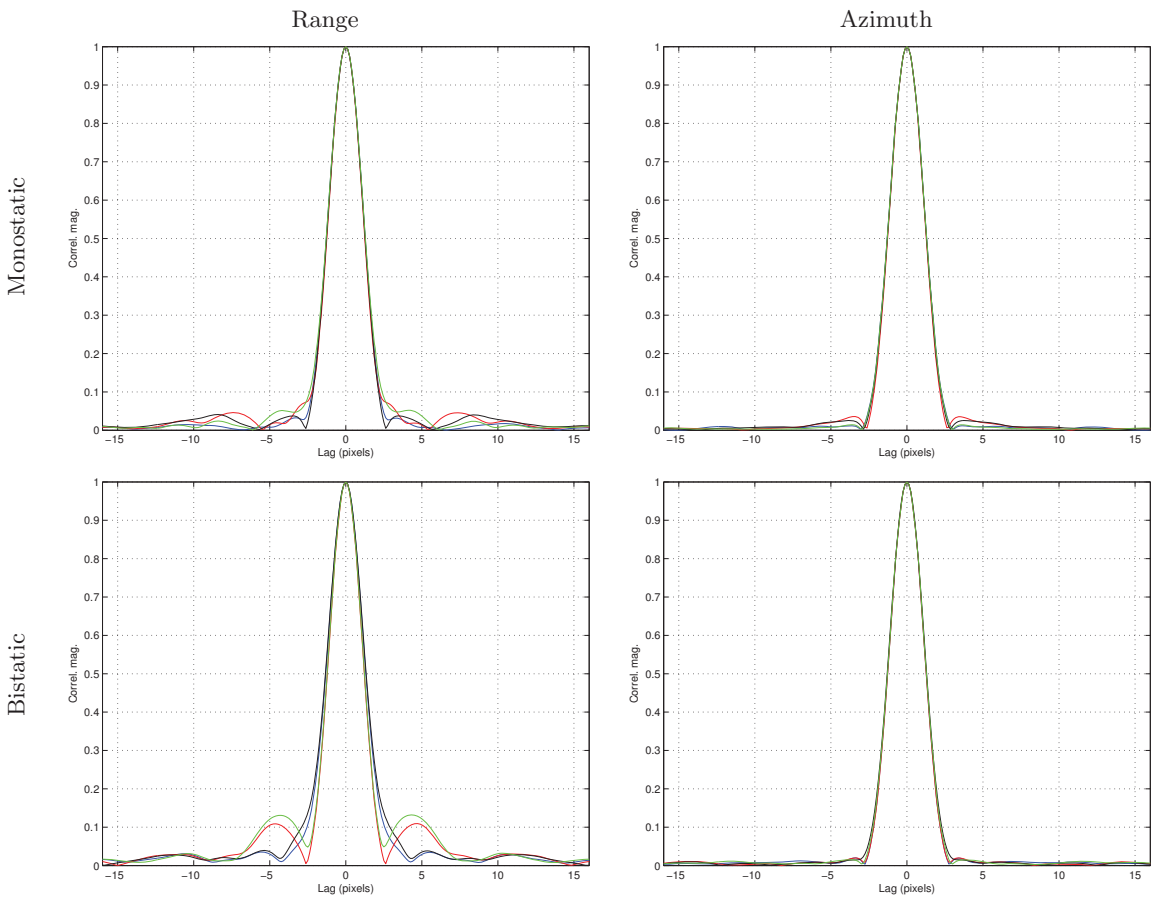

Figure 4.17: Correlation function of region used for covariance estimation at various lags along range and azimuth directions: red hh; green hv; blue vh; black vv. (Data was upsampled by a factor of eight.)

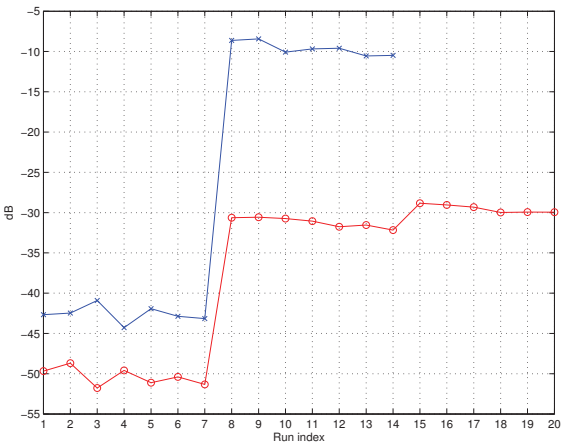

Figure 4.18: Plots of geometric means of hh and vv channel powers in observed covariance matrix $\mathbf{C_o}$, i.e. $\sqrt{\langle|o_{\mathrm{hh}}|^2\rangle\langle|o_{\mathrm{vv}}|^2\rangle}$: red ∘ March 2008; blue × December 2008. Run indices 1–7 are monostatic data from airborne receiver; indices 8 and above are bistatic data from ground-based receiver.

the uncalibrated co-/co-polarised covariance $\langle o_{\mathrm{hh}} o_{\mathrm{vv}}^* \rangle$ and the cross-/cross-polarised covariance $\langle o_{\mathrm{hv}} o_{\mathrm{vh}}^* \rangle$ are approximately 1–3 and 10–15 decibels lower than the co-polarised powers respectively, which is consistent with the values for geological terrain quoted in Table 4.1: this suggests that little scattering occurred from the short and dry crop stubble which was present in the field. For a polarimetric radar system with negligible cross-talk and uncorrelated noise between polarisations which is observing azimuthally symmetric terrain, the powers of the uncalibrated co-/cross-polarised covariances $\langle o_{ii} o_{ij}^* \rangle$ and $\langle o_{ii} o_{ji}^* \rangle$ may be expected to be very low, however moderate co-/cross-polarised powers from -24 to -12 dB are encountered in the data. One possible cause of such non-zero co-/cross-polarised covariances is a non-negligible azimuth slope of the terrain as observed by the radar [211]: however, from measurements of the transmitter and receiver positions, and an estimate of the local normal vector to the terrain surface (obtained by fitting a plane to GPS data collected by systematically traversing the site on foot with a hand-held GPS receiver), the estimated terrain azimuth slope in the observation geometry for this data is estimated to be a negligible 0.072°. Correlation of the noise processes in the different polarimetric channels is another possible cause of non-zero co-/cross-polarised covariances, but, barring the presence of leakage signals or RF interference, this is relatively unlikely. Hence, the observed co-/cross-polarised power levels suggest the existence of cross-talk requiring compensation by polarimetric calibration. Interestingly, however, despite the considerable variability in the various covariance terms (from Figure 4.20, ranges of 2–3 dB in magnitude and as much as 20–30° in phase are not uncommon—such variability renders the precise calculation of a polarimetric calibration solution difficult), it can be observed that there is a general tendency for similar values to occur in the covariance measurements made from the airborne and ground-based receiver data. Since there is no a priori reason to expect that the cross-talk ratios in the monostatic and bistatic data will be similar, this concordance between the covariance measurements is suspicious and suggests the possibility that the terrain co-/cross-polarised covariances are not really zero-valued as postulated, i.e. the cross-talk isolation of the airborne and ground-based systems is sufficiently high that the measured co-/cross-polarised covariances are actually a valid reflection of the terrain scattering characteristics.

In addition to the terrain covariance matrix, the polarised responses of the various calibration targets were also measured in the March and December 2008 data (such measurements are required for channel-imbalance calibration, i.e. estimation of α and k). The resultant target polarimetric measurements are shown

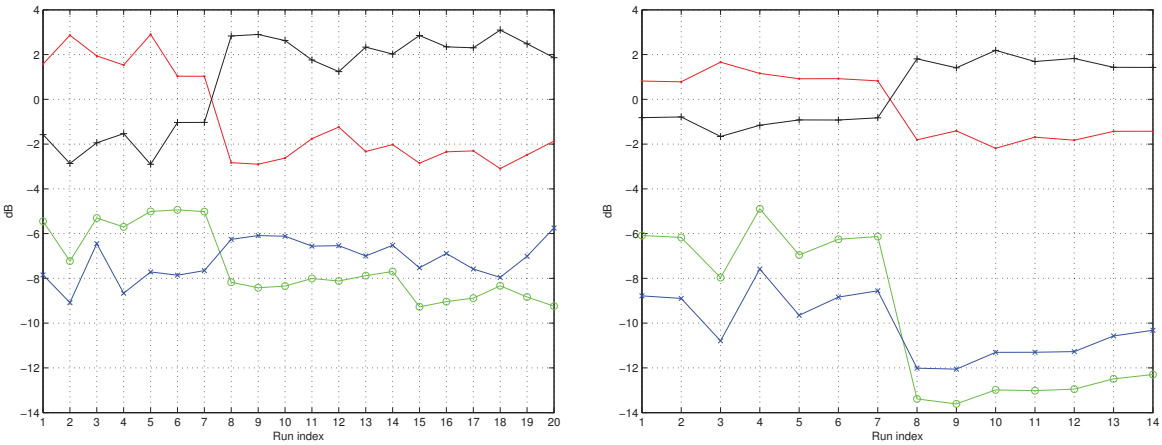

March 2008 December 2008

Figure 4.19: Plots of diagonal entries of observed distributed target covariance matrix $\mathbf{C_o}$: red $\cdot$ $\langle |o_{\mathrm{hh}}|^2 \rangle$; green $\circ$ $\langle |o_{\mathrm{hv}}|^2 \rangle$; blue $\times$ $\langle |o_{\mathrm{vh}}|^2 \rangle$; black $+$ $\langle |o_{\mathrm{vv}}|^2 \rangle$. Runs 1–7 are from airborne receiver; runs 8 and above are from ground-based receiver.

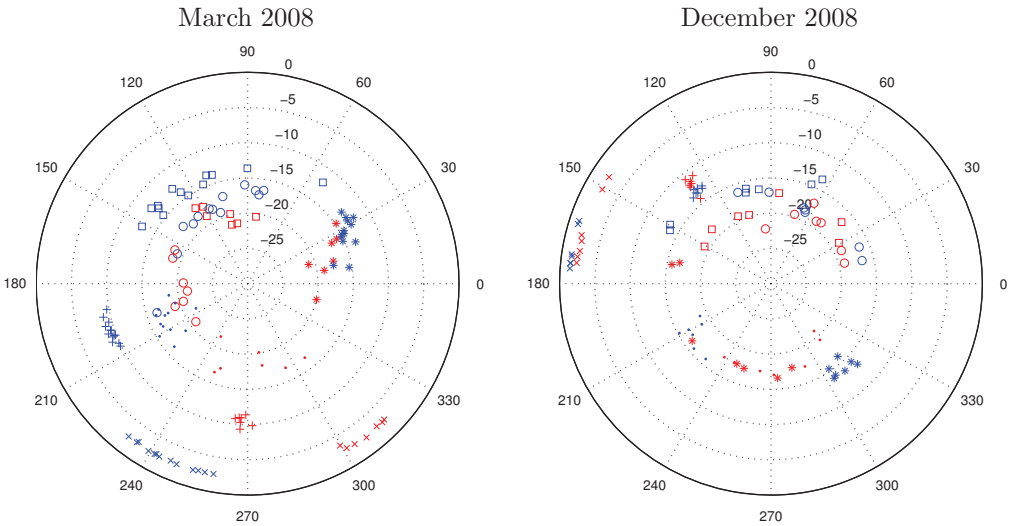

Figure 4.20: Polar plots of off-diagonal entries of observed distributed target covariance matrix $\mathbf{C_o}$: red airborne receiver; blue ground-based receiver; $\cdot$ $\langle o_{\mathrm{hh}} o_{\mathrm{hv}}^* \rangle$; $\circ$ $\langle o_{\mathrm{hh}} o_{\mathrm{vh}}^* \rangle$; $\times$ $\langle o_{\mathrm{hh}} o_{\mathrm{vv}}^* \rangle$; $+$ $\langle o_{\mathrm{hv}} o_{\mathrm{vh}}^* \rangle$; $*$ $\langle o_{\mathrm{hv}} o_{\mathrm{vv}}^* \rangle$; $\square$ $\langle o_{\mathrm{vh}} o_{\mathrm{vv}}^* \rangle$. Radial axis is in units of decibels; angular axis is in degrees.

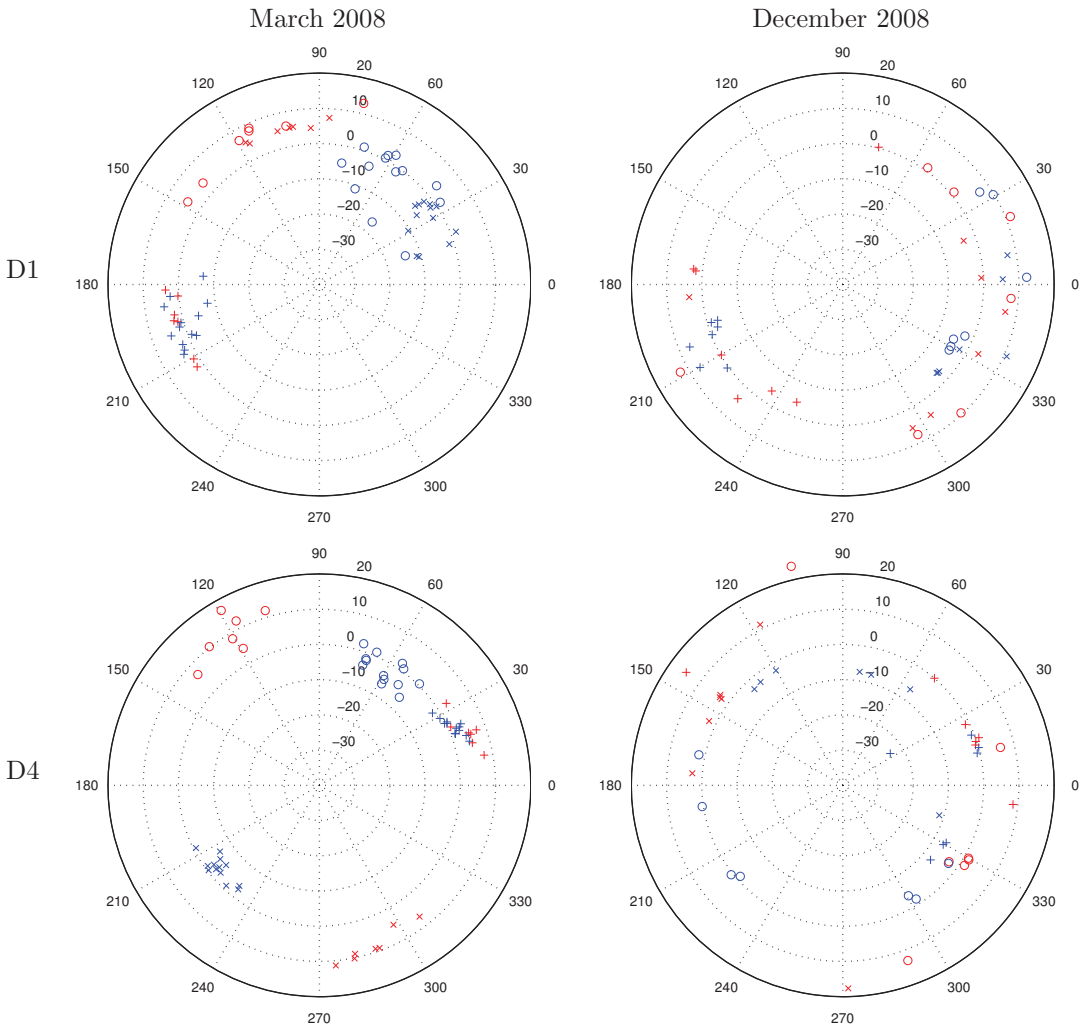

Figure 4.21: Polar plots of observed responses of tilted dihedral targets D1 and D4: ∘ $o_{\mathrm{hh}}/o_{\mathrm{vv}}$; × $o_{\mathrm{hv}}/o_{\mathrm{vv}}$; + $o_{\mathrm{vh}}/o_{\mathrm{vv}}$. Red and blue denote data from airborne and ground-based receivers respectively. Radial axis is in decibels; angular axis is in degrees.

in Figures 4.21 and 4.22: to facilitate comparison, the plots show ratios of the hh, hv and vh measurements to the vv channel measurement. Comparison of these plots with the theoretically expected values shown in Table 4.4 reveals poor agreement (especially in phase), indicating the need for polarimetric calibration. It may be observed, however, that a high degree of variability is present in the data: some possible causes include radar hardware instability, poor image focus quality, differences in target response with changes in radar viewing direction from run-to-run, and multipath interference from ground-bounce returns. Pending detailed investigation, the actual cause is not presently known, but this variability renders the task of precise polarimetric calibration challenging.

For the December 2008 data set, the data from the spotlight-mode SAR imaging collections are supplemented by measurements of the direct-path signal collected with the antennas of the airborne transmitter and ground-based receiver pointing boresight-to-boresight at each other, as depicted in Figure 4.11(b). To collect this data, the ground-based antenna was tilted upwards at an elevation angle of approximately 9.5° above the horizontal, and the airborne radar was flown through the main-lobe of the beampattern while being

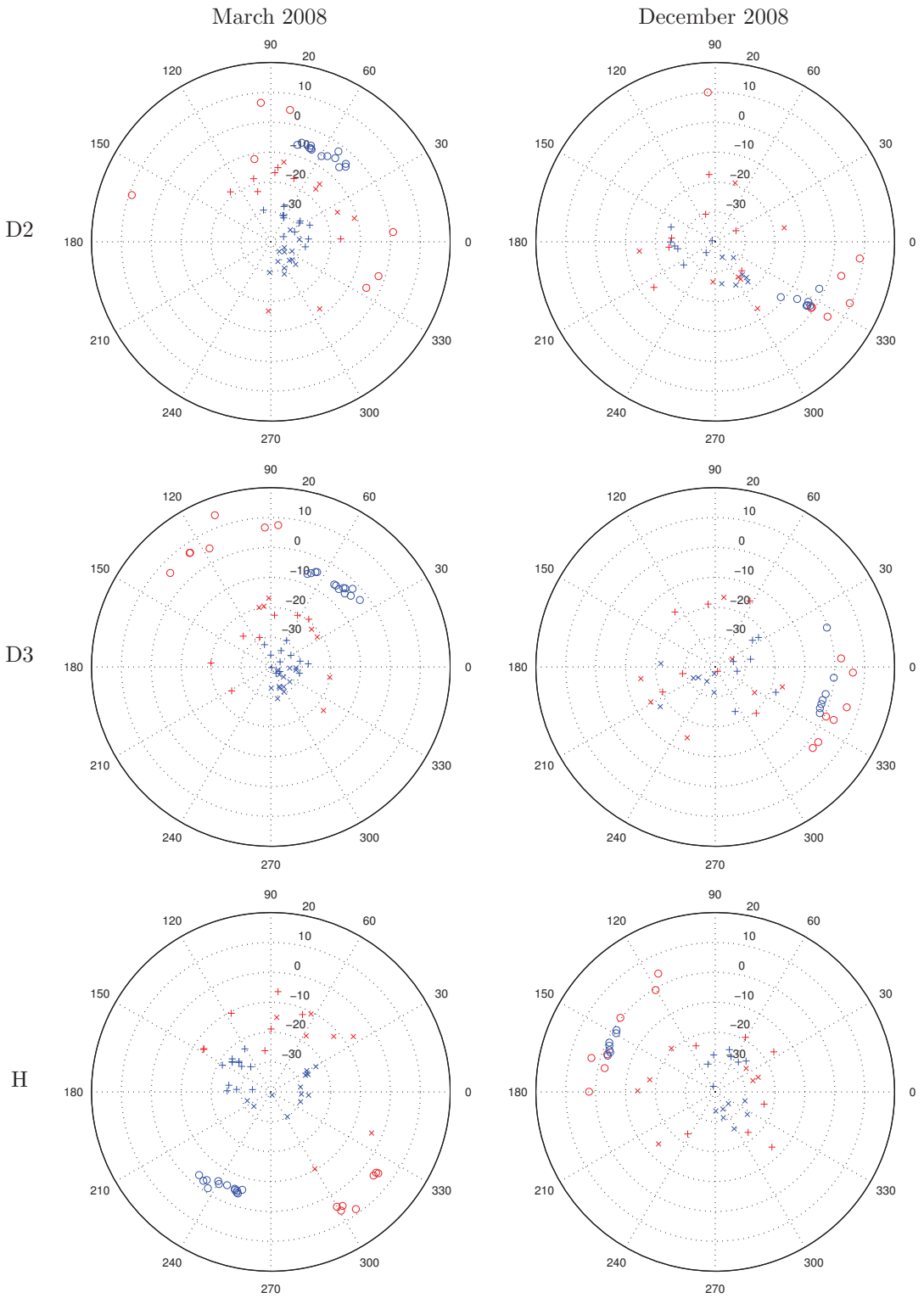

Figure 4.22: Polar plots of observed responses of upright dihedral targets D2 and D3 and hemisphere H: ∘ $o_{\mathrm{hh}}/o_{\mathrm{vv}}$; × $o_{\mathrm{hv}}/o_{\mathrm{vv}}$; + $o_{\mathrm{vh}}/o_{\mathrm{vv}}$. Red and blue denote data from airborne and ground-based receivers respectively. Radial axis is in decibels; angular axis is in degrees.

Table 4.4: Expected ratios of target scattering measurements as derived from **S** matrices in Figure 4.12.

Target	$s_{\mathrm{hh}}/s_{\mathrm{vv}}$	$s_{\mathrm{hv}}/s_{\mathrm{vv}}$	$s_{\mathrm{vh}}/s_{\mathrm{vv}}$
D1	-1	+1	+1
D2	-1	0	0
D3	-1	0	0
D4	-1	-1	-1
H	+1	0	0

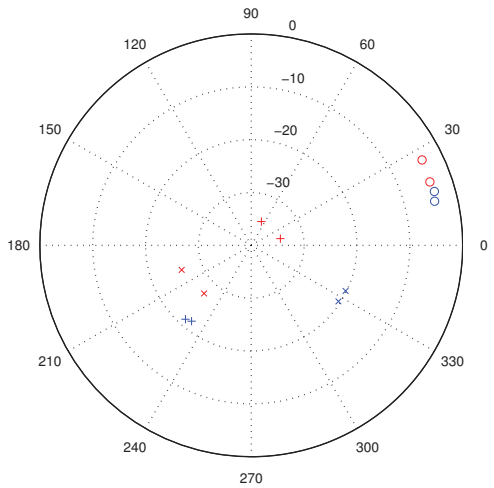

Figure 4.23: Polar plots of direct-path signal measurements from December 2008 data set: red aircraft level; blue aircraft pitched-down; $\circ$ $o_{\mathrm{hh}}/o_{\mathrm{vv}}$; $\times$ $o_{\mathrm{hv}}/o_{\mathrm{vv}}$; $+$ $o_{\mathrm{vh}}/o_{\mathrm{vv}}$. Radial axis is in units of decibels; angular axis is in degrees.

operated to image the site of the ground-based antenna. These direct-path measurements were performed both with the aircraft in level flight, so that the horizontal and vertical polarisation-axes of the two antennas were aligned, and with the nose of the aircraft pitched approximately 7° downwards in a gentle descent, so that a relative rotation was achieved between the antenna axes: the resultant measurements are plotted in Figure 4.23. The signal measured with the aircraft level will have low cross-polarised hv and vh powers, reflecting the polarisation isolation of the bistatic system: from Figure 4.23, these measurements suggest a cross-polarisation isolation of better than 25 dB for the bistatic system. By contrast, the signal measured with the aircraft descending will exhibit a degree of antenna-rotation-induced cross-polarisation: this mimics the behaviour of a cross-polarising target and so allows the estimation of the channel-imbalance parameters k and α as discussed in Section 4.5.

Although such direct-path signal measurements have the anticipated virtues of high signal-to-noise levels and relative freedom from clutter, the collection of these measurements was fraught with practical difficulties, some of which may have reduced their ultimate utility. Generally, these problems were a consequence of the high received signal strength of the direct-path signals, which may be expected from the product in the Frii's transmission equation of the high boresight gains of the transmitting and receiving antennas: the resultant direct-path signal level was significantly higher than the level of the scattered signals received during normal radar operation, and would have easily overloaded the receiver in the absence of special measures. Hence, for the direct-path signal collections, a long stand-off distance between the aircraft and ground-based receiver of almost 32 km was employed to exploit the spherical $1/R^2$ free-space attenuation loss and so reduce the strength of the signal arriving at the receiving antenna. This $1/R^2$ attenuation produced a comparatively modest signal strength reduction (especially when compared to the $1/R^4$ attenuation for radar scattering) so despite the long stand-off distance, the degree of free-space attenuation of the direct-path signal was insufficient to reduce the signal strength to "normal" levels: consequently, an additional 40 dB of attenuation, in the form of discrete RF attenuator components, was temporarily inserted into the receiver hardware for each received polarisation. (An unsuccessful earlier attempt to collect direct-path signal data was also made in March 2008 for which 20 dB attenuators were inserted: unfortunately, these attenuators were left in the receiver during the imaging collections, resulting in a degraded SNR. As a result, all additional attenuators were removed for the imaging collections made in December 2008: the 40 dB attenuators were only inserted for the direct-path signal collections.) For practical reasons, these RF attenuators could only be inserted downstream from the sensitive low-noise amplifier components in the receiver front-end, which, unfortunately, still left them exposed to higher-than-normal signal levels. Thus, unavoidable differences in system hardware and operation exist between the *normal* imaging collections and the *special* direct-path signal collections, which open the undesired possibility that the polarimetric calibration solutions may differ between the two.

Comparison of Figures 4.21 and 4.22 with Figure 4.23 suggests that the wide variability observed in the radar target measurements does not afflict the direct-path signal measurements. However, firm conclusions are hard to draw given the paucity of direct-path signal measurements in this data set. Nevertheless, with this caveat, the apparently greater consistency of the direct-path signal measurements as compared to the target measurements suggests that, if the aforementioned problems posed by the high signal strength can be mitigated, the use of the direct-path signal for calibration may be generally expected to produce a more precise and accurate calibration solution than the use of passive calibration targets.

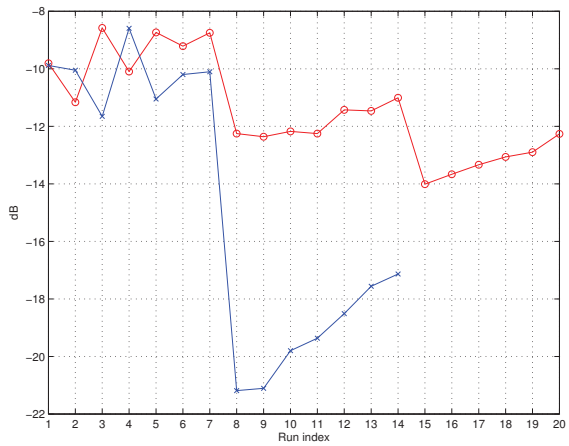

Figure 4.24: Plots of estimated noise powers $N_{22} = N_{33}$: red ∘ March 2008; blue × December 2008. Run indices 1–7 are monostatic data from airborne receiver; indices 8 and above are bistatic data from ground-based receiver.

4.6.2 Results

This section presents results from an analysis of the calibration data sets for the purpose of obtaining calibration solutions. Each calibration solution comprises a set of canonical values of the cross-talk ratios u, v, w, z and channel-imbalance ratios α and k, intended for subsequent use to polarimetrically calibrate data collected by the *Ingara* system. First the estimation of the cross-talk ratios is discussed, then the estimation of the α and k channel-imbalance parameters is covered, and finally the results of applying the calibration solutions obtained are shown.

To estimate the cross-talk ratios, the various covariance matrices $\mathbf{C}$ from each of the collection runs were used as input to the previously discussed hybrid Az/Ka algorithm with iterative noise-estimation (see Section 4.4.6) with the noise power ratio m set to unity: the resultant estimates of the noise powers are shown in Figure 4.24. As the input covariance matrices to the algorithms $\mathbf{C}$ were normalised by the mean hh and vv powers, these noise estimates have effectively been normalised by the same factors and may thus be interpreted as noise-to-signal levels, i.e. the reciprocal of the signal-to-noise (SNR) levels. In the data from both March and December 2008, differences in the noise levels are seen between the data collected by the airborne and ground-based receivers, with a higher noise level present in the monostatic data than in the bistatic. Possible explanations for this are the different stand-off distances from the scene and the different main-lobe beamwidths of the airborne and ground-based antennas: as the ground-based receiver was closer and had a higher antenna gain, it received more scattered energy and hence has a higher SNR. The plot also shows a noticeable trend of increasing noise power with run index in the bistatic data: this is attributable to the reduction in the received bistatically scattered energy as the grazing angle of the airborne transmitter increased (see Figures 4.13 and 4.18), which concomitantly increased the bistatic angle and lowered the SNR. While similar levels of noise were found in the monostatic data from both March and December 2008, a higher noise level is apparent in the bistatic data from March than from December: this is consistent with an SNR degradation associated with the presence of the discrete 20 dB attenuator components in the RF chain of the ground-based receiver during the March 2008 data collections.

The estimated values of the cross-talk ratios u, v, w and z from the iterative Az/Ka algorithm are shown in Figure 4.25. Generally, the distribution of the values of each cross-talk parameter is widely spread, which is presumably a consequence of the high variability of the co-/cross-polarised covariance terms, $\langle s_{ii} s_{ij}^* \rangle$

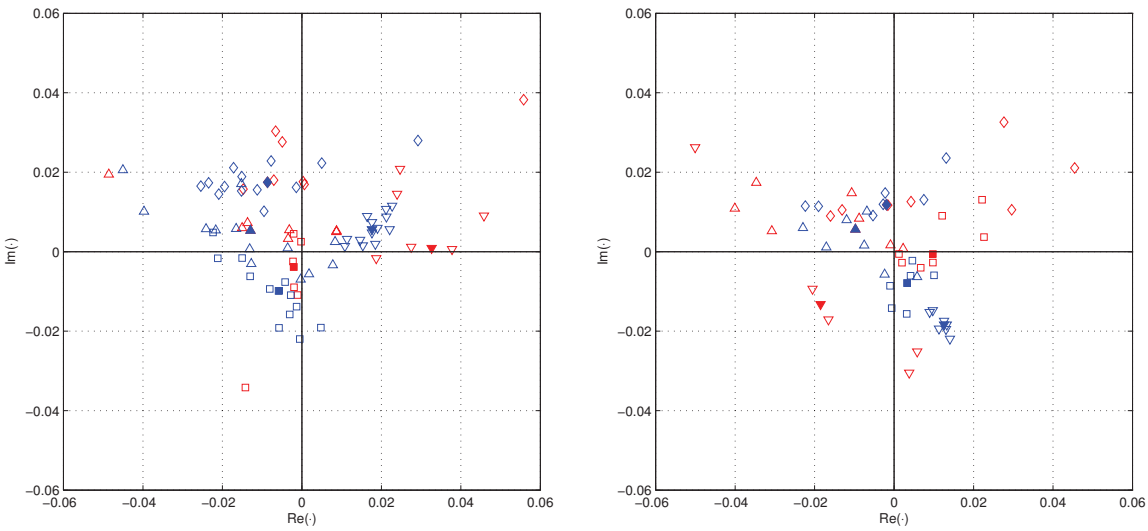

(a) March 2008 (b) December 2008

Figure 4.25: Plots of cross-talk ratios u, v, w and z as estimated by the Az algorithm from the noise-compensated covariance matrix $\mathbf{C}$. Unfilled markers represent estimates obtained from data collected by airborne and ground-based receivers in various data-collection runs: red airborne receiver; blue ground-based receiver; $\square$ u; $\Diamond$ v; $\bigtriangledown$ w; $\bigtriangleup$ z. Filled markers indicate canonical values used for calibration.

and $\langle s_{ii} s_{ji}^* \rangle$ where $i \neq j$, in the covariance matrices. However, there is a suspicious concordance of the estimated cross-talk values between the airborne and ground-based systems, which is presumably reflective of the observed concordance between the co-/cross-polarised covariances previously noted in Section 4.6.1: as discussed there, a possible explanation for this is the invalidity of the assumption of uncorrelated co-/cross-polarised scattering from the distributed target. Although this undermines the present effort at cross-talk calibration which relies on this assumption, we shall persist in the present exercise of determining canonical cross-talk values for polarimetric calibration. This may be justified by considering the variability in the data and the small magnitude of the cross-talk estimates, which indicates that cross-talk does not pose a limiting factor in the practical use of the data.

In Figure 4.25, the estimates for u and w from the ground-based receiver data appear comparatively tightly clustered, especially in the December 2008 data set: as u and w describe the cross-talk characteristics of the receiver (cf. equation (4.9)), this suggests a relatively high stability of the receiver characteristics. Such stability would be consistent with the fixed antenna and stationary position of the ground-based receiver, which is in contrast to the continually steered antenna and subjection to constant motion and vibration of the airborne system. Interestingly, the scatter in u and w also appears to be wider in the March data set and narrower in the December data set, which is consistent with the lower SNR of the March data due to the 20 dB attenuators. On a more general note, since the ratios v and z describe the cross-talk in the transmitter while u and w describe the cross-talk in the receiver, the parameters v and z may each be expected to have *common* values in the monostatic and bistatic data since both were collected using the *same* transmitter, while the parameters u and w may each be expected to have *distinct* values in the monostatic and bistatic data since each was collected with a *different* receiver. While the plotted data may be broadly consistent with this expected behaviour, the wide spread and paucity of data points renders the drawing of firm conclusions difficult. Nevertheless, we will proceed in deriving canonical values for the cross-talk ratios $u^{(\mathrm{air})}$, $v^{(\mathrm{air})}$, $w^{(\mathrm{air})}$, $z^{(\mathrm{air})}$ and $u^{(\mathrm{gnd})}$, $v^{(\mathrm{gnd})}$, $w^{(\mathrm{gnd})}$, $z^{(\mathrm{gnd})}$ as follows: for each of the parameters v and z, the estimates from the

Table 4.5: Method for choosing canonical values from the data for the polarimetric calibration solution.

Parameter	Monostatic data	Bistatic data
u	$u^{(\mathrm{air})}$ is the median of the estimates of u from the airborne receiver data only	$u^{(\mathrm{gnd})}$ is the median of the estimates of u from the ground-based receiver data only
v	$v^{(\mathrm{air})} = v^{(\mathrm{gnd})}$ is the median of the set of pooled estimates of v from both the airborne and ground-based receivers	
w	$w^{(\mathrm{air})}$ is the median of the estimates of w from the airborne receiver data only	$w^{(\mathrm{gnd})}$ is the median of the estimates of w from the ground-based receiver data only
z	$z^{(\mathrm{air})} = z^{(\mathrm{gnd})}$ is the median of the set of pooled estimates of z from both the airborne and ground-based receivers	
α	$\alpha^{(\mathrm{air})}$ is the median of the pooled estimates of α from terrain and dihedral reflector data from the airborne receiver data only	$\alpha^{(\mathrm{gnd})}$ is the median of the pooled estimates of α from terrain and dihedral reflector data from the ground-based receiver data only
k	$k^{(\mathrm{air})}$ is the median of the pooled estimates of k from dihedral reflector and hemisphere data from the airborne receiver data only	$k^{(\mathrm{gnd})}$ is the median of the pooled estimates of k from dihedral reflector and hemisphere data from the ground-based receiver data only

air and ground data are pooled together and $v^{(\mathrm{air})} = v^{(\mathrm{gnd})}$ and $z^{(\mathrm{air})} = z^{(\mathrm{gnd})}$ are each set to the medians of the pooled estimates while, for each of the parameters u and w, the estimates from the air and ground data are analysed separately and $u^{(\mathrm{air})}$, $u^{(\mathrm{gnd})}$, $w^{(\mathrm{air})}$ and $w^{(\mathrm{gnd})}$ are each set to the medians of the separate sets of air and ground data (see Table 4.5). In general, the 'median' of a set of complex numbers z_i is not defined but, in the present discussion, the term is used to refer to the complex number z whose real and imaginary parts are the respective medians of the real and imaginary parts of the z_i: for analysing this data, the median is used in preference to the mean for its robustness in coping with outliers. The resultant median-derived canonical estimates are displayed as the filled markers in Figure 4.25.

With values for the cross-talk ratios thus obtained, we may now turn to the estimation of the α channel-imbalance parameter. For the present analysis, two sets of estimates of α are available from the data: the first was produced from application of the Az/Ka algorithm to the covariance matrices $\mathbf{C}$ as discussed above, and the second is obtained from measurements of the tilted dihedrals D1 and D4. Figure 4.26 shows these various estimates of α. In both the airborne and ground-based receiver data, the estimates of α produced from the terrain measurements are quite tightly clustered. For the monostatic data, the α estimates from the dihedral reflector measurements are also relatively closely spread and in good agreement with the terrain-derived estimates. By contrast, in the bistatic data, the spread of the α estimates from the dihedral reflectors is wider, with several outliers apparent in the December 2008 data set. This may potentially be attributed to deviations of the reflector scattering response from the expected theoretical monostatic response (ref. Figure 4.12) due to a non-zero bistatic angle and possible misalignment of the reflector main-lobe with the radar look-direction. To obtain canonical values for the calibration solution, the medians of the pooled distribution of the terrain- and dihedral reflector-derived α estimates from the airborne and ground-based receiver data were calculated and assigned as the calibration solution parameters $\alpha^{(\mathrm{air})}$ and $\alpha^{(\mathrm{gnd})}$ (cf. Table 4.5): the resultant values are shown by the filled markers in Figure 4.26.

Having assigned values for u, v, w, z and α in the calibration solution, we now consider the final outstanding polarimetric calibration parameter k. For this analysis, estimates of the channel-imbalance ratio k were obtained from the data as follows: as per the discussion in Section 4.5, $\pm k$ was first calculated from the co-polarised ratios of the hemisphere H and the tilted and upright dihedral corner reflectors D1–D4 using (4.122) and (4.124), then the sign ambiguity was resolved from the co-/cross-polarised ratios from the tilted dihedral targets D1 and D4 via (4.125) and (4.126). The results are shown in Figure 4.27. In both the

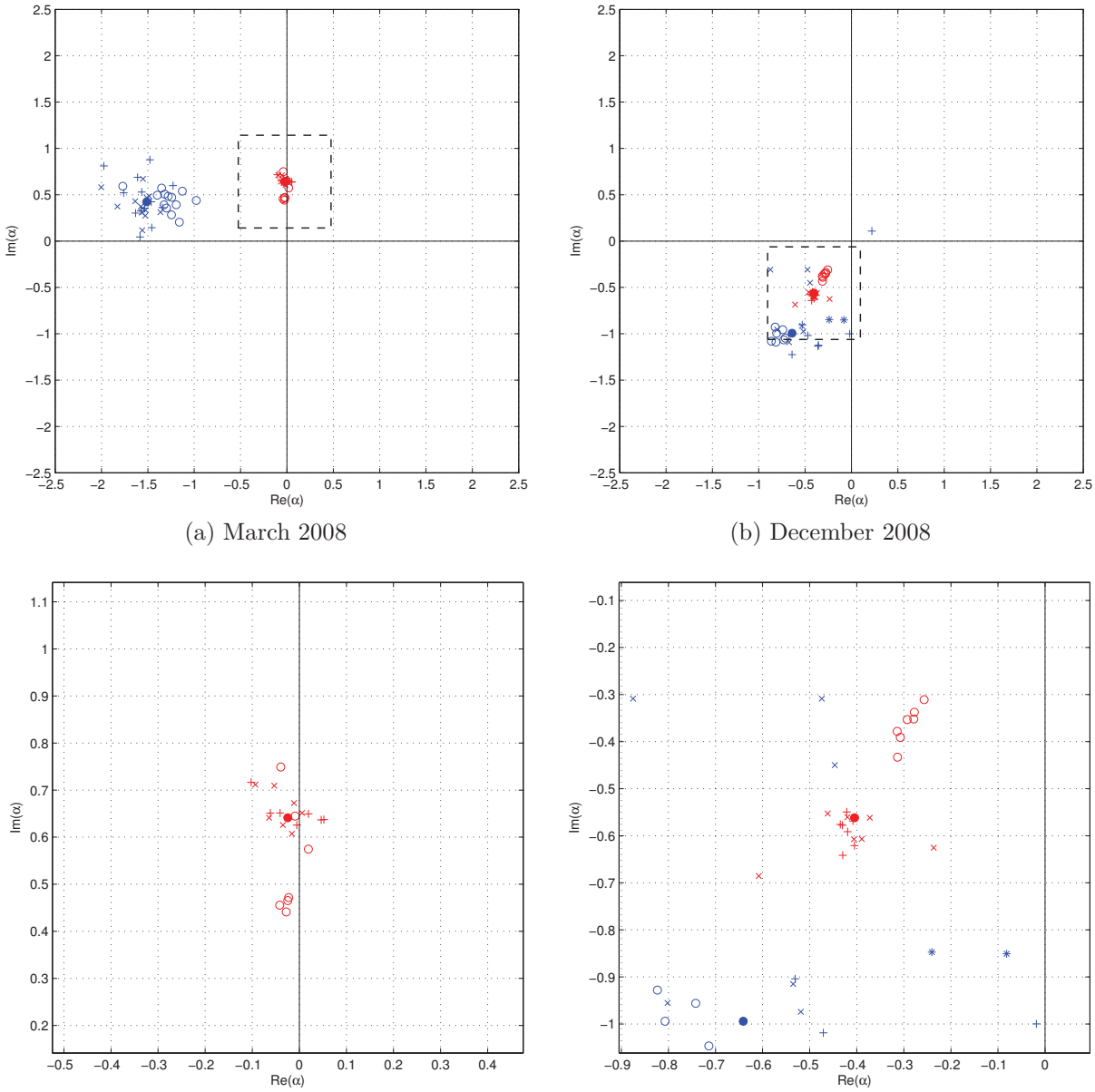

(a) March 2008

(b) December 2008

(c) Enlargement of (a)

(d) Enlargement of (b)

Figure 4.26: Plots of channel-imbalance parameter α as estimated by Az algorithm and measured rotated dihedral responses. Unfilled markers represent estimates obtained from various data-collection runs: red airborne receiver; blue ground-based receiver; $\circ$ Az; $\times$ D1; $+$ D4. Filled markers $\bullet$ denote values used for calibration. Blue $*$ denote estimates from direct-path signal measurements (Dec. 2008 only). For clarity, regions within dashed rectangles in (a) and (b) are shown magnified in (c) and (d).

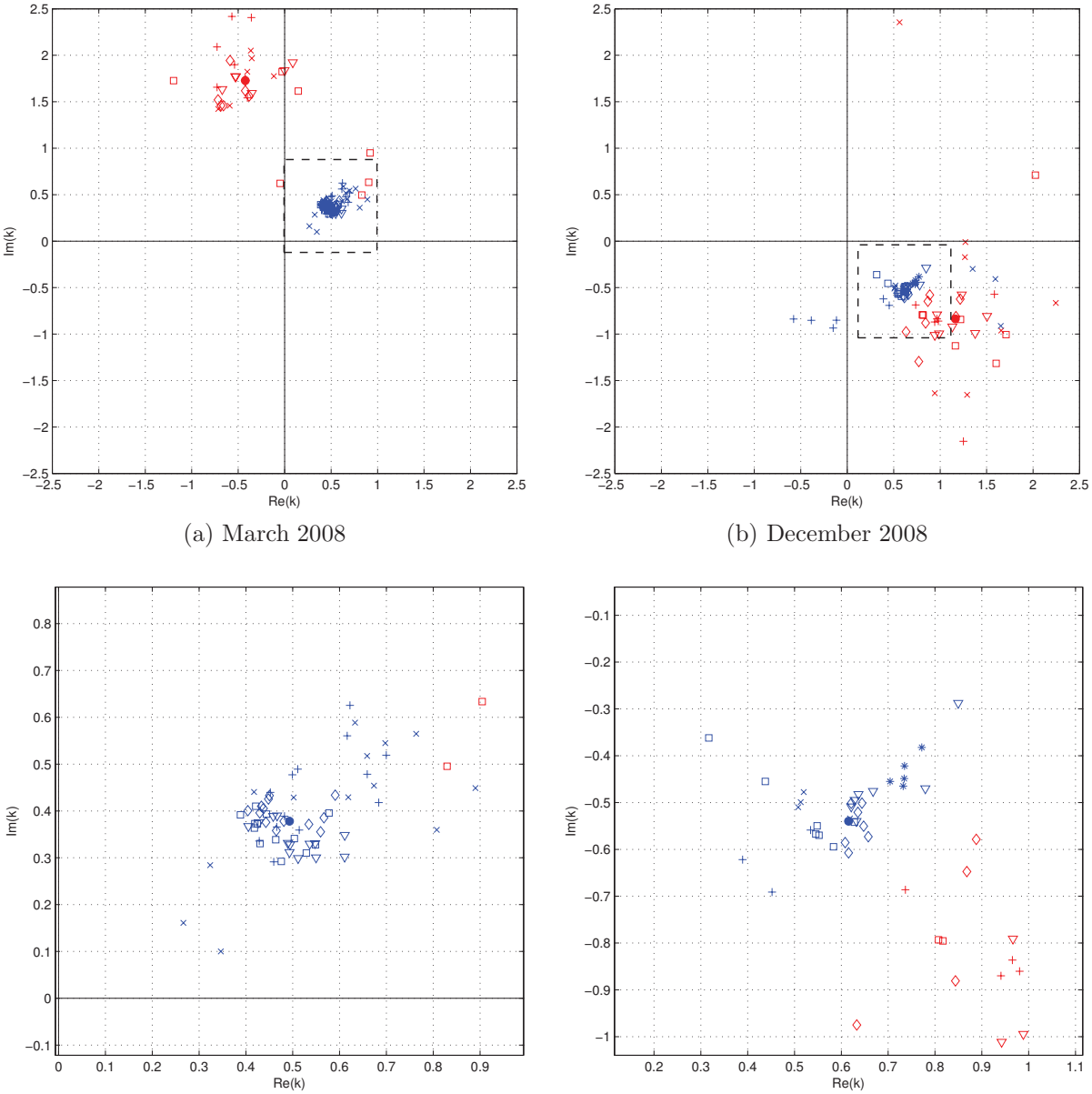

(a) March 2008

(b) December 2008

(c) Enlargement of (a)

(d) Enlargement of (b)

Figure 4.27: Plots of channel-imbalance parameter k as estimated from partially calibrated (after applying u, v, w, z and α corrections) measured responses of various calibration targets. Unfilled markers represent estimates obtained from various data-collection runs: red airborne receiver; blue ground-based receiver; $\times$ D1; $\square$ D2; $\bigtriangledown$ D3; $+$ D4; $\Diamond$ H. Filled markers $\bullet$ denote values used for calibration. Blue $*$ denote estimates from direct-path signal measurements (Dec. 2008 only). For clarity, regions within dashed rectangles in (a) and (b) are shown magnified in (c) and (d).

Table 4.6: Canonical calibration parameters for March and December 2008 data sets.

Parameter	March 2008				December 2008			
	Monostatic		Bistatic		Monostatic		Bistatic	
	$\lvert\cdot\rvert$	$\angle^\circ$	$\lvert\cdot\rvert$	$\angle^\circ$	$\lvert\cdot\rvert$	$\angle^\circ$	$\lvert\cdot\rvert$	$\angle^\circ$
Y	1.0000	0	1.0000	0	1.0000	0	1.0000	0
k	1.7791	103.7833	0.6214	37.4965	1.4328	-35.7122	0.8185	-41.2452
α	0.6419	92.1909	1.5704	164.3190	0.6923	-125.7786	1.1828	-122.8099
u	0.0044	-118.3803	0.0114	-120.3051	0.0098	-3.4389	0.0086	-67.3943
v	0.0195	116.3380	0.0195	116.3380	0.0120	99.1686	0.0120	99.1686
w	0.0326	1.5663	0.0185	17.6099	0.0228	-144.4355	0.0223	-55.5950
z	0.0140	157.7003	0.0140	157.7003	0.0112	150.0395	0.0112	150.0395

March and December 2008 data sets, the k estimates from the airborne receiver data are widely spread with a few extreme outliers apparent. In the March data set, the data points from the D2 upright dihedral reflector are especially widely scattered and in poor agreement with the general distribution of k estimates: this may presumably be attributed to a poor alignment of the scattering boresight direction with the look-direction of the radar. In contrast, the k estimates from the ground-based receiver data are generally more tightly clustered, although outliers are common in the D1 and D4 measurements: these outliers may again be attributed to poor alignment of the boresight scattering direction of these dihedral reflectors with the look direction, and is consistent with the previously observed looser clustering of α values from these targets (ref. Figure 4.26). The reasons for the generally wider scatter (ignoring outliers) of the k estimates in the airborne receiver data compared to the ground-based receiver data are unclear, but may be related to problems which were encountered in the steering of the airborne antenna which resulted in variations of the orientation of the antenna boresight relative to the imaged scene from run to run. For the calibration solution, canonical values of k were obtained from the medians of the pooled k estimates from all the reflectors (ref. Table 4.5): the resultant values are shown as the filled markers in Figure 4.27.

Due to reservations as to the validity of employing the direct-path signal measurements for polarimetric calibration of imaging data, the direct-path signal measurements were analysed separately from the terrain and reflector measurements. Direct-path-signal-derived estimates for α and k were obtained using (4.127), (4.128) and (4.129) by a procedure similar to that employed for the reflector measurements: the resultant estimates are also shown in the December 2008 plots of Figures 4.26 and 4.27. Reassuringly, there is general agreement between the direct-path signal estimates and those from the other methods applied to the ground-based receiver data, however the agreement for the k estimates appears closer than for the α estimates. This may be related to the large difference between the signal levels used for estimating α and k: the α estimates were obtained from the ratio of the cross-polarised hv and vh signals with the transmitting and receiving antennas rotated (i.e. when the aircraft was pitched down) whereas the k estimates are mainly determined by the co-polarised hh and vv signal ratios. Since the amount of antenna rotation which could be achieved by pitching was only $\theta \approx 7^\circ$ and the cross-to-co-polarised signal levels vary as $\tan^2\theta$, a large difference on the order of 18 dB exists between the cross-polarised and co-polarised channel levels which may be sufficient to distort the estimates obtained.

The numerical values of the calibration solutions obtained from the above analysis of the data are tabulated in Table 4.6. In general, different solutions are obtained from the March and December 2008 data sets, which may be attributed to hardware modifications and ageing between the two periods. The results of applying the calibration solutions to the measurements of the various calibration targets are shown in Figures 4.28 and 4.29. To facilitate comparison, the calibrated polarimetric responses have been normalised by the s_{vv}

response and only the ratios $s_{\mathrm{hh}}/s_{\mathrm{vv}}$, $s_{\mathrm{hv}}/s_{\mathrm{vv}}$ and $s_{\mathrm{vh}}/s_{\mathrm{vv}}$ are shown in the plots: for ease of comparison, the expected results are summarised in Table 4.4. In general, the calibrated responses of the targets are in good overall agreement with expectations: for all targets, the distribution of the calibrated $s_{\mathrm{hh}}/s_{\mathrm{vv}}$ ratios are clustered around the expected values at ± 1; similarly, for the tilted dihedrals D1 and D4, the $s_{\mathrm{hv}}/s_{\mathrm{vv}}$ and $s_{\mathrm{vh}}/s_{\mathrm{vv}}$ ratios are in the vicinity of ± 1 as expected; and, for the upright dihedrals D2 and D3, and the hemisphere H, the magnitudes of the cross-polarised $s_{\mathrm{hv}}/s_{\mathrm{vv}}$ and $s_{\mathrm{vh}}/s_{\mathrm{vv}}$ ratios are small compared to that of the co-polarised ratio $s_{\mathrm{hh}}/s_{\mathrm{vv}}$. The phase relationships between $s_{\mathrm{hh}}/s_{\mathrm{vv}}$, $s_{\mathrm{hv}}/s_{\mathrm{vv}}$ and $s_{\mathrm{vh}}/s_{\mathrm{vv}}$ for D1 and D4 are also as expected (the relevant points are clustered around ± 1 with the correct sign): this demonstrates that the sign ambiguity has been correctly resolved when calculating the channel-imbalance ratio k. In some of the plots, occasional outliers are present and a wide spread in the distribution of points is observed for D1 and D4 in the December 2008 data: as previously discussed, these observations are potentially attributable to poor alignment of the reflectors with the radar look-direction. Although a cross-to-co-polarised isolation on the order of 20 dB is obtained for the upright dihedrals D2 and D3, the isolation for the hemisphere H is lower, being only on the order of approximately 10 dB: this effect may be an artefact of the lower RCS of the hemisphere producing a lower signal-to-clutter ratio in the cross-polarised channels.

The effect of polarimetric calibration on the co-/cross-polarised covariances of the distributed target are shown in Figure 4.30. As expected from azimuthal symmetry, the general tendency is for calibration to reduce the magnitude of the measured covariances $\langle o_{ii} o_{ij}^* \rangle$ and $\langle o_{ii} o_{ji}^* \rangle$ with the typical reduction achieved being on the order of 5 dB. However, this reduction is not consistently achieved and *increases* are also occasionally observed in this data set: this is presumably a consequence of the wide variation of the observed co-/cross-polarised covariance values between runs (cf. Figure 4.20) so that a single choice of calibration solution is not equally suited to all the disparate cases.

The effect on the cross-/cross-polarised covariance terms of the polarimetric calibration solution are shown in Figure 4.31. From the principle of reciprocity, the expected effect of calibration is to equalise the hv and vh channel powers and make the $\langle s_{\mathrm{hv}} s_{\mathrm{vh}}^* \rangle$ covariance real-valued. Such a trend is generally observed in the results with the hv and vh channel powers in agreement to within a few decibels and the $s_{\mathrm{hv}} s_{\mathrm{vh}}^*$ angle within a few degrees of zero. However, a weaker tendency of calibration towards scattering reciprocity is observed for the March 2008 data: this is presumably the result of the wider scatter of the terrain- and tilted dihedral-derived estimates of the α parameter (see Figure 4.26) so that the median value used for $\alpha^{(\mathrm{gnd})}$ represents a compromise which is in only fair agreement with the centroid of the terrain-derived α estimates.

4.7 Conclusion

In the earlier part of this chapter, methods for the polarimetric calibration of a field-based bistatic SAR system with an airborne component were theoretically considered. Cross-talk and partial channel-imbalance calibration by means of expected distributed target polarised scattering statistics was investigated by comparing the performance of three distributed target-based algorithms previously reported in the literature by Klein [85], Quegan [86] and Ainsworth et al. [87]. In the absence of noise, although the α channel-imbalance parameter was accurately recovered by all algorithms, large differences in the cross-talk values were found with low accuracy exhibited by the methods of Quegan and Ainsworth et al. The reasons for this are most likely an uncompensated bias in Quegan's estimators (which is accounted for in a modified version of Quegan's algorithm proposed by Lopez-Martinez et al. [204]) and the accommodation of non-zero co-/cross-polarised correlations by the method of Ainsworth et al. (which appears to allow convergence to other spurious solutions)—if zero

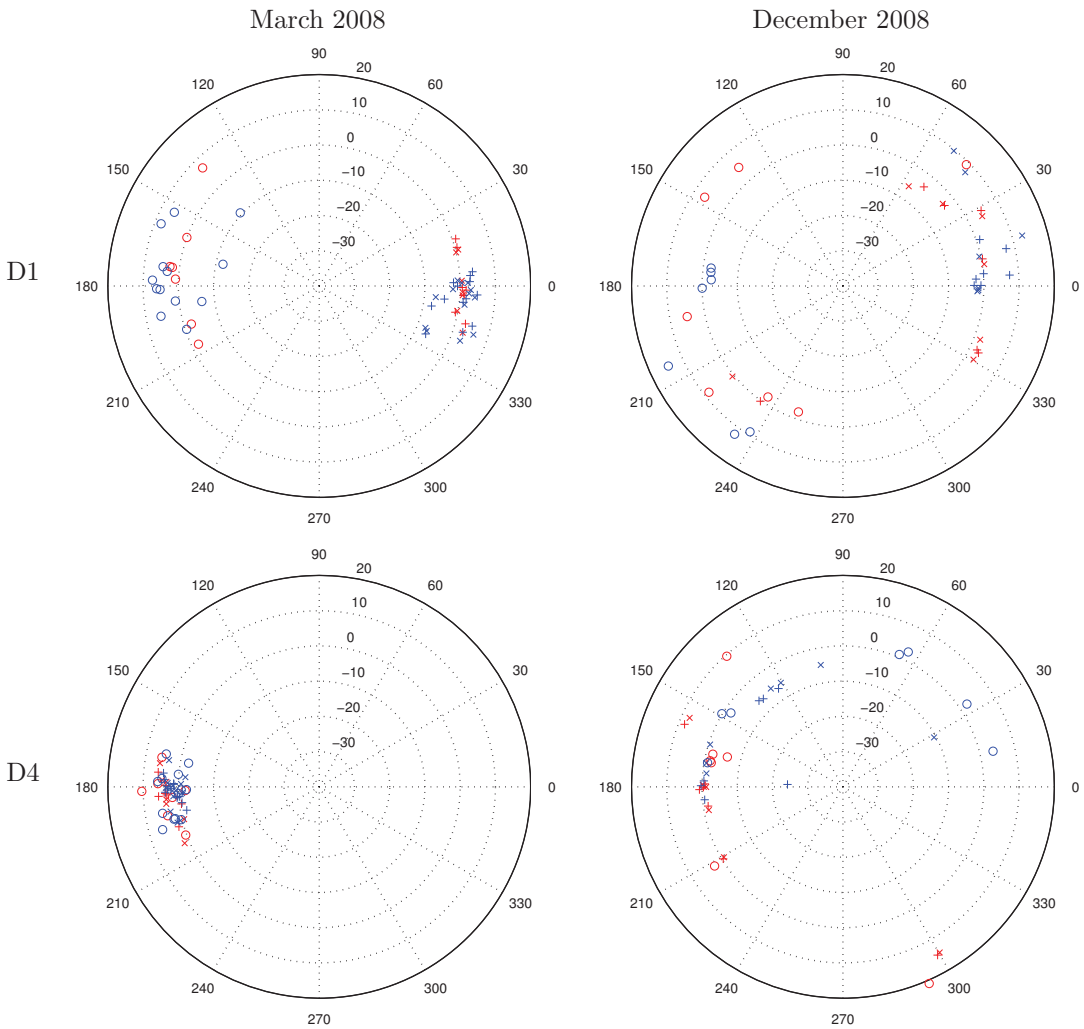

Figure 4.28: Polar plots of calibrated responses for rotated dihedral targets D1 and D4: ∘ $s_{\mathrm{hh}}/s_{\mathrm{vv}}$; × $s_{\mathrm{hv}}/s_{\mathrm{vv}}$; + $s_{\mathrm{vh}}/s_{\mathrm{vv}}$. Red and blue denote data from airborne and ground-based receivers respectively. Radial axis is in decibels; angular axis is in degrees.

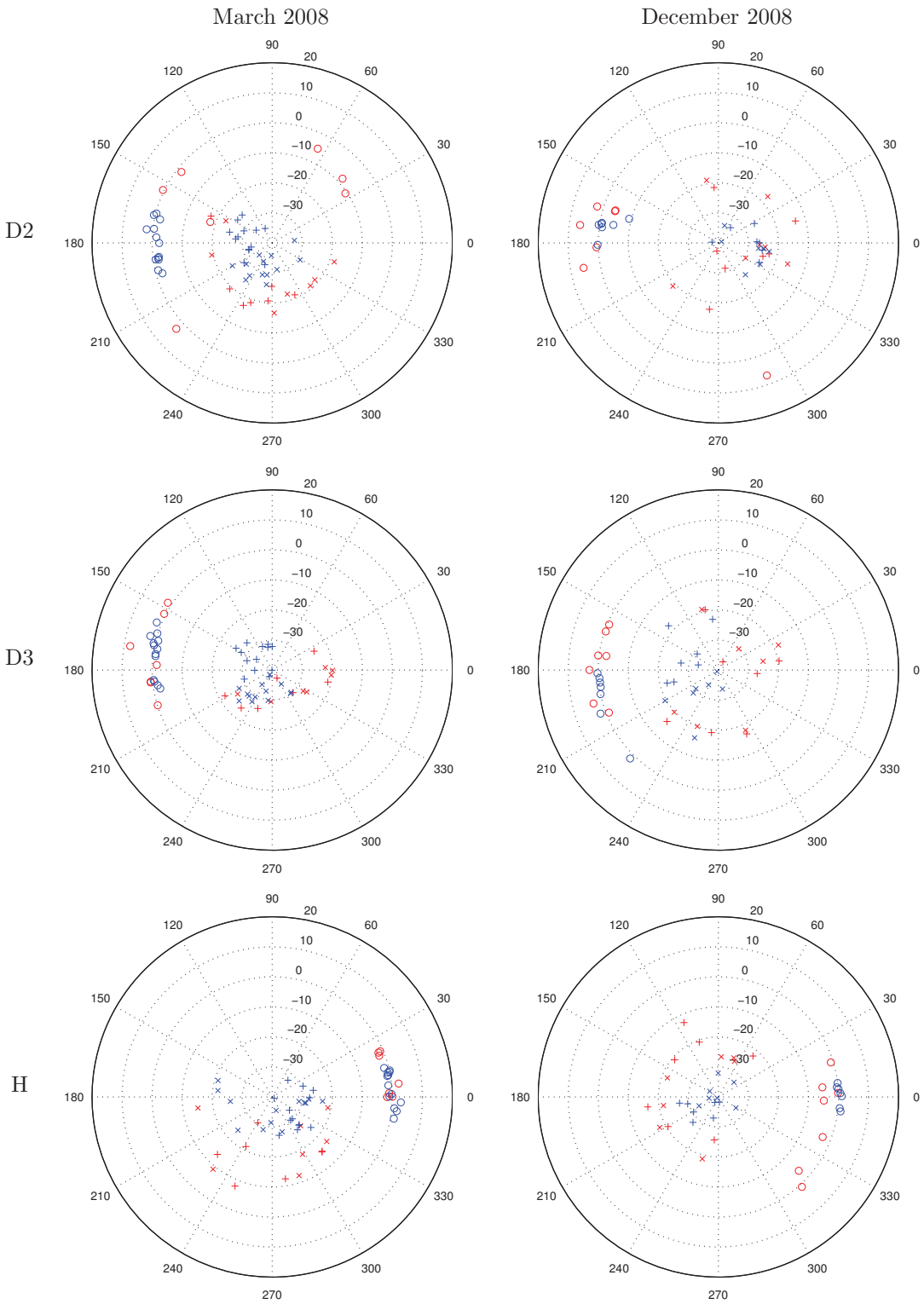

Figure 4.29: Polar plots of calibrated responses for upright dihedral targets D2 and D3 and hemisphere H: ○ $s_{\mathrm{hh}}/s_{\mathrm{vv}}$; × $s_{\mathrm{hv}}/s_{\mathrm{vv}}$; + $s_{\mathrm{vh}}/s_{\mathrm{vv}}$. Red and blue denote data from airborne and ground-based receivers respectively. Radial axis is in decibels; angular axis is in degrees.

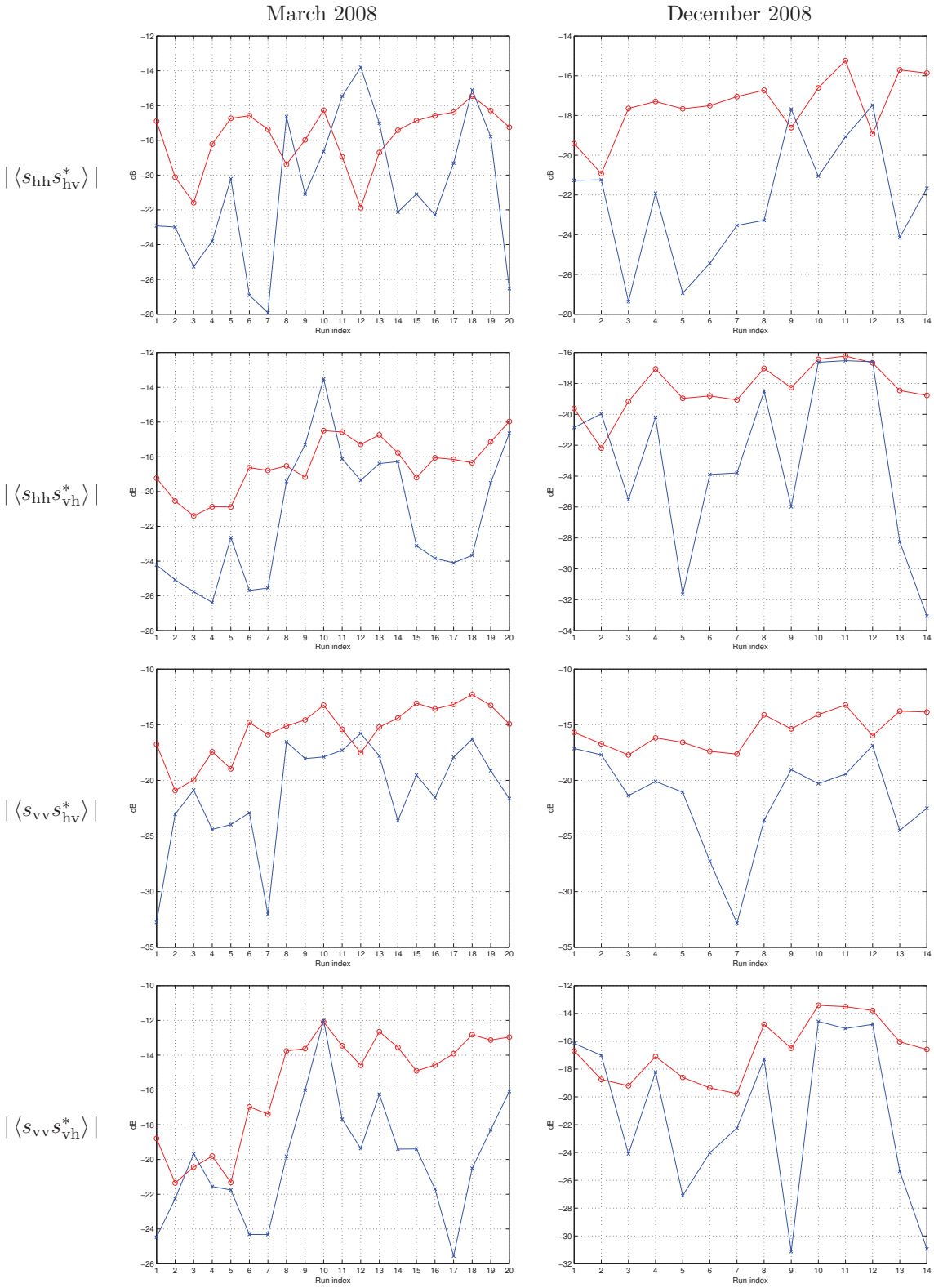

Figure 4.30: Magnitude of ratios of distributed target co-/cross-polarised covariances before and after polarimetric calibration: red ∘ before; blue × after. Run indices 1–7 are from airborne receiver, run indices 8–20 (March) or 8–14 (December) are from ground-based receiver.

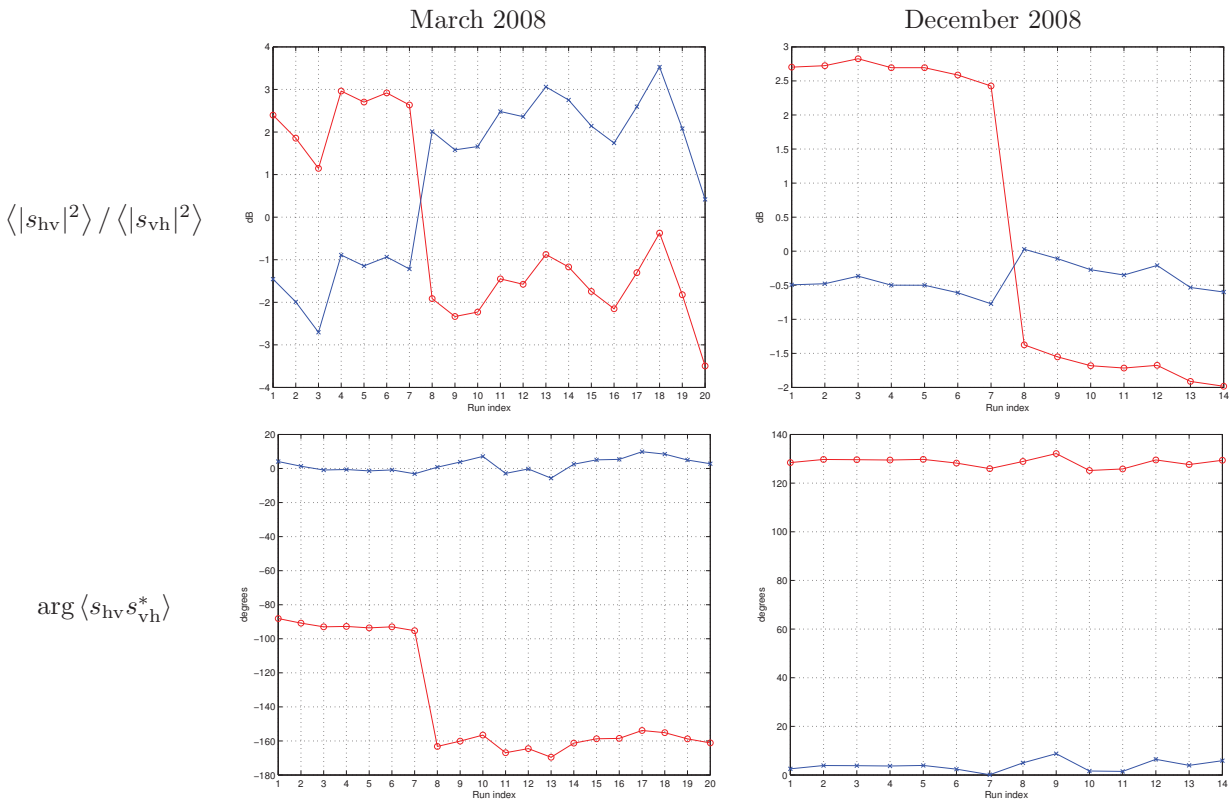

Figure 4.31: Magnitude of ratio of distributed target cross-polarised powers $\langle |s_{\mathrm{hv}}|^2 \rangle / \langle |s_{\mathrm{vh}}|^2 \rangle$, and phase of cross-polarised covariance $\langle s_{\mathrm{hv}} s_{\mathrm{vh}}^* \rangle$ before and after polarimetric calibration: red $\circ$ before; blue $\times$ after. Run indices 1–7 are from airborne receiver, run indices 8–20 (March) or 8–14 (December) are from ground-based receiver.

correlations are enforced, however, superior accuracy in cross-talk recovery is achieved by their method. With noise present, the most accurate recovery of α and the cross-talk were by a minor variant of Klein's algorithm and by the zero-correlation-enforced variant of the method of Ainsworth et al. respectively. From these results, a hybrid approach incorporating the two was proposed for distributed target-based polarimetric calibration which inherently takes account of the noise. A discussion of methods for completing channel-imbalance calibration by means of standard calibration targets and/or the direct-path signal was also presented in this chapter.

The later part of the chapter reported on the calibration of the *Ingara* monostatic and bistatic data sets, which was attempted using measurements of a distributed target, various calibration reflectors and specially collected measurements of the direct-path signal. The proposed hybrid of the distributed target-based polarimetric calibration methods of Klein and Ainsworth et al. was applied to the observed covariance matrix of the distributed target measurements from different collection runs to estimate the cross-talk parameters u, v, w, z and the channel-imbalance parameter α. Further estimates of α were calculated from measurements from different runs of tilted dihedral corner reflectors and the channel-imbalance parameter k was calculated from various calibration reflector measurements also from different collection runs. Independent values for α and k were also independently calculated from various direct-path signal measurements.

Accurate cross-talk calibration was hindered by possible non-zero correlation between co- and cross-polarised scattering from the distributed target. However, system cross-polarisation isolation is likely to be already high: for the bistatic system, the direct-path signal measurements suggest cross-polarisation isolation levels of better than 25 dB. Hence, considering the observed wide variability in the measurements and the small magnitudes of the cross-talk calibration solutions which were obtained, cross-talk calibration will likely not significantly affect system performance.

Calibration parameter estimates from different measurements were generally in fair agreement, albeit with significant outliers possibly attributable to misalignment between the calibration targets and radar antennas. Improved agreement with expectations of the target measurements and covariance matrices was found after calibration, suggesting the general validity of the calibration solutions obtained. However, high variability was observed in the measurements which is unaffected by calibration: this indicates the need for caution in inferring target properties from small numbers of polarimetric measurements.

Chapter 5

Conclusion

This thesis has presented methods for and results from processing fully polarimetric fine-resolution spotlight-mode bistatic (and associated monostatic) SAR data in order to produce fine-resolution SAR imagery and interferograms, and to polarimetrically calibrate the bistatic SAR system. The SAR data set used in this work was collected by the DSTO-built and operated *Ingara* airborne fully polarimetric X-band imaging radar supplemented with a dual-polarised stationary ground-based receiver: the system was operated in a fine-resolution (600 MHz transmitted bandwidth) circular spotlight mode where the airborne system continually circled a scene of interest and illuminated it with its transmitter, while both airborne and ground-based receivers simultaneously received the monostatically and bistatically scattered returns. Other similar experimental bistatic SAR systems have been fielded, e.g. a fully airborne spotlight-mode SAR was reported by Yates et al. [27] while a Canadian bistatic SAR experiment using an airborne radar with a fixed ground-based receiver was reported by Walterscheid et al. [23], but it appears the *Ingara* system is distinct in being fully polarimetric and operating in circular spotlight-mode. Thus, the *Ingara* monostatic and bistatic data set presents a particular mix of processing challenges, which motivated the work reported in this thesis.

5.1 Summary of contributions

The specific problems addressed in this thesis were the processing of spotlight-mode bistatic SAR data into fine-resolution imagery, the formation of interferograms using the bistatic and monostatic SAR data, and the polarimetric calibration of a field-based bistatic SAR where at least one element (the transmitter in the *Ingara* case) is on an airborne platform. The main achievements and conclusions reported in this thesis may be summarised as follows.

- **An exposition of the Polar Format Algorithm (PFA) for spotlight-mode bistatic SAR image formation.** Efficient algorithms for inverting bistatic SAR data into imagery covering extended scenes (i.e. large image swath covering a wide area) are an active area of current research, but an efficient albeit approximate inversion algorithm, the PFA, usually suffices for the small scene sizes imaged in spotlight-mode SAR. The application of the PFA to bistatic SAR processing has already been well expounded by Rigling and Moses [45] and the present work partly draws upon this and other sources. However, the discussion in Chapter 2 of this thesis is potentially unique as it emphasizes a unified framework for understanding the PFA-based processing of the monostatic and bistatic data from the circular-spotlight-SAR-with-stationary-receiver configuration. The detailed mechanics of the

processing are also covered, e.g. the determination of grids for the polar-to-parallelogram (polar-to-rectangular if monostatic) resampling and the implementation of a parallelogram-grid-based Discrete Fourier Transform.

- **The calculation of the size of the focussed region in PFA-processed spotlight-mode stationary-receiver bistatic imagery.** The derivation of the PFA relies on truncating the series expansion of the scatterer phase at the first-order (linear) term in $|\mathbf{R}|$, being the scatterer distance from the scene reference point: the elementary signal from a given scattering centre is thus modelled simply as a plane wave. However, this simple model is only valid for small $|\mathbf{R}|$, i.e. for a small region centred at the scene reference point: as $|\mathbf{R}|$ increases, the contribution from higher-order terms becomes significant and results in increasingly severe geometric distortion and defocussing. Generally, the defocussing effects dominate the distortion effects and severely limit the useful scene size in PFA-processed imagery. Thus, the size of the region which may be processed by the PFA without unacceptable defocussing is of interest. Whereas calculation of this size is relatively straightforward in the monostatic case [39], it is considerably more challenging in the bistatic case. Hence, a significant achievement reported in this thesis is the derivation of expressions for the size of this region, based on restricting the defocussing effect of the second-order phase term, for the specific case of a two-dimensional stationary-receiver bistatic imaging geometry with transmitter, receiver and scatterers all confined to a single common plane. Interestingly, it was found that complicated behaviour is exhibited by the boundaries of this 'good' region in this bistatic case which is not encountered in the monostatic case: in the latter, the region is bounded only by hyperbolas, whereas in the former, the region may be bounded by elliptical, linear or hyperbolic curves depending on the azimuthal separation of the transmitter and receiver and the ratio of the scene-to-transmitter and scene-to-receiver distances.

- **The demonstration of fine-resolution spotlight-mode bistatic SAR imaging with a stationary ground-based receiver.** Successful bistatic SAR imaging requires the maintenance of time and phase synchronisation between the spatially separated transmitter and receiver: inadequate synchronisation results in deterioration of the system impulse response and degraded imaging performance. General measures used for synchronisation include the performance of a synchronisation operation on free-running oscillators just prior to data collection, the use of the GPS 1PPS signal to continually discipline the oscillators, and the employment of high-quality low phase noise oscillators (e.g. Rubidium, Caesium) in the radar hardware (the *Ingara* system uses the GPS 1PPS signal in conjunction with Rubidium oscillators). Imaging performance is also degraded inter alia by deficiencies in motion compensation. Hence, the production of focussed bistatic SAR imagery is an important end-to-end test of the bistatic SAR imaging system as a whole. Also, while a multitude of bistatic SAR imaging experiments have been conducted in recent years involving various combinations of spaceborne, airborne and ground-based transmitters and receivers, relatively few have involved fine-resolution spotlight-mode operation with a ground-based receiver. Hence, the ability to produce focussed fine-resolution imagery with the *Ingara* circular spotlight-mode bistatic SAR data as reported in Chapter 2 is a significant achievement. Furthermore, the azimuthal phase error estimates from the Phase Gradient Algorithm (PGA) presented therein suggest that the effect of phase noise (from drifts in relative phase between the transmit and receive oscillator) in the bistatic data was small and dominated by the motion measurement errors (which commonly afflict airborne SAR data), from which it may be concluded that the use of the GPS 1PPS signal and a Rubidium frequency standard achieves acceptable levels of synchronisation for airborne SAR imaging.

- **The demonstration of interferometric coherence in fine-resolution interferograms from monostatic and bistatic spotlight-mode SAR data.** In the near future, significant contributions to SAR interferometry are expected from the planned deployment of multi-satellite constellations with the capability to collect interferometric data sets in a single-pass: large baselines to give high topographic sensitivity would be achievable while avoiding temporal decorrelation and atmospheric phase screen distortions in repeat-pass data. By its nature, interferometry relies on high levels of coherence between the data sets being interfered, and this coherence is reduced by any dissimilarities in the data sets. Such dissimilarities may arise from differences in the way the data were acquired, e.g. different viewing geometries and/or different hardware characteristics. Hence, such effects may be significant for interferometry using bistatic data: a large bistatic angle may change the scene scattering response, and idiosyncrasies in the distinct hardware of the transmit and receive systems may distort the system impulse response. The interferometric results presented in Chapter 3, which are potentially the first examples in the literature of interferograms formed from simultaneously collected monostatic and bistatic spotlight-mode SAR data, are thus encouraging in showing a moderate coherence between single-pass monostatic-and-bistatic data. This coherence is, however, lower than that observed between repeat-pass monostatic-and-monostatic or repeat-pass bistatic-and-bistatic data, but the reduction is likely attributable to volume decorrelation arising from a large difference in grazing angle between the single-pass monostatic and bistatic data, with a possible further contribution from hardware-induced differential signal distortion.

- **A common mathematical formulation of three distributed-target polarimetric calibration algorithms and a comparison of their accuracy.** Three well-known algorithms for polarimetric calibration using distributed-targets have previously been developed by Klein [85], Quegan [86] and Ainsworth et al. [87]. All employ the statistical characteristics of the backscattering response from extended radar targets but each takes a different approach to the non-linear problem. Hence, a comparison of their relative performance is of interest. Differences in notation between the writings of their respective authors renders comparison difficult, hence an extensive rederivation of the theoretical basis of the algorithms according to their authors' approaches but using common notation is useful: the results of this work were presented in Chapter 4. To investigate the relative performance of the algorithms, a Monte Carlo approach was developed to probe the complicated high-dimensional parameter space, and the results of the numerical simulations were also presented in the same chapter. From the simulation results for the case where no noise is present, all algorithms perform acceptably in estimating a channel imbalance parameter, α, but the methods of Quegan and Ainsworth et al. perform poorly in calculating cross-talk ratios. In the case of Quegan, this is due to bias in the estimators employed [204], while in the case of Ainsworth et al., the cause appears to be an attempt to accommodate non-zero co-/cross-polarised correlations which is made by this algorithm (the other algorithms do not do this). When the uncorrelated-co-/cross-polarisations-assumption is enforced, the approach of Ainsworth et al. achieves superior cross-talk estimation accuracy. With noise present, the method of Ainsworth et al. with the uncorrelated-polarisations-assumption produces the most accurate estimates of cross-talk while a minor variant of the algorithm of Klein estimates the α-parameter most accurately.

- **A hybrid method for distributed-target polarimetric calibration which accounts for noise.** The accuracy of polarimetric calibration is degraded by channel noise. This can be mitigated by estimating the noise power in the various polarisations and correcting the observed channel covariance matrix appropriately. Obtaining estimates of noise power generally requires special effort, e.g. measur-

ing "no-return" signals or applying the method of Freeman [208] for a reciprocal radar. However, from the results of the comparison study of distributed-target polarimetric calibration algorithms by Klein, Quegan and Ainsworth et al. discussed above, a new hybrid algorithm was developed employing minor variants of the methods of Klein and Ainsworth et al. which intrinsically estimates and accounts for noise (Chapter 4).

- **Calibration of a field-based bistatic SAR.** Polarimetric calibration of a radar system is required to correct system-induced polarimetric distortion and infer the true polarimetric scattering characteristics of the measured targets. In the literature, various calibration procedures for laboratory-type instrumentation bistatic radars have been reported: these rely heavily on achieving precise geometric alignment between the radar antennas and any calibration targets used. However, polarimetric calibration of field-based bistatic radars with dynamically moving airborne components for which precise alignment is difficult is not so well addressed. A polarimetric calibration procedure for such a bistatic SAR was presented in Chapter 4: this procedure mainly employs the hybrid distributed-target method alluded to above in conjunction with standard calibration targets (upright and tilted dihedrals and hemisphere/trihedral) imaged in a nearly monostatic geometry and/or measurements of the direct-path signal between the antennas when in boresight-to-boresight alignment.

5.2 Future work

Potential lines for future research to build upon the work reported in this thesis include the following.

- **Assessment of beamforming/backprojection algorithms for image formation.** Beamforming [94] or backprojection [89, 90] algorithms employ computationally intensive but rigorous processing to produce SAR imagery with potentially fewer distortions and artefacts than images formed by the commonly employed fast but approximate algorithms (e.g. the range-Doppler, range-migration, chirp-scaling and polar format algorithms [39, 44, 95]). Traditionally, the beamforming/backprojection approach has been considered unacceptably slow for general application but the recent advent of fast computing hardware (e.g. Graphics Processing Units) and fast backprojection techniques [91–93] may have mitigated this limitation. Hence, it would be of interest to implement and investigate the performance of such algorithms on modern computing hardware.

- **Investigation of the applicability of coherent change detection techniques to interferometric pairs comprising bistatic SAR data.** For maximum versatility, it is desirable that change detection should be able to employ any suitable available SAR images collected at different times, where the set of available SAR images may comprise both monostatic and bistatic data. High coherence in unchanged areas between observations is required for successful change detection, but only a moderate level of coherence was observed between the *Ingara* monostatic and bistatic images. It may thus be of interest to investigate the feasibility of coherent change detection on such moderately correlated monostatic-bistatic image pairs.

- **Application of range resolution enhancement techniques to a monostatic-bistatic data set.** A wider range bandwidth can be obtained by exploiting the wavenumber shift effect and coherently combining SAR data obtained at different grazing angles [56]: this has been demonstrated with multi-pass monostatic data [59, 212]. Temporal decorrelation limits the applicability of this technique to

repeat-pass data but single-pass monostatic and bistatic data sets are free from this. The utility of such monostatic/bistatic pairs for range resolution enhancement is thus worthy of investigation.

- **Investigation of apparent correlation between co- and cross-polarised data.** Standard models of surface scattering predict uncorrelated co- and cross-polarisations [200] but apparent correlation was observed in the *Ingara* data. The reasons for this observation are unclear: possibilities range from systematic measurement errors to idiosyncrasies of the target scattering behaviour. Further investigation to resolve this apparent contradiction may thus be informative.

- **Measurement of polarimetric bistatic clutter characteristics from a wide range of bistatic angles and look directions.** The current data base of bistatic clutter measurements is still relatively sparse, particularly with regard to out-of-plane scattering (when the transmitter, target and receiver are no longer in the same vertical plane). The *Ingara* bistatic data set covers a wide range of imaging geometries and thus has the potential to contribute. Work on the polarimetric calibration of the *Ingara* data has been done (Chapter 4), so a logical progression is to use the calibration solution and obtain calibrated measurements of the clutter polarimetric characteristics as a function of the bistatic geometry.

Appendix A

Resampling in one-dimension

As discussed in Chapter 2, in order to employ the Fast Fourier Transform (FFT) in the Polar Format Algorithm (PFA), it is first necessary to resample the data from a two-dimensional irregular polar grid to a two-dimensional regular rectangular or parallelogram grid. This two-dimensional resampling procedure can be implemented as a series of one-dimensional resampling operations, first along the radial direction of the original polar grid, then along the azimuthal direction (ref. Section 2.5.2). In this appendix, we summarise the theory and implementation of these one-dimensional resampling operations.

A.1 Basic theory

Let $x(t)$ be a bandlimited signal with a bandwidth less than the sampling frequency f_s: by the Nyquist-Shannon Sampling Theorem, the continuous signal $x(t)$ may then be unambiguously reconstructed from the samples $x_n = x(t_n)$, where $t_n = t_0 + n/f_s$ and the index n is an integer, through a weighted sum, viz.

$$x(t) = \sum_{n=-\infty}^{\infty} x_n \operatorname{sinc}[f_s(t - t_n)]. \tag{A.1}$$

Now, in the frequency domain, the signal $x(t)$ is represented by

$$\begin{aligned} X(f) &= \int_{-\infty}^{\infty} \mathrm{d}t \; e^{-j2\pi f t} \, x(t) \\ &= \left(\sum_{n=-\infty}^{\infty} x_n e^{-j2\pi f t_n} \right) \frac{1}{f_s} \operatorname{rect}\left(\frac{f}{f_s}\right). \end{aligned} \tag{A.2}$$

Observe that, on the right-hand-side of (A.2), the first term (comprised of the sum within parentheses) is the Discrete Time Fourier Transform (DTFT) of the sequence x_n.

Suppose we want to resample $x(t)$ at times $t'_m = t'_0 + m/f'_s$ where the index m is an integer: there are two cases to consider, depending on the relation between f'_s and f_s.

- Case 1: $f'_s \geq f_s$. In this case, the new sampling frequency is higher than the original so the resampled signal will not be undersampled. Thus, the required new samples may be obtained from $x'_m = x(t'_m)$.
- Case 2: $f'_s < f_s$. In this case, we are resampling at a lower frequency than before and $x(t)$ may potentially be undersampled: simply using $x(t'_m)$ for the x'_m would then produce aliasing.

To avoid aliasing in the second case, an anti-aliasing bandwidth reduction filter is required before the resampling process: the bandwidth of $x(t)$ must be reduced to no more than f_s' by a suitable low-pass filter to produce the new bandwidth-reduced signal $x'(t)$, whereupon the required alias-free samples can be obtained from $x_m' = x'(t_m')$. Let $H(f)$ be the representation of this filter in the frequency domain: generally, we will set $H(0) = 1$ and choose $|H(f)|$ to have a low-pass response with a flat plateau at low frequencies f such that $|f| < f_s'$ and vanish at high frequencies. The filtered signal in the frequency-domain is then

$$\begin{aligned} X'(f) &= X(f)\, H(f) \\ &= \left(\sum_{n=-\infty}^{\infty} x_n e^{-j2\pi f t_n} \right) \frac{1}{f_s} \operatorname{rect}\left(\frac{f}{f_s}\right) \cdot H(f), \end{aligned} \tag{A.3}$$

and, since the support of $H(f)$ is narrower than that of the rectangular function, this simplifies to

$$X'(f) = \frac{1}{f_s} \left(\sum_{n=-\infty}^{\infty} x_n e^{-j2\pi f t_n} \right) H(f). \tag{A.4}$$

Thus, in the time-domain, we will have

$$\begin{aligned} x'(t) &= \int_{-\infty}^{\infty} \mathrm{d}f\; e^{j2\pi f t}\, X'(f) \\ &= \frac{1}{f_s} \sum_{n=-\infty}^{\infty} x_n h(t - t_n), \end{aligned} \tag{A.5}$$

where $h(t)$ is the inverse Fourier transform of $H(f)$. Equation (A.5) has essentially the same form as (A.1) but with the filter $h(t)$ replacing the $\operatorname{sinc}(\cdot)$ function. The resampled signal is then

$$x_m' = x'(t_m') = \frac{1}{f_s} \sum_{n=-\infty}^{\infty} x_n h(t_m' - t_n). \tag{A.6}$$

A.2 Resampling filter

To carry out the resampling process specified by (A.6), a suitable low-pass filter $h(t)$ must be designed. Various elaborate methods of filter design exist but, for simplicity, we will employ a straightforward method based on a windowed sinc function: the idea behind this method is as follows.

First, observe that, by comparing (A.4) with (A.2), an obvious choice for the filter would be

$$H(f) = \operatorname{rect}\left(\frac{f}{b}\right), \tag{A.7}$$

where b is the filter's passband bandwidth: to avoid aliasing, b should satisfy $b \leq f_s'$. This choice gives

$$h(t) = b \operatorname{sinc}(bt), \tag{A.8}$$

which has infinite support in the time-domain: consequently, the weighted sum of x_n in (A.6) would involve a large number of terms and be computationally intensive to calculate. For computational efficiency, then, it is desirable to restrict the filter's support in the time domain: this may be done by truncating the sinc, e.g. at a specified number of one-sided zero-crossings N_z, so the total width of the truncated filter will be $2N_z/b$.

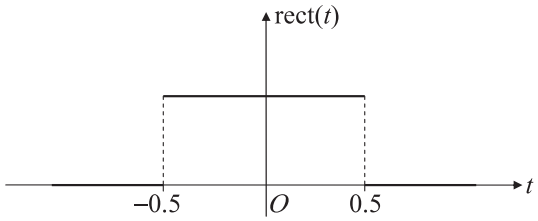

(a) Rectangular function

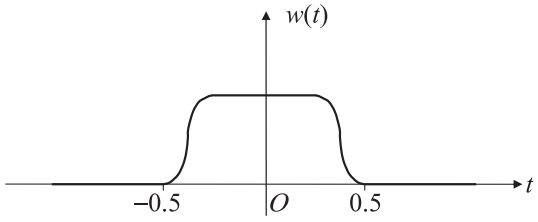

(b) Window function

Figure A.1: Graphs of rect(t) and $w(t)$.

Hence, an expression for the truncated filter in the time domain is

$$h(t) = b\,\mathrm{sinc}(bt) \cdot \mathrm{rect}\left(\frac{t}{2N_z/b}\right), \tag{A.9}$$

in which the support of the sinc function has been limited by multiplication with the rectangular function. However, in the frequency domain, the truncated filter is given by

$$H(f) = \mathrm{rect}\left(\frac{f}{b}\right) * \left(\frac{2N_z}{b}\right) \mathrm{sinc}\left(\frac{2N_z f}{b}\right), \tag{A.10}$$

where $*$ denotes convolution: our original choice of filter is now convolved with a sinc function in the frequency domain, which results in large passband ripples and high stopband side-lobes. These undesirable effects can be mitigated by using a gently tapered window function $w(\cdot)$ instead of the sharp 'on-off' rect$(\cdot)$ in the time-domain. To facilitate comparison, let us define $w(t)$ to have the same support as rect(t), i.e. over t such that $|t| < 1/2$ (see Fig. A.1). With this change, we now have

$$h(t) = b\,\mathrm{sinc}(bt) \cdot w\left(\frac{bt}{2N_z}\right) \tag{A.11}$$

and

$$H(f) = \mathrm{rect}\left(\frac{f}{b}\right) * \left(\frac{2N_z}{b}\right) W\left(\frac{2N_z f}{b}\right), \tag{A.12}$$

where $W(\cdot)$, the Fourier transform of $w(\cdot)$, will have lower side-lobes than the previous sinc. Hence, the function $H(f)$ will now have smaller ripples and side-lobes, but this comes at the expense of a broader transition band: consequently, to reduce aliased energy, it is necessary to reduce b by a bandwidth reduction factor, viz. we would set $b = f_s'/\beta$ for some suitably defined factor $\beta > 1$. For processing the *Ingara* data, the choice made for $w(\cdot)$ was a Blackman window with a width corresponding to $N_z = 8$ one-sided zero crossings of the time-domain sinc function, and the bandwidth reduction factor was set to $\beta = 1.2$.

A.3 Frequency-scaling

Different output sampling frequencies f_s' are required for the various resampling operations which are performed in the PFA. It is thus desirable to be able to modify the resampling filter to accommodate changes in f_s'. As discussed in this section, this can be done by rescaling the frequency axis of the frequency-domain representation of the filter.

Specifically, the problem is as follows. Suppose we are given a low-pass filter with bandwidth B having impulse response $h(t;B)$, i.e. the filter $h(t;B)$ blocks all frequencies f when $|f| > B/2$. We wish to obtain a new low-pass filter $h(t;B')$ with a new bandwidth B' by a suitable stretching (or compression) of the given filter $h(t;B)$ along the t-axis.

The desired new filter $h(t;B')$ may be obtained from $h(t;B)$ as follows. First, let the Fourier transform of $h(t;B)$ be denoted by $H(f;B)$. Then, in the frequency domain, it is easy to see that the new filter $H(f;B')$ can be related to the original filter $H(f;B)$ by a simple frequency-scaling, viz.

$$H(f;B') = H\left(\frac{B}{B'}f;B\right). \tag{A.13}$$

In (A.13), the scaling factor B/B' on the right-hand-side ensures that the old filter 'sees' its cut-off frequency $B/2$ when $|f|$ has the value $B'/2$. By using an inverse Fourier transform on (A.13), it is straightforward to obtain the required relationship between the filters in the time-domain:

$$h(t;B') = \frac{B'}{B}\, h\left(\frac{B'}{B}t;B\right). \tag{A.14}$$

From (A.14), it may be observed that scaling the filter's cut-off frequency results in a reciprocal rescaling of its impulse response width, i.e. if $h(t;B)$ has a impulse-response width of T, then the new filter $h(t;B')$ has a width of TB/B'. Hence, for example, if the new bandwidth B' is higher (or lower) than the original bandwidth B, then the impulse response width of the new filter is narrower (or broader respectively) than that of the original filter.

A.4 Implementation

Recall that in (A.6), in order to avoid aliasing, the filter $h(t)$, which was used to construct the resampled signal x_m' from the original samples x_n, was required to have a bandwidth of no more than f_s', since in this case, the new sampling rate f_s' of the resampled signal was less than the original sampling rate f_s of the original signal. If $f_s' \geq f_s$ however, then an alias-free resampled signal x_m' can still be obtained from (A.6) but now with f_s as the bandwidth of the resampling filter $h(t)$ (this reflects the fact that the sampling rate of the original samples x_n was f_s so, assuming the absence of aliasing, there is no frequency content outside a bandwidth of f_s). By using the $h(t;B)$ notation introduced in the previous section for a low-pass filter with a bandwidth of B, both these cases of $f_s' < f_s$ and $f_s' \geq f_s$ can be incorporated into the single equation

$$x_m' = \frac{1}{f_s}\sum_{n=-\infty}^{\infty} x_n h(t_m' - t_n; f_{s,\min}), \tag{A.15}$$

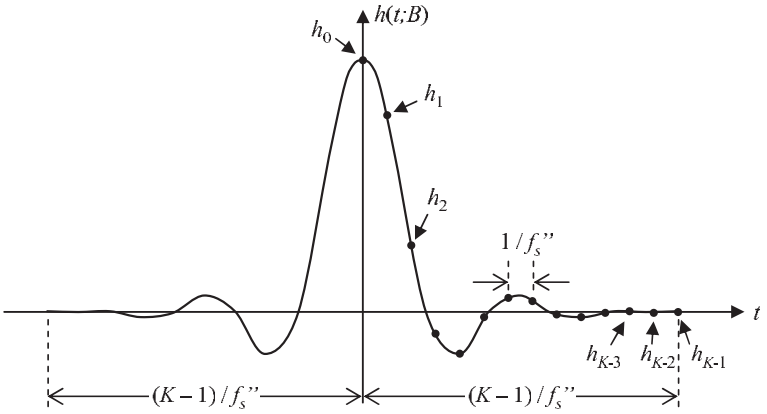

Figure A.2: Representation of filter impulse response $h(t;B)$ (assumed symmetric about $t=0$) by K samples h_k with sampling rate f_s''.

where $h(t;f_{s,\min})$ is a low-pass filter with bandwidth $f_{s,\min}=\min(f_s,f_s')$. If the filter $h(t;f_{s,\min})$ is obtained by frequency-scaling a low-pass filter prototype $h(t;B)$ having bandwidth B, then, from (A.14), we have

$$x_m' = \frac{f_{s,\min}}{Bf_s}\sum_{n=-\infty}^{\infty} x_n h\left(\frac{f_{s,\min}}{B}(t_m'-t_n);B\right). \tag{A.16}$$

In typical Digital Signal Processing (DSP) scenarios, only a discretised version h_k of the continuous-time low-pass filter $h(t;B)$ may be assumed to be available, i.e. $h(t;B)$ may, for example, be the windowed sinc of (A.11) or the product of a careful digital FIR filter design process but, however it is obtained, for DSP purposes it will be specified only by a finite set of discrete samples of its impulse response h_k. If we assume that the filter impulse response $h(t;B)$ is symmetric about $t=0$, i.e. $h(-t;B)=h(t;B)$, it suffices for the h_k to be chosen so as to represent only one symmetric half of the two-sided impulse response (this avoids redundancy as the other half can be easily obtained by reflection). Hence, as shown in Figure A.2, we may choose $t_k''=k/f_s''$, where $k=0,1,\ldots K-1$, to obtain the samples $h_k=h(t_k'';B)$ on the $t\geq 0$ side of the impulse response: with this choice of sampling grid, we will have $h_{-k}=h_k$.

To evaluate the summation in (A.16) with this set of K samples representing the filter, we will have to approximate the values of the quantities $h(f_{s,\min}(t_m'-t_n)/B;B)$ by appropriate values obtained from the supplied set of h_k. If the impulse response is highly oversampled (i.e. f_s'' is very large), then one possible way to efficiently approximate each required value of $h(f_{s,\min}(t_m'-t_n)/B;B)$ from the set of h_k is through a simple nearest-neighbour approach: for a given pair of (m,n) values, the corresponding value of the index k can be determined by setting t_k'' equal to $(t_m'-t_n)f_{s,\min}/B$ and solving for the closest integer value: the result is

$$k=\left[\frac{f_s''}{B}\left(\frac{f_{s,\min}}{f_s'}(m_0'+m)-\frac{f_{s,\min}}{f_s}(n_0+n)\right)\right] \tag{A.17}$$

where $m_0'=f_s't_0'$ and $n_0=f_st_0$,[1] and $[\cdot]$ denotes rounding to the nearest integer. Hence, when evaluating the summation in (A.16), each required value of $h(f_{s,\min}(t_m'-t_n)/B;B)$ is approximated (replaced) by a particular h_k where k is given by (A.17) (recall that $h_{-k}=h_k$).

There are two principal ways to calculate the x_m' using (A.16), namely output-centred convolution and input-centred convolution (when the input sampling times t_n are not evenly distributed, input-centred convo-

[1] As the notation indicates: t_0' is the value of t_m' when $m=0$; t_0 is the value of t_n when $n=0$.

(a) Output-centred convolution

```
for m from 0 to M − 1
   for n from n_lo to n_hi
      Δ := x_n h(f_s,min(t'_m − t_n)/B; B)
      x'_m := x'_m + (f_s,min/B f_s) Δ
   end
end
```

(b) Input-centred convolution

```
for n from 0 to N − 1
   for m from m_lo to m_hi
      Δ := x_n h(f_s,min(t'_m − t_n)/B; B)
      x'_m := x'_m + (f_s,min/B f_s) Δ
   end
end
```

Figure A.3: Illustrative implementations of (A.16) via output- and input-centred convolution (n_{lo}, n_{hi}, m_{lo}, m_{hi} are given in (A.19) to (A.22).)

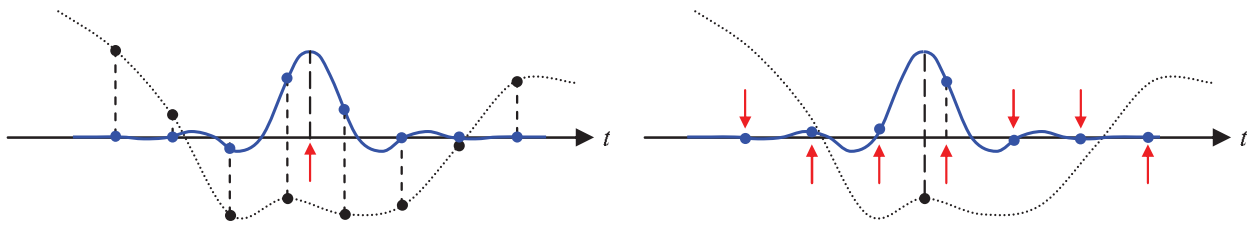

(a) Output-centred convolution (b) Input-centred convolution

Figure A.4: Illustration of output- and input-centred convolution: black dots represent samples of input signal x_n; blue curve (and dots) represent shifted copy of filter impulse response $h(f_{s,\min}(t'_m - t_n)/B; B)$; and red arrows indicate desired grid positions of output samples x'_m.

lution is considered the preferred approach [44]). As indicated by Figure A.3, the difference between output- and input-centred convolution is essentially whether the loop over the index n is nested within the loop over the other index m or vice versa. Hence, in output-centred convolution, for each value of m, the value of the corresponding x'_m is calculated by evaluating the summand for each value of n and accumulating the results (so each x'_m is calculated 'at one go'); while in input-centred convolution, for each value of n, the summand is evaluated for each value of m and each result is added to the appropriate accumulating variable corresponding to x'_m in which the terms of the summation are being accumulated (so the x'_m are calculated by accumulating 'one piece at a time' and their final values are only available at the end of the computation). These processes are further illustrated in Figure A.4: in output-centred convolution (ref. Fig. A.4(a)), for each desired position in the output sampling grid t'_m, a shifted copy of the impulse response (blue curve) is centred at the current output grid position (red arrow) and the current output sample is calculated as a sum of the input samples (black dots) weighted by the corresponding filter value (blue dots); while in input-centred convolution (ref. Fig. A.4(b)), for each input sample position t_n, a shifted copy of the impulse response (blue curve) is centred at the position of the current input sample (black dot), and the individual contributions made by this input sample at the various output grid positions (red arrows) are calculated as the product of this current input sample and the corresponding filter values at these output grid positions (blue dots).

For computational purposes, it is useful to have expressions for the range of indices to sum or loop over, i.e. $n_{\mathrm{lo}}, \ldots, n_{\mathrm{hi}}$ or $m_{\mathrm{lo}}, \ldots, m_{\mathrm{hi}}$ in Figure A.3 (a) and (b) respectively. These can be determined by considering when the term $f_{s,\min}(t'_m - t_n)/B$ lies within the support of the impulse response of the filter (if it lies outside, then $h(f_{s,\min}(t'_m - t_n)/B; B) = 0$ and the summand in (A.16) will make no contribution to x'_m and so need not be included in the summation). Since the impulse response half-width of $h(t; B)$ is $(K-1)/f''_s$ (ref.

Figure A.2), the essential condition is thus

$$\left|\frac{f_{s,\min}}{B}(t'_m - t_n)\right| \leq \frac{K-1}{f''_s}. \tag{A.18}$$

For the case of output-centred convolution, if the set of input samples x_n which must be summed over in (A.16) to calculate a particular x'_m are to be specified by indices n in the range $n_{\mathrm{lo}}, \ldots, n_{\mathrm{hi}}$, then, by substituting $t_n = t_0 + n/f_s$ into (A.18) and solving for n, we find that

$$n_{\mathrm{lo}} = \left\lceil f_s t'_m - \frac{f_s}{f_{s,\min}}\frac{B}{f''_s}(K-1) - f_s t_0 \right\rceil, \tag{A.19}$$

$$n_{\mathrm{hi}} = \left\lfloor f_s t'_m + \frac{f_s}{f_{s,\min}}\frac{B}{f''_s}(K-1) - f_s t_0 \right\rfloor, \tag{A.20}$$

in which $\lceil\cdot\rceil$ and $\lfloor\cdot\rfloor$ denote rounding to the next larger and smaller integers respectively. For input-centred convolution, if the set of output samples x'_m which receive contributions from a particular x_n are to be specified by indices m in the range $m_{\mathrm{lo}}, \ldots, m_{\mathrm{hi}}$, then, by substituting $t'_m = t'_0 + m/f'_s$ into (A.18) and solving for m, we find that

$$m_{\mathrm{lo}} = \left\lceil f'_s t_n - \frac{f'_s}{f_{s,\min}}\frac{B}{f''_s}(K-1) - f'_s t'_0 \right\rceil, \tag{A.21}$$

$$m_{\mathrm{hi}} = \left\lfloor f'_s t_n + \frac{f'_s}{f_{s,\min}}\frac{B}{f''_s}(K-1) - f'_s t'_0 \right\rfloor. \tag{A.22}$$

It may be observed that the resampling method discussed above is based on a straightforward time-domain filtering approach. However, such time-domain filtering is often not as efficient as frequency-domain filtering and the latter approach is generally preferred when feasible. It should thus be mentioned that it is also possible to implement the above resampling procedure through a more sophisticated approach involving polyphase filters which will permit filtering in the frequency-domain. Despite the potential advantages of the polyphase filter technique, however, for the present work, the data was simply processed using time-domain filtering as described above despite its shortcomings, largely on account of its relative ease of implementation.

Appendix B

Program code listings

The PFA-based image formation processor (previously described in Chapter 2) which was used to produce the monostatic and bistatic SAR images for this thesis was implemented in the MATLAB technical computing environment. In this appendix, the manner of implementation of this important SAR data processing functionality is illustrated with demonstrative code listings.

To begin, Section B.1 presents some example code to generate a set of paired monostatic and bistatic synthetic SAR raw echo data which is to be processed into imagery: this block of code serves to precisely illustrate the format and nature of the input data expected by the later processing code. This is followed in Section B.2 by a listing of some illustrative MATLAB code for processing the raw echo data into SAR images: this block of code thus represents an implementation of the PGA-based image formation processor proper. As both blocks of code in Sections B.1 and B.2 invoke various lower-level custom-defined functions in order to produce their results, for completeness, Section B.3 concludes this appendix with code listings of these supporting functions.

B.1 Test-data generation

Some example MATLAB code for producing a synthetic SAR raw echo data set is shown below. The primary result of this code is a pair of MATLAB data structures `T` and `R` containing the raw SAR echo data (and associated auxiliary metadata) from the airborne and ground-based receivers respectively which is to be processed into imagery. While this example code is useful for producing synthetic data to test the image formation processor, it should be stressed that *the main reason for its presentation here is to illustrate in detail the format and nature of the input data* expected by the actual SAR image formation processor code presented in Section B.2: to process a real data set collected by an actual SAR system into imagery, one just needs to package it into an analogous pair of `T` and `R` structures having the same format, then run it through the same image formation processor in the same way.

```
% Define parameters for generating test data.
DEG=pi/180; % Radians per degree.
sysprf=650; % System PRF in quad-polarised mode (Hz).
M=4096; % Number of fast time samples per pulse.
N=1024; % Number of pulses for each polarisation.
acspeed=100; % Speed of aircraft (metres per second).
pulsetimes=(-N:N-1)/sysprf; % Generation times of each pulse (seconds).
P1=6500; % Aircraft slant range (metres).
theta1=80*DEG; % Aircraft incidence angle.
```

```
phi1=0.2+pulsetimes*acspeed/(P1*sin(theta1)); % Aircraft azimuth angles.
P2=3500; % Ground-based Rx slant range (metres).
theta2=88*DEG; % Ground-based Rx incidence angle.
phi2=0; % Ground-based Rx azimuth angle.

% Specify scene centre.
reftgt.pos=[0,0,0].';

% Specify test target positions.
tsttgt.pos=[0,0,0;100,0,0;-100,0,0;0,100,0;0,-100,0].';

% Define radar operating parameters for airborne Rx data.
T.aux.fc=10.1e9; % Centre frequency (Hertz).
T.aux.bw=600e6; % Tx bandwidth (Hertz)
T.aux.pulsew=8e-6; % Pulse length (seconds)
T.aux.samprate=0.5e9; % Sampling rate (samples per second).
T.aux.numsamp=M; % Sampling rate (samples per second).

% Define radar operating parameters for ground-based Rx data.
R.aux.fc=T.aux.fc;
R.aux.bw=T.aux.bw;
R.aux.pulsew=T.aux.pulsew;
R.aux.samprate=T.aux.samprate;
R.aux.numsamp=T.aux.numsamp;

% Generate positions of aircraft at each pulse for each polarisation.
T.aux.rgdpos=cell(1,4); % for HH, HV, VH, VV respectively.
T.aux.rgdpos{1}=P1*[sin(theta1)*[cos(phi1(1:2:end));sin(phi1(1:2:end))];repmat(cos(theta1),1,N)];
T.aux.rgdpos{2}=T.aux.rgdpos{1}; % HH and HV are received simultaneously.
T.aux.rgdpos{3}=P1*[sin(theta1)*[cos(phi1(2:2:end));sin(phi1(2:2:end))];repmat(cos(theta1),1,N)];
T.aux.rgdpos{4}=T.aux.rgdpos{3}; % VH and VV are received simultaneously.

% Generate positions of ground-based Rx at each pulse for each polarisation.
for ch=1:4 % Iterate over polarisations.
  R.aux.rgdpos{ch}=repmat(P2*[sin(theta2)*[cos(phi2);sin(phi2)];cos(theta2)],1,N);
end

% Save pulse generation times of airborne radar for each polarisation.
T.aux.txgotms{1}=pulsetimes(1:2:end);
T.aux.txgotms{2}=T.aux.txgotms{1}; % same Tx'd pulse for HH and HV.
T.aux.txgotms{3}=pulsetimes(2:2:end);
T.aux.txgotms{4}=T.aux.txgotms{3}; % same Tx'd pulse for VH and VV.

% Generate start-of-dechirp and start-of-sampling times for airborne Rx.
% (NB. For airborne Rx data, dechirp times are stored in dechrptms field BUT for
% ground-based Rx, dechirp times are stored in txgotms field.)
for ch=1:4 % Iterate over polarisations.
  trd=txrxdelay(T.aux.rgdpos{ch},T.aux.rgdpos{ch},reftgt.pos); % Tx-scene-Rx delay.
  T.aux.dechrptms{ch}=T.aux.txgotms{ch}+trd;
  T.aux.samplingtms{ch}=T.aux.txgotms{ch}+trd;
end

% Generate start-of-dechirp and start-of-sampling times for ground-based Rx.
for ch=1:4 % Iterate over polarisations.
  trd=txrxdelay(T.aux.rgdpos{ch},R.aux.rgdpos{ch},reftgt.pos); % Tx-scene-Rx delay.
  R.aux.txgotms{ch}=T.aux.txgotms{ch}+trd; % Ground-based Rx dechirp time.
  R.aux.samplingtms{ch}=T.aux.txgotms{ch}+trd;
end

% Generate synthetic echo data.
% (NB. This signal model omits the exp(-i*2*pi*fc*Tdg) term since this would
% be equal to 1 for the Ingara radar: of course it could be included and then
% removed in a signal preprocessing step if total pedantry is required!)
gma=T.aux.bw/T.aux.pulsew; % Chirp rate.
uu=(0:M-1).'/T.aux.samprate; % Fast-time sampling grid.
```

```
T.ech=cell(1,4); % for HH, HV, VH, VV respectively.
R.ech=cell(1,4); % for HH, HV, VH, VV respectively.
for ch=1:4 % Iterate over polarisations.

  % Generate airborne Rx dechirped-on-receive echo data.
  T.ech{ch}=zeros(M,N);
  Tdg=T.aux.dechrptms{ch}-T.aux.txgotms{ch};
  uuu=repmat(uu-T.aux.pulsew/2,1,N)-repmat(T.aux.dechrptms{ch}-T.aux.samplingtms{ch},M,1);
  for ti=1:size(tsttgt.pos,2) % Iterate over targets.
    UU=txrxdelay(T.aux.rgdpos{ch},T.aux.rgdpos{ch},tsttgt.pos(:,ti))-Tdg;
    phs=-2*pi*(T.aux.fc+gma*uuu).*repmat(UU,M,1)+repmat(pi*gma*UU.^2,M,1);
    T.ech{ch}=T.ech{ch}+repmat(abs(UU)<T.aux.pulsew,M,1).*rect((uuu-repmat(UU,M,1)/2)./(T.aux.pulsew-repmat(abs(UU),M,1))).*exp(i*phs);
  end

  % Generate ground-based Rx dechirped-on-receive echo data.
  R.ech{ch}=zeros(M,N);
  Tdg=R.aux.txgotms{ch}-T.aux.txgotms{ch};
  uuu=repmat(uu-R.aux.pulsew/2,1,N)-repmat(R.aux.txgotms{ch}-R.aux.samplingtms{ch},M,1);
  for ti=1:size(tsttgt.pos,2) % Iterate over targets.
    UU=txrxdelay(T.aux.rgdpos{ch},R.aux.rgdpos{ch},tsttgt.pos(:,ti))-Tdg;
    phs=-2*pi*(R.aux.fc+gma*uuu).*repmat(UU,M,1)+repmat(pi*gma*UU.^2,M,1);
    R.ech{ch}=R.ech{ch}+repmat(abs(UU)<R.aux.pulsew,M,1).*rect((uuu-repmat(UU,M,1)/2)./(R.aux.pulsew-repmat(abs(UU),M,1))).*exp(i*phs);
  end
end
```

B.2 Image formation

Once the `T` and `R` input data structures (ref. Section B.1) containing the raw SAR echo data sets to be processed have been created in MATLAB, the following code can be used to carry out the processing of the raw data into imagery. This code thus represents an implementation of the PGA-based image formation processor discussed in Chapter 2.

```
doautofocus=1; % Autofocus flag.
reftgt.pos=zeros(3,1); % Define scene centre.

% Specify image plane tilt.
imgpln=struct('theta',0,'phi',0);

% Make resampling filter.
myresampfilt.filthalfwdth=8;
myresampfilt.K=1024;
myresampfilt.B=myresampfilt.filthalfwdth/(myresampfilt.K-1);
myresampfilt.h=windsinc(myresampfilt.B/1.2,myresampfilt.K);

% Specify window.
myfftwin.type='hamming';
myfftwin.winbroadfac=2;

% ---------------------------------------------------------------------
% Process airborne Rx data.

% Do motion compensation.
for ch=1:length(T.ech) % Iterate over all polarisations.
  % Calc. Tx-spotc-Rx delay.
  trd=txrxdelay(T.aux.rgdpos{ch},T.aux.rgdpos{ch},reftgt.pos);

  % Calc. the dechirp-delay error.
  dechirpdelay=T.aux.dechrptms{ch}-T.aux.txgotms{ch};
  T.aux.dechirpdelayerr{ch}=dechirpdelay-trd;

  % Calc. the sampling-delay error.
  samplingdelay=T.aux.samplingtms{ch}-T.aux.txgotms{ch};
```

```
  T.aux.samplingdelayerr{ch}=samplingdelay-trd;

  % Apply mocomp phase correction.
  T.ech{ch}=mocompstretch(T.ech{ch},T.aux.dechirpdelayerr{ch},T.aux.samplingdelayerr{ch},T.aux);
end

% Perform range-deskew procedure.
ggtmp=T.aux.bw/(T.aux.pulsew*T.aux.samprate.^2);
for ch=1:length(T.ech)
  T.ech{ch}=deskew(T.ech{ch},ggtmp);
end

% Calc. B vector.
for ch=1:length(T.ech)
  T.bvec{ch}=calcbvec(T.aux.rgdpos{ch},T.aux.rgdpos{ch},reftgt.pos);
end

% Calculate parameters for resampling.
Du=inf;Dv=inf;resu=1e-3;resv=1e-3;
T.aux.rsp=calcpfaresampparms(T.bvec,T.aux.dechirpdelayerr, ...
  T.aux.samplingdelayerr,T.aux,Du,Dv,resu,resv, ...
  'FiltHalfWdth',myresampfilt.filthalfwdth,'WinBroadFac', ...
  myfftwin.winbroadfac,'ImgPln',imgpln);

% Resample from polar to parallelogram grid.
for ch=1:length(T.ech)
  T.ech{ch}=pfaresample(T.ech{ch},T.aux.rsp{ch},'filter',myresampfilt.h,'bandwidth',myresampfilt.B,'DrawWaitBar',0);
end

% Calc. image formation parameters.
T.aux.ifp=calcimgformparm(T.bvec,T.aux.rsp,T.aux.rgdpos,T.aux.rgdpos);
T.kvmax=T.aux.rsp{1}.kv0+T.aux.rsp{1}.dkv*(T.aux.rsp{1}.kvnum-1);
T.kvmin=T.aux.rsp{1}.kv0;
T.kumin=T.aux.rsp{1}.ku0+T.aux.rsp{1}.dkv*floor(T.aux.rsp{1}.kvnum/2)*cot(T.aux.rsp{1}.alpha);
T.kumax=T.kumin+T.aux.rsp{1}.dku*(T.aux.rsp{1}.kunum-1);

% Compute auto-focus solution.
subimglimits=[1/3,2/3]; % Use middle third of image for PGA.
ch=1; % Use this polarisation channel for PGA.
subimglimitsidx=round(subimglimits*T.aux.rsp{ch}.kunum)+1;
% Adjust so it fits in range 1..kunum.
subimglimitsidx=max([1,1;subimglimitsidx]);
subimglimitsidx=min([T.aux.rsp{ch}.kunum,T.aux.rsp{ch}.kunum;subimglimitsidx]);

% Extract sub-set of range-compressed data.
subimg=fftshift(fft(T.ech{ch}),1); % Range-compress data.
subimg=subimg((subimglimitsidx(1):subimglimitsidx(2)),:); % Extract.

if doautofocus
  estphserr=pga(subimg,'ShowProgress',1,'PhsErrTol',0.1,'rbthresh',-5,'maxiter',9,'fixedwinwidth',0.1);
else
  estphserr=zeros(1,size(T.ech{ch},2));
end
clear subimg

% Apply estimated phase error to data.
T.img=cell(1,length(T.ech));
for ch=1:length(T.ech)
  phsterm=exp(-i*estphserr);
  T.img{ch}=mrtimes(T.ech{ch},phsterm);
end

% Form images.
echsize=[T.aux.rsp{ch}.kunum,T.aux.rsp{ch}.kvnum];
myfftwin.wrow=windowf(myfftwin.type,[1,echsize(2)],'Normalise',1);
```

```
myfftwin.wcol=windowf(myfftwin.type,[echsize(1),1],'Normalise',1);
fftsize=2.^ceil(log2(echsize)); % Find next higher power of 2.
%  fftsize=max([fftsize;1024,1024]);
dku=(T.kumax-T.kumin)/(T.aux.rsp{ch}.kunum-1);
dkv=(T.kvmax-T.kvmin)/(T.aux.rsp{ch}.kvnum-1);
if T.aux.rsp{ch}.alpha==pi/2
  tanAalpha=inf;
else
  tanAalpha=tan(T.aux.rsp{ch}.alpha);
end
for ch=1:length(T.img)
  T.img{ch}=pgfft(mrctimes(T.img{ch},(myfftwin.wrow),(myfftwin.wcol)),dkv/(dku*tanAalpha),fftsize(1),fftsize(2));
end

% Calc. image parameters.
T.vmin=-floor(fftsize(2)/2)*2*pi/(fftsize(2)*dkv);
T.vmax=(ceil(fftsize(2)/2)-1)*2*pi/(fftsize(2)*dkv);
T.vnum=fftsize(2);
T.umin=-floor(fftsize(1)/2)*2*pi/(fftsize(1)*dku);
T.umax=(ceil(fftsize(1)/2)-1)*2*pi/(fftsize(1)*dku);
T.unum=fftsize(1);
T.estphserr=estphserr;

% ----------------------------------------------------------------------
% Process ground-based Rx data.

% Do motion compensation.
for ch=1:length(R.ech) % Iterate over all polarisations.
  % Calc. Tx-spotc-Rx delay.
  trd=txrxdelay(T.aux.rgdpos{ch},R.aux.rgdpos{ch},reftgt.pos);

  % Calc. the dechirp-delay error.
  dechirpdelay=R.aux.txgotms{ch}-T.aux.txgotms{ch};
  R.aux.dechirpdelayerr{ch}=dechirpdelay-trd;

  % Calc. the sampling-delay error.
  samplingdelay=R.aux.samplingtms{ch}-T.aux.txgotms{ch};
  R.aux.samplingdelayerr{ch}=samplingdelay-trd;

  % Apply mocomp phase correction.
  R.ech{ch}=mocompstretch(R.ech{ch},R.aux.dechirpdelayerr{ch},R.aux.samplingdelayerr{ch},R.aux);
end

% Perform range-deskew procedure.
ggtmp=R.aux.bw/(R.aux.pulsew*R.aux.samprate.^2);
for ch=1:length(R.ech)
  R.ech{ch}=deskew(R.ech{ch},ggtmp);
end

% Calc. B vector.
for ch=1:length(R.ech)
  R.bvec{ch}=calcbvec(T.aux.rgdpos{ch},R.aux.rgdpos{ch},reftgt.pos);
end

% Calculate parameters for resampling.
Du=inf;Dv=inf;resu=1e-3;resv=1e-3;
R.aux.rsp=calcpfaresampparms(R.bvec,R.aux.dechirpdelayerr, ...
  R.aux.samplingdelayerr,R.aux,Du,Dv,resu,resv, ...
  'FiltHalfWdth',myresampfilt.filthalfwdth,'WinBroadFac', ...
  myfftwin.winbroadfac,'ImgPln',imgpln);

% Resample from polar to parallelogram grid.
for ch=1:length(R.ech)
  R.ech{ch}=pfaresample(R.ech{ch},R.aux.rsp{ch},'filter',myresampfilt.h,'bandwidth',myresampfilt.B,'DrawWaitBar',0);
end
```

```
% Calc. image formation parameters.
R.aux.ifp=calcimgformparm(R.bvec,R.aux.rsp,R.aux.rgdpos,R.aux.rgdpos);
R.kvmax=R.aux.rsp{1}.kv0+R.aux.rsp{1}.dkv*(R.aux.rsp{1}.kvnum-1);
R.kvmin=R.aux.rsp{1}.kv0;
R.kumin=R.aux.rsp{1}.ku0+R.aux.rsp{1}.dkv*floor(R.aux.rsp{1}.kvnum/2)*cot(R.aux.rsp{1}.alpha);
R.kumax=R.kumin+R.aux.rsp{1}.dku*(R.aux.rsp{1}.kunum-1);

% Compute auto-focus solution.
subimglimits=[1/3,2/3]; % Use middle third of image for PGA.
ch=1; % Use this polarisation channel for PGA.
subimglimitsidx=round(subimglimits*R.aux.rsp{ch}.kunum)+1;
% Adjust so it fits in range 1..kunum.
subimglimitsidx=max([1,1;subimglimitsidx]);
subimglimitsidx=min([R.aux.rsp{ch}.kunum,R.aux.rsp{ch}.kunum;subimglimitsidx]);

% Extract sub-set of range-compressed data.
subimg=fftshift(fft(R.ech{ch}),1); % Range-compress data.
subimg=subimg((subimglimitsidx(1):subimglimitsidx(2)),:); % Extract.

if doautofocus
  estphserr=pga(subimg,'ShowProgress',1,'PhsErrTol',0.1,'rbthresh',-5,'maxiter',9,'fixedwinwidth',0.1);
else
  estphserr=zeros(1,size(R.ech{ch},2));
end
clear subimg

% Apply estimated phase error to data.
R.img=cell(1,length(R.ech));
for ch=1:length(R.ech)
  phsterm=exp(-i*estphserr);
  R.img{ch}=mrtimes(R.ech{ch},phsterm);
end

% Form images.
echsize=[R.aux.rsp{ch}.kunum,R.aux.rsp{ch}.kvnum];
myfftwin.wrow=windowf(myfftwin.type,[1,echsize(2)],'Normalise',1);
myfftwin.wcol=windowf(myfftwin.type,[echsize(1),1],'Normalise',1);
fftsize=2.^ceil(log2(echsize)); % Find next higher power of 2.
%  fftsize=max([fftsize;1024,1024]);
dku=(R.kumax-R.kumin)/(R.aux.rsp{ch}.kunum-1);
dkv=(R.kvmax-R.kvmin)/(R.aux.rsp{ch}.kvnum-1);
if R.aux.rsp{ch}.alpha==pi/2
  tanAalpha=inf;
else
  tanAalpha=tan(R.aux.rsp{ch}.alpha);
end
for ch=1:length(R.img)
  R.img{ch}=pgfft(mrctimes(R.img{ch},(myfftwin.wrow),(myfftwin.wcol)),dkv/(dku*tanAalpha),fftsize(1),fftsize(2));
end

% Calc. image parameters.
R.vmin=-floor(fftsize(2)/2)*2*pi/(fftsize(2)*dkv);
R.vmax=(ceil(fftsize(2)/2)-1)*2*pi/(fftsize(2)*dkv);
R.vnum=fftsize(2);
R.umin=-floor(fftsize(1)/2)*2*pi/(fftsize(1)*dku);
R.umax=(ceil(fftsize(1)/2)-1)*2*pi/(fftsize(1)*dku);
R.unum=fftsize(1);
R.estphserr=estphserr;
```

B.3 Supporting functions

The various supporting functions invoked by the blocks of code previously presented in Sections B.1 and B.2 are shown below.

```
function b=calcbvec(P1,P2,R0)
%CALCBVEC   Calculate sum of unit vectors pointing towards Tx and Rx.
%   CALCBVEC(P1,P2,R0) sums the unit vectors in the directions of the
%   transmitter and receiver relative to a point at R0. P1 and P2 should
%   both be 3-by-N arrays whose columns are the position vectors of the Tx
%   and Rx in Cartesian coordinates. The resultant vector points along the
%   bisector of the bistatic angle for a scatterer at R0.
%
%   For example,
%      P1=[10;0;0];
%      P2=[0;10;0];
%      B=calcbvec(P1,P2,zeros(3,1));

% Check.
if ~all(isnumeric(P1)) && ~all(isnumeric(P2))
  error('P1 and P2 must be numeric.');
end
if any(size(P1)~=size(P2))
  error('P1 and P2 must be the same size.');
end
if size(P1,1)~=3
  warning('Expecting P1 to be a 3-by-N array.');
end
if size(P2,1)~=3
  warning('Expecting P2 to be a 3-by-N array.');
end
if any(size(R0)~=[3,1])
  warning('Expecting R0 to be a 3-by-1 array.');
end

% Shift origin of P1 and P2 to R0.
P1=P1-repmat(R0,1,size(P1,2));
P2=P2-repmat(R0,1,size(P2,2));

% Calc. lengths of P1 and P2 vectors.
lenP1=sqrt(sum(P1.^2));
lenP2=sqrt(sum(P2.^2));

% Normalise P1 and P2 to unity length.
idx=find(lenP1~=0);
for ii=1:3
  P1(ii,idx)=P1(ii,idx)./lenP1(idx);
end
idx=find(lenP2~=0);
for ii=1:3
  P2(ii,idx)=P2(ii,idx)./lenP2(idx);
end

% Add unit vectors in direction of P1 and P2.
b=zeros(size(P1));
for ii=1:3
  b(ii,:)=P1(ii,:)+P2(ii,:);
end
```

```
function ifp=calcimgformparm(B,rsp,txposatrgd,rxposatrgd)
%CALCIMGFORMPARM   Calc. image formation parameters.
%   CALCIMGFORMPARM(B,RSP,TXPOSATRGD,RXPOSATRGD) returns a structure
%   containing fields describing the image formation geometry.
```

```
% Check that all arguments are either cell arrays or not cell arrays.
allarecell=iscell(B) && iscell(rsp) && iscell(txposatrgd) && iscell(rxposatrgd);
allarenotcell=~iscell(B) && ~iscell(rsp) && ~iscell(txposatrgd) && ~iscell(rxposatrgd);
if ~allarecell && ~allarenotcell
  error('Some but not all input data are cell arrays');
end

% Repackage data as multi-channel.
if allarenotcell
  B={B};
  rsp={rsp};
  txposatrgd={txposatrgd};
  rxposatrgd={rxposatrgd};
end

% Determine number of channels.
numchannels=length(B);
if length(rsp)~=numchannels || length(txposatrgd)~=numchannels || length(rxposatrgd)~=numchannels
  error('All input data should have the same number of channels.');
end

kuc=zeros(1,numchannels);
kvc=zeros(1,numchannels);
txpos=cell(1,numchannels);
rxpos=cell(1,numchannels);
for ch=1:numchannels

  % Calc. centre for Fourier transform.
  tmp=floor(rsp{ch}.kvnum/2)*rsp{ch}.dkv;
  if rsp{ch}.alpha==pi/2
    tangentalpha=inf;
  else
    tangentalpha=tan(rsp{ch}.alpha);
  end
  kuc(ch)=rsp{ch}.ku0+floor(rsp{ch}.kunum/2)*rsp{ch}.dku+tmp/tangentalpha;
  kvc(ch)=rsp{ch}.kv0+tmp;

  % Calc. effective index of this centre.
  angle0=atan2(kvc(ch),kuc(ch));

  % Convert B vectors from ENU to image coords.
  ctN=cos(rsp{ch}.imgpln.theta);
  stN=sin(rsp{ch}.imgpln.theta);
  cfN=cos(rsp{ch}.imgpln.phi);
  sfN=sin(rsp{ch}.imgpln.phi);
  cr=cos(rsp{ch}.lkang);
  sr=sin(rsp{ch}.lkang);
  M=[cfN*cr*ctN-sfN*sr,sfN*cr*ctN+cfN*sr,-cr*stN;-cfN*sr*ctN-sfN*cr,cfN*cr-sfN*sr*ctN,sr*stN;cfN*stN,sfN*stN,ctN];
  B{ch}=M*B{ch};

  % Calc. azimuth angle of B vectors in image (u,v,w) coords.
  angleB=atan2(B{ch}(2,:),B{ch}(1,:));

  % Calc. txpos and rxpos at centre.
  tmp=interp1(angleB,[txposatrgd{ch}.',rxposatrgd{ch}.'],angle0).';
  txpos{ch}=tmp(1:3);
  rxpos{ch}=tmp(4:6);

end

% Fit the slant plane to B vectors in image coords.
[slantplanepsi,slantplaneeta]=findslantplane(B);

% Package up resampling parameters into structure.
```

```
if allarenotcell
  % Return results as non-cell array type.
  ifp.kuc=kuc;
  ifp.kvc=kvc;
  ifp.txpos=txpos{1};
  ifp.rxpos=rxpos{1};
  ifp.slantplanepsi=slantplanepsi;
  ifp.slantplaneeta=slantplaneeta;
else
  ifp=cell(1,numchannels);
  for ch=1:numchannels
    ifp{ch}.kuc=kuc(ch);
    ifp{ch}.kvc=kvc(ch);
    ifp{ch}.txpos=txpos{ch};
    ifp{ch}.rxpos=rxpos{ch};
    ifp{ch}.slantplanepsi=slantplanepsi;
    ifp{ch}.slantplaneeta=slantplaneeta;
  end
end
```

```
function resampparms= ...
  calcpfaresampparms(B,dechirpdelayerr,samplingdelayerr,aux,Du,Dv,rho_u,rho_v,varargin)
%CALCPFARESAMPPARMS   Calc. parms for resamp. PFA data sets to common grid.
%   CALCPFARESAMPPARMS(B,DECHIRPDELAYERR,SAMPLINGDELAYERR,AUX,DU,DV,...
%   RESU,RESV) returns a structure containing the parameters required for
%   resampling onto a common grid using the PFA resampling routine PFARESAMPLE
%   (see HELP PFARESAMPLE). B, DECHIRPDELAYERR, SAMPLINGDELAYERR will usually
%   be cell arrays containing the parameters for each data channel: data
%   from any combination of polarisation, collection run (pass) & receiver
%   (air/ground) may be combined, as long as B{I}, DECHIRPDELAYERR{I} and
%   SAMPLINGDELAYERR{I} refer to the same channel for a specific value of I.
%
%   CALCPFARESAMPPARMS(..., 'PropertyName', 'PropertyValue') allows
%   specifications of various options:
%
%   PropertyName   Description
%   ------------------------------------------------------------------
%   'LookAngle'    Desired look angle (in radians).
%   'FiltHalfWdth' Normalised width of one-sided filter impulse response.
%   'WinBroadFac'  Broadening factor of window to be used for final FFT.
%   'ImgPln'       Image plane tilt and rotation angles: specified as a
%                  structure with fields THETA and PHI.

% Set defaults.
lookangle=[];
filthalfwdth=0;
winbroadfac=1;
imgpln=struct('theta',0,'phi',0);

% Parse varargin.
ii=1;
while ii<=length(varargin)
  switch lower(varargin{ii})
    case 'lookangle'
      ii=ii+1;
      lookangle=lower(varargin{ii});
    case 'filthalfwdth'
      ii=ii+1;
      filthalfwdth=lower(varargin{ii});
    case 'winbroadfac'
      ii=ii+1;
      winbroadfac=lower(varargin{ii});
    case 'imgpln'
```

```
      ii=ii+1;
      imgpln=varargin{ii};
    otherwise
      error('Unknown option %s',varargin{ii});
  end
  ii=ii+1;
end

% Determine if we have multi-channel data; if not, repackage single-channel
% data as multi-channel.
iscellB=iscell(B);
iscelldechirpdelayerr=iscell(dechirpdelayerr);
iscellsamplingdelayerr=iscell(samplingdelayerr);
if ~(iscellB && iscelldechirpdelayerr && iscellsamplingdelayerr) ...
  && (iscellB || iscelldechirpdelayerr || iscellsamplingdelayerr)
  error('B and DECHIRPDELAYERR and SAMPLINGDELAYERR must all be either cell or non-cell arrays.');
end
ismultichannel=iscellB;
if ~ismultichannel
  % Repackage single-channel data into multi-channel format.
  B={B};
  dechirpdelayerr={dechirpdelayerr};
  samplingdelayerr={samplingdelayerr};
end
lengthB=length(B);
lengthdechirpdelayerr=length(dechirpdelayerr);
lengthsamplingdelayerr=length(samplingdelayerr);
if lengthB~=lengthdechirpdelayerr || lengthdechirpdelayerr~=lengthsamplingdelayerr
  error('B and DECHIRPDELAYERR and SAMPLINGDELAYERR must all have same number of channels.');
end
numchannels=lengthB;

% Calculate transformation matrix for conversion from ENU to image-plane coordinates.
ct=cos(imgpln.theta);
st=sin(imgpln.theta);
cf=cos(imgpln.phi);
sf=sin(imgpln.phi);
Ai=[ct*cf,ct*sf,-st;-sf,cf,0;st*cf,st*sf,ct];

% Convert B vectors from ENU to image-plane coordinates.
for ch=1:numchannels
  B{ch}=Ai*B{ch};
end

% Calc. spherical components of B vector.
Blen=cell(1,numchannels);
Btheta=cell(1,numchannels);
Bphi=cell(1,numchannels);
for ch=1:numchannels
  Blen{ch}=sqrt(sum(B{ch}.^2));
  Btheta{ch}=acos(B{ch}(3,:)./Blen{ch});
  Bphi{ch}=unwrap(atan2(B{ch}(2,:),B{ch}(1,:))); % Use unwrap to avoid discontinuities.
end

% Determine range of overlap of azimuth angles.
firstblen=zeros(1,numchannels);
lastblen=zeros(1,numchannels);
firstazi=zeros(1,numchannels);
lastazi=zeros(1,numchannels);
for ch=1:numchannels
  % Extract the first and last azi. angles from each channel.
  firstazi(ch)=Bphi{ch}(1);
  lastazi(ch)=Bphi{ch}(end);
  % Extract the projected lengths of the corresponding B vectors.
  firstblen(ch)=Blen{ch}(1)*sin(Btheta{ch}(1));
```

```
  lastblen(ch)=Blen{ch}(end)*sin(Btheta{ch}(end));
end
[firstoverlapazi,idx1]=max(firstazi);
[lastoverlapazi,idx2]=min(lastazi);

% Calc. azimuth angle reference and offsets.
if isempty(lookangle)
  lookangle=atan2(lastblen(idx2)*sin(lastoverlapazi)+firstblen(idx1)*sin(firstoverlapazi), ...
      lastblen(idx2)*cos(lastoverlapazi)+firstblen(idx1)*cos(firstoverlapazi));
end
Bphid=cell(1,numchannels);
for ch=1:numchannels
  Bphid{ch}=Bphi{ch}-lookangle; % B vector azimuth offset from aperture centre value.
end

% Calc. polar and azimuthal angles of look direction in ENU coordinate-frame.
% (Look direction vector lies in x'-y' plane of image-plane coordinates:
% need to apply inverse of transformation matrix to this vector.)
ca=cos(lookangle);
sa=sin(lookangle);
lkdir=struct('theta',acos(-ca*st),'phi',atan2(ca*ct*sf+sa*cf,ca*ct*cf-sa*sf));

% Calc. useful constants.
C=3e8;
gma=aux.bw/aux.pulsew;
cc1=cell(1,numchannels);
for ch=1:numchannels
  cc1{ch}=2*pi*Blen{ch}.*sin(Btheta{ch})/C;
end

% Determine angle between axes of parallelogram (or rectangular) grid.
tmpalphas=zeros(1,numchannels);
for ch=1:numchannels
  % Project B vector to horizontal (ground) plane and work out req'd angle
  % between axes for parallelogram grid.
  Bproj=[cos(Bphid{ch});sin(Bphid{ch})].*repmat(Blen{ch}.*sin(Btheta{ch}),2,1);
  tmp=Bproj(1,:)/[ones(1,size(Bproj,2));Bproj(2,:)];
  cotalpha=tmp(2);
  tmpalphas(ch)=atan(1/cotalpha);
  if tmpalphas(ch)<0, tmpalphas(ch)=tmpalphas(ch)+pi; end % Adjust alpha into range 0 to pi.
end
alpha=mean(tmpalphas);

% Calc. extent of support of data.
kr0=cell(1,numchannels);
tmpkinns=zeros(1,numchannels);
tmpkouts=zeros(1,numchannels);
tmpklefts=zeros(1,numchannels);
tmpkrights=zeros(1,numchannels);
for ch=1:numchannels
  kc=cc1{ch}*aux.fc;
  Dk=cc1{ch}*gma*aux.pulsew;
  kd=cc1{ch}*gma.*dechirpdelayerr{ch};
  ks=cc1{ch}*gma.*samplingdelayerr{ch};

  % Dechirping-chirp boundaries.
  krinn_d=kc+kd-Dk/2;
  krout_d=krinn_d+Dk;
  if any(krinn_d<0)
    warning('Inner dechirping-chirp boundary calculated as negative.')
  end

  % Sampling-window boundaries.
  krinn_s=kc-Dk/2+ks;
  krout_s=krinn_s+cc1{ch}*gma*(aux.numsamp-1)/aux.samprate;
```

```
  if any(krinn_s<0)
    warning('Inner sampling-window boundary calculated as negative.')
  end

  % Combined boundaries.
  krinn_c=max([krinn_d;krinn_s]);
  krout_c=min([krout_d;krout_s]);

  kr0{ch}=krinn_s;

  tmpkinns(ch)=max(krinn_c.*sin(alpha-Bphid{ch})/sin(alpha));
  tmpkouts(ch)=min(krout_c.*sin(alpha-Bphid{ch})/sin(alpha));
  tmpklefts(ch)=krinn_c(1)*sin(Bphid{ch}(1));
  tmpkrights(ch)=krinn_c(end)*sin(Bphid{ch}(end));
end
kinn=max(tmpkinns);
kout=min(tmpkouts);
kleft=max(tmpklefts);
kright=min(tmpkrights);

Lu=kout-kinn; Lv=kright-kleft; % Calc. available support.

% Calc. resampling parameters ...
% Calc. sampling interval along radial direction.
% Calc. approximate sampling interval along kv direction.
dkr=cell(1,numchannels);
estimatedmaxdkv=zeros(1,numchannels);
for ch=1:numchannels
  dkr{ch}=cc1{ch}*gma/aux.samprate;
  estimatedmaxdkv(ch)=max(diff(kout.*tan(Bphid{ch}))); % Don't use krout_c because of timing-jumps.
end

% Calc. sampling interval in spatial frequency domain.
dku_desired=2*pi/Du;
dkv_desired=2*pi/Dv;

dku_available=-inf;
for ch=1:numchannels
  dku_available=max([dku_available,dkr{ch}.*cos(Bphid{ch})]);
end
dkv_available=max(estimatedmaxdkv);
dku=max([dku_desired,dku_available]);
dkv=max([dkv_desired,dkv_available]);

% Calc. extent of support in spatial frequency domain.
Dku_desired=2*pi/rho_u*winbroadfac;
Dkv_desired=2*pi/rho_v*winbroadfac;
Dku_available=inf;
for ch=1:numchannels
  Dku_available=min([Dku_available,Lu-2*filthalfwdth*max([dku,dkr{ch}*sin(alpha)./sin(alpha-Bphid{ch})])]);
end
Dkv_available=Lv-2*filthalfwdth*max([dkv,estimatedmaxdkv]);
Dku=min([Dku_desired,Dku_available]);
Dkv=min([Dkv_desired,Dkv_available]);

% Calc. number of resampled grid points.
kunum=floor(Dku/dku+1);
kvnum=floor(Dkv/dkv+1);

% Calc. bottom-left corner of resampling grid.
kuc=(kinn+kout)/2;
kv0=-floor(kvnum/2)*dkv; % Ensures that grid centre lies on u-axis.
ku0=kuc-floor(kunum/2)*dku+kv0/tan(alpha);
```

```
% Package up resampling parameters into structure.
if ~ismultichannel
  % If original B and dechirpdelayerr and samplingdelayerr were of non-cell array type, then return
  % results as non-cell array type also.
  resampparms.kr0=kr0{1};
  resampparms.dkr=dkr{1};
  resampparms.phid=Bphid{1};
  resampparms.lkang=lookangle;
  resampparms.ku0=ku0;
  resampparms.kv0=kv0;
  resampparms.dku=dku;
  resampparms.dkv=dkv;
  resampparms.alpha=alpha;
  resampparms.kunum=kunum;
  resampparms.kvnum=kvnum;
  resampparms.imgpln=imgpln;
  resampparms.lkdir=lkdir;
else
  resampparms=cell(1,numchannels);
  for ch=1:numchannels
    resampparms{ch}.kr0=kr0{ch};
    resampparms{ch}.dkr=dkr{ch};
    resampparms{ch}.phid=Bphid{ch};
    resampparms{ch}.lkang=lookangle;
    resampparms{ch}.ku0=ku0;
    resampparms{ch}.kv0=kv0;
    resampparms{ch}.dku=dku;
    resampparms{ch}.dkv=dkv;
    resampparms{ch}.alpha=alpha;
    resampparms{ch}.kunum=kunum;
    resampparms{ch}.kvnum=kvnum;
    resampparms{ch}.imgpln=imgpln;
    resampparms{ch}.lkdir=lkdir;
  end
end
```

```
function Y=deskew(X,G)
%DESKEW   Range deskew data array.
%   DESKEW(X,G) returns the result of applying the range deskew
%   procedure to the columns of the data array X. G should be the
%   value of the chirp rate divided by the square of the sampling
%   frequency.

M=size(X,1);
Y=fft(X,2*M); % NB. Need to double FFT length so that circular shift doesn't
                % shift stuff into the other end!!!
Y=mctimes(Y,exp(-i*pi/(G*(2*M)^2)*([0:M-1,-M:-1].^2).'));
Y=ifft(Y);
Y=Y(1:M,:); % Trim length 2*M values back to just M.
```

```
function [psi,eta]=findslantplane(B)
%FINDSLANTPLANE   Fit plane to B vectors.
%   [PSI,ETA]=FINDSLANTPLANE(B) returns the parameters describing the
%   plane-of-best-fit to the vectors B. The resultant plane has the
%   form
%                Z = X * TAN(PSI) + Y * TAN(ETA).
%
%   The returned values are in units of radians.
%
%   For example,
%      N=2048;psi=5*pi/180;eta=-2*pi/180;
%      phi=[-floor(N/2):ceil(N/2)-1]*0.1/N;
```

```
%      B=[cos(phi);sin(phi);zeros(1,N)];
%      B(3,:)=B(1,:)*tan(psi)+B(2,:)*tan(eta)+randn(1,N)*1e-3;
%      [estpsi,esteta]=findslantplane(B);

% Calc. sums.
if iscell(B)
  Suv=0; Svw=0; Swu=0; Suu=0; Svv=0;
  for ch=1:length(B)
    Suv=Suv+B{ch}(1,:)*B{ch}(2,:).';
    Svw=Svw+B{ch}(2,:)*B{ch}(3,:).';
    Swu=Swu+B{ch}(3,:)*B{ch}(1,:).';
    Suu=Suu+B{ch}(1,:)*B{ch}(1,:).';
    Svv=Svv+B{ch}(2,:)*B{ch}(2,:).';
  end
else
  Suv=B(1,:)*B(2,:).';
  Svw=B(2,:)*B(3,:).';
  Swu=B(3,:)*B(1,:).';
  Suu=B(1,:)*B(1,:).';
  Svv=B(2,:)*B(2,:).';
end

% Calc. tangents.
DD=Suv^2-Suu*Svv;
tanpsi=(Suv*Svw-Svv*Swu)/DD;
taneta=(Suv*Swu-Suu*Svw)/DD;

% Calc. angles.
psi=atan(tanpsi)*180/pi;
eta=atan(taneta)*180/pi;
```

```
function R=mctimes(A,C)
%MCTIMES   Matrix-column multiply.
%   MCTIMES(M,C) returns the element-by-element product of each column of
%   the matrix M with the column vector C.

R=A.*repmat(C,1,size(A,2));
```

```
function ech2=mocompstretch(ech,dechirpdelayerr,samplingdelayerr,parms)
%MOCOMPSTRETCH   Perform range motion compensation on dechirped signal.
%   MOCOMPSTRETCH(ECH,DECHIRP_OFFSET,SAMPLING_OFFSET,PARMS) returns the motion-
%   -compensated dechirped echo data by compensating the phase for dechirp-
%   -delay offsets, while taking the sampling-delay offset into account.
%   ECH is an array containing the complex envelope of the dechirped echo
%   data for a single channel. DECHIRP_OFFSET are the dechirp-delay offsets,
%   being the signed difference (the first minus the second) between the times
%   of generation of the dechirp signals and the times when the scattered
%   signal from the scene centre arrives at the dechirp-mixer. SAMPLING_OFFSET
%   are the signed difference between the times at which the sampled data is
%   beginning to be recorded and the times of arrival at the ADCs of the
%   scattered signal from scene centre. PARMS is a structure containing the
%   fields FC, BW, PULSEW, SAMPRATE.

% Define parms.
gma=parms.bw/parms.pulsew;
dechirpdelayerrsqr=dechirpdelayerr.^2;

% Apply mocomp-phase correction.
[M,N]=size(ech);
ech2=zeros(M,N);
mm=[0:M-1]';
for n=1:N
```

```
  ech2(:,n)=exp(-j*pi*(2*(parms.fc+gma*(mm/parms.samprate ...
    +samplingdelayerr(n)-parms.pulsew/2)).*dechirpdelayerr(n)-gma ...
    *dechirpdelayerrsqr(n))).*ech(:,n);
end
```

```
function R=mrctimes(A,R,C)
%MRCTIMES   Matrix-row-column multiply.
%   MRCTIMES(M,R,C) returns the element-by-element product of the matrix M
%   with the row vector R and the column vector C.

R=A.*repmat(R,size(A,1),1).*repmat(C,1,size(A,2));
```

```
function R=mrtimes(A,R)
%MRTIMES   Matrix-row multiply.
%   MRTIMES(M,R) returns the element-by-element product of each row of the
%   matrix M with the row vector R.

R=A.*repmat(R,size(A,1),1);
```

```
function [smnf,smnw]=pfadoresampling(smn,rsp,bandwidth,filter,varargin)
%PFADORESAMPLING   Resample from polar to rectangular grid.
%   F=PFADORESAMPLING(S,R,B,H) resamples the polar formatted data array S
%   according to the resampling parameters R, using the low-pass filter with
%   (pass and transition) bandwidth B (i.e. the filter rejects frequencies in
%   excess of B/2) and the one-sided impulse response H. R is typically
%   obtained using CALCPFARESAMPPARMS.
%
%   [F,W]=PFADORESAMPLING(...) also returns the intermediate result following
%   radial resampling and corner-turning in W.
%
%   PFADORESAMPLING((..., 'PropertyName', 'PropertyValue') allows
%   specification of various options:
%
%   PropertyName  Description
%   ---------------------------------------------------------------------
%   'DrawWaitBar' Indicate progress with wait bar: 0 or 1*.
%
%   N.B. The functionality of this M-file is duplicated by the MEX-file
%   PFADORESAMPLING_: the latter, being faster, is intended for actual use in
%   signal processing applications; the former is intended merely for testing
%   and verifying the latter.

% Set defaults.
drawwaitbar=1;

% Parse varargin.
ii=1;
while ii<=length(varargin)
  switch lower(varargin{ii})
    case 'drawwaitbar'
      ii=ii+1;
      drawwaitbar=varargin{ii};
    otherwise
      error('Unknown option %s',varargin{ii});
  end
  ii=ii+1;
end

% Determine array size.
[M,N]=size(smn);
```

```
% Allocate working (intermediate) and final arrays.
smnw=zeros(rsp.kunum,N);
smnf=zeros(rsp.kunum,rsp.kvnum);

% Determine filter length.
K=length(filter);

% Radial resample by output-centred convolution.
if drawwaitbar
  h=waitbar(0,'Radial resample');
end
for n=1:N
  fs=1/rsp.dkr(n);
  fsp=sin(rsp.alpha-rsp.phid(n))./(rsp.dku*sin(rsp.alpha));
  p0=fs*rsp.kr0(n);
  ku0axis=rsp.ku0-rsp.kv0/tan(rsp.alpha); % rsp.ku0 offset on ku axis.
  q0=fsp*ku0axis*sin(rsp.alpha)/sin(rsp.alpha-rsp.phid(n));
  fsmin=min([fsp;fs]);
  B=bandwidth;

  % Calc. output sample indices within input data support.
  qlo=ceil(fsp/fs*p0+B*fsp/fsmin*(K-1)-q0);
  qhi=floor(fsp/fs*(p0+M-1)-B*fsp/fsmin*(K-1)-q0);

  % Adjust to fit in range 0 to rsp.kunum-1.
  qlo=max([qlo,0]);
  qhi=min([qhi,rsp.kunum-1]);

  % Warn if no output samples lie within input data support.
  if qlo>=qhi
    warning('Filter too long for data support: %d %d.',qlo,qhi);
  end

  % Calc. scaling constant.
  AA=fsmin/(B*fs);

  % Calc. each output sample value.
  for q=qlo:qhi
    % Calc. range of input samples to sum over.
    plo=ceil((q0+q)/(fsp/fs)-B*(K-1)*fs/fsmin-p0);
    phi=floor((q0+q)/(fsp/fs)+B*(K-1)*fs/fsmin-p0);

    % Adjust to fit within data support.
    plo=max([plo,0]);
    phi=min([phi,M-1]);

    % Convolve input samples with resampling filter.
    plist=plo:phi;
    k=abs(round(((q0+q)/(fsp/fsmin)-(p0+plist)/(fs/fsmin))/B));
    smnw(q+1,n)=AA*filter((k+1))*smn(plist+1,n);

  end
  if drawwaitbar
    waitbar(n/N,h);
  end
end
if drawwaitbar
  close(h);
end

% Corner-turn the working and output buffers to exploit processor cache
% for computational speed.
smnw=smnw.';
smnf=smnf.';
```

```
% Azimuth resample by input-centred convolution.
fsp=sin(rsp.alpha)/rsp.dkv;
q0=fsp*rsp.kv0/sin(rsp.alpha);
if drawwaitbar
  h=waitbar(0,'Azimuth resample...');
end
for m=1:rsp.kunum
  % Calc. initial sample positions along slant lines.
  tp=(ku0axis+rsp.dku*(m-1))*sin(rsp.phid)./sin(rsp.alpha-rsp.phid);

  % Loop over each input sample.
  for p=0:N-1
    % Calc. local sampling frequency.
    if p==0
      fs=1/(tp(2)-tp(1));
    elseif p==N-1
      fs=1/(tp(N)-tp(N-1));
    else
      fs=2/(tp(p+2)-tp(p));
    end

    % Calc. fsmin.
    fsmin=min([fs,fsp]);

    % Calc. range of output sample positions based on current input sample
    % position.
    qlo=ceil(fsp*(tp(p+1)-B*(K-1)/fsmin)-q0);
    qhi=floor(fsp*(tp(p+1)+B*(K-1)/fsmin)-q0);

    % Adjust to fit in suitable range based on first and last input sample
    % positions and first and last requested output sample points.
    qlo=max([qlo,ceil(fsp*(tp(1)+B*(K-1)/fsmin)-q0),0]);
    qhi=min([qhi,floor(fsp*(tp(N)-B*(K-1)/fsmin)-q0),rsp.kvnum-1]);

    % Calc. scaling constant.
    AA=fsmin/(B*fs);

    % Calc. weighted contribution of this input sample to each output
    % sample.
    qlist=(qlo:qhi);
    k=abs(round(fsmin/B*((q0+qlist)/fsp-tp(p+1))));
    %smnf(m,qlist+1)=smnf(m,qlist+1)+AA*smnw(m,p+1)*filter(k+1);
    smnf(qlist+1,m)=smnf(qlist+1,m)+AA*smnw(p+1,m)*filter(k+1).';
  end
  if drawwaitbar
    waitbar(m/rsp.kunum,h);
  end
end
if drawwaitbar
  close(h);
end

% Corner-turn the output buffer back.
smnf=smnf.';
```

```
function [smnf,smnw,smntest]=pfaresample(smn,rsp,varargin)
%PFARESAMPLE   Resample polar format array.
%   PFARESAMPLE(S,RSP) resamples a
%   given M-by-N 2-D polar format array S onto a regular parallelogram
%   grid. Each column of S contains the fast-time samples for a single
%   pulse with fast-time increasing down the rows. RSP is a structure
%   containing the various resampling parameters:
%
%      KR0:   1-by-N vector of radial distance values for samples S(1, J).
```

```
%      DKR:   1-by-N vector of initial radial sampling intervals for each
%             pulse.
%      PHID:  1-by-N vector of azimuth direction angles in radians.
%      KU0:   Scalar value being KU offset of lower-left corner of output
%             grid.
%      KV0:   Scalar value being KV offset of lower-left corner of output
%             grid.
%      DKU:   Scalar value being KU sampling interval of output grid.
%      DKV:   Scalar value being KV sampling interval of output grid.
%      ALPHA: Scalar value being angle between axes of output grid.
%      NU:    Number of samples along KU direction of output grid.
%      NV:    Number of samples along KV direction of output grid.
%
%   The initial radial positions of the samples S(I, J) in the spatial
%   frequency domain are KR0 + REPMAT([0:M-1].',1,N) * DKR; the initial
%   radial directions are REPMAT(PHI,M,1) in radians. The output sample
%   positions are at Cartesian coordinates
%     KU = REPMAT(KU0 + DKU * [0:NU-1].',1,NV) + DKV*[0:NV-1] / TAN(ALPHA)
%     KV = REPMAT(KV0 + DKV * [0:NV-1]),NU,1)
%
%   PFARESAMPLE(..., 'ParameterName', 'ParameterValue') allows
%   specification of various optional parameters:
%
%   ParameterName Description
%   -----------------------------------------------------------------
%   'Bandwidth'   Bandwidth of interpolation filter.
%   'Filter'      One-sided impulse response of interpolation filter
%

% Check that resampling parameters are valid.
if rsp.dku<=0 || rsp.dkv<=0 || rsp.kunum<=0 || isinf(rsp.kunum) ...
|| isnan(rsp.kunum) || rsp.kvnum<=0 || isinf(rsp.kvnum) || isnan(rsp.kvnum)
  warning('Invalid resampling parameters.');
  smnf=[]; smnw=[];
  return;
end
if any(diff(rsp.phid)<0)
  error('phi values must be monotonically increasing.');
end
if rsp.alpha<0
  alphatmp=rsp.alpha+pi*ceil(-rsp.alpha/pi);
  warning('rsp.alpha = %f is not in required range 0 to pi: using %f instead',rsp.alpha,alphatmp);
  rsp.alpha=alphatmp;
end

% Set defaults.
numonesidedfilterpoints=1024;
bandwidth=8/(numonesidedfilterpoints-1);
filter=windsinc(bandwidth/1.2,numonesidedfilterpoints);
drawwaitbar=1;

% Parse varargin.
ii=1;
while ii<=length(varargin)
  switch lower(varargin{ii})
    case 'bandwidth'
      ii=ii+1;
      bandwidth=varargin{ii};
    case 'filter'
      ii=ii+1;
      filter=varargin{ii};
    case 'drawwaitbar'
      ii=ii+1;
      drawwaitbar=varargin{ii};
    otherwise
```

```
      error('Unknown option %s',varargin{ii});
  end
  ii=ii+1;
end

% Call M-function.
[smnf,smnw]=pfadoresampling(smn,rsp,bandwidth,filter,'DrawWaitBar',drawwaitbar);
```

```
function phserr=pga(z,varargin)
%PGA   Phase Gradient Autofocus
%   PGA(Z) returns an estimated phase error obtained by applying the
%   Phase Gradient Autofocus (PGA) algorithm to the complex image Z
%   assuming a one-dimensional phase error exists along the horizontal
%   dimension.
%
%   PGA(..., 'PropertyName', 'PropertyValue') allows specifications of
%   various options:
%
%   PropertyName   Description
%   ------------------------------------------------------------------
%   RBThresh       Threshold (dB) for selecting range-bins to process.
%   MaxIter        Maximum number of iterations.
%   PhsErrTol      Tolerance (radians) for convergence.
%   ShowProgress   Display progress visually.
%   FixedWinWidth  Width of PGA window as fraction of image width.

% Set defaults.
rbthresh=-20;
maxiter=10;
phserrtol=0.1;
showprogress=0;
fixedwinwidth=0.1;

% Parse varargin.
ii=1;
while ii<=length(varargin)
  switch lower(varargin{ii})
    case 'rbthresh'
      ii=ii+1;
      rbthresh=lower(varargin{ii});
    case 'maxiter'
      ii=ii+1;
      maxiter=lower(varargin{ii});
    case 'phserrtol'
      ii=ii+1;
      phserrtol=lower(varargin{ii});
    case 'showprogress'
      ii=ii+1;
      showprogress=lower(varargin{ii});
    case 'fixedwinwidth'
      ii=ii+1;
      fixedwinwidth=lower(varargin{ii});
    otherwise
      error('Unknown option %s',varargin{ii});
  end
  ii=ii+1;
end

[M,N]=size(z);
phserr=zeros(1,N);
z=fft(z,[],2);

numiter=0;
phihat=repmat(inf,1,N);
```

```
while max(abs(phihat))>phserrtol && numiter<maxiter

  % Centre shift.
  [tmp,idx]=max(abs(z),[],2);
  for ii=1:M
    z(ii,:)=circshift(z(ii,:),[0,floor(N/2)-idx(ii)+1]);
  end

  if showprogress
    if ~exist('fhi','var')
      fhi=figure;
    else
      figure(fhi);
    end
    subplot(1,2,1);
    imagesc(20*log10(abs(z)));
  end

  % Pick out range-bins with high powers.
  pprb=10*log10(abs(z(:,floor(N/2))));
  idxrb=find(pprb>(max(pprb)+rbthresh));

  % Determine a window for the PGA.
  pp=10*log10(sum(abs(z(idxrb,:)).^2,1));
  pp=pp-max(pp(:));
  if showprogress
    figure(fhi);
    subplot(1,2,2);
    plot(pp); hold on;
    drawnow;
  end
  winc=round(length(pp)/2);
  winw=round(fixedwinwidth*length(pp));
  if winw<N && ceil(winw/2)<winc
    ww=[zeros(1,winc-ceil(winw/2)),windowf('Hamming',winw),zeros(1,N-winc-floor(winw/2))];
  else
    ww=windowf('Hamming',N);
  end

  % Apply PGA window to the data.
%  zw=z(idxrb,:).*repmat(ww,length(idxrb),1);
  zw=mrtimes(z(idxrb,:),ww);

  % Transform to cross-range-uncompressed domain.
  zw=ifft(ifftshift(zw,2),[],2);

  % Calculate phase error.
  deltaphihat=zeros(1,N);
  deltaphihat(2:end)=angle(sum(times(conj(zw(:,1:end-1)),zw(:,2:end)),1));
  phihat=cumsum(deltaphihat);

  % Fit regression line and remove linear term.
  a=[ones(N,1),(0:N-1).']\phihat.';
  phihat=phihat-a(1)-a(2)*(0:N-1);

  % Accumulate total phase error.
  phserr=phserr+phihat;

  % Apply phase error correction.
  z=fft(mrtimes(ifft(z,[],2),exp(-i*phihat)),[],2);

  numiter=numiter+1;

end
```

```
if showprogress
  close(fhi);
end
```

```
function dftdata=pgfft(sampledata,cycleshift,Mo,No,varargin)
%PGFFT   Apply 2-D FFT on parallelogram grid.
%   PGFFT(DATA,CYCLESHIFT) applies a 2-D FFT to samples DATA(I,J) of a
%   2-D function S(X,Y) where X = I*DELTAX + J*DELTAY*COT(ALPHA) and
%   Y=J*DELTAY: DATA(I,J) is thus S(X,Y) sampled on a parallelogram
%   grid, with grid-spacings DELTAX and DELTAY and where ALPHA is the
%   angle between the axes of the parallelogram. The parameter
%   CYCLESHIFT is DELTAY * COT(ALPHA)/DELTAX. By default, the zero
%   spatial-coordinate term is assumed to be in the centre of the DATA
%   array and the result is shifted so that the zero spatial-frequency
%   term lies in the middle of the transformed array.
%
%   PGFFT(DATA,CYCLESHIFT,MROWS,NROWS) pads DATA with zeros to size
%   MROWS-by-NCOLS before transforming. MROWS and NROWS must not be
%   less than the size of DATA.
%
%   PGFFT(...,'PropertyName','PropertyValue') allows specification of
%   various options.
%
%   PropertyName   Description
%   ---------------------------------------------------------------
%   'PreIFFTShift' Assume zero spatial-coord. term is in centre of
%                  input array: 0 or 1*.
%   'PostFFTShift' Shift zero spatial-freq. term to middle of output
%                  array: 0 or 1*.
%
%   For example,
%      x=complex(randn(64,32),randn(64,32)); % Make example data.
%      y=pgfft(x,1,70,40); % Transform to rectangular grid.
%      z=ipgfft(y,1,64,32); % Inv. transform to parallelogram grid.
%      all(abs(x-z)<1e-13), % Check result.
%
%   See also PGIFFT.

% Set defaults.
preifftshift=1;
postfftshift=1;

% Parse varargin.
ii=1;
while ii<=length(varargin)
  switch lower(varargin{ii})
    case 'preifftshift'
      ii=ii+1;
      preifftshift=varargin{ii};
    case 'postfftshift'
      ii=ii+1;
      postfftshift=varargin{ii};
    otherwise
      error('Unknown option %s',varargin{ii});
  end
  ii=ii+1;
end

% Work out size of input array.
[Mi,Ni]=size(sampledata);

% Set-up size of output array.
if ~exist('Mo','var') || isempty(Mo), Mo=Mi; end
if ~exist('No','var') || isempty(No), No=Ni; end
```

```
% Check grid sizes.
if Mi>Mo || Ni>No
  error('Input grid size %d-by-%d exceeds output grid size %d-by-%d', ...
      Mi,Ni,Mo,No);
end

% Define constants.
TWOPI=2*pi;

if 0 && cycleshift==0
  % Rectangular grid.
  if preifftshift
    sampledata=ifftshift(sampledata);
  end
  dftdata=mtfft2(sampledata,Mo,No);
  if postfftshift
    dftdata=fftshift(dftdata);
  end

else
  % Parallelogram grid.

  if postfftshift
    % Apply phase ramps to shift zero frequency to centre of output image.
    % (Cannot just use fftshift because sidelobe pattern is not generally
    % continuous across edges of output image.)

    mfactor=floor(Mo/2)/Mo;
    nfactor=floor(No/2)/No;

    sampledata=mrctimes(sampledata,exp(i*TWOPI*(mfactor*cycleshift+nfactor)*(0:Ni-1)),exp(i*TWOPI*mfactor*(0:Mi-1).'));
  end

  % FFT along column.
  dftdata=fft(sampledata,Mo,1);

  % Apply column-dependent phase ramp.
  rmp=exp(-i*TWOPI/Mo*cycleshift*(0:Mo-1)'*(0:Ni-1));
  dftdata=rmp.*dftdata;

  % FFT along rows.
  dftdata=fft(dftdata,No,2);

  % Apply phase ramps to simulate ifftshift of data prior to FFT.
  if preifftshift
    dftdata=mrctimes(dftdata,exp(i*TWOPI*floor(Ni/2)/No*[-floor(No/2):ceil(No/2)-1]), ...
    exp(i*TWOPI*(floor(Mi/2)+floor(Ni/2)*cycleshift)/Mo*[-floor(Mo/2):ceil(Mo/2)-1]'));
  end
end
```

```
function y=rect(x);
%RECT   Rectangle function.
%   RECT(X) returns 1 wherever abs(X(I))<0.5 and 0 otherwise.

y=zeros(size(x));
idx=find(abs(x)<0.5);
if ~isempty(idx)
  y(idx)=ones(size(idx));
end
```

```
function y=sinc(x);
```

```
%SINC   Sinc function.
%   SINC(X) returns the value of SIN(PI*X)/(PI*X).

y=ones(size(x));
idx=find(x~=0);
if ~isempty(idx)
  y(idx)=sin(pi*x(idx))./(pi*x(idx));
end
```

```
function tt=txrxdelay(P1,P2,R0,varargin)
%TXRXDELAY   Tx-to-Rx delay.
%   TXRXDELAY(P1,P2,R0) returns the propagation time for scattering from a
%   point at R0. P1 and P2 are the positions of the transmitter and receiver.

% Set defaults.
polyfitorder=[];

% Parse varargin.
ii=1;
while ii<=length(varargin)
  switch lower(varargin{ii})
    case 'polyfitorder'
      ii=ii+1;
      polyfitorder=lower(varargin{ii});
    otherwise
      error('Unknown option %s',varargin{ii});
  end
  ii=ii+1;
end

c=3e8;

tt=(sqrt(sum((P1-repmat(R0,1,size(P1,2))).^2))+sqrt(sum((P2-repmat(R0,1,size(P2,2))).^2)))/c;
if ~(isempty(polyfitorder) || isinf(polyfitorder))
  disp(sprintf('Smoothing Tx-Rx-delay: order %d ...',polyfitorder));
  tt=fitpoly(tt,polyfitorder);
end
```

```
function w=windowf(wname,M,varargin)
%WINDOWF   Window function.
%   WINDOWF('WindowName', N) or WINDOWF('WindowName', N, 'WParms', WPARMS)
%   returns the N-point window of the requested type. Supported window-types
%   include:
%
%   'WindowName'   WPARMS
%   ----------------------------------------------------------------
%   'rect'         []
%   'Hann'         []
%   'Hamming'      []
%   'Blackman'     []
%
%   WINDOWF('WindowName', [M,N], ...) returns a 2-D window.
%
%   WINDOWF('WindowName', [M,N], 'ParameterName', 'ParameterValue')
%   allows specification of various optional parameters:
%
%   ParameterName Description
%   ----------------------------------------------------------------
%   'Normalise'   Normalise window so DC term has unit magnitude: 0* or 1.

% Set defaults.
normalise=0;
```

```
% Parse varargin.
ii=1;
while ii<=length(varargin)
  switch lower(varargin{ii})
    case 'wparms'
      ii=ii+1;
      wparms=varargin{ii};
    case 'normalise'
      ii=ii+1;
      normalise=varargin{ii};
    otherwise
      error('Unknown option %s',varargin{ii});
  end
  ii=ii+1;
end

% Check arguments.
if ~isnumeric(M)
  error('M should be an integer array.');
end

% Unpack size specification.
if length(M)==2
  N=M(2);
  M=M(1);
elseif length(M)==1
  N=[];
else
  error('M should have size 1-by-2.');
end

switch lower(wname)
  case 'rect'
    if isempty(N)
      w=ones(1,M);
    else
      w=ones(M,N);
    end

  case 'hann'
    if isempty(N)
      w=hannw(M);
    else
      wm=hannw(M);
      wn=hannw(N);
      w=zeros(M,N);
      for ii=1:M
        w(ii,:)=wm(ii)*wn;
      end
    end

  case 'hamming'
    if isempty(N)
      w=hammingw(M);
    else
      wm=hammingw(M);
      wn=hammingw(N);
      w=zeros(M,N);
      for ii=1:M
        w(ii,:)=wm(ii)*wn;
      end
    end

  case 'blackman'
```

```
    if isempty(N)
      w=blackmanw(M);
    else
      wm=blackmanw(M);
      wn=blackmanw(N);
      w=zeros(M,N);
      for ii=1:M
        w(ii,:)=wm(ii)*wn;
      end
    end

end

if normalise
  w=w./sum(w(:));
end

function w=hannw(M)
w=(1-cos(2*pi*[0:M-1]/M))/2;

function w=hammingw(M)
w=0.53836-0.46164*cos(2*pi*[0:M-1]/M);

function w=blackmanw(M)
tmp=2*pi*[0:M-1]/M;
w=0.42-0.5*cos(tmp)+0.08*cos(2*tmp);
```

```
function [h,Nz]=windsinc(B,K,varargin)
%WINDSINC   Windowed-sinc.
%   WINDSINC(B,K) returns the one-sided windowed sinc function with frequency
%   parameter (filter bandwidth) B with K samples. The resultant filter will
%   pass frequencies up to approximately B/2.
%
%   [H,NZ]=WINDSINC(...) returns the number of one-sided zero crossings in Nz.
%
%   For example,
%      K=1024;B=8/(K-1);
%      [h1s,Nz]=windsinc(B,K);
%      h=fftshift([h1s,fliplr(h1s(2:end))]);
%      plot([-K+1:K-1],h,'.-');
%      figure;
%      plot([0:65535]/65536,20*log10(abs(fft(h,65536))))

% Set defaults.
windowtouse='blackman';

% Parse varargin.
ii=1;
while ii<=length(varargin)
  switch lower(varargin{ii})
    case 'rect'
      windowtouse='rect';
    case 'hann'
      windowtouse='hann';
    case 'hamming'
      windowtouse='hamming';
    case 'blackman'
      windowtouse='blackman';
    otherwise
      error(sprintf('Unknown option %s',varargin{ii}));
  end
  ii=ii+1;
end
```

```
% Calc. number of zero-crossings on one-side of impulse response.
% Effective sampling frequency fs'' is unity.
Nz=(K-1)*B;

% Calc. filter impulse response.
t=[0:K-1]; % One-sided grid values sampled at unit rate.
h=B*sinc(B*t);
switch windowtouse
  case 'hann'
    h=h.*halfhannwin(2*K-1);
  case 'hamming'
    h=h.*halfhammingwin(2*K-1);
  case 'blackman'
    h=h.*halfblackmanwin(2*K-1);
end

function w=halfhannwin(N)
% N is two-sided window length.
w=(1-cos(2*pi*[floor(N/2):N-1]/N))/2;

function w=halfhammingwin(N)
w=0.53836-0.46164*cos(2*pi*[floor(N/2):N-1]/N);

function w=halfblackmanwin(N)
tmp=2*pi*[floor(N/2):N-1]/N;
w=0.42-0.5*cos(tmp)+0.08*cos(2*tmp);
```

Bibliography

[1] C. A. Wiley, "Synthetic aperture radars: a paradigm for technology evolution," *IEEE Trans. Aerosp. Electron. Syst.*, vol. 21, no. 3, pp. 440–443, May 1985.

[2] N. J. Willis, *Bistatic Radar*. Artech House, 1991.

[3] N. J. S. Stacy and M. P. Burgess, "*Ingara*: the Australian imaging radar system," in *Proc. IEEE Int. Geosci. Remote Sens. Symp., IGARSS*, Pasadena, USA, Aug. 1994, pp. 2240–2242.

[4] N. J. S. Stacy, M. P. Burgess, M. R. Muller, and R. Smith, "*Ingara*: an integrated airborne imaging radar system," in *Proc. IEEE Int. Geosci. Remote Sens. Symp., IGARSS*, Lincoln, USA, May 1996, pp. 1618–1620.

[5] N. J. S. Stacy, D. Badger, A. S. Goh, M. Preiss, and M. L. Williams, "The DSTO *Ingara* X-band SAR polarimetric upgrade: first results," in *Proc. IEEE Int. Geosci. Remote Sens. Symp., IGARSS*, Toulouse, France, Jul. 2003, pp. 4474–4476.

[6] N. J. Willis and H. D. Griffiths, *Advances in Bistatic Radar*. SciTech Publishing, 2007.

[7] A. Moccia, N. Chiacchio, and A. Capone, "Spaceborne bistatic synthetic aperture radar for remote sensing applications," *Int. J. Remote Sens.*, vol. 21, no. 18, pp. 3395–3414, 2000.

[8] G. Krieger, H. Fiedler, J. Mittermayer, K. Papathanassiou, and A. Moreira, "Analysis of multistatic configurations for spaceborne SAR interferometry," *IEE Proc.—Radar Sonar Navig.*, vol. 150, no. 3, pp. 87–96, Jun. 2003.

[9] G. Krieger and A. Moreira, "Spaceborne bi- and multistatic SAR: potential and challenges," *IEE Proc.—Radar Sonar Navig.*, vol. 153, no. 3, pp. 184–198, Jun. 2006.

[10] D. Massonnet, "The interferometric cartwheel: a constellation of passive satellites to produce radar images to be coherently combined," *Int. J. Remote Sens.*, vol. 22, no. 12, pp. 2413–2430, 2001.

[11] D. Massonnet, "Capabilities and limitations of the Interferometric Cartwheel," *IEEE Trans. Geosci. Remote Sens.*, vol. 39, no. 3, pp. 506–520, Mar. 2001.

[12] A. Moccia, G. Salzillo, M. D'Errico, G. Rufino, and G. Alberti, "Performance of spaceborne bistatic synthetic aperture radar," *IEEE Trans. Aerosp. Electron. Syst.*, vol. 41, no. 4, pp. 1383–1395, Oct. 2005.

[13] G. Krieger, A. Moreira, H. Fiedler, I. Hajnsek, M. Werner, M. Younis, and M. Zink, "TanDEM-X: a satellite formation for high-resolution SAR interferometry," *IEEE Trans. Geosci. Remote Sens.*, vol. 45, no. 11, pp. 3317–3341, Nov. 2007.

[14] G. Krieger, H. Fiedler, and A. Moreira, "Bi- and multistatic SAR: potentials and challenges," in *Proc. Eur. Conf. Synthetic Aperture Radar, EUSAR*, Ulm, Germany, May 2004, pp. 365–370.

[15] J. Klare, I. Walterscheid, A. R. Brenner, and J. H. G. Ender, "Evaluation and optimisation of configurations of a hybrid bistatic SAR experiment between TerraSAR-X and PAMIR," in *Proc. IEEE Int. Geosci. Remote Sens. Symp., IGARSS*, Denver, USA, Jul./Aug. 2006, pp. 1200–1203.

[16] M. Cherniakov, "Space-surface bistatic synthetic aperture radar—prospective and problems," in *Proc. IEE RADAR*, Oct. 2002, pp. 22–26.

[17] C. H. Gierull, "Bistatic synthetic aperture radar: TIF report (phase I)," Defence R&D Canada—Ottawa, Tech. Rep., 2004.

[18] J. Sanz-Marcos, P. Lopez-Dekker, J. J. Mallorqui, A. Aguasca, and P. Prats, "SABRINA: a SAR bistatic receiver for interferometric applications," *IEEE Geosci. Remote Sens. Lett.*, vol. 4, no. 2, pp. 307–311, Apr. 2007.

[19] R. Saini, R. Zuo, and M. Cherniakov, "Problem of signal synchronisation in space-surface bistatic synthetic aperture radar based on global navigation satellite emissions—experimental results," *IET Radar Sonar Navig.*, vol. 4, no. 1, pp. 110–125, 2010.

[20] D. Martinsek and R. Goldstein, "Bistatic radar experiment," in *Proc. Eur. Conf. Synthetic Aperture Radar, EUSAR*, Friedrichshafen, Germany, May 1998, pp. 31–34.

[21] M. Rodriguez-Cassola, S. V. Baumgartner, G. Krieger, and A. Moreira, "Bistatic TerraSAR-X/F-SAR spaceborne-airborne SAR experiment: description, data processing, and results," *IEEE Trans. Geosci. Remote Sens.*, vol. 48, no. 2, pp. 781–794, Feb. 2010.

[22] I. Walterscheid, T. Espeter, A. R. Brenner, J. Klare, J. H. G. Ender, H. Nies, R. Wang, and O. Loffeld, "Bistatic SAR experiments with PAMIR and TerraSAR-X—setup, processing and image results," *IEEE Trans. Geosci. Remote Sens.*, vol. 48, no. 8, pp. 3268 –3279, Aug. 2010.

[23] I. Walterscheid, T. Espeter, C. Gierull, J. Klare, A. R. Brenner, and J. H. G. Ender, "Results and analysis of hybrid bistatic SAR experiments with spaceborne, airborne and stationary sensors," in *Proc. IEEE Int. Geosci. Remote Sens. Symp., IGARSS*, Cape Town, South Africa, Jul. 2009.

[24] A. Barmettler, L. Zuberbühler, E. Meier, L. Ulander, A. Gustavsson, and P. Wellig, "Swiss airborne monostatic and bistatic dual-pol. SAR experiment at the VHF-band," in *Proc. Eur. Conf. Synthetic Aperture Radar, EUSAR*, Friedrichshafen, Germany, Jun. 2008, pp. 139–142.

[25] A. S. Goh, M. Preiss, N. J. S. Stacy, and D. A. Gray, "The *Ingara* bistatic SAR upgrade: first results," in *Int. Conf. Radar*, Adelaide, Australia, Sep. 2008, pp. 329–334.

[26] T. Espeter, I. Walterscheid, J. Klare, C. Gierull, A. Brenner, J. Ender, and O. Loffeld, "Progress of hybrid bistatic SAR: synchronisation experiments and first imaging results," in *Proc. Eur. Conf. Synthetic Aperture Radar, EUSAR*, Friedrichshafen, Germany, Jun. 2008, pp. 217–220.

[27] G. Yates, A. Horne, A. Blake, and R. Middleton, "Bistatic SAR image formation," *IEE Proc.—Radar Sonar Navig.*, vol. 153, no. 3, pp. 208–213, Jun. 2006.

[28] P. Dubois-Fernandez, H. Cantalloube, B. Vaizan, G. Krieger, R. Horn, M. Wendler, and V. Giroux, "ONERA-DLR bistatic SAR campaign: planning, data acquisition, and first analysis of bistatic scattering behaviour of natural and urban targets," *IEE Proc.—Radar Sonar Navig.*, vol. 153, no. 3, pp. 214–223, Jun. 2006.

[29] J. Ender, I. Walterscheid, and A. R. Brenner, "Bistatic SAR—translational invariant processing and experimental results," *IEE Proc.—Radar Sonar Navig.*, vol. 153, no. 3, pp. 177–183, Jun. 2006.

[30] I. Walterscheid, J. Ender, A. Brenner, and O. Loffeld, "Bistatic SAR processing and experiments," *IEEE Trans. Geosci. Remote Sens.*, vol. 44, no. 10, pp. 2710–2717, Oct. 2006.

[31] M. Eineder, "Oscillator clock drift compensation in bistatic interferometric SAR," in *Proc. IEEE Int. Geosci. Remote Sens. Symp., IGARSS*, Toulouse, France, Jul. 2003, pp. 1449–1451.

[32] M. Weiss, "Time and frequency synchronisation aspects for bistatic SAR systems," in *Proc. Eur. Conf. Synthetic Aperture Radar, EUSAR*, Ulm, Germany, May 2004, pp. 395–398.

[33] G. Krieger and M. Younis, "Impact of oscillator noise in bistatic and multistatic SAR," *IEEE Geosci. Remote Sens. Lett.*, vol. 3, no. 3, pp. 424–428, Jul. 2006.

[34] M. D'Errico and A. Moccia, "Attitude and antenna pointing design of bistatic radar formations," *IEEE Trans. Aerosp. Electron. Syst.*, vol. 39, no. 3, pp. 949–960, Jul. 2003.

[35] W.-Q. Wang and J. Cai, "Antenna directing synchronisation for bistatic synthetic aperture radar systems," *IEEE Antennas Wireless Propag. Lett.*, vol. 9, pp. 307–310, 2010.

[36] G. Nico and M. Tesauro, "On the existence of coverage and integration time regimes in bistatic SAR configurations," *IEEE Geosci. Remote Sens. Lett.*, vol. 4, no. 3, pp. 426–430, Jul. 2007.

[37] I. Walterscheid, A. R. Brenner, and J. H. G. Ender, "Results on bistatic synthetic aperture radar," *Electron. Lett.*, vol. 40, no. 19, pp. 1224–1225, Sep. 2004.

[38] G. P. Cardillo, "On the use of the gradient to determine bistatic SAR resolution," in *Antennas and Propagation Society International Symposium*, 1990, pp. 1032–1035.

[39] C. V. Jakowatz, Jr., D. E. Wahl, P. H. Eichel, D. C. Ghighlia, and P. A. Thompson, *Spotlight-mode Synthetic Aperture Radar: A Signal Processing Approach.* Kluwer, 1996.

[40] T. Zeng, M. Cherniakov, and T. Long, "Generalised approach to resolution analysis in BSAR," *IEEE Trans. Aerosp. Electron. Syst.*, vol. 41, no. 2, pp. 461–474, Apr. 2005.

[41] O. Loffeld, H. Nies, V. Peters, and S. Knedlik, "Models and useful relations for bistatic SAR processing," *IEEE Trans. Geosci. Remote Sens.*, vol. 42, no. 10, pp. 2031–2038, Oct. 2004.

[42] R. K. Raney, "A new and fundamental Fourier transform pair," in *Proc. IEEE Int. Geosci. Remote Sens. Symp., IGARSS*, Houston, USA, May 1992, pp. 106–107.

[43] Y. Neo, F. Wong, and I. Cumming, "A two-dimensional spectrum for bistatic SAR processing using series reversion," *IEEE Geosci. Remote Sens. Lett.*, vol. 4, no. 1, pp. 93–96, Jan. 2007.

[44] W. G. Carrara, R. S. Goodman, and R. M. Majewski, *Spotlight Synthetic Aperture Radar Signal Processing Algorithms.* Artech House, 1995.

[45] B. D. Rigling and R. L. Moses, "Polar format algorithm for bistatic SAR," *IEEE Trans. Aerosp. Electron. Syst.*, vol. 40, no. 4, pp. 1147–1159, Oct. 2004.

[46] X. Wang, D. Zhu, and Z. Zhu, "An implementation of bistatic PFA using chirp scaling," *J. Electromagn. Waves Appl.*, vol. 24, pp. 745–753, 2010.

[47] R. Bamler and P. Hartl, "Synthetic aperture radar interferometry," *Inverse Prob.*, vol. 14, pp. R1–R54, 1998.

[48] P. A. Rosen, S. Hensley, I. R. Joughin, F. K. Li, S. N. Madsen, E. Rodríguez, and R. M. Goldstein, "Synthetic aperture radar interferometry," *Proc. IEEE*, vol. 88, no. 3, pp. 333–382, Mar. 2000.

[49] D. Massonnet, M. Rossi, C. Carmona, F. Adragna, G. Peltzer, K. Feigl, and T. Rabaute, "The displacement field of the Landers earthquake mapped by radar intererometry," *Nature*, vol. 364, pp. 138–142, Jul. 1993.

[50] D. Massonnet, P. Briole, and A. Arnaud, "Deflation of Mount Etna monitored by spaceborne radar interferometry," *Nature*, vol. 375, pp. 567–570, Jun. 1995.

[51] M. Preiss, D. Gray, and N. J. S. Stacy, "Detecting scene changes using synthetic aperture radar interferometry," *IEEE Trans. Geosci. Remote Sens.*, vol. 44, no. 8, pp. 2041–2054, Aug. 2006.

[52] M. Cherniakov, T. Zeng, and E. Plakidis, "Analysis of space-surface interferometric bistatic radar," in *Proc. IEEE Int. Geosci. Remote Sens. Symp., IGARSS*, Toulouse, France, Jul. 2003, pp. 778–780.

[53] G. Krieger, I. Hajnsek, K. P. Papathanassiou, M. Younis, and A. Moreira, "Interferometric synthetic aperture radar (SAR) missions employing formation flying," *Proc. IEEE*, vol. 98, no. 5, pp. 816–843, May 2010.

[54] H. Cantalloube, M. Wendler, V. Giroux, P. Dubois-Fernandez, and R. Horn, "A first bistatic airborne SAR interferometry experiment—preliminary results," in *IEEE Sensor Array and Multichannel Signal Processing Workshop*, 2004, pp. 667–671.

[55] S. Duque, P. López-Dekker, and J. J. Mallorqui, "Single-pass bistatic SAR interferometry using fixed-receiver configurations: theory and experimental validation," *IEEE Trans. Geosci. Remote Sens.*, vol. 48, no. 6, pp. 2740–2749, Jun. 2010.

[56] F. Gatelli, A. Monti Guarnieri, F. Parizzi, P. Pasquali, C. Prati, and F. Rocca, "The wavenumber shift in SAR interferometry," *IEEE Trans. Geosci. Remote Sens.*, vol. 32, no. 4, pp. 855–865, Jul. 1994.

[57] C. Prati and F. Rocca, "Improving slant-range resolution with multiple SAR surveys," *IEEE Trans. Aerosp. Electron. Syst.*, vol. 29, no. 1, pp. 135–144, Jan. 1993.

[58] M. Suess, M. Völker, J. J. W. Wilson, and C. H. Buck, "Superresolution: range resolution improvement by coherent combination of repeat pass images," in *Proc. Eur. Conf. Synthetic Aperture Radar, EUSAR*, Friedrichshafen, Germany, May 1998, pp. 565–569.

[59] S. Guillaso, A. Reigber, L. Ferro-Famil, and E. Pottier, "Range resolution improvement of airborne SAR images," *IEEE Geosci. Remote Sens. Lett.*, vol. 3, no. 1, pp. 135–139, Jan. 2006.

[60] D. Cristallini, D. Pastina, and P. Lombardo, "Efficient configurations of SAR sensors for improved range resolution," in *Proc. IEEE Int. Geosci. Remote Sens. Symp., IGARSS*, Cape Town, South Africa, Jul. 2009, pp. 52–55.

[61] M. Preiss and A. S. Goh, "Coherent processing of bistatic and monostatic SAR imagery for range resolution enhancement," in *Proc. Eur. Conf. Synthetic Aperture Radar, EUSAR*, Aachen, Germany, Jun. 2010.

[62] S. R. Cloude and K. P. Papathanassiou, "Polarimetric SAR interferometry," *IEEE Trans. Geosci. Remote Sens.*, vol. 36, no. 5, pp. 1551–1565, Sep. 1998.

[63] F. T. Ulaby and C. Elachi, *Radar Polarimetry for Geoscience Applications.* Artech House, 1990.

[64] A.-L. Germond, E. Pottier, and J. Saillard, "Nine polarimetric bistatic target equations," *Electron. Lett.*, vol. 33, no. 17, pp. 1494–1495, Aug. 1997.

[65] Z. H. Czyz, "On theoretical foundations of coherent bistatic radar polarimetry," in *SPIE Conference on Wideband Interferometric Sensing and Imaging Polarimetry*, vol. 3120, Dec. 1997, pp. 69–105.

[66] S. R. Cloude, "On the status of bistatic polarimetry theory," in *Proc. IEEE Int. Geosci. Remote Sens. Symp., IGARSS*, Seoul, Korea, Jul. 2005, pp. 2003–2006.

[67] F. Xu and Y.-Q. Jin, "Imaging simulation of bistatic synthetic aperture radar and its polarimetric analysis," *IEEE Trans. Geosci. Remote Sens.*, vol. 46, no. 8, pp. 2233–2248, Aug. 2008.

[68] J.-C. Souyris and C. Tison, "Polarimetric analysis of bistatic SAR images from polar decomposition: a quaternion approach," *IEEE Trans. Geosci. Remote Sens.*, vol. 45, no. 9, pp. 2701–2714, Sep. 2007.

[69] C. Titin-Schnaider, "Physical meaning of bistatic polarimetric parameters," *IEEE Trans. Geosci. Remote Sens.*, vol. 48, no. 5, pp. 2349–2356, May 2010.

[70] P. Ferrazzoli, L. Guerriero, C. I. DelMonaco, and D. Solimini, "A further insight into the potential of bistatic SAR in monitoring the earth surface," in *Proc. IEEE Int. Geosci. Remote Sens. Symp., IGARSS*, Toulouse, France, Jul. 2003, pp. 776–777.

[71] P. Liang, L. E. Pierce, and M. Moghaddam, "Radiative transfer model for microwave bistatic scattering from forest canopies," *IEEE Trans. Geosci. Remote Sens.*, vol. 43, no. 11, pp. 2470–2483, Nov. 2005.

[72] N. Pierdicca, L. Pulvirenti, F. Ticconi, and M. Brogioni, "Radar bistatic configurations for soil moisture retrieval: a simulation study," *IEEE Trans. Geosci. Remote Sens.*, vol. 46, no. 10, pp. 3252–3264, Oct. 2008.

[73] L. Thirion-Lefevre, E. Colin-Koeniguer, and C. Dahon, "Bistatic scattering from forest components. Part I: coherent polarimetric modelling and analysis of simulated results," *Waves in Random and Complex Media*, vol. 20, no. 1, pp. 36–61, Feb. 2010.

[74] E. Colin-Koeniguer and L. Thirion-Lefevre, "Bistatic scattering from forest components. Part II: first validation of a bistatic polarimetric forest model in the VHF-UHF band [225–475 MHz] using indoor measurements," *Waves in Random and Complex Media*, vol. 20, no. 1, pp. 62–85, Feb. 2010.

[75] D. R. Sheen, N. P. Malinas, D. W. Kletzli, Jr, T. B. Lewis, and J. F. Roman, "Foliage transmission measurements using a ground-based ultrawide band (300–1300 MHz) SAR system," *IEEE Trans. Geosci. Remote Sens.*, vol. 32, no. 1, pp. 118–130, Jan. 1994.

[76] D. Singh, S. K. Sharan, S. K. Sharan, and R. Sao, "Composite effect of crop (wheat) on microwave (X-band) for remote sensing," in *International Conference on Computational Electromagnetics and its Applications*, 1999, pp. 509–512.

[77] A. Y. Nashashibi and F. T. Ulaby, "Millimeter-wave polarimetric bistatic radar scattering from rough soil surfaces," in *Proc. IEEE Int. Geosci. Remote Sens. Symp., IGARSS*, Toulouse, France, Jul. 2003, pp. 788–790.

[78] H. D. Griffiths, W. A. Al-Ashwal, K. D. Ward, R. J. A. Tough, C. J. Baker, and K. Woodbridge, "Measurement and modelling of bistatic radar sea clutter," *IET Radar Sonar Navig.*, vol. 4, no. 2, pp. 280–290, 2010.

[79] D. J. McLaughlin, Y. Wu, W. G. Stevens, X. Zhang, M. J. Sowa, and B. Weijers, "Fully polarimetric bistatic radar scattering behaviour of forested hills," *IEEE Trans. Antennas Propag.*, vol. 50, no. 2, pp. 101–110, Feb. 2002.

[80] A. Freeman, "SAR calibration: an overview," *IEEE Trans. Geosci. Remote Sens.*, vol. 30, no. 6, pp. 1107–1121, Nov. 1992.

[81] A. Parfitt and N. Nikolic, "A dual-polarised wideband planar array for X-band synthetic aperture radar," in *Proc. IEEE Antennas Propag. Soc. Int. Symp.*, 2001, pp. 464–467.

[82] C. J. Bradley, P. J. Collins, J. Fortuny-Guasch, M. L. Hastriter, G. Nesti, A. J. Terzuoli, Jr., and K. S. Wilson, "An investigation of bistatic calibration objects," *IEEE Trans. Geosci. Remote Sens.*, vol. 43, no. 10, pp. 2177–2184, Oct. 2005.

[83] C. J. Bradley, P. J. Collins, J. Fortuny-Guasch, M. L. Hastriter, G. Nesti, A. J. Terzuoli, Jr., and K. S. Wilson, "An investigation of bistatic calibration techniques," *IEEE Trans. Geosci. Remote Sens.*, vol. 43, no. 10, pp. 2185–2191, Oct. 2005.

[84] F. Daout, A. Khenchaf, and J. Saillard, "Calibration of bistatic polarimetric scatterometers," in *Proc. IEEE Int. Geosci. Remote Sens. Symp., IGARSS*, Lincoln, USA, May 1996, pp. 746–748.

[85] J. D. Klein, "Calibration of complex polarimetric SAR imagery using backscatter correlations," *IEEE Trans. Aerosp. Electron. Syst.*, vol. 28, no. 1, pp. 183–194, Jan. 1992.

[86] S. Quegan, "A unified algorithm for phase and cross-talk calibration of polarimetric data—theory and observations," *IEEE Trans. Geosci. Remote Sens.*, vol. 32, no. 1, pp. 89–99, Jan. 1994.

[87] T. L. Ainsworth, L. Ferro-Famil, and J.-S. Lee, "Orientation angle preserving *a posteriori* polarimetric SAR calibration," *IEEE Trans. Geosci. Remote Sens.*, vol. 44, no. 4, pp. 994–1003, Apr. 2006.

[88] A. S. Goh, M. Preiss, D. A. Gray, and N. J. S. Stacy, "Comparison of parameter estimation accuracy of distributed-target polarimetric calibration techniques," in *Proc. IEEE Int. Geosci. Remote Sens. Symp., IGARSS*, Barcelona, Spain, Jul. 2007.

[89] D. C. Munson, Jr., J. D. O'Brien, and W. K. Jenkins, "A tomographic formulation of spotlight-mode synthetic aperture radar," *Proc. IEEE*, vol. 71, no. 8, pp. 917–925, Aug. 1983.

[90] M. D. Desai and W. K. Jenkins, "Convolution backprojection image reconstruction for spotlight mode synthetic aperture radar," *IEEE Trans. Image Process.*, vol. 1, no. 4, pp. 505–517, Oct. 1992.

[91] L. M. H. Ulander, H. Hellsten, and G. Stenström, "Synthetic-aperture radar processing using fast factorised back-projection," *IEEE Trans. Aerosp. Electron. Syst.*, vol. 39, no. 3, pp. 760–776, Jul. 2003.

[92] S. Xiao, D. C. Munson, Jr., S. Basu, and Y. Bresler, "An $N^2 \log N$ back-projection algorithm for SAR image formation," in *Conference Record of the Thirty-Fourth Asilomar Conference on Signals, Systems and Computers*, Pacific Grove, California, USA, Oct. 2000, pp. 3–7.

[93] J. W. McCorkle and M. Rofheart, "Order $N^2 \log(N)$ backprojector algorithm for focussing wide-angle wide-bandwidth arbitrary-motion synthetic aperture radar," in *Radar Sensor Technology, Proc. of SPIE 2747*, Orlando, Florida, USA, Apr. 1996.

[94] C. V. Jakowatz, Jr., D. E. Wahl, and D. A. Yocky, "A beamforming algorithm for bistatic SAR image formation," in *Algorithms for Synthetic Aperture Imagery XVII, Proc. of SPIE 7699*, Orlando, Florida, USA, Apr. 2010.

[95] I. G. Cumming and F. H. Wong, *Digital processing of Synthetic Aperture Radar Data: Algorithms and Implementation.* Artech House, 2005.

[96] R. Bamler, "A comparison of range-Doppler and wavenumber domain SAR focussing algorithms," *IEEE Trans. Geosci. Remote Sens.*, vol. 30, no. 4, pp. 706–713, Jul. 1992.

[97] I. G. Cumming, Y. L. Neo, and F. H. Wong, "Interpretations of the Omega-K algorithm and comparisons with other algorithms," in *Proc. IEEE Int. Geosci. Remote Sens. Symp., IGARSS*, Toulouse, France, Jul. 2003, pp. 1455–1458.

[98] D. D'Aria, A. M. Guarnieri, and F. Rocca, "Focussing bistatic synthetic aperture radar using dip move out," *IEEE Trans. Geosci. Remote Sens.*, vol. 42, no. 7, pp. 1362–1376, Jul. 2004.

[99] J. L. Bauck and W. K. Jenkins, "Convolution-backprojection image reconstruction for bistatic synthetic aperture radar," in *Proc. IEEE Int. Symp. on Circ. and Syst., ISCAS*, Portland, Oregon, USA, May 1989, pp. 1512–1515.

[100] Y. Ding and D. C. Munson, Jr., "A fast back-projection algorithm for bistatic SAR imaging," in *IEEE Int. Conf. on Image Processing*, 2002, pp. 449–452.

[101] C. E. Yarman, B. Yazici, and M. Cheney, "Bistatic synthetic aperture radar imaging for arbitrary flight trajectories," *IEEE Trans. Image Process.*, vol. 17, no. 1, pp. 84–93, Jan. 2008.

[102] R. Bamler, F. Meyer, and W. Liebhart, "Processing of bistatic SAR data from quasi-stationary configurations," *IEEE Trans. Geosci. Remote Sens.*, vol. 45, no. 11, pp. 3350–3358, Nov. 2007.

[103] V. Giroux, H. Cantalloube, and F. Daout, "An Omega-K algorithm for SAR bistatic systems," in *Proc. IEEE Int. Geosci. Remote Sens. Symp., IGARSS*, Seoul, Korea, Jul. 2005, pp. 1060–1063.

[104] A. M. Guarnieri and F. Rocca, "Reduction to monostatic focussing of bistatic or motion uncompensated SAR surveys," *IEE Proc.—Radar Sonar Navig.*, vol. 153, no. 3, pp. 199–207, Jun. 2006.

[105] R. Wang, O. Loffeld, Q. Ul-Ann, H. Nies, A. Medrano Ortiz, and A. Samarah, "A bistatic point target reference spectrum for general bistatic SAR processing," *IEEE Geosci. Remote Sens. Lett.*, vol. 5, no. 3, pp. 517–521, Jul. 2008.

[106] R. Wang, O. Loffeld, Y. L. Neo, H. Nies, and Z. Dai, "Extending Loffeld's bistatic formula for the general bistatic SAR configuration," *IET Radar Sonar Navig.*, vol. 4, no. 1, pp. 74–84, 2010.

[107] K. Yang, F. He, and D. Liang, "A two-dimensional spectrum for general bistatic SAR processing," *IEEE Geosci. Remote Sens. Lett.*, vol. 7, no. 1, pp. 108–112, Jan. 2010.

[108] Y. L. Neo, F. H. Wong, and I. G. Cumming, "A comparison of point target spectra derived for bistatic SAR processing," *IEEE Trans. Geosci. Remote Sens.*, vol. 46, no. 9, pp. 2481–2492, Sep. 2008.

[109] F. Wang and X. Li, "A new method of deriving spectrum for bistatic SAR processing," *IEEE Geosci. Remote Sens. Lett.*, vol. 7, no. 3, pp. 483 –486, Jul. 2010.

[110] X. Geng, H. Yan, and Y. Wang, "A two-dimensional spectrum model for general bistatic SAR," *IEEE Trans. Geosci. Remote Sens.*, vol. 46, no. 8, pp. 2216–2223, Aug. 2008.

[111] Y. L. Neo, F. H. Wong, and I. G. Cumming, "Processing of azimuth-invariant bistatic SAR data using the range-Doppler algorithm," *IEEE Trans. Geosci. Remote Sens.*, vol. 46, no. 1, pp. 14–21, Jan. 2008.

[112] F. Li, S. Li, and Y. Zhao, "Focussing azimuth-invariant bistatic SAR data with chirp scaling," *IEEE Geosci. Remote Sens. Lett.*, vol. 5, no. 3, pp. 484–486, Jul. 2008.

[113] F. H. Wong, I. G. Cumming, and Y. L. Neo, "Focussing bistatic SAR data using the nonlinear chirp scaling algorithm," *IEEE Trans. Geosci. Remote Sens.*, vol. 46, no. 9, pp. 2493–2505, Sep. 2008.

[114] R. Wang, O. Loffeld, H. Nies, S. Knedlik, and J. H. G. Ender, "Chirp-scaling algorithm for bistatic SAR data in the constant-offset configuration," *IEEE Trans. Geosci. Remote Sens.*, vol. 47, no. 3, pp. 952–964, Mar. 2009.

[115] M. Antoniou, M. Cherniakov, and C. Hu, "Space-surface bistatic SAR image formation algorithms," *IEEE Trans. Geosci. Remote Sens.*, vol. 47, no. 6, pp. 1827–1843, Jun. 2009.

[116] X. Qiu, D. Hu, and C. Ding, "An improved NLCS algorithm with capability analysis for one-stationary BiSAR," *IEEE Trans. Geosci. Remote Sens.*, vol. 46, no. 10, pp. 3179–3186, Oct. 2008.

[117] J. Li, Z. Bi, Z.-S. Liu, and K. Knaell, "Use of curvilinear SAR for three-dimensional target feature extraction," *IEE Proc.—Radar Sonar Navig.*, vol. 144, no. 5, pp. 275–283, Oct. 1997.

[118] B. D. Rigling and R. L. Moses, "Flight path strategies for 3-D scene reconstruction from bistatic SAR," *IEE Proc.—Radar Sonar Navig.*, vol. 151, no. 3, pp. 149–157, Jun. 2004.

[119] A. Reigber and A. Moreira, "First demonstration of airborne SAR tomography using multibaseline L-band data," *IEEE Trans. Geosci. Remote Sens.*, vol. 38, no. 5, pp. 2142–2152, Sep. 2000.

[120] C. V. Jakowatz, Jr. and D. E. Wahl, "Three-dimensional tomographic imaging for foliage penetration using multiple-pass spotlight-mode SAR," in *Conference Record of the Thirty-Fifth Asilomar Conference on Signals, Systems and Computers*, Pacific Grove, California, USA, Nov. 2001, pp. 121–125.

[121] G. Fornaro, F. Lombardini, and F. Serafino, "Three-dimensional multipass SAR focussing: experiments with long-term spaceborne data," *IEEE Trans. Geosci. Remote Sens.*, vol. 43, no. 4, pp. 702–714, Apr. 2005.

[122] N. Marechal, "High frequency phase errors in SAR imagery and implications for autofocus," in *Proc. IEEE Int. Geosci. Remote Sens. Symp., IGARSS*, Lincoln, USA, May 1996.

[123] D. Geudtner, M. Zink, C. Gierull, and S. Shaffer, "Interferometric alignment of the X-SAR antenna system on the Space Shuttle radar topography mission," *IEEE Trans. Geosci. Remote Sens.*, vol. 40, no. 5, pp. 995–1006, May 2002.

[124] L. C. Graham, "Synthetic interferometer radar for topographic mapping," *Proc. IEEE*, vol. 62, no. 6, pp. 763–768, Jun. 1974.

[125] H. A. Zebker and R. M. Goldstein, "Topographic mapping from interferometric synthetic aperture radar observations," *J. Geophys. Res.*, vol. 91, no. B5, pp. 4993–4999, Apr. 1986.

[126] A. K. Gabriel and R. M. Goldstein, "Crossed orbit interferometry: theory and experimental results from SIR-B," *Int. J. Remote Sens.*, vol. 9, no. 5, pp. 857–872, 1988.

[127] R. M. Goldstein and H. A. Zebker, "Interferometric radar measurement of ocean surface currents," *Nature*, vol. 328, pp. 707–709, Aug. 1987.

[128] R. M. Goldstein, T. P. Barnett, and H. A. Zebker, "Remote sensing of ocean currents," *Science*, vol. 246, pp. 1282–1285, Dec. 1989.

[129] A. K. Gabriel, R. M. Goldstein, and H. A. Zebker, "Mapping small elevation changes over large areas: differential radar interferometry," *J. Geophys. Res.*, vol. 94, no. B7, pp. 9183–9191, Jul. 1989.

[130] T. Strozzi, U. Wegmüller, C. L. Werner, A. Wiesmann, and V. Spreckels, "JERS SAR interferometry for land subsidence monitoring," *IEEE Trans. Geosci. Remote Sens.*, vol. 41, no. 7, pp. 1702–1708, Jul. 2003.

[131] R. M. Goldstein, H. Engelhardt, B. Kamb, and R. M. Frolich, "Satellite radar interferometry for monitoring ice sheet motion: application to an Antarctic ice stream," *Science*, vol. 262, pp. 1525–1530, Dec. 1993.

[132] P. Prats, R. Scheiber, A. Reigber, C. Andres, and R. Horn, "Estimation of the surface velocity field of the Aletsch Glacier using multibaseline airborne SAR interferometry," *IEEE Trans. Geosci. Remote Sens.*, vol. 47, no. 2, pp. 419–430, Feb. 2009.

[133] D. G. Corr and A. Rodrigues, "Coherent change detection of vehicle movements," in *Proc. IEEE Int. Geosci. Remote Sens. Symp., IGARSS*, Seattle, USA, Jul. 1998, pp. 2451–2453.

[134] P. Wright, T. Macklin, C. Willis, and T. Rye, "Coherent change detection with SAR," in *Proc. Eur. Radar Conf., EURAD*, Paris, France, Oct. 2005, pp. 17–20.

[135] L. M. H. Ulander, M. Lundberg, W. Pierson, and A. Gustavsson, "Change detection for low-frequency SAR ground surveillance," *IEE Proc.—Radar Sonar Navig.*, vol. 152, no. 6, pp. 413–420, Dec. 2005.

[136] H. Tarayre and D. Massonnet, "Effects of a refractive atmosphere on interferometric processing," in *Proc. IEEE Int. Geosci. Remote Sens. Symp., IGARSS*, Pasadena, USA, Aug. 1994, pp. 717–719.

[137] R. F. Hanssen, T. M. Weckwerth, H. A. Zebker, and R. Klees, "High-resolution water vapor mapping from interferometric radar measurements," *Science*, vol. 283, pp. 1297–1299, Feb. 1999.

[138] D. Just and R. Bamler, "Phase statistics of interferograms with applications to synthetic aperture radar," *Appl. Opt.*, vol. 33, no. 20, pp. 4361–4368, Jul. 1994.

[139] H. A. Zebker and J. Villasenor, "Decorrelation in interferometric radar echoes," *IEEE Trans. Geosci. Remote Sens.*, vol. 30, no. 5, pp. 950–959, Sep. 1992.

[140] F. K. Li and R. M. Goldstein, "Studies of multibaseline spaceborne interferometric synthetic aperture radars," *IEEE Trans. Geosci. Remote Sens.*, vol. 28, no. 1, pp. 88–97, Jan. 1990.

[141] A. L. Gray and P. J. Farris-Manning, "Repeat-pass interferometry with airborne synthetic aperture radar," *IEEE Trans. Geosci. Remote Sens.*, vol. 31, no. 1, pp. 180–191, Jan. 1993.

[142] H. A. Zebker, C. L. Werner, P. A. Rosen, and S. Hensley, "Accuracy of topographic maps derived from ERS-1 interferometric radar," *IEEE Trans. Geosci. Remote Sens.*, vol. 32, no. 4, pp. 823–836, Jul. 1994.

[143] K. P. Papathanassiou and S. R. Cloude, "Single-baseline polarimetric SAR interferometry," *IEEE Trans. Geosci. Remote Sens.*, vol. 39, no. 11, pp. 2352–2363, Nov. 2001.

[144] S. R. Cloude and K. P. Papathanassiou, "Three-stage inversion process for polarimetric SAR interferometry," *IEE Proc.—Radar Sonar Navig.*, vol. 150, no. 3, pp. 125–134, Jun. 2003.

[145] H. A. Zebker, T. G. Farr, R. P. Salazar, and T. H. Dixon, "Mapping the world's topography using radar interferometry: the TOPSAT mission," *Proc. IEEE*, vol. 82, no. 12, pp. 1774–1786, Dec. 1994.

[146] P. F. Lee and K. James, "The RADARSAT-2/3 topographic mission," in *Proc. IEEE Int. Geosci. Remote Sens. Symp., IGARSS*, Sydney, Australia, Jul. 2001, pp. 499–501.

[147] R. Girard, P. F. Lee, and K. James, "The RADARSAT-2&3 topographic mission: an overview," in *Proc. IEEE Int. Geosci. Remote Sens. Symp., IGARSS*, Toronto, Canada, Jun. 2002, pp. 1477–1479.

[148] R. Caves, A. P. Luscombe, P. F. Lee, and K. James, "Topographic performance evaluation of the RADARSAT-2/3 tandem mission," in *Proc. IEEE Int. Geosci. Remote Sens. Symp., IGARSS*, Toronto, Canada, Jun. 2002, pp. 961–963.

[149] G. Krieger, I. Hajnsek, K. Papathanassiou, M. Eineder, M. Younis, F. De Zan, P. Prats, S. Huber, M. Werner, H. Fiedler, A. Freeman, P. Rosen, S. Hensley, W. Johnson, L. Veilleux, B. Grafmueller, R. Werninghaus, R. Bamler, and A. Moreira, "The Tandem-L mission proposal: monitoring Earth's dynamics with high resolution SAR interferometry," in *Proc. IEEE Radar Conf., RADAR*, May 2009, pp. 1–6.

[150] M. D'Errico and A. Moccia, "The BISSAT mission: a bistatic SAR operating in formation with COSMO/SkyMed X-band radar," in *IEEE Aerospace Conference Proceedings*, 2002, pp. 2–809–2–818.

[151] A. Moccia, G. Rufino, M. D'Errico, G. Alberti, and G. Salzillo, "BISSAT: a bistatic SAR for Earth observation," in *Proc. IEEE Int. Geosci. Remote Sens. Symp., IGARSS*, Toronto, Canada, Jun. 2002, pp. 2628–2630.

[152] A. Renga, A. Moccia, M. D'Errico, S. Dellepiane, E. Angiati, G. Vernazza, P. Lombardo, F. Colone, M. Sedehi, D. Cristallini, S. Pignataro, Q. Rioli, G. Milillo, C. Bruno, F. Di Giogio, and M. Labriola, "From the expected scientific applications to the functional specifications, products and performance of the SABRINA missions," in *Proc. IEEE Radar Conf., RADAR*, Rome, Italy, May 2008.

[153] A. Renga and A. Moccia, "Performance of stereoradargrammetric methods applied to spaceborne monostatic-bistatic synthetic aperture radar," *IEEE Trans. Geosci. Remote Sens.*, vol. 47, no. 2, pp. 544–560, Feb. 2009.

[154] P. Dubois-Fernandez, H. Cantalloube, B. Vaizan, G. Krieger, and A. Moreira, "Airborne bistatic synthetic aperture radar," in *Bistatic Radar: Emerging Technology*, M. Cherniakov, Ed. Wiley, 2008, ch. 5, pp. 159–213.

[155] S. Duque, P. Lopez-Dekker, J. J. Mallorqui, and J. C. Merlano, "Back and forward bistatic interferometry," in *Proc. IEEE Int. Geosci. Remote Sens. Symp., IGARSS*, Boston, USA, Jul. 2008, pp. 601–604.

[156] R. Touzi and A. Lopes, "Statistics of the Stokes parameters and of the complex coherence parameters in one-look and multilook speckle fields," *IEEE Trans. Geosci. Remote Sens.*, vol. 34, no. 2, pp. 519–531, Mar. 1996.

[157] R. Touzi, A. Lopes, J. Bruniquel, and P. W. Vachon, "Coherence estimation for SAR imagery," *IEEE Trans. Geosci. Remote Sens.*, vol. 37, no. 1, pp. 135–149, Jan. 1999.

[158] D. C. Ghiglia and M. D. Pritt, *Two-Dimensional Phase Unwrapping: Theory, Algorithms and Software.* Wiley, 1998.

[159] N. Marechal, "Tomographic formulation of interferometric SAR for terrain elevation mapping," *IEEE Trans. Geosci. Remote Sens.*, vol. 33, no. 3, pp. 726–739, May 1995.

[160] D. Giuli, "Polarisation diversity in radars," *Proc. IEEE*, vol. 74, no. 2, pp. 245–269, Feb. 1986.

[161] W.-M. Boerner, *Introduction to Synthetic Aperture Radar (SAR) Polarimetry.* Wexford Press, 2008.

[162] H. McNairn, J. Shang, X. Jiao, and C. Champagne, "The contribution of ALOS PALSAR multipolarisation and polarimetric data to crop classification," *IEEE Trans. Geosci. Remote Sens.*, vol. 47, no. 12, pp. 3981–3992, Dec. 2009.

[163] M. Santoro, J. E. S. Fransson, L. E. B. Eriksson, M. Magnusson, L. M. H. Ulander, and H. Olsson, "Signatures of ALOS PALSAR L-band backscatter in Swedish forest," *IEEE Trans. Geosci. Remote Sens.*, vol. 47, no. 12, pp. 4001–4019, Dec. 2009.

[164] Y. Oh, "Quantitative retrieval of soil moisture content and surface roughness from multipolarised radar observations of bare soil surfaces," *IEEE Trans. Geosci. Remote Sens.*, vol. 42, no. 3, pp. 596–601, Mar. 2004.

[165] K. Nakamura, H. Wakabayashi, K. Naoki, F. Nishio, T. Moriyama, and S. Uratsuka, "Observation of sea-ice thickness in the Sea of Okhotsk by using dual-frequency and fully polarimetric airborne SAR (Pi-SAR) data," *IEEE Trans. Geosci. Remote Sens.*, vol. 43, no. 11, pp. 2460–2469, Nov. 2005.

[166] M. Migliaccio, A. Gambardella, F. Nunziata, M. Shimada, and O. Isoguchi, "The PALSAR polarimetric mode for sea oil slick observation," *IEEE Trans. Geosci. Remote Sens.*, vol. 47, no. 12, pp. 4032–4041, Dec. 2009.

[167] J.-C. Souyris, P. Imbo, R. Fjørtoft, S. Mingot, and J.-S. Lee, "Compact polarimetry based on symmetry properties of geophysical media: the $\pi/4$ mode," *IEEE Trans. Geosci. Remote Sens.*, vol. 43, no. 3, pp. 634–646, Mar. 2005.

[168] R. K. Raney, "Dual-polarised SAR and Stokes parameters," *IEEE Geosci. Remote Sens. Lett.*, vol. 3, no. 3, pp. 317–319, Jul. 2006.

[169] R. K. Raney, "Hybrid-polarity SAR architecture," *IEEE Trans. Geosci. Remote Sens.*, vol. 45, no. 11, pp. 3397–3404, Nov. 2007.

[170] P. C. Dubois-Fernandez, J.-C. Souyris, S. Angelliaume, and F. Garestier, "The compact polarimetry alternative for spaceborne SAR at low frequency," *IEEE Trans. Geosci. Remote Sens.*, vol. 46, no. 10, pp. 3208–3222, Oct. 2008.

[171] A. L. Gray, P. W. Vachon, C. E. Livingstone, and T. I. Lukowski, "Synthetic aperture radar calibration using reference reflectors," *IEEE Trans. Geosci. Remote Sens.*, vol. 28, no. 3, pp. 374–383, May 1990.

[172] J. J. van Zyl, B. D. Chapman, P. Dubois, and J. Shi, "The effect of topography on SAR calibration," *IEEE Trans. Geosci. Remote Sens.*, vol. 31, no. 5, pp. 1036–1043, Sep. 1993.

[173] S. H. Yueh, J. A. Kong, R. M. Barnes, and R. T. Shin, "Calibration of polarimetric radars using in-scene reflectors," *J. Electromagn. Waves Appl.*, vol. 4, no. 1, pp. 27–48, 1990.

[174] K. Sarabandi, F. T. Ulaby, and M. A. Tassoudji, "Calibration of polarimetric radar systems with good polarisation isolation," *IEEE Trans. Geosci. Remote Sens.*, vol. 28, no. 1, pp. 70–75, Jan. 1990.

[175] K. Sarabandi and F. T. Ulaby, "A convenient technique for polarimetric calibration of single-antenna radar systems," *IEEE Trans. Geosci. Remote Sens.*, vol. 28, no. 6, pp. 1022–1033, Nov. 1990.

[176] M. W. Whitt and F. T. Ulaby, "A polarimetric radar calibration technique with insensitivity to target orientation," *Radio Sci.*, vol. 25, no. 6, pp. 1137–1143, Nov./Dec. 1990.

[177] J. D. Klein and A. Freeman, "Quadpolarisation SAR calibration using target reciprocity," *J. Electromagn. Waves Appl.*, vol. 5, no. 7, pp. 735–751, 1991.

[178] W. Wiesbeck and D. Kähny, "Single reference, three target calibration and error correction for monostatic, polarimetric free space measurements," *Proc. IEEE*, vol. 79, no. 10, pp. 1551–1558, Oct. 1991.

[179] K. Sarabandi, Y. Oh, and F. T. Ulaby, "Measurement and calibration of differential Mueller matrix of distributed targets," *IEEE Trans. Antennas Propag.*, vol. 40, no. 12, pp. 1524–1532, Dec. 1992.

[180] C. M. H. Unal, R. J. Niemeijer, J. S. van Sinttruyen, and L. P. Ligthart, "Calibration of a polarimetric radar using a rotatable dihedral corner reflector," *IEEE Trans. Geosci. Remote Sens.*, vol. 32, no. 4, pp. 837–845, Jul. 1994.

[181] J.-R. J. Gau and W. D. Burnside, "New polarimetric calibration technique using a single calibration dihedral," *IEE Proc.—Microw. Antennas Propag.*, vol. 142, no. 1, pp. 19–25, Feb. 1995.

[182] W. Xiong, "Polarimetric calibration using a genetic algorithm," *IEEE Geosci. Remote Sens. Lett.*, vol. 4, no. 3, pp. 421–425, Jul. 2007.

[183] A. Freeman, Y. Shen, and C. L. Werner, "Polarimetric SAR calibration experiment using active radar calibrators," *IEEE Trans. Geosci. Remote Sens.*, vol. 28, no. 2, pp. 224–240, Mar. 1990.

[184] J. J. van Zyl, "Calibration of polarimetric radar images using only image parameters and trihedral corner reflector responses," *IEEE Trans. Geosci. Remote Sens.*, vol. 28, no. 3, pp. 337–348, May 1990.

[185] A. Freeman, J. J. van Zyl, J. D. Klein, H. A. Zebker, and Y. Shen, "Calibration of Stokes and scattering matrix format polarimetric SAR data," *IEEE Trans. Geosci. Remote Sens.*, vol. 30, no. 3, pp. 531–539, May 1992.

[186] K. Sarabandi, "Calibration of a polarimetric synthetic aperture radar using a known distributed target," *IEEE Trans. Geosci. Remote Sens.*, vol. 32, no. 3, pp. 575–582, May 1994.

[187] K. Sarabandi, L. E. Pierce, Y. Oh, M. C. Dobson, F. T. Ulaby, A. Freeman, and P. Dubois, "Cross-calibration experiment of JPL AIRSAR and truck-mounted polarimetric scatterometer," *IEEE Trans. Geosci. Remote Sens.*, vol. 32, no. 5, pp. 975–985, Sep. 1994.

[188] K. Sarabandi, L. E. Pierce, M. C. Dobson, F. T. Ulaby, J. M. Stiles, T. C. Chiu, R. De Roo, R. Hartikka, A. Zambetti, and A. Freeman, "Polarimetric calibration of SIR-C using point and distributed targets," *IEEE Trans. Geosci. Remote Sens.*, vol. 33, no. 4, pp. 858–866, Jul. 1995.

[189] M. Fujita, T. Masuda, Y. Fujino, and M. Satake, "Polarimetric calibration of the SIR-C C-band channel using active radar calibrators and polarisation selective dihedrals," *IEEE Trans. Geosci. Remote Sens.*, vol. 36, no. 6, pp. 1872–1878, Nov. 1998.

[190] A. Freeman, "Calibration of linearly polarised polarimetric SAR data subject to Faraday rotation," *IEEE Trans. Geosci. Remote Sens.*, vol. 42, no. 8, pp. 1617–1624, Aug. 2004.

[191] J. C. Mura, A. H. Correia, and C. C. Freitas, "A new unified approach to channel imbalance and cross-talk calibration of polarimetric data," in *Proc. IEEE Int. Geosci. Remote Sens. Symp., IGARSS*, Denver, USA, Jul./Aug. 2006, pp. 1273–1275.

[192] M. Satake, T. Matsuoka, T. Umehara, A. Nadai, S. Uratsuka, and H. Fukuchi, "Polarimetric calibration experiment of ALOS PALSAR with polarisation selective-dihedrals," in *Proc. IEEE Int. Geosci. Remote Sens. Symp., IGARSS*, Barcelona, Spain, Jul. 2007, pp. 1596–1598.

[193] H. Kimura, "Calibration of polarimetric PALSAR imagery affected by Faraday rotation using polarisation orientation," *IEEE Trans. Geosci. Remote Sens.*, vol. 47, no. 12, pp. 3943–3950, Dec. 2009.

[194] R. Touzi and M. Shimada, "Polarimetric PALSAR calibration," *IEEE Trans. Geosci. Remote Sens.*, vol. 47, no. 12, pp. 3951–3959, Dec. 2009.

[195] M. W. Whitt, F. T. Ulaby, P. Polatin, and V. V. Liepa, "A general polarimetric radar calibration technique," *IEEE Trans. Antennas Propag.*, vol. 39, no. 1, pp. 62–67, Jan. 1991.

[196] D. Kähny, K. Schmitt, and W. Wiesbeck, "Calibration of bistatic polarimetric radar systems," *IEEE Trans. Geosci. Remote Sens.*, vol. 30, no. 5, pp. 847–852, Sep. 1992.

[197] W. Wiesbeck and S. Riegger, "A complete error model for free space polarimetric measurements," *IEEE Trans. Antennas Propag.*, vol. 39, no. 8, pp. 1105–1110, Aug. 1991.

[198] T.-J. Chen, T.-H. Chu, and F.-C. Chen, "A new calibration algorithm of wide-band polarimetric measurement system," *IEEE Trans. Antennas Propag.*, vol. 39, no. 8, pp. 1188–1192, Aug. 1991.

[199] T.-J. Chen and T.-H. Chu, "Calibration of wide-band polarimetric measurement system using three perfectly polarisation-isolated calibrators," *IEEE Trans. Antennas Propag.*, vol. 40, no. 12, pp. 1573–1576, Dec. 1992.

[200] S. V. Nghiem, S. H. Yueh, R. Kwok, and F. K. Li, "Symmetry properties in polarimetric remote sensing," *Radio Sci.*, vol. 27, no. 5, pp. 693–711, Sep./Oct. 1992.

[201] R. A. Cordey, "On the accuracy of crosstalk calibration of polarimetric SAR using natural clutter statistics," *IEEE Trans. Geosci. Remote Sens.*, vol. 31, no. 2, pp. 447–454, Mar. 1993.

[202] H. Skriver, J. Dall, and S. Nørvang Madsen, "External polarimetric calibration of the Danish polarimetric C-band SAR," in *Proc. IEEE Int. Geosci. Remote Sens. Symp., IGARSS*, Pasadena, USA, Aug. 1994, pp. 1105–1107.

[203] H. Kimura, T. Mizuno, K. P. Papathanassiou, and I. Hajnsek, "Improvement of polarimetric SAR calibration based on the Quegan algorithm," in *Proc. IEEE Int. Geosci. Remote Sens. Symp., IGARSS*, Anchorage, USA, Sep. 2004, pp. 184–187.

[204] C. López-Martinez, A. Cortés, and X. Fàbregas, "Analysis and improvement of polarimetric calibration techniques," in *Proc. IEEE Int. Geosci. Remote Sens. Symp., IGARSS*, Barcelona, Spain, Jul. 2007.

[205] D. J. McLaughlin, Z. Ren, and Y. Wu, "A bistatic polarimeter calibration technique," *IEEE Trans. Geosci. Remote Sens.*, vol. 33, no. 3, pp. 796–799, May 1995.

[206] H. A. Zebker, J. J. van Zyl, and D. N. Held, "Imaging radar polarimetry from wave synthesis," *J. Geophys. Res.*, vol. 92, no. B1, pp. 683–701, Jan. 1987.

[207] R. Touzi, C. E. Livingstone, J. R. C. Lafontaine, and T. I. Lukowski, "Consideration of antenna gain and phase patterns for calibration of polarimetric SAR data," *IEEE Trans. Geosci. Remote Sens.*, vol. 31, no. 6, pp. 1132–1145, Nov. 1993.

[208] A. Freeman, "A new system model for radar polarimeters," *IEEE Trans. Geosci. Remote Sens.*, vol. 29, no. 5, pp. 761–767, Sep. 1991.

[209] A. Freeman, "An algorithm for estimating the noise levels in polarimetric SAR image data," *IEEE Trans. Geosci. Remote Sens.*, vol. 30, no. 6, pp. 1107–1121, Nov. 1992.

[210] D. R. Sheen, E. L. Johansen, L. P. Elenbogen, and E. S. Kasischke, "The gridded trihedral: a new polarimetric SAR calibration reflector," *IEEE Trans. Geosci. Remote Sens.*, vol. 30, no. 6, pp. 1149–1153, Nov. 1992.

[211] J.-S. Lee, D. L. Schuler, and T. L. Ainsworth, "Polarimetric SAR data compensation for terrain azimuth slope variation," *IEEE Trans. Geosci. Remote Sens.*, vol. 38, no. 5, pp. 2153–2163, Sep. 2000.

[212] G. Fornaro, V. Pascazio, and G. Schirinzi, "Resolution improvement via multipass SAR imaging," in *Proc. IEEE Int. Geosci. Remote Sens. Symp., IGARSS*, Sydney, Australia, Jul. 2001, pp. 2734–2736.